2018

Macromolecular soft templates for synthesis and self-assembly of functional nanomaterials

Srikanth Nayak
Iowa State University

Macromolecular soft templates for synthesis and self-assembly of functional nanomaterials

by

Srikanth Nayak

A dissertation submitted to the graduate faculty

in partial fulfillment of the requirements for the degree of

DOCTOR OF PHILOSOPHY

Major: Chemical Engineering

Program of Study Committee:
Surya Mallapragada, Major Professor
Alex Travesset
Andrew Hillier
Derrick K Rollins
Ian C Schneider

The student author, whose presentation of the scholarship herein was approved by the program of study committee, is solely responsible for the content of this dissertation. The Graduate College will ensure this dissertation is globally accessible and will not permit alterations after a degree is conferred.

Iowa State University

Ames, Iowa

2018

TABLE OF CONTENTS

Page

LIST OF TABLES

Page

LIST OF FIGURES

Page

ACKNOWLEDGEMENTS

There are many people who have played significant roles in shaping me as a researcher and in producing the work presented here. I would like to take this opportunity to specifically thank those individuals who collectively provided the scaffold on which I could build this dissertation.

I wish to express my most sincere gratitude to Dr. Mallapragada for her prudent guidance and constant support throughout my Ph.D studies. I thank her for being a role model in the conduct of research and training me to be a self-sufficient researcher. I would also like to thank my program of study committee members: Dr. Andrew C Hillier, Dr. Derrick K Rollins, Dr. Alex Travesset, and Dr. Ian C Schneider for their valuable guidance and support.

I also would like to offer my appreciation to all my collaborators in the bioinspired materials project at DMSE, Ames Laboratory. I thank Dr. David Vaknin for his patience in training me, helping me in developing research ideas and his invaluable help in improving my writing, Dr. Alex Travesset for his research insight and many helpful discussions, Dr. Wenjie Wang for his help in data analysis and constant emotional support. I thank all other collaborators including Nathan Horst, Max Fieg, Dr. Wei Bu, Dr. Marit Nilsen-Hamilton, Dr. Andrew Hillier, Dr. Mufit Akinc, Dr. Thomas Koschny, Dr. Tanya Prozorov, Dr. Pierre E. Palo, Dr. Lee Bendickson and Dr. Alejandra Londono-Calderon for their kind collaborations.

I would like to thank the current and former members of Dr. Mallapragada's group: Dr. Xunpei Liu, Dr. Justin Adams, Dr. Honghu Zhang, Dr. Metin Uz, Benjamin Schlichtmann, and Sujata Senapati. In particular, I would like to thank Dr. Honghu Zhang for teaching me many things both inside and outside the lab, and for his constant encouragement. I am also fortunate to have worked with undergraduate students who enthusiastically (I hope!) reduced some of the burden while working in the lab. Specifically, I would like to thank Maya Harris, Grace Elonen, Ju Hyung Jung, Ahsas Malik Bermudez, and Jonah Brown from Dr. Mallapragada's group, and Jack Lawrence from Dr. Vaknin's group.

On a personal note, I would like to thank all my friends in Ames who have made my stay here particularly enjoyable and relaxing, and for being my safety valve. Special thanks to my roommate of more than five years, Amarsagar Reddy, for his jovial company, and for his convenient and arcane knowledge of the second law with regards to housekeeping. Finally, I would not be who I am today without my parent's support. I am deeply grateful to my mother for being my rock.

This work was supported by the U.S. Department of Energy (DOE), Office of Basic Energy Sciences at the Ames Laboratory under contract number DE-C02-07CH11358. Ames Laboratory is operated for the DOE by Iowa State University. The document number assigned to this thesis/dissertation is IS-T 3256.

ABSTRACT

Nanostructured composite materials made of organic matrices and inorganic nanoparticles (NPs) represent the new paradigm of functional hybrid materials. This dissertation is focused on the synthesis and self-assembly of NPs within organic matrices which act as templates, targeting the formation of use-inspired structures. Particularly, self-assembly of macromolecules such as proteins and polymers, and polymer-functionalized NPs is utilized to create ordered assemblies of NPs. Inspired by the formation of chains of magnetic NPs in a group of bacteria referred to as Magnetotactic bacteria, we used Mms6, a biomineralization protein, as a template towards the formation of self-assembled arrays of magnetic NPs. Surface sensitive techniques such as atomic force microscopy, scanning electron microscopy and X-ray photoelectron spectroscopy, show the formation of these arrays on solid substrates. An alternative to the use of templates is to directly control the interactions between the NPs. In the presence of short dithiol tethers, gold nanoparticles crosslink covalently and form assemblies with short ranged FCC-like order. PEG functionalized nanoparticles, obtained by ligand exchange procedure, form a crystalline monolayer at the vapor-liquid interface in the presence of electrolytes in the suspension. In the presence of a complexing polymer (specifically, neutral PAA) the crystallinity of these monolayers decreases and NPs aggregate in the bulk. Analysis of these aggregates shows that in contrast to the covalent linkage, non-covalent interactions (hydrogen bonds and van der Waal's forces, via inter-polymer complexes) between the poly(ethylene glycol) (PEG) functionalized NPs, lead to the formation of FCC superlattices of NPs. Theoretical considerations of the variation of inter-particle distances show the significance of van der Waal's forces in these superlattices. Self-assembly processes used to create ordered assemblies of nanoparticles developed here are promising routes to fabricate functional nanomaterials such as metamaterials.

CHAPTER 1. GENERAL INTRODUCTION

1.1 Introduction

Nanomaterials and nanotechnology are focused research areas in the quest for fabrication of functional materials with tailorable properties. In fact, there have been many commercial successes for nanotechnology in diverse fields such as healthcare, coatings, electronics etc. In fabricating such devices, there are three main features of the nanomaterial that account for its functional properties. They are: 1) composition, 2) morphology of nanoparticles (NPs), and 3) assembly properties, i.e. correlations in inter-particle positions of the NPs. Although there has been tremendous progress in synthesizing nanoparticles with a variety of chemical compositions and morphology, creating ordered structures of nanoparticles with particle level control remains a major challenge. In addition, synthesis of nanoparticles with complex morphologies, such as a ring, for example, is a major technical hurdle in the fabrication of functional nanodevices. The work reported in this dissertation is a collection of our efforts towards using macromolecules to address the challenges in synthesis and assembly of nanoparticles.

There are broadly two approaches to create ordered structures at the nanoscale: top-down and bottom-up. In top-down approach a bulk material is reduced to smaller structures and this approach includes techniques such as electron beam lithography and photolithography. Bottom-up approach utilizes self-assembly of smaller units to build larger nanostructures. Top down methods are generally more expensive and time consuming compared to the bottom up methods. Thus self-assembly is expected to play a major role in the scalable fabrication of novel functional materials.[1,2]

Self-assembly refers to the process by which individual chemical moieties interact non-covalently with other moieties to form well-ordered structures, reproducibly and in the absence of external agents. Self-assembly can occur at multiple levels of physical dimensions; for example, alkyl thiols self-assemble on gold at a sub-nanometer scale[3] whereas the self-assembly of Janus particles

occurs at a micrometer scale.[4] Integrating such multiple levels of self-assembly hierarchically can lead to structures whose properties can be tuned at multiple length scales. Such tunable structures are attractive in a wide range of fields such as photonics,[5] nanoelectronics[6,7] and chemical/bio sensors.[8,9]

Self-assembly is an ubiquitous phenomenon in nature, and biology, in particular, is replete with self-assembling structures. Macromolecules such as proteins, DNA and cellulose self-assemble into various structures that provide unique functional properties to the organisms. These structures have nanoscale features making them ideal for applications in nanotechnology. Inspired by this, self-assembly of macromolecules (natural or synthetic) has been applied towards fabrication of ordered nanomaterials. For the fabrication of inorganic nanocomposites in particular, self-assembly of macromolecules is used as a template to direct the synthesis and assembly of inorganic nanoparticles. Another approach is to use the macromolecules as surface modifiers on the pre-synthesized nanoparticles and induce assembly of the nanoparticles by tuning the interparticle interactions via the macromolecules. The second approach includes solvent evaporation, DNA base-pairing, and covalent cross-linking among other methods.

1.2 Overall Objectives

The overall objective of this work is to demonstrate different strategies to synthesize and assemble nanoparticles into ordered structures with functional properties. Specifically, we explore the use of macromolecules as templates for the assembly of nanoparticles. The specific goals of this work are to:

1. utilize self-assembled structures of biological macromolecules as templates for controlled synthesis of nanoparticles

2. develop a synergy of top-down approaches such as soft lithography with self-assembly, and thus to combine the high precision of top-down approaches with the advantages of bottom-up methods,

3. develop methods to assemble nanoparticles suspended in solutions into two and three dimensional superlattices with controllable lattice features such as inter-particle distances, utilizing the tunable properties of macromolecules such as polymers, and

4. evaluate the effect of material properties such as nanoparticle size, polymer molecular weight and solution conditions on the assembly formation and its structural properties.

Materials characterization techniques such as atomic force microscopy (AFM), X-ray photoelectron spectroscopy (XPS), scanning (transmission) electron microscopy (S/TEM) and X-ray scattering methods are used to study the structural properties of the assemblies.

1.3 Dissertation Organization

This dissertation is organized into 7 chapters. Chapter 2 provides a review of the recent literature on the use of various macromolecular templates for the synthesis and assembly of nanomaterials. Chapter 3 is modified from a paper published in *RSC Advances*. In this paper, Mms6, is used as a template towards the formation of self-assembled arrays of magnetic NPs by employing a combination approach of soft-lithography and biomimetic crystallization. This work is well aligned with goals 1 and 2, namely, the templated synthesis of nanoparticles and their assembly using a synergistic approach. The subsequent three chapters are particularly aimed at addressing objectives 3 and 4, namely, polymer-mediated self-assembly of suspended nanoparticles into superlattices. Chapter 4 focuses on the use of short, water soluble dithiol chains to obtain cross-linked assemblies of gold nanoparticles. This work is published in the journal *Particles and Particle Systems Characterization*. In Chapter 5, self-assembly of poly(ethylene glycol) functionalized gold nanoparticles at the vapor-liquid interface induced by electrolytes and the effect of inter-polymer complexation on the formed assemblies are examined. Results from this work are submitted for publication in the journal *Langmuir*. Chapter 6 demonstrates the use of inter-polymer complexation as a strategy for self-assembly of nanoparticles into three dimensional crystalline lattices. This work is under review for publication in the *Journal of Physical Chemistry C*. Chapter 7 provides ma-

jor conclusions of this dissertation and some perspectives on the proposed future work relating to polymer-mediated assembly of nanoparticles.

References

[1] Whitesides, G. M., Mathias, J. P., and Seto, C. T. *Science* **254**(5036), 1312–1319 (1991).

[2] Whitesides, G. M. and Grzybowski, B. *Science* **295**(5564), 2418–2421 (2002).

[3] Nuzzo, R. G., Zegarski, B. R., and Dubois, L. H. *Journal of the American Chemical Society* **109**(3), 733–740 (1987).

[4] Walther, A. and Müller, A. H. E. *Chemical reviews* **113**(7), 5194 (2013).

[5] Wang, H. and Zhang, K. Q. *Sensors* **13**(4), 4192–4213 (2013).

[6] Dupraz, C. J. F., Nickels, P., Beierlein, U., Huynh, W. U., and Simmel, F. C. *Superlattices and Microstructures* **33**(5), 369–379 (2003).

[7] Welser, J., Bourianoff, G., Zhirnov, V., and Cavin, R. *An Interdisciplinary Forum for Nanoscale Science and Technology* **10**(1), 1–10 (2008).

[8] Yonzon, C. R., Stuart, D. A., Zhang, X., McFarland, A. D., Haynes, C. L., and Van Duyne, R. P. *Talanta* **67**(3), 438–448 (2005).

[9] Paul, A. *Nature Biotechnology* **22**(1), 47 (2003).

CHAPTER 2. LITERATURE REVIEW

2.1 Introduction

This chapter reviews some of the major developments in the synthesis and fabrication of ordered assemblies of nanoparticles, as relevant to the work presented in this report. Broadly, templated synthesis and templated assembly of nanoparticles are discussed. With respect to templated synthesis, biomimetic mineralization and polymer-mediated synthesis are discussed. Templated assembly of nanoparticles with biomolecules and polymers is reviewed in the penultimate section. The last section discuses some of the potential applications of assemblies of ordered nanoparticles in the context of presented work.

2.2 Templated synthesis of nanoparticles

Over the years a number of strategies for templated synthesis of nanoparticles have been studied.[1] Templating agents can act as reducing agents, stabilizers and scaffolds for the growth of nanoparticles and thus influence the morphology of the nanoparticles.[2] A review of templated synthesis of nanoparticles with soft macromolecular templates such as proteins and polymers is presented here.

2.2.1 Templated synthesis of nanoparticles with biomineralization proteins and peptides

2.2.1.1 Biomineralization in nature

Biomineralization processes, wherein complex structures of inorganic materials is achieved within organic matrices by various organisms, have been a rich source of ideas and inspirations for the material chemists.[3] There has been intensive research over the past decade in the field of in vivo biomineralization and in vitro biomimetic mineralization.[1,4–12] Some examples of biomineralization include the formation of bones and cartilages in birds and mammals, shells of the

mollusks, cell walls in diatoms and magnetic crystals in magnetotactic bacteria. Bones and cartilages inorganic composites of hydroxyapatite, shells are made of calcium carbonate, and the cell walls of diatoms are made of amorphous silica. The organic matrix includes macromolecules such as proteins, lipids and polysaccharides.[4,13] Typically, the organisms have genetic control over the formation of these biomineral composites.

Biomineralization involves the classic steps involved in crystallization i.e., nucleation and growth. Adsorption of surface active organic molecules like proteins on the growing nuclei can direct the formation of the crystals or inorganic aggregates.[10,14] These surface active molecules can lead to the formation of crystal morphologies that are not stable otherwise, by step-wise reduction of energy barriers. Thus the final crystal morphology is dictated by the kinetics of biomineralization rather than the thermodynamic driving forces.[2] These surface active molecules typically favor growth of certain crystal morphologies selectively. In addition some organisms can also inhibit crystallization over a period of time leading to a metastable equilibrium.[15] It is thought that the organic molecules form templates, presenting charged groups on which the precursor ions from the solution adsorb.[4] Adsorption of counter ions and the repetitions of this procedure finally results in the formation of a crystalline lattice. Presence of acidic groups on many of the biomineralization proteins supports this hypothesis.[16–18] On the other hand, it has also been suggested that the organic molecules and the preformed nuclei co-assemble to form the ordered structures.[10] Formation of amorphous or short range ordered precursors before crystallization is also a common occurrence in biomineralization.[5,19,20]

2.2.1.2 Biomineralization in magnetotactic bacteria

Magnetotactic bacteria refers to a group of bacteria that biologically produce magnetic crystals in their cells which enables them to swim (preferentially) along the geomagnetic field lines. Since their discovery in 1975,[21] magnetotactic bacteria have been studied by researchers in multiple disciplines such as microbiology, physics, and material science. There have been several review articles written on the science and applications of biomineralization in magnetotactic bacteria.[8,22–33] Magnetic bacteria have an intracellular protein rich organelles called the magnetosome which

templates and houses the magnetic crystals. Within these magnetosomes, ordered structures of single domain magnetite nanoparticles and ferromagnetic greigite (Fe_3S_4) have been observed in numerous species of bacteria.[22,24,34] The shape and sizes of the particles is genetically controlled and is species specific. The magnetosome membranes are formed by invagination of the cell membrane and they enable high local concentration of inorganic precursors which is essential for the formation of magnetic crystals. Formation of magnetosome membranes and the magnetic crystals in them is an area of active research[33] and though much has been discovered about the significance of different agents involved such as membrane proteins, concrete understanding of the full process still eludes the researchers. Several membrane proteins that are instrumental in the biomineralization steps such as the formation of a filamental scaffold,[35] attachment of the magnetosome to the membrane,[35] iron transport[36] and size and shape control of the magnetic crystal[17,37] have been identified.

2.2.1.3 Biomimetic in vitro synthesis of nanomaterials

Bottom-up chemical routes inspired from such biological processes, offer a level of control in the fabrication of nanostructures that cannot be obtained with top-down approaches. Excellent reviews on biomineralization[4,5,7,38–42] and biomimetic mineralization have been presented.[2,9,10,12,43] Attempts to mimic biomineralization in laboratory settings have generally proceeded in two directions: with only synthetic chemicals and substrates that mimic the biological systems, or with a combination of synthetic chemicals and natural biological macromolecules that are active in biomineralization. Biological templates obtained directly from living organisms have been used to simulate biomineralization in vitro, when effective mimics for the biological templating agents are difficult to design. For example, membrane proteins of magnetotactic bacteria have been used to template the formation of magnetite nanoparticles, while collagen,[44] fibronectin and elastin[45] have been used to template the formation of calcium phosphate minerals. Mimicking the mineralization of bone, collagens have been used to template the formation of collagen-hydroxyapatite nanocomposites.[46–49] Silicatein filaments have been used as templates for the in vitro formation of oxides of silicon and titanium and gallium.[50–52]

2.2.1.4 Bioinspired and biomimetic in vitro synthesis of magnetite using biomineralization

Of the several membrane proteins found in magnetotactic bacteria Mms6 from Magnetospirillum magneticum strain AMB-1 has been found to control the size and shape of magnetite nanoparticles that form in the magnetosome membrane.[17] In contrast, inorganic room temperature synthesis procedures like co-precipitation produce multi-domain particles with large polydispersity in size and shape. Thus, Mms6 has been an attractive macromolecule to template the formation of magnetite nanoparticles in vitro. Mms6 is an amphiphilic protein found attached to the surfaces of magnetite nanoparticles in the magnetosomes. It has a hydrophobic N-terminus and a hydrophilic C-terminal that is rich in carboxylic acid groups.[17] Mms6 forms micelles in water due to its amphiphilicity and has a net negative charge at neutral pH.[17] Wang et.al., have shown that the micelles have molecular weight in the range of 200kDa – 400kDa with each micelle having approximately 20-40 Mms6 monomeric units.[53] Small angle X-ray scattering studies have shown that the micelles respond to the addition of iron ions in solution, forming larger disc like aggregates.[54] Iron binding of was found to be pH dependent, with low binding at low pH possibly due to the protonation of carboxylic acids.[53] In situ transmission electron microscopy studies on iron binding to Mms6 has shown the formation of an amorphous precursor to magnetite on the surface of the Mms6 micelle.[55] The carboxyl rich C terminal has been found to be crucial in the binding of iron ions to the protein.[17,56] By studying the micellar structure of Mms6 and its mutants in water, this study also suggested that disrupting the amino acid sequence in the C-terminal domain caused disruptions in the multimeric structures. Thus Mms6 appears to have an integrated structure that is structurally as well as functionally responsive to iron ions.[53,56]

Room temperature co-precipitation (RTCP) and a hydrothermal method, partial oxidation of ferrous hydroxide (POFH), have been tested for biomimetic synthesis procedures for magnetite nanoparticles.[17,57,58] Both the methods are water-based and require anoxic conditions. Membrane proteins, especially, Mms6 from magnetosomes have been used as the templating agents for the formation of magnetite nanoparticles. Uniform superparamagnetic magnetite crystals around 30 nm in size were reported with RTCP method in the presence of Mms6 and recombinant Mms6.[17,58]

In order to enhance the magnetic coercivity of the formed particles, cobalt has been introduced in the reaction leading to the formation of cobalt doped ferrite particles.[59] Cobalt doping in presence of Mms6 with RTCP increases the crystallinity of the nanoparticles.[60] Synthetic peptides mimicking the C-terminal domain of Mms6 have also been used to template the formation of cobalt ferrite particles. Peptides covalently bound to a gel-forming triblock copolymer were found to template formation of larger crystals.[59]

2.2.2 Other biomolecules as biological templates for nanoparticle synthesis

Other biomolecules such as peptides and entire cells have also been used as templates in nanoparticle synthesis. Peptides, prokaryotic and eukaryotic cells have been used in the synthesis of nanoparticles of gold,[61–63] silver[64–67] and semiconductors such as CdS.[68] Rationally designed peptides with the objective of nanomaterial synthesis have been reported in the literature. For example, synthetic peptides containing redox active tyrosine residues were found to reduce and stabilize gold and silver nanoparticles.[69–72] Synthesis of inorganic nanoparticles using naturally occurring and synthetic peptides were reviewed by Chun-Long et. al.[73] Polysaccharides such as chitosan have also been used for templating the formation of nanoparticles. Chitosan and starch have been used to template the formation of iron oxide nanoparticles.[74] Chitosan and heparin were separately used to reduce and stabilize gold and silver nanoparticles.[75,76] Use of polysaccharides as templates for the synthesis of inorganic nanoparticles has been reviewed by Ling et. al.[77]

2.2.3 Polymer mediated synthesis of nanoparticles

Polymers are widely used in the synthesis, stabilization and assembly of nanoparticles. Nanoparticles can be functionalized with polymers in various ways such as polymer capped synthesis, post synthesis ligand exchange, polymer grafting from the nanoparticle surface and physical adsorption.[78] Polymers can act as reducing agents or capping agents or both during the formation of nanoparticles. They can stabilize the formed nanoparticles by charge, steric effects and/or favorable interactions with the solvent. The combination of reducing agent and the stabilizing agent

affects the morphology of the particles formed. For example, reduction of silver nitrate with ascorbic acid results in the formation of different particle morphologies with different stabilizing agents: rice ball like particles with Pluronic, leaf like structures with poly(vinyl pyrrolidone) (PVP),[79] and nearly spherical nanoparticles with citrate.[80] Several such combinations of synthesis conditions have also been reported for controlling the size and shape of silver nanoparticles[81–83] and gold nanoparticles.[84]

Block copolymers (bcp) are especially attractive in the synthesis and assembly of polymer nanocomposites due to their inherent ability to form nanoscale domains.[85,86] Block copolymers with blocks of poly(styrene) (PS), poly(acrylic acid) (PAA), poly (4-vinyl pyridine) (P4VP) and poly(ethylene oxide) (PEO) are commonly used in the synthesis of metal nanoparticles.[87] Heteroatoms in these polymers such as oxygen in PEO and nitrogen in PVP stabilize the nanoparticles by forming complexes.[88] Hydrogels such as poly(acrylamide) (PAAm) gels and have also been used as templates for the formation of nanoparticles.[89–92]

2.2.3.1 Synthesis of gold nanoparticles with Pluronic block copolymers

Pluronic is the commercial name of a group of triblock copolymers of polyethers with poly(ethylene oxide) and poly(propylene oxide) blocks. Pluronic polymers have ABA type linear architecture with poly(ethylene oxide) (PEO) as the A block and poly(propylene oxide) (PPO) as the B block. Due to the Lower Critical Solution Temperature (LCST) behavior of PEO and PPO, Pluronics show amphiphilic behavior at a range of temperature and solution concentrations. LCST depends on the chain length and the monomeric unit. The higher LCST of PEO block (70 - 90 ^{o}C) compared to that of PPO (2 - 8 ^{o}C) makes the PPO block more hydrophobic, and this leads to the micro – phase separation in water and thus the formation of micelles and physically entangled gels.

Pluronic solutions have been used as structure directing templates in the formation of gold[93] and silver nanoparticles.[94,95] An interpenetrating network of Pluronic and PAAm hydrogel was used as a template for the in situ formation of silver nanoparticles by reducing silver nitrate with sodium borohydride.[96] The concentration of silver nanoparticles in the hydrogel was found to increase with the Pluronic concentration.

In situ formation of gold nanoparticles in Pluronic solutions without any additional reducing or stabilizing agent was first demonstrated in 2004 by Sakai et. al.[93] Interestingly, poly(ethylene oxide) solutions were found to be ineffective for the formation of gold nanoparticles. Chain length of both PEO and PPO blocks were found to affecting the kinetics of nanoparticle formation. They proposed the following mechanism for the formation (Fig. 7.8):[97] 1) reduction of $AuCl_4^{-1}$ by psuedo-crown ether structures formed by Pluronic around the metal ion, 2) Absorption of Pluronic chains on the forming gold cluster and further reduction of $AuCl_4^{-1}$ on the cluster surface, and 3) growth and stabilization of the nanoparticle. A pseudo first order rate equation was proposed for the depletion of $AuCl_4^{-1}$ ions. Reducing activity of Pluronic was found to increase with increasing PEO content, which is in accordance with the increasing psuedo-crown ether formations in solution. With increasing $AuCl_4^{-1}$ concentration, formation of large single crystalline triangular and hexagonal nanoparticles was observed and was attributed to the selective adsorption of Pluronic chains on crystallographic planes of the seed particles.[98]

In summary, nanoparticle seed formation is influenced by the Pluronic chain conformation (which depends on specific pluronic type and its concentration in water) and the interaction between the PEO blocks and $AuCl_4^{-1}$ (which depends on solvent quality and temperature). Particle growth is controlled by competing reduction of $AuCl_4^{-1}$ in the bulk and the seed surface (which is stabilized by hydrophobic PPO blocks).[93,97–99]

2.3 Templated assembly of nanomaterials

Nanoparticles can be assembled into ordered lattices in suspensions, at interfaces and in polymer/biological matrices. Tuning the interactions between nanoparticles (forces such as Van der Waal's, electrostatic, hydrogen bonding etc.) or between templating matrix and the nanoparticles can create ordered assemblies of nanoparticles. Templates can be "hard" such as porous anodic aluminum oxide (AAO), or "soft" such as polymers. While "hard" templates offer structural rigidity, they lack sized tenability and other dynamic features offered by "soft" templates.[100] A review of some soft templates for the assembly of nanomaterials is presented here.

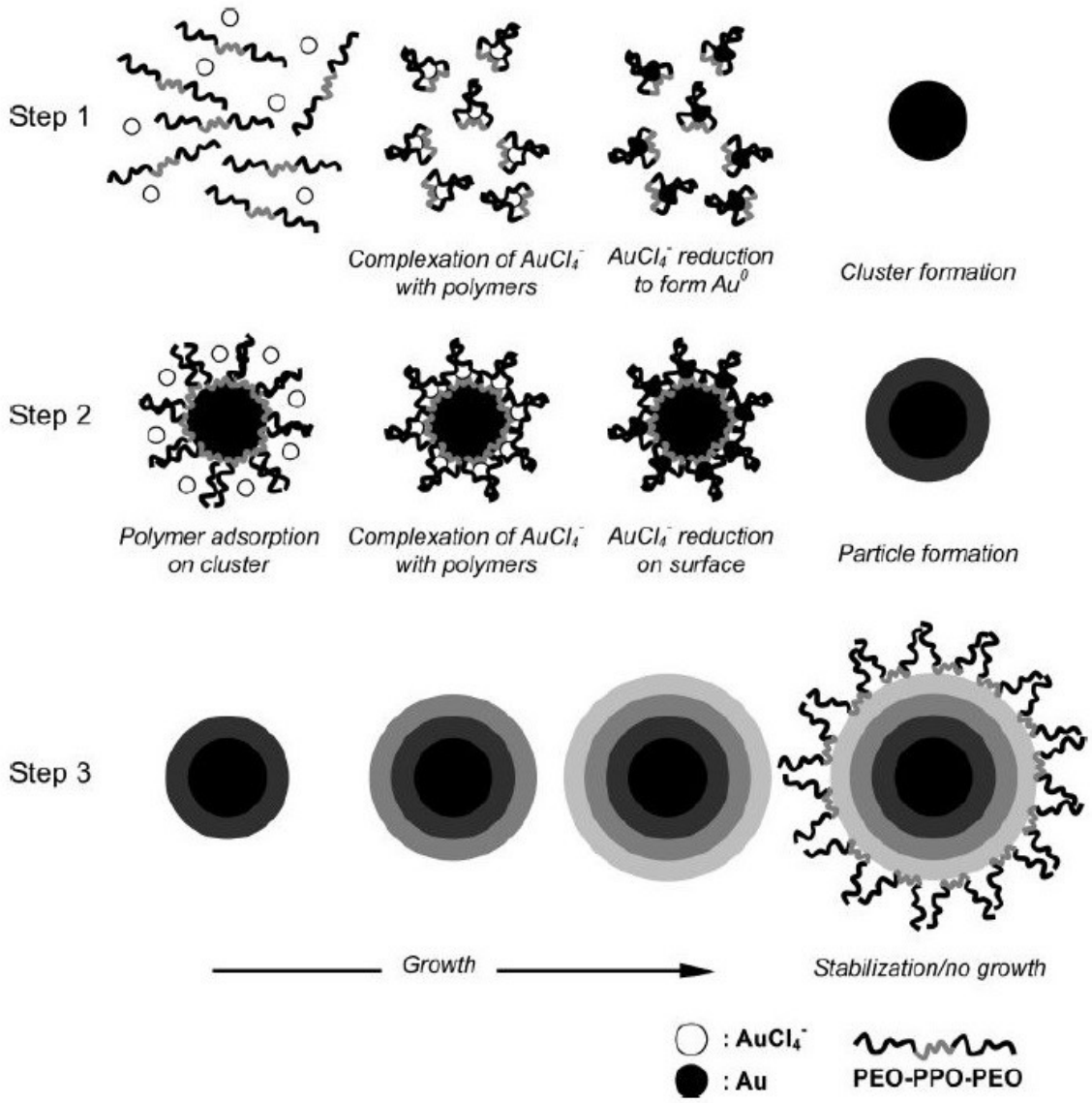

Figure 2.1. Proposed mechanism for the formation of gold nanoparticles in aqueous solutions of Pluronic polymers. Adapted from T. Sakai and P. Alexandridis, *Journal of Physical Chemistry B*, **2005**, *109*, 7766-7777. Copyright ©2005, American Chemical Society.

2.3.1 Proteins and peptides as templates for assembling nanoparticles

The structural and functional properties of proteins and peptides in biology, have made them an attractive candidate for templating assemblies of inorganic materials. Extensive research on their properties such as folding has provided the required tools for protein and peptide based self-assembly. Naturally occurring protein conformations such as α-helices and β-sheets have been

used as templates for the formation of nanofibrous inorganic materials.[101–103] Surfaces patterned with peptides have been used as templates for immobilizing nanoparticles to obtain nanoparticle arrays.[102,104,105] Amphiphilic peptides such as bola-amphiphile peptides that self-assemble into nanotubes have been used in the fabrication of metallic nanowires.[106–108] Reviews on the application of proteins and peptides in assembling inorganic materials have been presented in literature.[61,109–112]

2.3.1.1 Biomimetic assembly of magnetic nanoparticles with biomineralization proteins

Surface immobilization of Mms6 has been used to template the formation of arrays of magnetite nanoparticles on various substrates using both RTCP and POFH methods. Covalent linking of Mms6 to functionalized gold surface followed by POFH method resulted in the formation of large crystals (340±53 nm) of magnetite on the surface. Recombinant Mms6 with a cysteine modified N-terminal has been used to create arrays of magnetite and cobalt ferrite nanoparticles on gold coated surface.[113] The thiol group on the cysteine binds covalently to gold and this was used as the template to create arrays of magnetic nanoparticles with a hydrothermal method of magnetite formation on the patterned protein.

Taking advantage of the amphiphilicity of Mms6 a more biomimetic templating method has been demonstrated with Mms6 immobilization on hydrophobic surfaces.[114] The hydrophobic self-assembled monolayer covered surface was observed to become significantly hydrophilic upon immobilization of Mms6, indicating that the C-terminal domain is exposed and free to bind iron ions. Mms6 was found to form network like structure on the hydrophobic SAM and promote the formation of magnetite crystals with the RTCP method.

2.3.1.2 Biomimetic assembly of nanoparticles with synthetic analogs

In the biomimetic approach, much of the effort has been on creating scaffolds or templates that mimic their biological counterparts and synthesizing the inorganic minerals within the scaffolds. These templates have domains with different chemical or physical properties separated in space that interact differently with the inorganic precursors. Such templates can be obtained by

top-down methods such as photolithography or self-assembly. Langmuir monolayers of charged molecules with carboxylic ends have been used to template the formation of calcite crystals.[103,115–117] Self-assembled monolayers (SAMs) are another option for creating templating patterns for mineralization of inorganic crystals on surfaces. Patterns of alkane thiols created on gold surfaces by soft lithography were used as templates for the formation of calcite arrays[118,119] and magnetite nanoparticle arrays.[120] Polymer matrices that mimic biological matrices during biomineralization have been used control the formation of calcite crystals on SAM patterns.[121] Hydrogels have been used as 3-D templates for the formation of calcium phosphate[122–125] and calcite crystals.[126] Biomimetic principles have also been used with block copolymer templated formation of nanocomposites.[123,125]

2.3.2 DNA templated nanoparticle assemblies

Inorganic nanoparticles can be assembled into ordered assemblies using DNA in broadly two ways: (a) using electrostatic interactions between the negatively charged phosphate groups on the DNA backbone and nanoparticles and (b) using base pair interactions between complementary strands.[127] First approach has been used to create nanowires and nanoparticle networks on surfaces using immobilizing DNA on substrates and treating it with charged nanoparticles functionalized to have positive surface charge.[128,129] Linear assemblies of nanoparticles formed in solution with the same approach have also been reported.[130,131] Using DNA origami developed by Rothemund[132] and Douglas et al.,[133] various nanoparticle super-structures have been fabricated.[134–140] Further, DNA tiling wherein a relatively smaller number of DNA strands assemble to form complex structures, has also been used as templates for materials assembly.[141,142] Molecular recognition features of the base-pair interaction approach has been demonstrated to template the assembly of mixed nanoparticles system where two more nanoparticle types differing in morphology or composition can be assembled together.[143,144] Excellent reviews on the use of DNA as templates for assembling materials by design have been reported in literature.[145–148]

2.3.3 Polymer-templated assembly of nanoparticles

While polymers can be used to control nanoparticle properties, ordered assemblies in polymer matrices is also of great significance. Inclusion of nanostructured inorganic compounds into polymer matrices can enhance the properties of both the polymers and the nanoparticles. For example, intercalation of layered silicates into polymers lead to the formation of nanocomposites with superior tensile strength.[149] Polymer composites with carbon nanotubes also show similar enhancement in mechanical properties.[150] Polymer nanocomposites refer to composites of polymer matrices and structural elements that have physical features in the nanoscale. These are promising candidates for novel optical,[151–156] magnetic,[157,158] electronic,[157,159]and antibacterial materials.[157] Several reviews on their synthesis and applications have been written in the recent years.[151,160–168] Shenhar et. al. list three functions of polymer scaffold in a polymer nanocomposite: assembly of clusters, inducing order and anisotropic orientation and providing functional properties, such as dielectric or stimuli responsive functions.[169]

Block copolymers (bcp) show different phase behaviors such as cubic, lamellar, and bicontinuous in melts and solutions with nanoscale ordering. This makes them an excellent templating material for assembling nanoparticles. The interactions between the different blocks of the bcp and the nanoparticle dictate the equilibrium phase of the nanocomposite. When a nanoparticle is included in a bcp matrix, there is an enthalpic penalty due to chain stretching at the interface, which limits the size of nanoparticle that can be included in bcp domains. Considering symmetry requirements, best pairs of bcp microphase and nanoparticle shape would be dot/sphere, rod/cylinder, tripod/gyroid, and plate/lamellae.[168] Theoretical models based on density functional theory (DFT) and self-consistent field theory (SCFT) have been used to predict assembly of nanoparticles in different bcp microphases depending nanoparticle morphology.[170,171] Interaction between nanoparticles and block copolymers is found to depend on the particle curvature (size) and radius of gyration of the block copolymer.[172,173] Nature of interaction between the nanoparticle and the domains of bcp also affect its dispersion in the matrix. Ideally, the nanoparticle would have favorable interaction with one of the blocks (more favorable compared to self-interaction of that block) and unfavorable interactions with all other blocks.

Polymer matrices can be used as structure directing templates in broadly two ways:[174] 1) in situ formation of nanoparticles in the polymer matrices and 2) mixing preformed nanoparticles with polymer solutions or blends (so called the ex situ methods) (Fig. 2.2). Mixing preformed nanoparticles with polymer solutions to obtain polymer nanoparticle composites has been used to create a wide variety of composites. In order to avoid phase separation due to nanoparticle aggregation, nanoparticles are commonly coated with polymer brushes that have favorable interactions with the polymer matrix. In the second approach in situ formation of metal nanoparticles in polymer matrices typically involves the reduction of a precursor metal salt and the growth of the nanoparticle. The precursor can be reduced with heat, photochemical methods or a reducing agent incorporated in the matrix.[175]

2.3.3.1 In situ formation and assembly of nanoparticles in polymer matrices

Various metal nanoparticles have been synthesized in situ in various polymer matrices, but obtaining ordered assemblies by this approach has been challenging. Block copolymer micelles and other microphases have been used as nanoreactors for the formation of metal[176,177] and metal oxide nanoparticles.[178] Using the periodic arrangement of these nanoreactors, assemblies of nanoparticles are obtained. The basic principle is to selectively reduce an inorganic precursor and kinetically trap and stabilize the growing nuclei in one of the blocks of the block copolymer. Obtaining homogenous reaction conditions within the nanoreactors throughout the matrix is difficult to achieve, and hence polydisperse particles are generally observed.[174] This approach can be used to create continuous films or networks of inorganic materials as the growth of the inorganic is limited to the domain size and this has been used in the fabrication of mesoporous materials templated by block copolymers.[179,180]

Forster et al. described the general steps in the formation of nanoparticles within block copolymer micelles or microphases as follows:[181] First, the precursors are loaded into micelles or microphases of the bcp to a predetermined degree of supersaturation. The degree of saturation, and the interfacial tension between the formed nucleus and the medium determine the size of the nucleus, which in turn determines nuclei density in the micelle/microphase. The interfacial

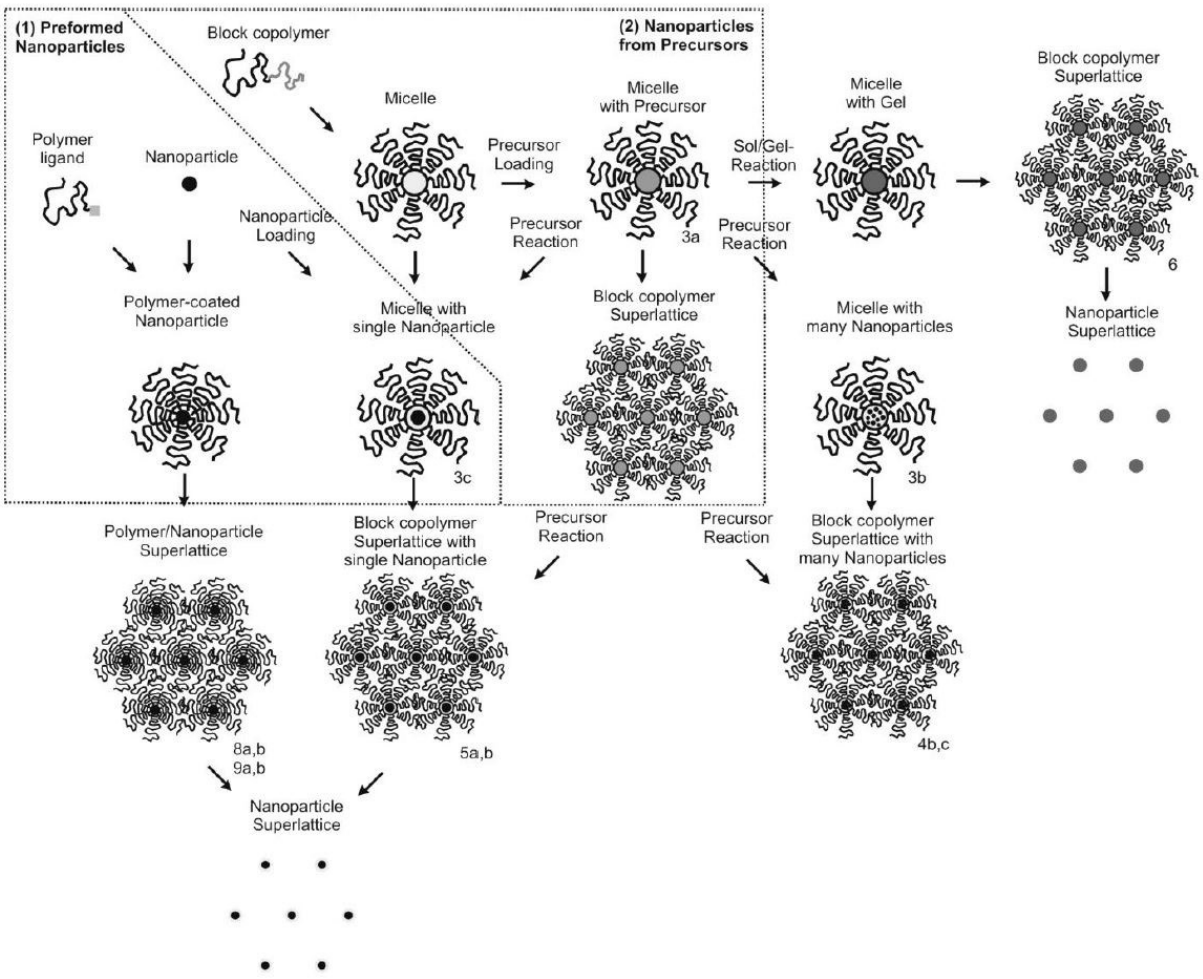

Figure 2.2. Synthetic routes for the formation of polymer nanocomposites. Route (1) shows polymer nanocomposite fromation using ex situ methods and route (2) shows polymer nanocomposite formation using in situ methods. Adapted from S. M. Taheri, S. Fischer and S. Forster, *Polymers*, **2011**, *3*, 662-673. Licensed under CC BY 3.0.

tension between the nucleus and the medium depends on the interaction between the bcp and the nanoparticle. Particle diffusivity and solubility affects Ostwald ripening and hence contribute towards final particle morphology.

Progress in this field has been mainly seen in the fabrication of ordered arrays of nanoparticles in block copolymer thin films on various substrates. Two dimensional hexagonal patterns of spherical metal nanoparticles were obtained by reduction of a precursor in a bcp matrix formed by PS-b-PAA copolymer.[182] Arrays of palladium nanoparticles in P2VP lamellae formed by poly(isoprene)-b-poly(2-vinylpyridine) (PI-b-P2VP) were obtained by thermal reduction of palladium acetate pre-

cursor in crosslinked block copolymer matrix.[183] Monolayers of PS-b-P2VP on silicon wafers with pH tunable morphology were sued as nanoreactors for the formation of metallic nanowires.[184] Thin films of PS-b-P4VP were used as templates for the formation of arrays of metallic nanoparticles and nanowires.[185] Three dimensional assemblies with continuous metal films with block copolymers have been recently reported with seeded growth in bicontinuous gyroid phases of poly(styrene)-b-poly(isoprene)-b-poly(propylene carbonate),[186] poly(styrene)-b-poly(isoprene)[187] and poly(styrene)-b-poly(L-lactide).[188]

2.3.3.2 In situ formation and assembly of nanoparticles in Pluronic gels

Liquid crystalline phases shown by Pluronic bcps are good candidates for templating the formation of ordered polymer nanocomposites because they are water based, temperature responsive and commercially available. The ordered phase that forms in these liquid crystals (ex. hexagonal close packing, lamellar, cubic close packing and bicontinuous phases) depends on the chain length fraction, the inter-block Flory-Huggins interaction parameter, the solution temperature and concentration. The micro-phase separated domains can act as nano-reactors for the in-situ formation of inorganic component or they can be selectively etched and backfilled with suitable precursors to form the inorganic component. Using this approach, mesoporous structures of oxides of Si, Zr, Ti, Al, Nb, W etc and porous silver monoliths have been synthesized with Pluronic polymers.[189] The precursor solution diffuses into the water-rich phase (PEO) and hence the PPO-rich phase forms the pores. The ordered packing of PPO blocks makes the Pluronics a good template for the formation of such mesoporous materials. Mesoporous carbon materials, alumina–carbon, and MgO–carbon composites with ordered pore structures have been fabricated by crosslinking resols in different Pluronic gels by evaporation induced self-assembly.[190–195] Fabrication of such templated structures with other morphologies such as lamellae and bicontinuous phases has been a challenge for the Pluronic based systems. Although they have been used extensively in the formation of mesoporous materials,[189,196] there are not many reports on their use in the formation of nanocomposites.

Simulations have shown that triblock ABA type polymers when mixed with inorganic precursors can form gyroid, columnar and lamellar phases.[197–200] End modified polymers with ends that have attractive affinity towards the crystallizing inorganic component were employed in the simulation.[199] Different phases were predicted when interactions between the crystallizing components and the polymer end and interactions in between the crystallizing components were simultaneously varied. When the interaction between the polymer end and the inorganic was greater than that amongst the inorganic components, formation of gyroid phase was predicted. Interestingly, this result was predicted even with ABA polymer that do not show these phases in solution. The authors attributed this to the strong interaction the polymer ends have with the inorganic precursors, leading to the crystallization of the inorganic component. In their later work, the authors generalized these results with different polymer architectures.[198] A balance between the polymer-inorganic interaction and inorganic-inorganic interactions was found to be the key to the formation of various morphologies. Their results are shown in Figure 2.3. For end modified triblock copolymers with $CA_9B_7A_9C$ architecture, where C is the end modification, A is the hydrophilic block and B is the hydrophobic block, gyroid phase is predicted. The inner chain architecture ($A_9B_7A_9$) roughly corresponds to that of Pluronic F127. In fact, Pluronic F127 with end-modifications (cationic, anionic and zwitterionic) have been shown to template the formation of calcium phosphate nanocomposites by ionic interactions with the precursors containing calcium and phosphate ions.[123,125]

2.3.3.3 Assembly of nanoparticles by physical dispersion in polymer matrices (ex situ methods)

One of the disadvantages of obtaining polymer nanocomposites by in situ methods lies in the lack of sufficient control over the morphology of the formed nanoparticle in comparison to ex situ methods. Since in the ex situ methods, the nanoparticles are preformed in solvents, greater degree of control over morphology is obtained. A common problem with the ex situ methods is the incompatibility of capping agents on the nanoparticle and the polymer matrix leading to phase separation.[174] Van der Waal's interactions and polymer depletion induced aggregations typically

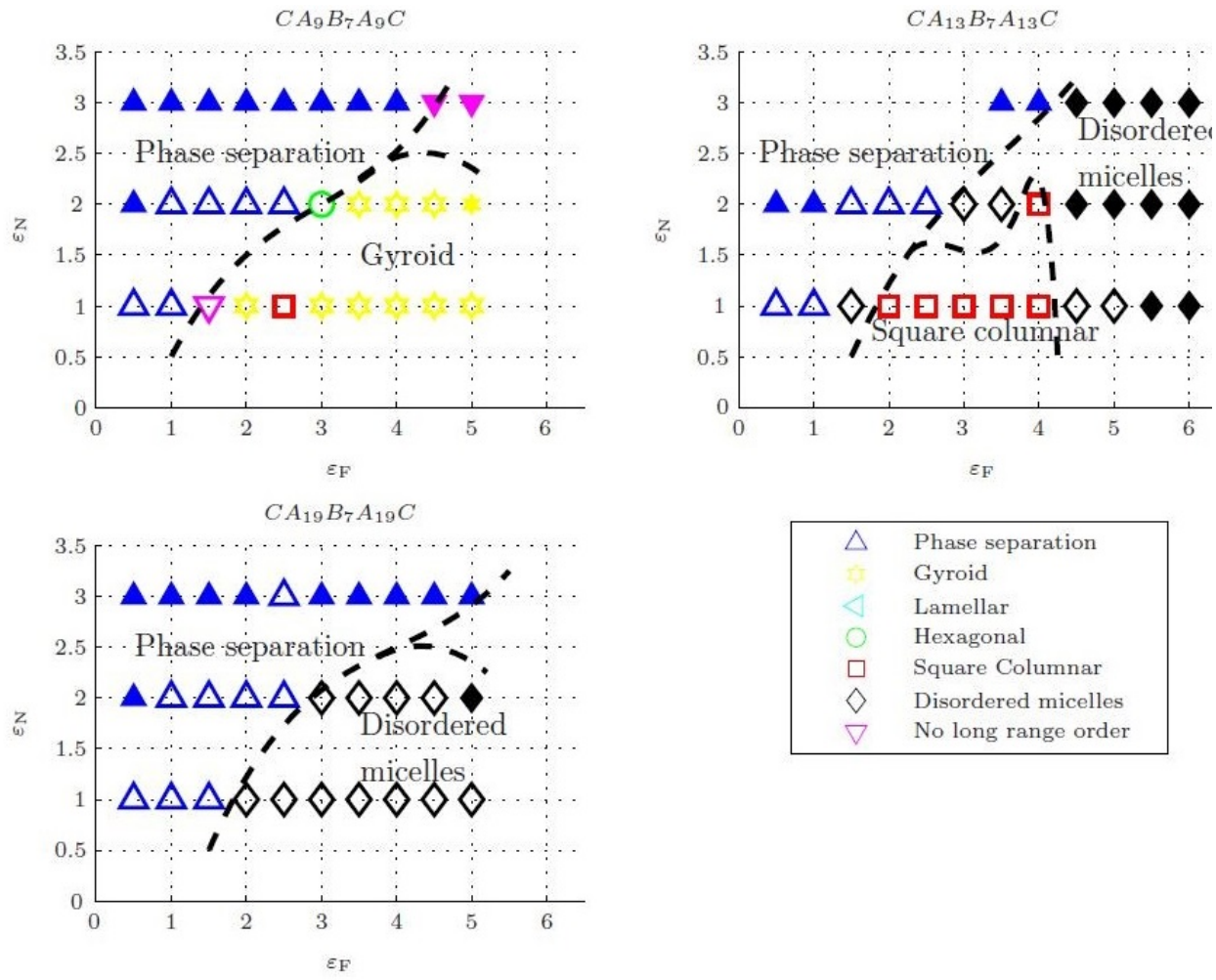

Figure 2.3. Phase diagram for polymer nanocomposites with packing fraction = 0.25 for different polymers, as a function of polymer-inorganic and inorganic-inorganic interactions. Reprinted with permission from J. A. Anderson, R. Sknepnek and A. Travesset, *Physical Review E*, **2010**, *82*, 021803. Copyright (2010) by the American Physical Society.

cause nanoparticle aggregation and thus judicious choice of bcp matrix, nanoparticle size and surface functionalization and particle concentration are required.

Thermodynamics of nanoparticle dispersion in polymer matrices has been studied theoretically[173,200–203] and experimentally.[204–206] When nanoparticles are dispersed in polymer matrices there is enthalpic penalty due to the creation of new surfaces, loss of entropy for the polymer chains and gain of translational entropy for the nanoparticles. The enthalpy contribution can be manipulated by the particle morphology and capping. Entropic contributions are dependent on the size of nanoparticle in relation the bcp domain size.[204] Loss of conformational entropy for

the polymer was found to limit nanoparticle loading in the matrix when nanoparticles had sizes comparable to domain size.[204] Nanoparticle dispersion in bcp matrices have a few advantages over dispersions in homopolymers including control over morphology and tunable, selective incorporation in nanoscale bcp domains.[204] A common problem with bcps in general and bcp-nanoparticle composites is the kinetic entrapment of the system in a metastable phase. Strategies such as thermal annealing and the use of selective solvents that swell one of the blocks have been used to overcome this hurdle in accessing different equilibrium phases.[207–209] Tuning the properties of either the polymer matrix or the nanoparticle brush can be used to control the nanocomposite morphology. For example, Hu et.al., were able to transfer silica nanoparticles from micelle core to corona or vice versa by varying the LCST of the nanoparticle brush compared to the LCST of the micelle forming polymer.[210] Utilizing these principles, nanocomposites of gold nanoparticles,[211] nanorods,[212] CdSe nanoparticles,[213] magnetite nanoparticles,[214] silica nanoparticles[215] etc have been assembled into ordered morphologies using block copolymers. Magnetite nanoparticles obtained by co-precipitation method have been selectively deposited in PMMA thin films by coating the nanoparticles with oleic acid.[216]

In a kind of role reversal, nanoparticles introduced in polymer matrices have been used to tune the morphology of the polymers. For example, PS coated gold nanoparticles were used as "surfactants" to tune the assembly of PS-b-PVP to obtain lamellar and bicontinuous morphologies with gold nanoparticles decorating the interfaces.[217] Similarly, inclusion of CdS nanoparticles in P4VP blocks of PS-b-P4VP induced morphological change from hexagonally close packed cylinders to lamellae.[218] This transformation was attributed to strong hydrogen bonding interactions between the nanoparticles due to their surface functionalization. Trimethylsilylated silica nanoparticles have been shown to control the morphology of PS-b-PDMS polymer melts.[219] In gold/Poly(tert-butacrylate)-b-PEO composites, by varying the nanoparticle weight fraction, different morphologies were obtained.[220]

Similar to the simulation results for the in situ crystallization of inorganic materials in concentrated solutions of end modified triblock amphiphilic copolymers, nanoparticle driven self-assembly of the same polymers has also been shown.[200] Simulations predict the formation of vari-

ous nanocomposite morphologies with increasing overall packing fraction (volume fraction of the polymer and nanoparticle in the simulation box), nanoparticle concentration and the strength of the interaction between the nanoparticle and the end modified polymer (Fig. 2.4).[200] End modified polymers with attractive affinity towards the nanoparticles ($d \sim R_g$ of the polymer) were employed in the simulation. Nanoparticle diffusion within the matrix is found to be suppressed after the formation of the assembly. At low overall packing fractions the polymer micelles and the nanoparticles are in a disordered state. At high nanoparticle concentrations, and polymer packing fractions, formation of square and hexagonal columnar phases, perforated lamellae gyroid networks of nanoparticles is predicted when the interaction between the polymer end and the nanoparticle is greater than the thermal energy, k_BT. Formation of columnar phases is explained to be due to close packing of spheres of unequal sizes at different concentrations. At higher polymer packing fractions formation of gyroid networks are predicted as to minimize surface tension between the hydrophilic and hydrophobic blocks by the formation of a minimum surface (gyroid). Similar results are also reported with end modified amphiphilic polymers and nanorods.[221] Such nanoparticle driven assembly is seen in Pluronic P123 in the presence of Laponite.[222] Phase transition from hexagonal packing of rod like micelles to lamellar phase is observed with increasing temperature.

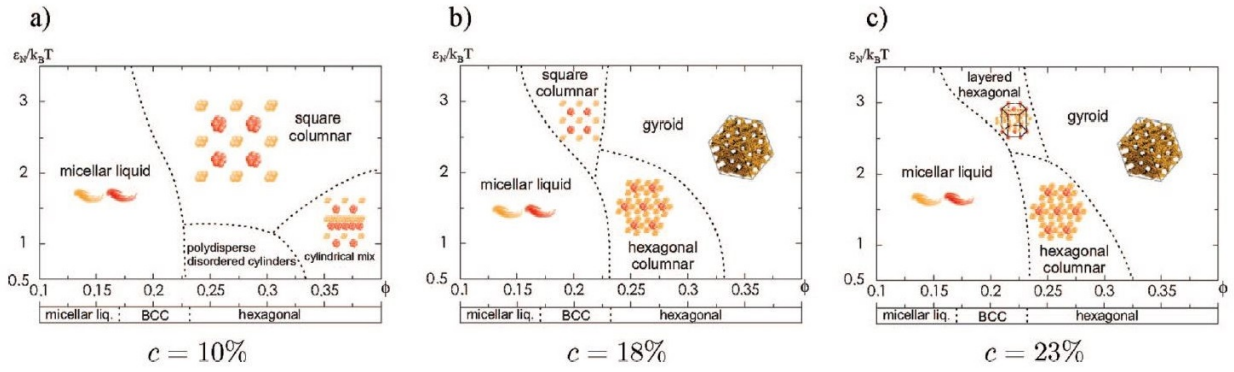

Figure 2.4. Phase diagram for polymer nanocomposites as a function of polymer packing fraction and nanoparticle-polymer interaction for three nanoparticle concentrations (c= 10%, 18% and 23%). Adapted from R. Sknepnek, J. A. Anderson, M. H. Lamm, J. Schmalian and A. Travesset, *ACS Nano*, **2008**, *2*, 1259-1265. Copyright ©2008, American Chemical Society.

2.4 Self-assembly of nanoparticles into crystalline superlattices

2.4.1 Evaporation induced self-assembly

Evaporation induced self-assemnly of nanoparticles into superlattices is the earliest method of crystallizing nanoparticles.[223,224] Nanoaprticles coated with organic ligands such as dodecane thiol, oleaic acid, and trioctylphosphine oxide suspended in volatile organic solvents such as toluene and hexane are drop-casted on a solid or liquid substrate and the solvent is removed by controlled evaporation.[225] This leads to saturation conditions and packing of nanoparticles to maximize van der Waal's interactions. Nanoparticles of various compositions have been assembles into complex superlattices including quazicrystalline structures by this approach.[226–230] Further, due to the typical short inter-particle separations in these assemblies, they have been used to demonstrate the collective behavior (lattice modes) of nanoparticles.[231–233]

2.4.2 Polymer-mediated self-assembly

Polymers in solutions show a rich phase behavior depending on the medium conditions such as composition, temperature and ionic strength.[234–236] Polymers are also used as nanoparticle surface ligands to provide colloidal stability. Thus, utilizing the tunable behavior of polymers in solutions, polymer stabilized nanoparticles have been chains, sheets and 3D crystals. Si et al., provide a list of nanoparticle assemblies formed mediated by polymers.[237] To functionalize polymers onto nanoparticles, there are two approaches: "grafting to" and "grafting from". In "grafting to", a polymer with suitable end group is chemically adsorbed to the nanoparticle, whereas in the "grafting from" approach, a polymer is grown on the nanoparticle by polymerization procedures such as SI-ATRP (surface initiated - atom transfer radical polymerization),[238] RAFT (reversible addition - fragmentation chain transfer),[239] and ROMP(ring-opening metathesis polymerization).[240] Although "grafting from" leads to higher grafting density, simulations show that "grafting to" leads to more uniform grafting.[241]Noble metal nanoparticles have been functionalized with thiol-terminated polymers, such as pol(ethylene glycol)-thiol and poly(N-isopropylacrylamide)-thiol

and assembled into 2D and 3D superlattices.[237,242–244] Functionalizing nanoparticles with block copolymers is being explored for obtaining anisotropic assemblies.[245]

2.4.3 DNA-mediated self-assembly

Reversible aggregation of gold nanoparticles was demonstrated for the first time using DNA linkers by Mirkin et al., and Alivisatos et al., in 1996.[246,247] Since then, the formation of superlattices using this method[248,249] various aspects of formation of these assemblies have been studied.[143,250–260] Nanoparticles are functionalized with single stranded DNA, typically via the thiol group, and the pendant DNA strand hybridizes with the complementary chain on a neighboring particles (directly,[248] or via a linker chain[249]). Hybridization of complementary strands are the dominant forces that control the structure of the assembly and the excluded volume interactions of hybridized DNA strands are the dominant repulsive forces.[248,261] Since the hybridization of DNA strands can be reversed by heating, thermal annealing is employed to obtain crystals. In the absence of thermal annealing, RLCA clusters are obtained with the same method.[250] In DNA-mediated assembly of nanoparticles length of the DNA linker strands is found to affect both the kinetics of aggregation[262] and the structure of the aggregates.[252,262] Increasing the duplex DNA length (spacer) was found to increase inter-particle distance but decreases crystal quality (i.e., the number of unit cells in a crystallite).[252] While results from Mirkin group showed that shorter DNA spacers lead to better crystallization,[249] Nykypanchyk et al., reported the opposite.[248] Further, Mcfarlane et.al., obtained a phase diagram for these systems where they report a lower and upper bound for the DNA linker length for a given nanoparticle size.[254] The lower limit was attributed to the thermodynamic penalty of assembling NP with size polydispersity higher than the flexibility of the DNA linker. Shorter DNA linkers have lower flexibility and hence the lower limit in the "zone of crystallization".[254] The upper limit was explained by kinetic limitations in rearrangement of the lattice to attain thermodynamic equilibrium of ordered structure with a longer DNA linker.

2.5 Potential applications

2.5.1 High density data storage

Current data storage technology is based on perpendicular magnetic recording, wherein a collection of particles form a storage unit. Areal density of magnetic data storage can be increased by reducing the number of particles per bit or by reducing the size of a single particle. The foremost hurdle in increasing the data storage density is the superparamagnetic limit, which causes the loss of data in individual bits due to thermal fluctuations. The onset of superparamagnetism depends on the size of the particles, the magnetic anisotropy of the material and temperature. Reducing the number of particles per bit reduces the signal to noise ratio[263] which causes the read head to function unreliably. So, research has focused on obtaining single domain magnets with an optimal coercivity to function as the data storage medium.[264–266] The current technology of sputtering, where a continuous film is deposited as the data storage medium, limits the spatial separation between the bits.[267] Physical proximity of bits causes exchange coupling, which leads to loss of data. Bit patterned media offers a solution to this problem, where individual bits are physically separated, with discontinuity of material between them.[268,269] This can increase the data storage density up to 5 TB/sq.inch.[270] In addition, magnetic nanoparticles also find applications in various sensors based on their magnetic relaxation and magnetoresistance properties.[271–273] Surface patterning of magnetic nanoparticles with enhanced magnetic properties can thus aid in their efficient device integration as sensors.

2.5.2 Metamaterials

Metamaterials is a new and exciting field of materials research where the physical properties of the materials are dependent on the structure of constituent materials rather than their chemical composition. Plasmonic metamaterials refer to materials whose electromagnetic properties, characterized by dielectric permittivity and permeability (ϵ and μ) are dependent on the structure of the constituent units that are polarizable and are hence different from the properties of bulk materials. While negative permittivity is observed in bulk metals and metal nanoparticles for certain

regions of the EM spectrum, simultaneous negative ϵ and μ have never been observed in nature. The possibility of manipulating μ to create materials with simultaneously negative ϵ and μ and thereby creating negative refraction media ($n^2 = \epsilon\mu$) has resulted in a large amount of research in this area. Most of the everyday materials have μ approximately equal to 1, but by creating induced current loops in the constituent units, electromagnetic responses of the material can be coupled to the magnetic part of the EM waves. Negative refractive index materials were first theoretically discussed by Veselago in 1968.[274] Pendry et. al proposed different structures made of metals that would have such a negative refractive index, including split ring structures[275] and was first demonstrated by Smith et. al in the microwave range.[276] Since then, there have been many attempts to create metamaterials for shorter wavelengths.

Fabrication of metamaterials requires high control over the shape of the individual constituent unit and the spacing between the constituent units of the metamaterial. The limiting values for both these dimensions are mainly determined by the wavelength of interest. For optical metamaterials, these conditions translate to the fabrication of shape controlled nanoparticles with nanoscale order. Conservative estimates for the inter-unit spacing is around ten times the wavelength of interest.[277] Initial designs of metamaterials were conceptually based on resonating LC circuits and hence the materials were analogous to conductor loops. So, metals were used as constituent units as they have negative permittivity below their plasma frequency. Shapes such as split rings have been demonstrated to provide metamaterial properties in the microwave region.[276,278] Further, other shapes like tuning forks have also been proposed to function as constituent units for metamaterials. Using these negative index metamaterials, applications such as electromagnetic cloaking[279] and hyper-lenses[239] have been developed. One of the first demonstrations of cloaking with metamaterials was with copper split ring resonators to "hide" a cylinder of copper from microwaves.[279] Ergin et. al used direct laser writing on negative photo resists to create a woodpile structure photonic crystal with a tailored distribution of refractive index to demonstrate optical cloaking at near IR wavelengths.[277] Multilayers of the woodpile structure allowed certain three dimensional characteristic to the material. Dolling et. al fabricated a metamaterial with negative

refractive index at 780 nm with a fishnet structure of silver with $\sim$ 100nm square holes, using e-beam lithography.[280]

Apart from the LC resonator circuit based designs where electromagnetic properties of the constituent units are manipulated so as to superimpose electric and magnetic resonances, chiral materials have also been proposed to provide metamaterial responses.[281,282] Chiral materials have different refractive indices for the different polarizations of electromagnetic wave and by tuning the chirality parameter, effective refractive index of the medium can be negative.[281] Strong optical activity of the material increases the chirality parameter and hence the possibility of negative refraction for some polarization of the EM wave. Plum et. al demonstrated this phenomena in multilayers of twisted metallic rosettes in the microwave region[283] while Zhang et. al used two dimensional out of plain structures for chiral response in the far IR region.[284] Although these materials do show giant optical rotation per unit length, due to the low thickness of the material, the effective optical rotation from these materials is low.[283]

In all the above examples, top-down fabrication methods were used to create the constituent units of the metamaterial due to their high precision. However, due to their cost, low scale of production and difficulties in producing three dimensional regularity, these methods are limited towards the fabrication of three dimensional macroscale metamaterials. Thus, self-assembly processes towards the fabrication of metamaterials have received a great deal of attention in the recent years.[285–289] In addition to addressing the issue of macroscale assembly, it is easier to reduce the dimensions of the assemblies with self-assembly compared to traditional drop down approaches. The self-assembly of block copolymers is being explored as a route to templated assembly for fabricating metamaterials. There are multiple ways in which block copolymers can be used to template the formation of metamaterials, which follow from the two methods of obtaining metamaterials in general (simultaneous electric and magnetic resonances, and strong chirality). Nanostructures with simultaneous negative permittivity and permeability can be assembled in the polymer matrix using the general methods that have been established for assembling simpler nanoparticles, namely: in situ and ex situ methods. Discrete chiral units can also be assembled into ordered lattices using the same approach. On the other hand, continuous metallic films with chiral ge-

ometries such as helix or gyroid that have metamaterial properties can also be templated by block copolymers. These two methods are discussed in some detail below.

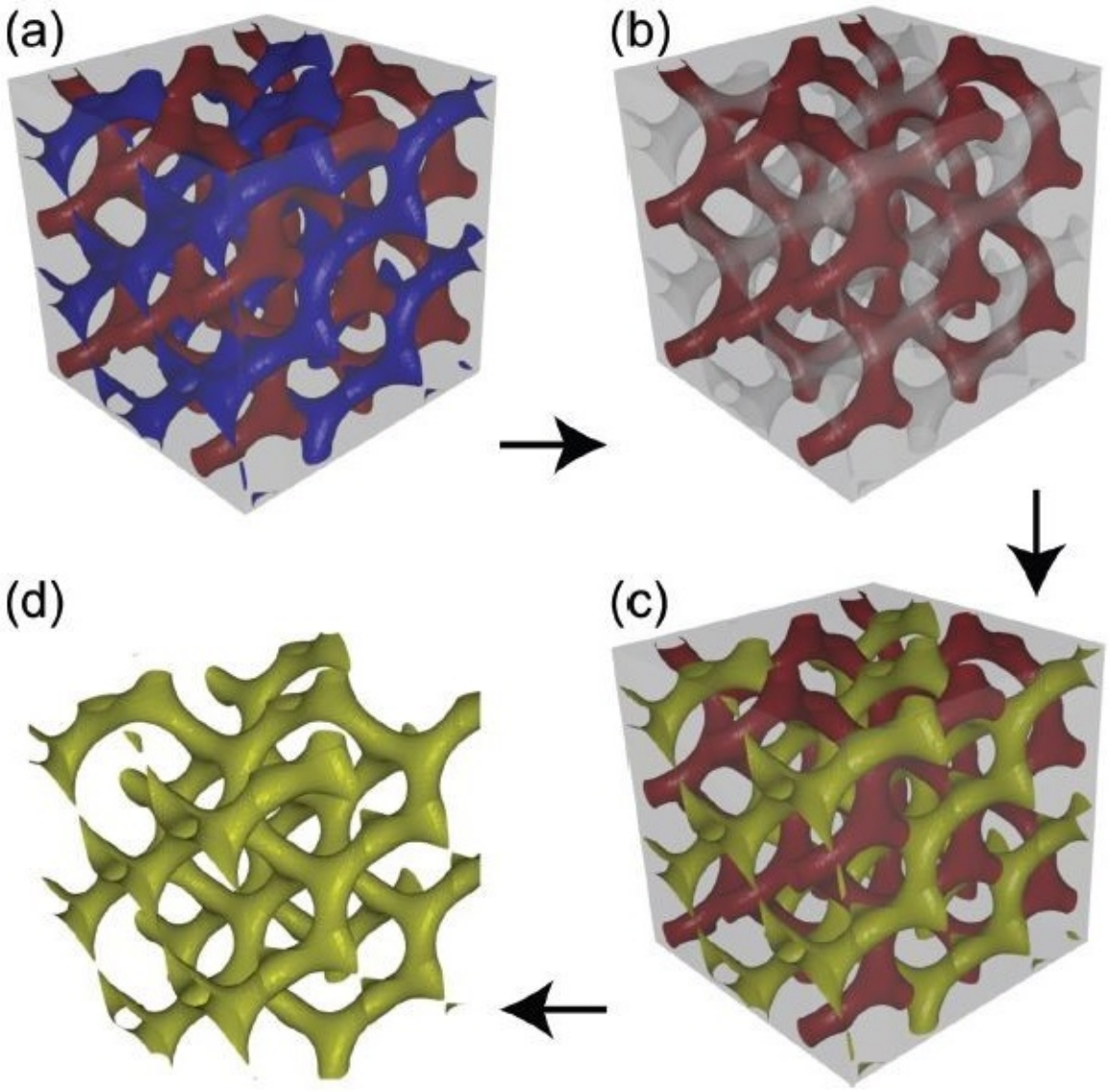

Figure 2.5. Schematic representation of block copolymer templated gyroid networks of gold. The block copolymers were used as static and sacrificial templates here. (a) Interpenetrating network of gyroids formed by poly(isoprene) and poly(ethylene oxide) blocks of PI-PS-PEO block copolymer. Blue represents the PI block, red represents the PEO block and grey represents the PS block. (b) Selective removal of PI block by UV and chemical etching, (c) electrodeposition of gold in the voids left behind by removal of PI and (d) Gold gyroid networks obtained by plasma etching. Figure reproduced from S. Vignolini, N. A. Yufa, P. S. Cunha, S. Guldin, I. Rushkin, M. Stefik, K. Hur, U. Wiesner, J. J. Baumberg and U. Steiner, *Advanced Optical Materials*, **2012**, *24*, 23-27.

Three dimensional negative refractive index metamaterials using chiral assemblies of block copolymers were first theoretically predicted by Hur et. al in 2011.[290] Triply periodic, bicontinuous gyroid network of gold has been fabricated by electrodeposition using poly(isoprene)-b-poly(styrene)-b-poly(ethylene oxide) (PI-PS-PEO) as template[291] as shown in Figure 2.5. PI and PEO blocks formed an interpenetrating gyroid network and selective removal of PI block by UV and chemical etching left behind a porous void with gyroid structure.[291] The voids were then backfilled with gold by electrodeposition to a thickness of 200 nm to 1000 nm. Plasma frequency of the obtained network was found to be lower than that of bulk gold[291] and the optical responses could further be tuned by the extent of gold deposition.[292] The gold gyroid networks were found to be optically active, but negative refraction was not reported. The thickness of the gyroid networks ($< 1\mu$m) was probably too small to affect sufficient optical rotation.

Such gyroid networks have been realized in other block copolymer composites as well. Gyroid networks formed by poly(styrene)-b-poly(L-lactide) as templates for electroless deposition of nickel after selective hydrolytic removal of PLLA block.[188] Similar results were also observed with poly(tert-butoxystyrene)-block-polystyrene-block-poly(4-vinylpyridine) triblock copolymers.[293] The electroless deposition method is preferred over electrochemical deposition as it removes the necessity of a conducting substrate required as an electrode in the case of electrochemical deposition. On the other hand, growth of continuous metal films or rods is more difficult to control in electroless deposition.[1] The other approach to using block copolymers is the assembly of discrete metamaterial constituents into ordered assemblies with sub-wavelength periodicity. Synthesis of stable suspensions of metallic constituent units with complex shapes such as split rings, tuning fork shapes or the U shape is challenging. Lack of progress in this field has likely constrained the use of this approach.

References

[1] Jones, M. R., Osberg, K. D., Macfarlane, R. J., Langille, M. R., and Mirkin, C. A. *Chemical Reviews* **111**(6), 3736–3827 (2011).

[2] Xu, A. W., Ma, Y. R., and Colfen, H. *Journal of Materials Chemistry* **17**(5), 415–449 (2007).

[3] Yao, H. B., Fang, H. Y., Wang, X. H., and Yu, S. H. *Chemical Society Reviews* **40**(7), 3764–3785 (2011).

[4] Addadi, L. and Weiner, S. *Angewandte Chemie-International Edition in English* **31**(2), 153–169 (1992).

[5] Addadi, L., Raz, S., and Weiner, S. *Advanced Materials* **15**(12), 959–970 (2003).

[6] Weiner, S. and Addadi, L. *Journal of Materials Chemistry* **7**(5), 689–702 (1997).

[7] Weiner, S. and Addadi, L. *Crystallization pathways in biomineralization*, volume 41 of *Annual Review of Materials Research*, 21–40. (2011).

[8] Mirabello, G., Lenders, J. J. M., and Sommerdijk, N. *Chemical Society Reviews* **45**(18), 5085–5106 (2016).

[9] Nudelman, F. and Sommerdijk, N. *Angewandte Chemie-International Edition* **51**(27), 6582–6596 (2012).

[10] Colfen, H. and Mann, S. *Angewandte Chemie-International Edition* **42**(21), 2350–2365 (2003).

[11] Cölfen, H. and Yu, S.-h. *MRS Bulletin* **30**(10), 727–735 (2005).

[12] Colfen, H. *Nature Materials* **9**(12), 960–961 (2010).

[13] Goulletquer, P. and Wolowicz, M. *Journal of the Marine Biological Association of the United Kingdom* **69**(3), 563–572 (1989).

[14] Huo, Q. S., Margolese, D. I., Ciesla, U., Demuth, D. G., Feng, P. Y., Gier, T. E., Sieger, P., Firouzi, A., Chmelka, B. F., Schuth, F., and Stucky, G. D. *Chemistry of Materials* **6**(8), 1176–1191 (1994).

[15] Lowenstam, H. A. and Weiner, S. *Science* **227**(4682), 51–53 (1985).

[16] Bonucci, E. *Journal of Bone and Mineral Metabolism* **27**(3), 255–264 (2009).

[17] Arakaki, A., Webb, J., and Matsunaga, T. *The Journal of biological chemistry* **278**(10), 8745 (2003).

[18] Addadi, L. and Weiner, S. *Proceedings of the National Academy of Sciences of the United States of America* **82**(12), 4110–4114 (1985).

[19] Beniash, E., Aizenberg, J., Addadi, L., and Weiner, S. *Proceedings of the Royal Society B-Biological Sciences* **264**(1380), 461–465 (1997).

[20] Baumgartner, J., Morin, G., Menguy, N., Gonzalez, T. P., Widdrat, M., Cosmidis, J., and Faivre, D. *Proceedings of the National Academy of Sciences of the United States of America* **110**(37), 14883–14888 (2013).

[21] Blakemore, R. *Science* **190**(4212), 377–379 (1975).

[22] Blakemore, R. P. *Annual Review of Microbiology* **36**, 217–238 (1982).

[23] MANN, S., SPARKS, N., and BOARD, R. *Advances in Microbial Physiology* **31**, 125–181 (1990).

[24] Bazylinski, D. A. and Frankel, R. B. *Nature Reviews Microbiology* **2**(3), 217–230 (2004).

[25] Faivre, D. and Schueler, D. *Chemical Reviews* **108**(11), 4875–4898 (2008).

[26] Prozorov, T., Bazylinski, D. A., Mallapragada, S. K., and Prozorov, R. *Materials Science & Engineering R-Reports* **74**(5), 133–172 (2013).

[27] Faivre, D. and Godec, T. U. *Angewandte Chemie-International Edition* **54**(16), 4728–4747 (2015).

[28] Staniland, S. S. and Rawlings, A. E. *Biochemical Society Transactions* **44**, 883–890 (2016).

[29] Peigneux, A., Valverde-Tercedor, C., Lopez-Moreno, R., Perez-Gonzalez, T., Fernandez-Vivas, M. A., and Jimenez-Lopez, C. *Journal of Structural Biology* **196**(2), 75–84 (2016).

[30] Uebe, R. and Schuler, D. *Nature Reviews Microbiology* **14**(10), 621–637 (2016).

[31] Mathuriya, A. S. *Critical Reviews in Biotechnology* **36**(5), 788–802 (2016).

[32] Jacob, J. J. and Suthindhiran, K. *Materials Science & Engineering C-Materials for Biological Applications* **68**, 919–928 (2016).

[33] Barber-Zucker, S. and Zarivach, R. *Acs Chemical Biology* **12**(1), 13–22 (2017).

[34] Mann, S., Sparks, N. H. C., Frankel, R. B., Bazylinski, D. A., and Jannasch, H. W. *Nature* **343**(6255), 258–261 (1990).

[35] Scheffel, A., Gruska, M., Faivre, D., Linaroudis, A., Plitzko, J. M., and Schuler, D. *Nature* **440**(7080), 110–114 (2006).

[36] Uebe, R., Junge, K., Henn, V., Poxleitner, G., Katzmann, E., Plitzko, J. M., Zarivach, R., Kasama, T., Wanner, G., Posfai, M., Bottger, L., Matzanke, B., and Schuler, D. *Molecular Microbiology* **82**(4), 818–835 (2011).

[37] Arakaki, A., Yamagishi, A., Fukuyo, A., Tanaka, M., and Matsunaga, T. *Molecular Microbiology* **93**(3), 554–567 (2014).

[38] Schuler, D. and Frankel, R. B. *Applied Microbiology and Biotechnology* **52**(4), 464–473 (1999).

[39] Weiner, S. and Dove, P. M. *Biomineralization* **54**, 1–29 (2003).

[40] Young, J. R. and Henriksen, K. *Biomineralization* **54**, 189–215 (2003).

[41] Bauerlein, E. *Angewandte Chemie-International Edition* **42**(6), 614–641 (2003).

[42] Weiner, S. *Journal of Structural Biology* **163**(3), 229–234 (2008).

[43] Mann, S. *Nature* **365**(6446), 499–505 (1993).

[44] Lausch, A. J., Quan, B. D., Miklas, J. W., and Sone, E. D. *Advanced Functional Materials* **23**(39), 4906–4912 (2013).

[45] Ba, X., Rafailovich, M., Meng, Y. Z., Pernodet, N., Wirick, S., Furedi-Milhofer, H., Qin, Y. X., and DiMasi, E. *Journal of Structural Biology* **170**(1), 83–92 (2010).

[46] Wang, Y. J., Yang, C. R., Chen, X. F., and Zhao, N. R. *Advanced Engineering Materials* **8**(1-2), 97–100 (2006).

[47] Liao, S., Ngiam, M., Chan, C. K., and Ramakrishna, S. *Biomedical Materials* **4**(2) (2009).

[48] Kikuchi, M., Ikoma, T., Itoh, S., Matsumoto, H. N., Koyama, Y., Takakuda, K., Shinomiya, K., and Tanaka, J. *Composites Science and Technology* **64**(6), 819–825 (2004).

[49] Tampieri, A., Celotti, G., Landi, E., Sandri, M., Roveri, N., and Falini, G. *Journal of Biomedical Materials Research Part A* **67A**(2), 618–625 (2003).

[50] Brutchey, R. L. and Morse, D. E. *Chemical Reviews* **108**(11), 4915–4934 (2008).

[51] Kroger, N., Dickerson, M. B., Ahmad, G., Cai, Y., Haluska, M. S., Sandhage, K. H., Poulsen, N., and Sheppard, V. C. *Angewandte Chemie-International Edition* **45**(43), 7239–7243 (2006).

[52] Kisailus, D., Truong, Q., Amemiya, Y., Weaver, J. C., and Morse, D. E. *Proceedings of the National Academy of Sciences of the United States of America* **103**(15), 5652–5657 (2006).

[53] Wang, W., Bu, W., Wang, L., Palo, P. E., Mallapragada, S., Nilsen-Hamilton, M., and Vaknin, D. *Langmuir* **28**(9), 4274–4282 (2012).

[54] Zhang, H., Liu, X., Feng, S., Wang, W., Schmidt-Rohr, K., Akinc, M., Nilsen-Hamilton, M., Vaknin, D., and Mallapragada, S. *Langmuir* **31**(9), 2818–2825 (2015).

[55] Kashyap, S., Woehl, T. J., Liu, X., Mallapragada, S. K., and Prozorov, T. *Acs Nano* **8**(9), 9097–9106 (2014).

[56] Feng, S., Wang, L., Palo, P., Liu, X., Mallapragada, S. K., and Nilsen-Hamilton, M. *International Journal of Molecular Sciences* **14**(7), 14594–14606 (2013).

[57] Amemiya, Y., Arakaki, A., Staniland, S. S., Tanaka, T., and Matsunaga, T. *Biomaterials* **28**(35), 5381–5389 (2007).

[58] Prozorov, T., Mallapragada, S. K., Narasimhan, B., Wang, L., Palo, P., Nilsen-hamilton, M., Williams, T. J., Bazylinski, D. A., Prozorov, R., and Canfield, P. C. *Advanced Functional Materials* **17**(6), 951–957 (2007).

[59] Prozorov, T., Palo, P., Wang, L., Nilsen-Hamilton, M., Jones, D., Orr, D., Mallapragada, S. K., Narasimhan, B., Canfield, P. C., and Prozorov, R. *Acs Nano* **1**(3), 228–233 (2007).

[60] Galloway, J. M., Arakaki, A., Masuda, F., Tanaka, T., Matsunaga, T., and Staniland, S. S. *Journal of Materials Chemistry* **21**(39), 15244–15254 (2011).

[61] Dickerson, M. B., Sandhage, K. H., and Naik, R. R. *Chemical Reviews* **108**(11), 4935–4978 (2008).

[62] Slocik, J. M. and Wright, D. W. *Biomacromolecules* **4**(5), 1135–1141 (2003).

[63] Slocik, J. M., Stone, M. O., and Naik, R. R. *Small* **1**(11), 1048–1052 (2005).

[64] Nair, B. and Pradeep, T. *Crystal Growth & Design* **2**(4), 293–298 (2002).

[65] Southam, G. and Beveridge, T. J. *Geochimica et Cosmochimica Acta* **60**(22), 4369–4376 (1996).

[66] Klaus, T., Joerger, R., Olsson, E., and Granqvist, C.-G. *Proceedings of the National Academy of Sciences* **96**(24), 13611–13614 (1999).

[67] Mukherjee, P., Ahmad, A., Mandal, D., Senapati, S., Sainkar, S. R., Khan, M. I., Parishcha, R., Ajaykumar, P. V., Alam, M., Kumar, R., and Sastry, M. *Nano Letters* **1**(10), 515–519 (2001).

[68] Ahmad, A., Mukherjee, P., Mandal, D., Senapati, S., Khan, M. I., Kumar, R., and Sastry, M. *Journal of the American Chemical Society* **124**(41), 12108–12109 (2002).

[69] Bhattacharjee, R. R., Das, A. K., Haldar, D., Si, S., Banerjee, A., and Mandal, T. K. *Journal of Nanoscience and Nanotechnology* **5**(7), 1141–1147 (2005).

[70] Si, S., Bhattacharjee, R. R., Banerjee, A., and Mandal, T. K. *Chemistry - A European Journal* **12**(4), 1256–1265 (2006).

[71] Ray, S., Das, A. K., and Banerjee, A. *Chemical Communications* (26), 2816–2818 (2006).

[72] Si, S. and Mandal, T. K. *Langmuir* **23**(1), 190–195 (2007).

[73] Chen, C. L. and Rosi, N. L. *Angewandte Chemie-International Edition* **49**(11), 1924–1942 (2010).

[74] Nidhin, M., Indumathy, R., Sreeram, K. J., and Nair, B. U. *Bulletin of Materials Science* **31**(1), 93–96 (2008).

[75] Huang, H. Z. and Yang, X. R. *Colloids and Surfaces a-Physicochemical and Engineering Aspects* **226**(1-3), 77–86 (2003).

[76] Huang, H. Z. and Yang, X. R. *Carbohydrate Research* **339**(15), 2627–2631 (2004).

[77] Lin, N., Huang, J., and Dufresne, A. *Nanoscale* **4**(11), 3274–3294 (2012).

[78] Shan, J. and Tenhu, H. *Chemical Communications* (44), 4580–4598 (2007).

[79] Widoniak, J., Eiden-Assmann, S., and Maret, G. *Colloids and Surfaces a-Physicochemical and Engineering Aspects* **270**, 340–344 (2005).

[80] Qin, Y. Q., Ji, X. H., Jing, J., Liu, H., Wu, H. L., and Yang, W. S. *Colloids and Surfaces a-Physicochemical and Engineering Aspects* **372**(1-3), 172–176 (2010).

[81] Singha, D., Barman, N., and Sahu, K. *Journal of Colloid and Interface Science* **413**, 37–42 (2014).

[82] Dadosh, T. *Materials Letters* **63**(26), 2236–2238 (2009).

[83] Wan, Y., Guo, Z., Jiang, X., Fang, K., Lu, X., Zhang, Y., and Gu, N. *Journal of Colloid and Interface Science* **394**, 263–268 (2013).

[84] Grzelczak, M., Perez-Juste, J., Mulvaney, P., and Liz-Marzan, L. M. *Chemical Society Reviews* **37**(9), 1783–1791 (2008).

[85] Park, C., Yoon, J., and Thomas, E. L. *Polymer* **44**(22), 6725–6760 (2003).

[86] Shchukin, D. G. and Sukhorukov, G. B. *Advanced Materials* **16**(8), 671–682 (2004).

[87] Pang, X. C., Zhao, L., Han, W., Xin, X. K., and Lin, Z. Q. *Nature Nanotechnology* **8**(6), 426–431 (2013).

[88] Pastoriza-Santos, I. and Liz-Marzan, L. M. *Advanced Functional Materials* **19**(5), 679–688 (2009).

[89] Thomas, V., Yallapu, M. M., Sreedhar, B., and Bajpai, S. K. *Journal of Colloid and Interface Science* **315**(1), 389–395 (2007).

[90] Saravanan, P., Raju, M. P., and Alam, S. *Materials Chemistry and Physics* **103**(2-3), 278–282 (2007).

[91] Anastasiadis, S. H. and Vamvakaki, M. *International Journal of Nanotechnology* **6**(1-2), 46–70 (2009).

[92] Mei, Y., Lu, Y., Polzer, F., Ballauff, M., and Drechsler, M. *Chemistry of Materials* **19**(5), 1062–1069 (2007).

[93] Sakai, T. and Alexandridis, P. *Langmuir* **20**(20), 8426–8430 (2004).

[94] Yahyaei, B. and Azizian, S. *Journal of Dispersion Science and Technology* **35**(1), 98–102 (2014).

[95] Angelescu, D. G., Vasilescu, M., Anastasescu, M., Baratoiu, R., Donescu, D., and Teodorescu, V. S. *Colloids and Surfaces a-Physicochemical and Engineering Aspects* **394**, 57–66 (2012).

[96] Park, S., Murthy, P. S. K., Mohan, Y. M., and Koh, W. G. *Journal of Industrial and Engineering Chemistry* **17**(2), 293–297 (2011).

[97] Sakai, T. and Alexandridis, P. *Journal of Physical Chemistry B* **109**(16), 7766–7777 (2005).

[98] Sakai, T. and Alexandridis, P. *Nanotechnology* **16**(7), S344–S353 (2005).

[99] Sakai, T. and Alexandridis, P. *Langmuir* **21**(17), 8019–8025 (2005).

[100] Nie, Z. H., Petukhova, A., and Kumacheva, E. *Nature Nanotechnology* **5**(1), 15–25 (2010).

[101] Altunbas, A., Sharma, N., Lamm, M. S., Yan, C. Q., Nagarkar, R. P., Schneider, J. P., and Pochan, D. J. *Acs Nano* **4**(1), 181–188 (2010).

[102] Lamm, M. S., Sharma, N., Rajagopal, K., Beyer, F. L., Schneider, J. P., and Pochan, D. J. *Advanced Materials* **20**(3), 447–+ (2008).

[103] Cavalli, S., Popescu, D. C., Tellers, E. E., Vos, M. R. J., Pichon, B. P., Overhand, M., Rapaport, H., Sommerdijk, N., and Kros, A. *Angewandte Chemie-International Edition* **45**(5), 739–744 (2006).

[104] Sharma, N., Top, A., Kiick, K. L., and Pochan, D. J. *Angewandte Chemie-International Edition* **48**(38), 7078–7082 (2009).

[105] Nochomovitz, R., Amit, M., Matmor, M., and Ashkenasy, N. *Nanotechnology* **21**(14) (2010).

[106] Djalali, R., Chen, Y., and Matsui, H. *Journal of the American Chemical Society* **124**(46), 13660–13661 (2002).

[107] Li, L. S. and Stupp, S. I. *Angewandte Chemie-International Edition* **44**(12), 1833–1836 (2005).

[108] Sone, E. D. and Stupp, S. I. *Journal of the American Chemical Society* **126**(40), 12756–12757 (2004).

[109] Rajagopal, K. and Schneider, J. P. *Current Opinion in Structural Biology* **14**(4), 480–486 (2004).

[110] Gao, X. Y. and Matsui, H. *Advanced Materials* **17**(17), 2037–2050 (2005).

[111] de la Rica, R. and Matsui, H. *Chemical Society Reviews* **39**(9), 3499–3509 (2010).

[112] Cavalli, S., Albericio, F., and Kros, A. *Chemical Society Reviews* **39**(1), 241–263 (2010).

[113] Bird, S. M., Galloway, J. M., Rawlings, A. E., Bramble, J. P., and Staniland, S. S. *Nanoscale* **7**(16), 7340–7351 (2015).

[114] Liu, X., Zhang, H., Nayak, S., Parada, G., Anderegg, J., Feng, S., Nilsen-Hamilton, M., Akinc, M., and Mallapragada, S. K. *Industrial & Engineering Chemistry Research* **54**(42), 10284–10292 (2015).

[115] Volkmer, D., Fricke, M., Agena, C., and Mattay, J. *Journal of Materials Chemistry* **14**(14), 2249–2259 (2004).

[116] Fricke, M., Volkmer, D., Krill, C. E., Kellermann, M., and Hirsch, A. *Crystal Growth & Design* **6**(5), 1120–1123 (2006).

[117] Donners, J., Nolte, R. J. M., and Sommerdijk, N. *Journal of the American Chemical Society* **124**(33), 9700–9701 (2002).

[118] Travaille, A. M., Donners, J., Gerritsen, J. W., Sommerdijk, N., Nolte, R. J. M., and van Kempen, H. *Advanced Materials* **14**(7), 492–+ (2002).

[119] Aizenberg, J., Black, A. J., and Whitesides, G. M. *Nature* **398**(6727), 495–498 (1999).

[120] Galloway, J. M., Bramble, J. P., Rawlings, A. E., Burnell, G., Evans, S. D., and Staniland, S. S. *Small* **8**(2), 204–208 (2012).

[121] Balz, M., Barriau, E., Istratov, V., Frey, H., and Tremel, W. *Langmuir* **21**(9), 3987–3991 (2005).

[122] Nonoyama, T., Ogasawara, H., Tanaka, M., Higuchi, M., and Kinoshita, T. *Soft Matter* **8**(45), 11531–11536 (2012).

[123] Enlow, D., Rawal, A., Kanapathipillai, M., Schmidt-Rohr, K., Mallapragada, S., Lo, C. T., Thiyagarajan, P., and Akinc, M. *Journal of Materials Chemistry* **17**(16), 1570–1578 (2007).

[124] Kanapathipillai, M., Yusufoglu, Y., Rawal, A., Hu, Y. y., Lo, C. t., Thiyagarajan, P., Kalay, Y. E., Akinc, M., Mallapragada, S., and Schmidt-rohr, K. *Chemistry of Materials* **20**(18), 5922–5932 (2008).

[125] Yusufoglu, Y., Hu, Y., Kanapathipillai, M., Kramer, M., Kalay, Y. E., Thiyagarajan, P., Akinc, M., Schmidt-rohr, K., and Mallapragada, S. *Journal of Materials Research* **23**(12), 3196–3212 (2008).

[126] Nindiyasari, F., Ziegler, A., Griesshaber, E., Fernandez-Diaz, L., Huber, J., Walther, P., and Schmahl, W. W. *Crystal Growth & Design* **15**(6), 2667–2685 (2015).

[127] Deng, Z. X., Tian, Y., Lee, S. H., Ribbe, A. E., and Mao, C. D. *Angewandte Chemie-International Edition* **44**(23), 3582–3585 (2005).

[128] Wu, A. G., Cheng, W. L., Li, Z. A., Jiang, J. G., and Wang, E. K. *Talanta* **68**(3), 693–699 (2006).

[129] Patolsky, F., Weizmann, Y., Lioubashevski, O., and Willner, I. *Angewandte Chemie-International Edition* **41**(13), 2323–2327 (2002).

[130] Warner, M. G. and Hutchison, J. E. *Nature Materials* **2**(4), 272–277 (2003).

[131] Nakao, H., Shiigi, H., Yamamoto, Y., Tokonami, S., Nagaoka, T., Sugiyama, S., and Ohtani, T. *Nano Letters* **3**(10), 1391–1394 (2003).

[132] Rothemund, P. W. K. *Nature* **440**(7082), 297–302 (2006).

[133] Douglas, S. M., Dietz, H., Liedl, T., Hogberg, B., Graf, F., and Shih, W. M. *Nature* **459**(7245), 414–418 (2009).

[134] Sun, W., Boulais, E., Hakobyan, Y., Wang, W. L., Guan, A., Bathe, M., and Yin, P. *Science* **346**(6210) (2014).

[135] Lau, K. L., Hamblin, G. D., and Sleiman, H. F. *Small* **10**(4), 660–666 (2014).

[136] Liu, Q., Song, C., Wang, Z. G., Li, N., and Ding, B. Q. *Methods* **67**(2), 205–214 (2014).

[137] Schreiber, R., Do, J., Roller, E.-M., Zhang, T., Schüller, V. J., Nickels, P. C., Feldmann, J., and Liedl, T. *Nature nanotechnology* **9**(1), 74 (2014).

[138] Roller, E. M., Khorashad, L. K., Fedoruk, M., Schreiber, R., Govorov, A. O., and Liedl, T. *Nano Letters* **15**(2), 1368–1373 (2015).

[139] Gür, F. N., Schwarz, F. W., Ye, J., Diez, S., and Schmidt, T. L. *ACS Nano* **10**(5), 5374–5382 (2016).

[140] Wang, P. F., Gaitanaros, S., Lee, S., Bathe, M., Shih, W. M., and Ke, Y. G. *Journal of the American Chemical Society* **138**(24), 7733–7740 (2016).

[141] Tian, C., Li, X., Liu, Z. Y., Jiang, W., Wang, G. S., and Mao, C. D. *Angewandte Chemie-International Edition* **53**(31), 8041–8044 (2014).

[142] Lin, C. X., Liu, Y., Rinker, S., and Yan, H. *Chemphyschem* **7**(8), 1641–1647 (2006).

[143] Zhang, Y. G., Lu, F., Yager, K. G., van der Lelie, D., and Gang, O. *Nature Nanotechnology* **8**(11), 865–872 (2013).

[144] Siavashpouri, M., Wachauf, C. H., Zakhary, M. J., Praetorius, F., Dietz, H., and Dogic, Z. *Nature materials* **16**(8), 849 (2017).

[145] Aldaye, F. A., Palmer, A. L., and Sleiman, H. F. *Science* **321**(5897), 1795–1799 (2008).

[146] Jones, M. R., Seeman, N. C., and Mirkin, C. A. *Science* **347**(6224) (2015).

[147] Seeman, N. C. *Annual Review of Biochemistry, Vol 79* **79**, 65–87 (2010).

[148] Samanta, A. and Medintz, I. L. *Nanoscale* **8**(17), 9037–9095 (2016).

[149] Giannelis, E. P. *Advanced Materials* **8**(1), 29–& (1996).

[150] Sahoo, N. G., Rana, S., Cho, J. W., Li, L., and Chan, S. H. *Progress in Polymer Science* **35**(7), 837–867 (2010).

[151] Caseri, W. *Macromolecular Rapid Communications* **21**(11), 705–722 (2000).

[152] Kyprianidouleodidou, T., Caseri, W., and Suter, U. W. *Journal of Physical Chemistry* **98**(36), 8992–8997 (1994).

[153] Weibel, M., Caseri, W., Suter, U. W., Kiess, H., and Wehrli, E. *Polymers for Advanced Technologies* **2**(2), 75–80 (1991).

[154] Dirix, Y., Bastiaansen, C., Caseri, W., and Smith, P. *Advanced Materials* **11**(3), 223–+ (1999).

[155] Dirix, Y., Darribere, C., Heffels, W., Bastiaansen, C., Caseri, W., and Smith, P. *Applied Optics* **38**(31), 6581–6586 (1999).

[156] Caseri, W. *Journal of Materials Chemistry* **20**(27), 5582–5592 (2010).

[157] Faupel, F., Zaporojtchenko, V., Greve, H., Schuermann, U., Chakravadhanula, V. S. K., Hanisch, C., Kulkarni, A., Gerber, A., Quandt, E., and Podschun, R. *Contributions to Plasma Physics* **47**(7), 537–544 (2007).

[158] Schallibaum, J., Dalla Torre, F. H., Caseri, W. R., and Loffler, J. F. *Nanoscale* **1**(3), 374–381 (2009).

[159] Takele, H., Jebril, S., Strunskus, T., Zaporojchenko, V., Adelung, R., and Faupel, F. *Applied Physics a-Materials Science & Processing* **92**(2), 345–350 (2008).

[160] Faupel, F., Zaporojtchenko, V., Strunskus, T., and Elbahri, M. *Advanced Engineering Materials* **12**(12), 1177–1190 (2010).

[161] Althues, H., Henle, J., and Kaskel, S. *Chemical Society Reviews* **36**(9), 1454–1465 (2007).

[162] Hanemann, T. and Szabo, D. V. *Materials* **3**(6), 3468–3517 (2010).

[163] Paul, D. R. and Robeson, L. M. *Polymer* **49**(15), 3187–3204 (2008).

[164] Krishnamoorti, R. *Mrs Bulletin* **32**(4), 341–347 (2007).

[165] Clifford, D. C., Castano, C. E., and Rojas, J. V. *Radiation Physics and Chemistry* **132**, 52–64 (2017).

[166] Yi, C. L., Zhang, S. Y., Webb, K. T., and Nie, Z. H. *Accounts of Chemical Research* **50**(1), 12–21 (2017).

[167] Balazs, A. C., Emrick, T., and Russell, T. P. *Science* **314**(5802), 1107–1110 (2006).

[168] Bockstaller, M. R., Mickiewicz, R. A., and Thomas, E. L. *Advanced Materials* **17**(11), 1331–1349 (2005).

[169] Shenhar, R., Norsten, T. B., and Rotello, V. M. *Advanced Materials* **17**(6), 657–669 (2005).

[170] Huh, J., Ginzburg, V. V., and Balazs, A. C. *Macromolecules* **33**(21), 8085–8096 (2000).

[171] Thompson, R. B., Ginzburg, V. V., Matsen, M. W., and Balazs, A. C. *Science* **292**(5526), 2469–2472 (2001).

[172] Qiu, X. and Wang, Z. G. *Journal of Colloid and Interface Science* **167**(2), 294–300 (1994).

[173] Mackay, M. E., Tuteja, A., Duxbury, P. M., Hawker, C. J., Van Horn, B., Guan, Z. B., Chen, G. H., and Krishnan, R. S. *Science* **311**(5768), 1740–1743 (2006).

[174] Taheri, S. M., Fischer, S., and Forster, S. *Polymers* **3**(2), 662–673 (2011).

[175] Lu, J. X., Moon, K. S., Wong, C. P., and Ieee. In *56th Electronic Components and Technology Conference*, Electronic Components and Technology Conference, 1841–+, (2006).

[176] Mayer, A. B. R. and Mark, J. E. *Colloid and Polymer Science* **275**(4), 333–340 (1997).

[177] Spatz, J. P., Mossmer, S., and Moller, M. *Chemistry-a European Journal* **2**(12), 1552–1555 (1996).

[178] Spatz, J., Mossmer, S., Moller, M., Kocher, M., Neher, D., and Wegner, G. *Advanced Materials* **10**(6), 473–+ (1998).

[179] Soler-Illia, G., Crepaldi, E. L., Grosso, D., and Sanchez, C. *Current Opinion in Colloid & Interface Science* **8**(1), 109–126 (2003).

[180] Hamley, I. W. *Nanotechnology* **14**(10), R39–R54 (2003).

[181] Forster, S. and Antonietti, M. *Advanced Materials* **10**(3), 195–+ (1998).

[182] Boontongkong, Y. and Cohen, R. E. *Macromolecules* **35**(9), 3647–3652 (2002).

[183] Akasaka, S., Mori, H., Osaka, T., Mareau, V. H., and Hasegawa, H. *Macromolecules* **42**(4), 1194–1202 (2009).

[184] Chai, J. and Buriak, J. M. *Acs Nano* **2**(3), 489–501 (2008).

[185] Cho, H., Park, H., Park, S., Choi, H., Huang, H., and Chang, T. *Journal of Colloid and Interface Science* **356**(1), 1–7 (2011).

[186] Cowman, C. D., Padgett, E., Tan, K. W., Hovden, R., Gu, Y., Andrejevic, N., Muller, D., Coates, G. W., and Wiesner, U. *Journal of the American Chemical Society* **137**(18), 6026–6033 (2015).

[187] Adachi, M., Okumura, A., Sivaniah, E., and Hashimoto, T. *Macromolecules* **39**(21), 7352–7357 (2006).

[188] Hsueh, H. Y., Huang, Y. C., Ho, R. M., Lai, C. H., Makida, T., and Hasegawa, H. *Advanced Materials* **23**(27), 3041–+ (2011).

[189] Yang, P. D., Zhao, D. Y., Margolese, D. I., Chmelka, B. F., and Stucky, G. D. *Nature* **396**(6707), 152–155 (1998).

[190] Gorka, J., Fenning, C., and Jaroniec, M. *Colloids and Surfaces a-Physicochemical and Engineering Aspects* **352**(1-3), 113–117 (2009).

[191] Deng, Y., Liu, C., Yu, T., Liu, F., Zhang, F., Wan, Y., Zhang, L., Wang, C., Tu, B., Webley, P. A., Wang, H., and Zhao, D. *Chemistry of Materials* **19**(13), 3271–3277 (2007).

[192] Meng, Y., Gu, D., Zhang, F. Q., Shi, Y. F., Cheng, L., Feng, D., Wu, Z. X., Chen, Z. X., Wan, Y., Stein, A., and Zhao, D. Y. *Chemistry of Materials* **18**(18), 4447–4464 (2006).

[193] She, L., Li, J., Wan, Y., Yao, X. D., Tu, B., and Zhao, D. Y. *Journal of Materials Chemistry* **21**(3), 795–800 (2011).

[194] Xu, J. M., Wang, A. Q., Wang, X. D., Su, D. S., and Zhang, T. *Nano Research* **4**(1), 50–60 (2011).

[195] Ji, Z. H., Ye, L., Tao, X. Y., Li, H., Qiu, W. F., Cai, T., Jiang, Y. B., and Zhao, T. *Materials Letters* **71**, 88–90 (2012).

[196] Yang, P. D., Zhao, D. Y., Margolese, D. I., Chmelka, B. F., and Stucky, G. D. *Chemistry of Materials* **11**(10), 2813–2826 (1999).

[197] Anderson, J. A. and Travesset, A. *Macromolecules* **39**(15), 5143–5151 (2006).

[198] Anderson, J. A., Sknepnek, R., and Travesset, A. *Physical Review E* **82**(2) (2010).

[199] Knorowski, C. D., Anderson, J. A., and Travesset, A. *Journal of Chemical Physics* **128**(16) (2008).

[200] Sknepnek, R., Anderson, J. A., Lamm, M. H., Schmalian, J., and Travesset, A. *Acs Nano* **2**(6), 1259–1265 (2008).

[201] Cheng, S. W., Mirigian, S., Carrillo, J. M. Y., Bocharova, V., Sumpter, B. G., Schweizer, K. S., and Sokolov, A. P. *Journal of Chemical Physics* **143**(19) (2015).

[202] Harton, S. E. and Kumar, S. K. *Journal of Polymer Science Part B-Polymer Physics* **46**(4), 351–358 (2008).

[203] Ganesan, V., Ellison, C. J., and Pryamitsyn, V. *Soft Matter* **6**(17), 4010–4025 (2010).

[204] Sarkar, B. and Alexandridis, P. *Langmuir* **28**(45), 15975–15986 (2012).

[205] Banerjee, D. and Schweizer, K. S. *Journal of Polymer Science Part B-Polymer Physics* **53**(16), 1098–1111 (2015).

[206] Jouault, N., Zhao, D., and Kumar, S. K. *Macromolecules* **47**(15), 5246–5255 (2014).

[207] Lo, C. T., Lee, B., Winans, R. E., and Thiyagarajan, P. *Macromolecules* **40**(3), 641–647 (2007).

[208] She, M. S., Lo, T. Y., and Ho, R. M. *Acs Nano* **7**(3), 2000–2011 (2013).

[209] Seshimo, T., Maeda, R., Odashima, R., Takenaka, Y., Kawana, D., Ohmori, K., and Hayakawa, T. *Scientific Reports* **6** (2016).

[210] Hu, B., Henn, D. M., Wright, R. A. E., and Zhao, B. *Langmuir* **30**(37), 11212–11224 (2014).

[211] Li, W. K., Liu, S. Q., Deng, R. H., and Zhu, J. T. *Angewandte Chemie-International Edition* **50**(26), 5865–5868 (2011).

[212] Li, W., Zhang, P., Dai, M., He, J., Babu, T., Xu, Y., Deng, R., Liang, R., Lu, M., Nie, Z., and Zhu, J. *Macromolecules* **46**(6), 2241–2248 (2013).

[213] Gupta, S., Zhang, Q. L., Emrick, T., Balazs, A. C., and Russell, T. P. *Nature Materials* **5**(3), 229–233 (2006).

[214] Xu, C., Ohno, K., Ladmiral, V., Milkie, D. E., Kikkawa, J. M., and Composto, R. J. *Macromolecules* **42**(4), 1219–1228 (2009).

[215] Grabowski, C. A., Koerner, H., Meth, J. S., Dang, A., Hui, C. M., Matyjaszewski, K., Bockstaller, M. R., Durstock, M. F., and Vaia, R. A. *Acs Applied Materials & Interfaces* **6**(23), 21500–21509 (2014).

[216] Gas, J., Poddar, P., Almand, J., Srinath, S., and Srikanth, H. *Advanced Functional Materials* **16**(1), 71–75 (2006).

[217] Kim, B. J., Fredrickson, G. H., Hawker, C. J., and Kramer, E. J. *Langmuir* **23**(14), 7804–7809 (2007).

[218] Yeh, S. W., Wei, K. H., Sun, Y. S., Jeng, U. S., and Liang, K. S. *Macromolecules* **38**(15), 6559–6565 (2005).

[219] Kim, G., Swier, S., Lee, H.-J., and Wang, C. *Macromolecules* **49**(19), 7370–7378 (2016).

[220] Song, D. P., Gai, Y., Yavitt, B. M., Ribbe, A., Gido, S., and Watkins, J. J. *Macromolecules* **49**(17), 6480–6488 (2016).

[221] Knorowski, C. and Travesset, A. *Epl* **100**(5) (2012).

[222] Castelletto, V., Ansari, I. A., and Hamley, I. W. *Macromolecules* **36**(5), 1694–1700 (2003).

[223] Murray, C. B., Kagan, C. R., and Bawendi, M. G. *Science* **270**(5240), 1335–1338 (1995).

[224] Motte, L., Billoudet, F., and Pileni, M. *Journal Of Physical Chemistry* **99**(44), 16425–16429 (1995).

[225] Reichhelm, A., Haubold, D., and Eychmüller, A. *Advanced Functional Materials* **27**(39), 1700361 (2017).

[226] Shevchenko, E. V., Talapin, D. V., Kotov, N. A., O'Brien, S., and Murray, C. B. *Nature* **439**, 55 (2006).

[227] Dong, A., Ye, X., Chen, J., and Murray, C. B. *Nano Letters* **11**(4), 1804–1809 (2011).

[228] Ye, X. C., Zhu, C. H., Ercius, P., Raja, S. N., He, B., Jones, M. R., Hauwiller, M. R., Liu, Y., Xu, T., and Alivisatos, A. P. *Nature Communications* **6** (2015).

[229] Ye, X., Chen, J., Eric Irrgang, M., Engel, M., Dong, A., Glotzer, S. C., and Murray, C. B. *Nature materials* **16**(2), 214 (2017).

[230] Ushakova, E. V., Cherevkov, S. A., Litvin, A. P., Parfenov, P. S., Kasatkin, I. A., Fedorov, A. V., Gun'Ko, Y. K., and Baranov, A. V. *Nanoscale* **10**(17), 8313–8319 (2018).

[231] Taleb, A., Petit, C., and Pileni, M. *Journal of Physical Chemistry B* **102**(12) (1998).

[232] Pileni, M., Jaeger, H., Sorensen, C., Klabunde, K., Tobin, J. G., Co, D. T., and Saykally, R. *Journal of Physical Chemistry B* **105**(17) (2001).

[233] Pileni, M. *Accounts Of Chemical Research* **40**(8), 685–693 (2007).

[234] Teraoka, I. *Polymer solutions : an introduction to physical properties / Iwao Teraoka.* Wiley, New York, (2002).

[235] Wohlfarth, C. *CRC handbook of phase equilibria and thermodynamic data of aqueous polymer solutions / Christian Wohlfarth.* Taylor & Francis, Boca Raton, FL, (2013).

[236] Knychala, P., Timachova, K., Banaszak, M., and Balsara, N. P. *Macromolecules* **50**(8) (2017).

[237] Si, K. J., Chen, Y., Shi, Q., and Cheng, W. *Advanced science (Weinheim, Baden-Wurttemberg, Germany)* **5**(1) (2018).

[238] Zoppe, J. O., Ataman, N. C., Mocny, P., Wang, J., Moraes, J., and Klok, H.-A. *Chemical reviews* **117**(3) (2017).

[239] Liu, Z. W., Lee, H., Xiong, Y., Sun, C., and Zhang, X. *Science* **315**(5819), 1686–1686 (2007).

[240] Achilleos, D. and Vamvakaki, M. *Materials* **3**(3), 1981–2026 (2010).

[241] Asai, M., Zhao, D., and Kumar, S. K. *ACS Nano* **11**(7), 7028–7035 (2017). PMID: 28618225.

[242] Zhang, H., Wang, W., Mallapragada, S., Travesset, A., and Vaknin, D. *Nanoscale* **9**(1), 164–171 (2016).

[243] Zhang, H., Wang, W., Akinc, M., Mallapragada, S., Travesset, A., and Vaknin, D. *Nanoscale* **9**(25), 8710–8715 (2017).

[244] Wang, W., Lawrence, J. J., Bu, W., Zhang, H., and Vaknin, D. *Langmuir* **34**(28), 8374–8378 (2018).

[245] Yi, C., Zhang, S., Webb, K. T., and Nie, Z. *Accounts of chemical research* **50**(1) (2017).

[246] Mirkin, C. A., Letsinger, R. L., Mucic, R. C., and Storhoff, J. J. *Nature* **382**(6592), 607–609 (1996).

[247] Alivisatos, A. P., Johnsson, K. P., Peng, X. G., Wilson, T. E., Loweth, C. J., Bruchez, M. P., and Schultz, P. G. *Nature* **382**(6592), 609–611 (1996).

[248] Nykypanchuk, D., Maye, M. M., van der Lelie, D., and Gang, O. *Nature* **451**(7178), 549–552 (2008).

[249] Park, S. Y., Lytton-Jean, A. K. R., Lee, B., Weigand, S., Schatz, G. C., and Mirkin, C. A. *Nature* **451**, 553 (2008).

[250] Park, S. Y., Lee, J. S., Georganopoulou, D., Mirkin, C. A., and Schatz, G. C. *Journal of Physical Chemistry B* **110**(25), 12673–12681 (2006).

[251] Nykypanchuk, D., Maye, M. M., van Der Lelie, D., and Gang, O. *Langmuir : the ACS journal of surfaces and colloids* **23**(11) (2007).

[252] Hill, H. D., Macfarlane, R. J., Senesi, A. J., Lee, B., Park, S. Y., and Mirkin, C. A. *Nano Letters* **8**(8), 2341–2344 (2008).

[253] Xiong, H., van der Lelie, D., and Gang, O. *Journal of the American Chemical Society* **130**(8), 2442–2443 (2008).

[254] Macfarlane, R. J., Jones, M. R., Senesi, A. J., Young, K. L., Lee, B., Wu, J., and Mirkin, C. A. *Angewandte Chemie (International ed. in English)* **49**(27), 4589 (2010).

[255] Maye, M. M., Kumara, M. T., Nykypanchuk, D., Sherman, W. B., and Gang, O. *Nat Nano* **5**(2), 116–120 (2010).

[256] Macfarlane, R. J., Lee, B., Jones, M. R., Harris, N., Schatz, G. C., and Mirkin, C. A. *Science* **334**(6053), 204–208 (2011).

[257] Senesi, A. J., Eichelsdoerfer, D. J., Brown, K. A., Lee, B., Auyeung, E., Choi, C. H. J., Macfarlane, R. J., Young, K. L., and Mirkin, C. A. **26**(42), 7235 (2014).

[258] Pal, S., Zhang, Y., Kumar, S. K., and Gang, O. *Journal of the American Chemical Society* **137**(12), 4030–4033 (2015).

[259] Lu, F., Yager, K. G., Zhang, Y., Xin, H., and Gang, O. *Nature Communications* **6**, 6912 (2015).

[260] Thaner, R. V., Eryazici, I., Macfarlane, R. J., Brown, K. A., Lee, B., Nguyen, S. T., and Mirkin, C. A. *Journal of the American Chemical Society* **138**(19), 6119–6122 (2016).

[261] Seo, S. E., Li, T., Senesi, A. J., Mirkin, C. A., and Lee, B. *Journal of the American Chemical Society* **139**(46), 16528–16535 (2017).

[262] Storhoff, J. J., Lazarides, A. A., Mucic, R. C., Mirkin, C. A., Letsinger, R. L., and Schatz, G. C. *Journal of the American Chemical Society* **122**(19), 4640–4650 (2000).

[263] Wood, R. *Ieee Transactions on Magnetics* **36**(1), 36–42 (2000).

[264] Ross, C. *Annual Review of Materials Research* **31**, 203–235 (2001).

[265] Todorovic, M., Schultz, S., Wong, J., and Scherer, A. *Applied Physics Letters* **74**(17), 2516–2518 (1999).

[266] Fernandez, A., Bedrossian, P. J., Baker, S. L., Vernon, S. P., and Kania, D. R. *Ieee Transactions on Magnetics* **32**(5), 4472–4474 (1996).

[267] Weller, D., Moser, A., Folks, L., Best, M. E., Lee, W., Toney, M. F., Schwickert, M., Thiele, J. U., and Doerner, M. F. *Ieee Transactions on Magnetics* **36**(1), 10–15 (2000).

[268] Griffiths, R. A., Williams, A., Oakland, C., Roberts, J., Vijayaraghavan, A., and Thomson, T. *Journal of Physics D-Applied Physics* **46**(50) (2013).

[269] Dobisz, E. A., Bandic, Z. Z., Wu, T.-W., and Albrecht, T. *Proceedings of the Ieee* **96**(11), 1836–1846 (2008).

[270] Shiroishi, Y., Fukuda, K., Tagawa, I., Iwasaki, H., Takenoiri, S., Tanaka, H., Mutoh, H., and Yoshikawa, N. *Ieee Transactions on Magnetics* **45**(10), 3816–3822 (2009).

[271] Koh, I. and Josephson, L. *Sensors* **9**(10), 8130–8145 (2009).

[272] Haun, J. B., Yoon, T. J., Lee, H., and Weissleder, R. *Wiley Interdisciplinary Reviews-Nanomedicine and Nanobiotechnology* **2**(3), 291–304 (2010).

[273] Jung, J. H., Lee, J. H., and Shinkai, S. *Chemical Society Reviews* **40**(9), 4464–4474 (2011).

[274] Veselago, V. G. *Soviet Physics Uspekhi-Ussr* **10**(4), 509–& (1968).

[275] Pendry, J. B., Holden, A. J., Robbins, D. J., and Stewart, W. J. *Ieee Transactions on Microwave Theory and Techniques* **47**(11), 2075–2084 (1999).

[276] Smith, D. R. and Kroll, N. *Physical Review Letters* **85**(14), 2933–2936 (2000).

[277] Ergin, T., Stenger, N., Brenner, P., Pendry, J. B., and Wegener, M. *Science* **328**(5976), 337–339 (2010).

[278] Shelby, R. A., Smith, D. R., and Schultz, S. *Science* **292**(5514), 77–79 (2001).

[279] Schurig, D., Mock, J. J., Justice, B. J., Cummer, S. A., Pendry, J. B., Starr, A. F., and Smith, D. R. *Science* **314**(5801), 977–980 (2006).

[280] Dolling, G., Wegener, M., Soukoulis, C. M., and Linden, S. *Optics Letters* **32**(1), 53–55 (2007).

[281] Pendry, J. B. *Science* **306**(5700), 1353–1355 (2004).

[282] Tretyakov, S., Nefedov, I., Sihvola, A., Maslovski, S., and Simovski, C. *Journal of Electromagnetic Waves and Applications* **17**(5), 695–706 (2003).

[283] Plum, E., Zhou, J., Dong, J., Fedotov, V. A., Koschny, T., Soukoulis, C. M., and Zheludev, N. I. *Physical Review B* **79**(3) (2009).

[284] Zhang, S., Park, Y. S., Li, J. S., Lu, X. C., Zhang, W. L., and Zhang, X. *Physical Review Letters* **102**(2) (2009).

[285] Vukovic, I., ten Brinke, G., and Loos, K. *Polymer* **54**(11), 2591–2605 (2013).

[286] Muehlig, S., Cunningham, A., Dintinger, J., Scharf, T., Buergi, T., Lederer, F., and Rockstuhl, C. *Nanophotonics* **2**(3), 211–240 (2013).

[287] Guldin, S. and Steiner, U. *Soft matter design principles for inorganic photonic nanoarchitectures in photovoltaics, colorimetric sensing and self-cleaning antireflective coatings*, volume 9083 of *Proceedings of SPIE*. (2014).

[288] Stefik, M., Guldin, S., Vignolini, S., Wiesner, U., and Steiner, U. *Chemical Society Reviews* **44**(15), 5076–5091 (2015).

[289] Fontana, J. and Ratna, B. R. *Applied Optics* **54**(31), F61–F69 (2015).

[290] Hur, K., Francescato, Y., Giannini, V., Maier, S. A., Hennig, R. G., and Wiesner, U. *Angewandte Chemie-International Edition* **50**(50), 11985–11989 (2011).

[291] Vignolini, S., Yufa, N. A., Cunha, P. S., Guldin, S., Rushkin, I., Stefik, M., Hur, K., Wiesner, U., Baumberg, J. J., and Steiner, U. *Advanced Materials* **24**(10), OP23–OP27 (2012).

[292] Salvatore, S., Demetriadou, A., Vignolini, S., Oh, S. S., Wuestner, S., Yufa, N. A., Stefik, M., Wiesner, U., Baumberg, J. J., Hess, O., and Steiner, U. *Advanced Materials* **25**(19), 2713–2716 (2013).

[293] du Sart, G. G., Vukovic, I., Vukovic, Z., Polushkin, E., Hiekkataipale, P., Ruokolainen, J., Loos, K., and ten Brinke, G. *Macromolecular Rapid Communications* **32**(4), 366–370 (2011).

CHAPTER 3. PROTEIN PATTERNS TEMPLATE ARRAYS OF MAGNETIC NANOPARTICLES

A paper published in the Journal RSC Advances

Srikanth Nayak, Honghu Zhang, Xunpei Liu, Shuren Feng, Pierre Palo, Marit Nilsen-Hamilton, Mufit Akinc, and Surya Mallapragada [1]

Abstract

Controlling the morphology of magnetic nanoparticles and their spatial arrangement is crucial for manipulating their functional properties. The commonly available inorganic processes for the synthesis of uniform magnetic nanoparticles typically require extreme reaction conditions such as high temperatures or harsh reagents, rendering them unsuitable for making functionalized magnetic nanoparticles with tunable properties controlled by biomolecules. Biomimetic procedures, inspired by the production of uniform magnetite and greigite crystals in magnetotactic bacteria, provide an alternative method, which can allow synthesis and spatial arrangement under ambient conditions. Mms6, an amphiphilic protein found in magnetosome membranes in *Magnetospirillum magneticum* strain AMB-1, can control the morphology of magnetite nanoparticles, both in vivo and in vitro. In this work, we have demonstrated the patterning of Mms6 and the formation of patterns of magnetic nanoparticles on selective regions of surfaces by directed self-assembly and control over surface chemistry, enabling facile spatial control in applications such as high density data storage and biosensors. Using microcontact printing we have obtained various patterns of 1-octadecane thiol (ODT) and protein resistant poly(ethylene glycol)methyl ether thiol (PEG) layers on gold surfaces. Atomic force microscopy (AFM) and fluorescence microscopy studies show the patterning of Mms6 on the ODT patterns and not on the PEG regions. Magnetic nanoparticles were grown on these surfaces by a co-precipitation method over immobilized protein. AFM and

[1] Author for correspondence

scanning electron microscopy (SEM) results show the localized growth of magnetic nanocrystals selectively on the Mms6 template, which in turn was determined by the ODT regions. Magnetic force measurements were conducted to assess the localization of magnetic nanoparticles on the pattern.

3.1 Introduction

Ordered assemblies of magnetic nanoparticles are of particular interest in the fields of high density data storage,[1] and sensing.[2] Magnetic properties of arrays of magnetic nanoparticles depend on the crystal properties as well as the physical structure of the assemblies.[3,4] These assemblies can be created by combining bottom-up processes to control crystal morphology with top-down processes to control the physical structure.[5]

Conventional synthesis procedures for magnetic nanoparticles do not allow for easy control over crystal morphology, especially at ambient conditions. By contrast, biomineralization of chains of uniform magnetite nanoparticles in magnetotactic bacteria occurs at ambient conditions in vivo.[6,7] An ensemble of biomolecules is thought to be involved in the formation of these structures.[8] Mms6, an amphiphilic protein found in the magnetosomes of Magnetospirillum magneticum, can control the size, shape and monodispersity of magnetite nanoparticles, both in vivo[9,10] and in vitro[9,11,12] using a room temperature co-precipitation (RTCP) method. While with the RTCP route, larger magnetite nanoparticles are formed in the presence of Mms6,[12–14] with other synthesis methods such as the partial oxidation of ferrous hydroxide (POFH) route, in the presence of Mms6, the reverse has been observed.[14,15] Galloway et. al further concluded that for obtaining either magnetite or cobalt ferrite particles in the single domain range, RTCP is preferred as POFH produces multi-domain particles.[15] The difference in particle sizes observed in the two routes was attributed to the difference in the concentration of OH- ions in the reaction mixture[15] and might potentially also be the result of the higher temperatures ($\sim 80^{o}$C) used in the POFH method that might have a detrimental effect on Mms6 activity. Recent work by Oestreicher et. al has shown the localization of Mms6 in the magnetosome during the crystal growth, wherein it was found to be in direct contact with the crystals indicating its significance in their formation.[16] Using

in-situ liquid cell High Angle Annular Dark Field - Scanning Transmission Electron Microscopy (HAADF-STEM), Kashyap et.al reported the surface localization of ferric ions on the negatively charged Mms6 micelles, which forms an amorphous precursor phase to iron oxide, upon slow addition of NaOH.[17] Further, in the presence of Mms6, nucleation was observed only on the Mms6 micelle surface and not in the bulk. In contrast, in-vivo studies have shown that Mms6 is not involved in the nucleation, but only in the crystal growth.[10,16]

The hydrophilic C-terminal domain of Mms6 plays a critical role in the formation of these particles.[9,11,18] m2Mms6, a synthetic C-terminal domain mutant of the wild type Mms6, does not template the formation of larger, uniform magnetite crystals.[11] With respect to the wild-type Mms6, this mutant has its C-terminal domain altered such that it has the same hydropathy profile, but the amino acid residues containing hydroxyl groups and carboxyl groups have been shuffled with respect to each other.[18] Wild-type Mms6 is known to form micelles in aqueous solutions, with the glycine – leucine repeats and the bulky hydrophobic groups on tryptophan residues in the N-terminal being crucial to this self-assembly.[18] In addition, structural changes at the C-terminal domain in the mutant reduces iron binding significantly and alters the assembly of the protein, which suggests that the C-terminal domain plays an important role in the formation of these micelles.[18] Further, unlike m2Mms6, Mms6 has been observed to form network-like structures and template the formation of magnetite nanoparticles on hydrophobic surfaces.[19]

Several templates have been used for fabricating 1-D magnetic nanowires of metals and alloys, such as porous anodic aluminum oxide (AAO)[4,20,21] silicon nanowires fabricated by chemical etching[22] and nuclear etched nanoporous polycarbonate films.[3] These techniques are limited in their abilities to create a wide range of physical structures for templating ordered assemblies. Further, electrodeposition, used for depositing the magnetic material on these AAO templates, lacks the control over the formation of crystals provided by the biomineralization routes.[23] In contrast, soft lithography can create complex templates with multiple functionalities[24] and has been extensively used to create patterned surfaces for immobilizing proteins and cells.[25–27]

Arrays of Mms6 on surfaces have been created by microcontact printing and interferometric lithographic patterning of a cysteine-tagged protein (with an N-terminal thiol group) on Au sur-

face via thiol-Au interactions[28,29] or by covalently attaching the protein to a self-assembled monolayer of carboxyl-terminated alkane chains.[30] While the former requires genetic engineering of the protein, the latter lacks the required specificity. Further, such covalent binding of the protein can alter its structure and hence the function, which was not addressed in the above studies. Considering Mms6's isolation from the magnetosome membrane,[9] its integration into liposomes,[11] and its interaction with hydrophobic surfaces without loss of biomineralization activity,[19] it is desirable to create Mms6 patterns by non-covalent interactions between Mms6 and hydrophobic surfaces. Previous works on fabricating patterns of magnetite via the patterns of Mms6 have used POFH to induce the formation of magnetite[15,28–30] although the role of Mms6 in this synthesis route is not clear at the higher temperatures used, as mentioned earlier. No control groups for studying the role of immobilized proteins on the formation of magnetite nanoparticles were considered in these studies. Hence, it is not clear whether the results obtained with POFH are specific to Mms6 or whether any immobilized protein could produce the same result.

In this work, we demonstrate, for the first time, a room temperature facile synthesis method to create surfaces with patterns of magnetic nanoparticles using a bioinspired route involving the biomineralization protein Mms6. To study the specific effect of protein structure on the formation of these assemblies, two control proteins (m2mms6 and BSA) have been used. We have capitalized on the immobilization and network formation of Mms6 on hydrophobic surfaces as opposed to hydrophilic surfaces, based on our previous work[12,19] to create the patterned substrates. A template stripped gold surface was patterned with a hydrophobic self-assembled monolayer of 1-octadecane thiol (ODT) by micro-contact printing and backfilled with a protein resistant poly (ethylene glycol) methyl ether thiol (PEG) layer. These surfaces were used as templates for the assembly of Mms6 and the subsequent assembly of magnetic nanoparticles. Our results in this work show that the ODT-PEG pattern can direct the assembly of Mms6 and the pattern is retained even after RTCP and the magnetic nanoparticles are localized mainly in the ODT/Mms6 regions.

3.2 Materials and Methods

Materials Poly (dimethyl siloxane) (PDMS) pre-polymer, Slygard 184 Silicone Elastomer Kit, was purchased from Dow Corning Corporation. 1 - Octadecanethiol (ODT), poly (ethylene glycol) methyl ether thiol (average $M_n = 800$), iron (III) chloride hexahydrate ($FeCl_3.6H_2O$, $\geq 98\%$), iron (II) chloride tetrahydrate ($FeCl_2.4H_2O$, 99.99%), lyophilized Bovine Serum Albumin (BSA) powder (Cohn fraction V), Tween-20 and Pluronic F-127 were purchased from Sigma-Aldrich. Potassium chloride (KCl, $\geq$ 99%) and Tris base ($\geq$ 99.8%) were purchased from Fisher Scientific. Anti-6X His tag antibody (FITC) ab1206 was purchased from Abcam. TALON Metal Affinity Resin was purchased from BD Biosciences.

Recombinant Mms6 and its mutant m2Mms6 were expressed and prepared as reported earlier.[12,18] The proteins were obtained at 0.2 mg/ml concentration in 25 mM Tris and 100 mM KCl buffer at pH = 7.5. Both proteins were expressed in E.coli and extracted from cell lysates under denaturing conditions by way of their N-terminal poly-histidine tags using TALON affinity resin. The proteins were refolded at 4^o C by a sequential dialysis protocol to remove the urea in incremental steps over a period of about 18 h. An anti-His antibody (rabbit polyclonal) conjugated with FITC was used to fluorescently tag the poly-histidine, as a way of identifying Mms6 on the surface. BSA and m2Mms6 were used as control groups for studying Mms6 assembly on the patterned surfaces.

PDMS stamp PDMS (Poly(dimethyl siloxane)) stamps were prepared by standard soft lithography techniques.[31] Masks for different patterns were drawn in AutoCAD and printed on mylar by FineLine Imaging, Colorado Springs, CO. Negative SU-8 was developed on Silicon wafer and subsequently, PDMS stamps were cast on the Silicon template by curing the pre-polymer at 70^oC for 2 hours.

Surface preparation Template-stripped gold on glass substrates were prepared as described before.[19] ODT was applied to the patterned side of the PDMS stamp by a cotton swab and the excess was dried with nitrogen stream. The ODT soaked stamp was pressed on the gold surface for 2 min. The sample was then washed with ethanol and placed in the PEG solution for 2 hours. The surfaces were again rinsed with ethanol and dried with nitrogen. These surfaces were treated with

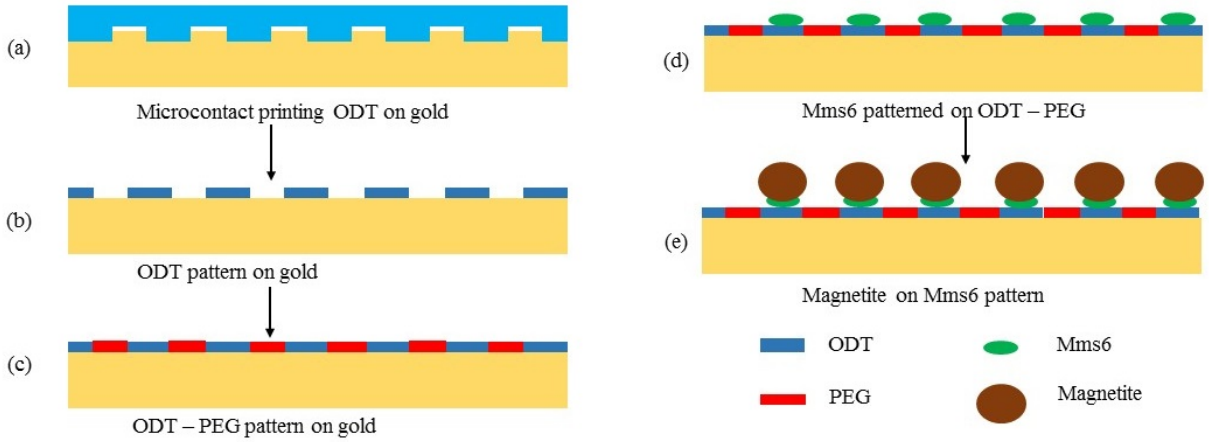

Figure 3.1. Outline of the pattern generation process for growth of magnetic nanoparticles. An ODT-PEG pattern is formed by microcontact printing on a template-stripped gold surface (a-c). A drop of protein is incubated on the resulting surface (d) and subsequently, magnetite nanoparticles are grown by co-precipitation method (e)

the proteins as described earlier.[19] Briefly, 30μL of the protein solution was dropped on the surface and stored at 4^{o}C under humid conditions, overnight. The samples were then washed in 0.2 wt% Tween-20 solution in buffer, rinsed with ethanol and dried with nitrogen. For fluorescence studies, 20μL of anti-6X His tagged antibody was incubated on the protein patterned surfaces overnight. The samples were then washed in 0.2 wt% Tween-20 solution in water, rinsed with ethanol and dried with nitrogen. Magnetic nanoparticles synthesis: Magnetite nanoparticles were grown on the protein patterned surfaces by co-precipitation as described earlier19. In brief, 0.25 M $FeCl_2$, 0.5 M $FeCl_3$ and, 25 wt% Pluronic F127 solution were mixed in 1:1:2 volume proportions. The sample surfaces were placed in a 24-well plate in a glovebox, under Argon atmosphere. Then 0.3 mL of this solution was dropped on the protein coated surfaces. After 2 h, the pH of the solution was raised by adding 0.6 mL of 0.1M NaOH and the resulting magnetite nanoparticles were allowed to grow for 5 days at the ambient temperature. The well-plate was kept covered throughout the synthesis, except when necessary, so that the reactants do not evaporate. The glovebox was purged periodically with Argon to avoid oxidation of the formed particles. The samples were washed in 0.2 wt% Tween 20 in deionized water (Millipore, MILLI-Q water system), rinsed with ethanol and dried with nitrogen.

Measurements Atomic force microscopy images were acquired by Nanoscope III Digital Instruments AFM (Veeco) and Bruker TESPA probes under tapping mode. MFM images were obtained at the Center for Nanoscale Materials at the Argonne National Lab, by a Scanning probe microscope, VeecoMultiMode 8 and Bruker MESP probes. Both AFM and MFM images were analyzed using Nanoscope Analysis software. Step heights were measured by cross sectional analysis with heights averaged over ten different rectangular areas (1μm $\times 20\mu$m). Fluorescence images were captured with a CoolSNAP EZ camera, from Nikon Eclipse TE2000-E microscope with a 10X objective and HQ Wide Blue filter. Patterning of magnetite nanoparticles on the surfaces was examined with scanning electron microscopy (SEM, FEI Quanta 250). Backscattered electron images were taken with an accelerating voltage of 3kV. X-ray photoelectron spectroscopy (XPS) surface analysis was performed with a PHI 5500 spectrometer using Al-Kα1 radiation with a 45^o electron collection angle, corresponding to the maximal penetration depth of about 10 nm. Au4f7/2 peak (84 eV) was used to calibrate the data and CasaXPS was used for fitting the models.

3.3 Results and Discussions

3.3.1 Microcontact printing of ODT-PEG pattern on gold surface

Microcontact printing was used to make different patterns of ODT and PEG on the template-stripped gold surface. Specifically, stripes of 30μm of ODT separated by 30μm PEG, stripes of 4.5μm of ODT separated by 2.5μm of PEG and 50μm $\times 50\mu$m squares of PEG separated center-to-center by 100μm, with ODT between the squares were created. The samples with the 30μm stripes and 50μm square patterns were used for fluorescence microscopy and samples with 4.5μm stripes were used for AFM imaging. These patterns were found to have negligible height difference between the ODT and PEG layers (Fig. 3.2(a)) but provided a clear contrast in hydrophobicity (Fig. 3.2(b)). This result is useful in analyzing the templating action of the pattern, as any subsequent height difference would be due to the difference in surface treatments and not the initial ODT-PEG template itself.

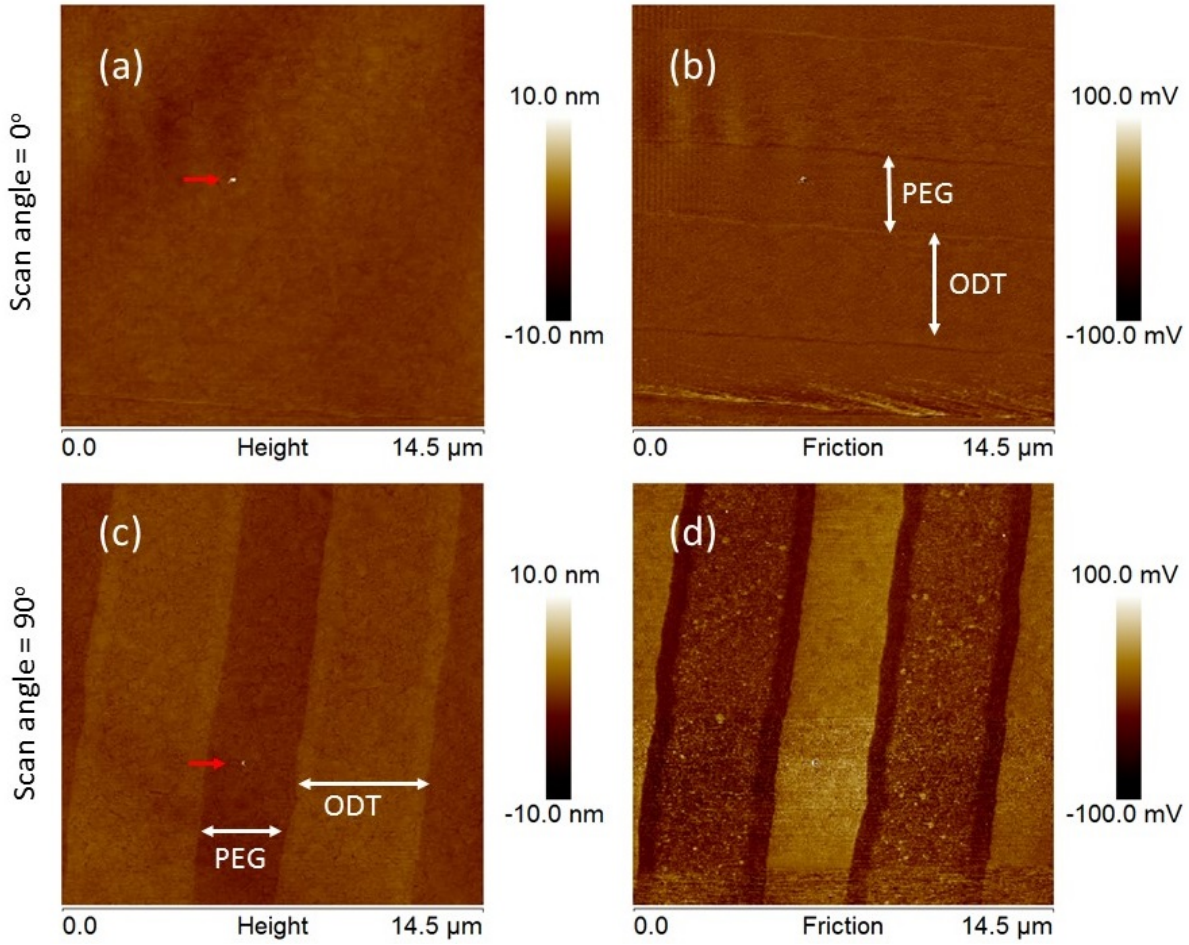

Figure 3.2. Contact mode AFM (a) and the corresponding Lateral Force Microscopy image (b) of $4.5\mu m \times 2.5\mu m$ ODT - PEG pattern on template-stripped gold. The template provides insignificant contrast in height, but a clear contrast in surface properties, making it ideal for analyzing the assembly of the proteins on hydrophobic - hydrophilic patterns

3.3.2 Immobilization of Mms6 on the ODT-PEG pattern

Tapping mode AFM images for 4.5μm $\times 2.5\mu$m striped patterned surfaces treated with different protein solutions are presented in Figure 3.3 and 3.4. For the patterned surfaces treated with a protein-free buffer, the PEG layer is on average 3 nm taller than the ODT layer (Fig. 3.4(a), and Table 3.1). The increase in the PEG layer height compared to the bare template is likely to be caused by the swelling of PEG in water.[32] However, patterned surfaces with Mms6 showed the protein coated ODT layer to be on average 5 nm (measured from edge to edge) taller than the PEG layer (Fig. 3.3(b), and Table 3.1). For the ODT-PEG patterned surfaces treated with m2Mms6, the

m2Mms6-ODT layer was slightly shorter compared to Mms6, at 2.3 nm from PEG layer (Fig. 3.3(c), and Table 3.1). Similar surface profiles were observed for the surfaces treated with BSA and buffer (Fig. 3.3(a) and (d)), indicating the importance of the structure of Mms6 in its integration into the hydrophobic layers. Mms6 also formed a network-like structure (Fig. 3.4(b)) on the ODT layer similar to that seen on uniform ODT coated surfaces.[19] m2Mms6, having the same hydropathy profile as Mms6, was also templated by the pattern, but the network structure within the ODT layer was absent (Fig. 3.4(a)). This result shows the inability of m2Mms6 to form a network structure (Fig. 3.3(a)) on hydrophobic surfaces as shown in previous studies.[19] This observation is consistent with the relaxed structural integrity of m2Mms6 multimers and isolated m2Mms6 terminal domains.[12,18]

Table 3.1. Average step heights computed from cross-sectional analysis of AFM images for the protein patterned surfaces. Heights were measured from edge of the ODT layer to the edge of the PEG layer on the boundary. Fig. S3 gives an example of the sectional analysis followed to obtain these results

Protein	**Buffer**	**Mms6**	**m2Mms6**	**BSA**
Height/nm (before RTCP)	-3.1 ± 0.9	5 ± 0.8	2.3 ± 0.2	-5.1 ± 0.6
Height/nm (after RTCP)	N/A	28.9 ± 8.3	12.5 ± 4.4	N/A

The patterns used for fluorescence studies were $30\mu \times 30\mu$ stripes and $50\mu \times 50\mu$ squares separated center to center by 100μ. In the squares pattern, PEG was coated on the square whereas ODT self-assembled in the space between the PEG squares. The fluorescence images (Fig. 3.5) confirm our previous observations[19] that PEG regions effectively blocked the adsorption of Mms6 whereas ODT regions allowed for immobilization of Mms6 by hydrophobic interactions. In the absence of Mms6, no fluorescence was observed.

XPS technique was employed to confirm the presence of Mms6 on ODT patterned surfaces. The patterned surface treated with the buffer showed no peak in the N1s region (Fig. 3.6), whereas the surface patterned with Mms6 showed C 1s and N1s peaks that correspond to amine and carboxamide groups (Fig. 3.6, and 3.7). The C1s peak can be deconvoluted into three peaks corresponding to C-C (285 eV), C-O (286.2 eV) and C=O (287.5 eV) indicating the presence of protein on the surface.

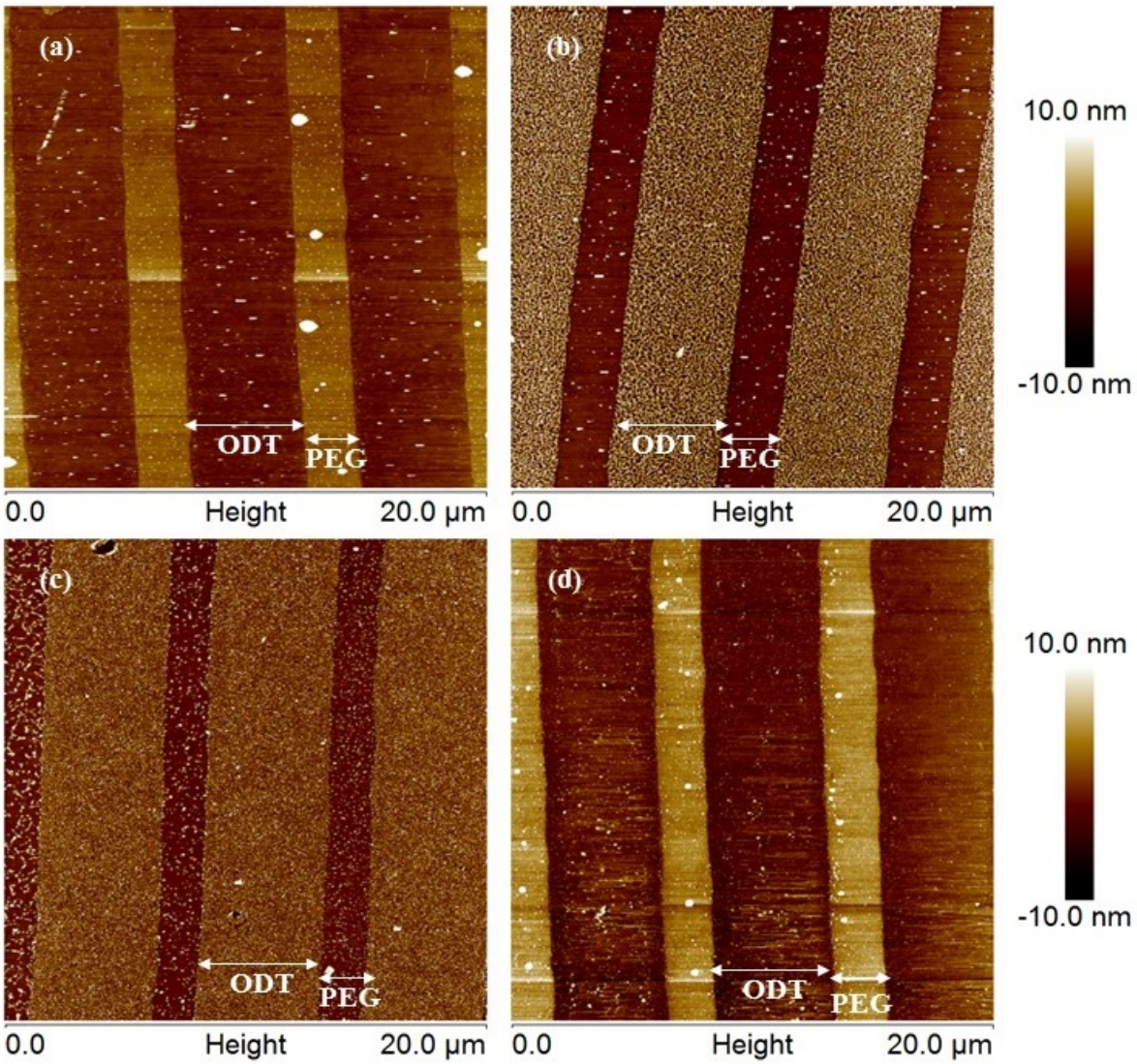

Figure 3.3. Tapping mode AFM images for protein patterned on ODT-PEG templates: (a) buffer, (b) Mms6 (c) m2Mms6 and (d) BSA.

3.3.3 Growth of magnetite nanoparticles on Mms6 pattern

Topographic data from magnetic force microscopy of patterned surfaces, after co-precipitation without protein do not show templated growth of nanoparticles (Fig. 3.8(a). The few large particles dispersed on the surface are probably non-specific adsorption of iron oxide particles to the surface after a prolonged period of co-precipitation. The magnetic force microscopy images of

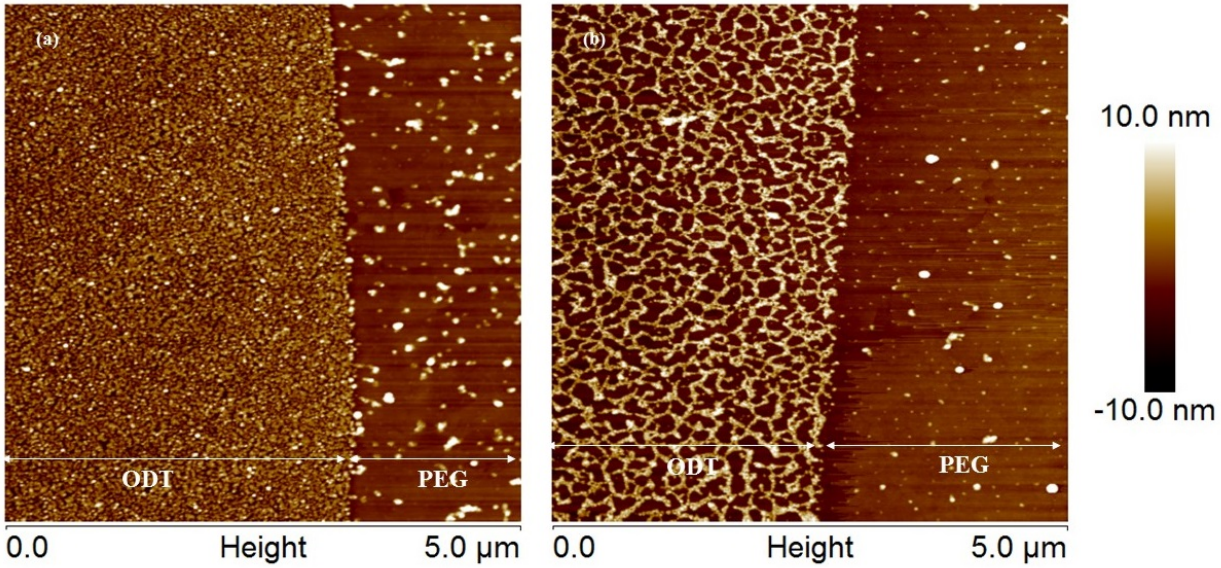

Figure 3.4. Tapping mode AFM images showing the network-like structure of Mms6 on ODT region (b). m2Mms6 did not show such network-like structure although it did adhere to ODT (a).

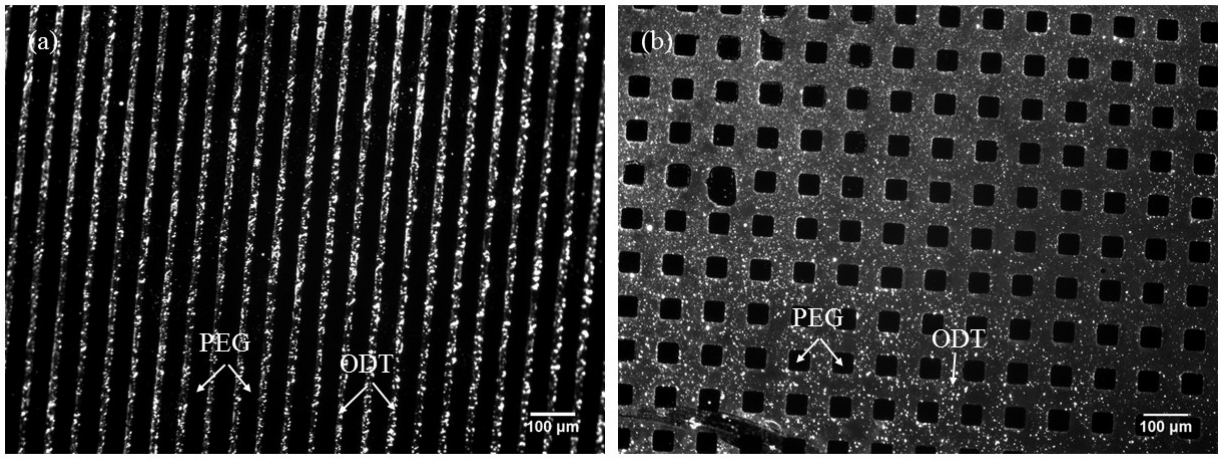

Figure 3.5. Fluorescence microscope images of Mms6 protein patterned on the ODT-PEG template, tagged with a FITC-conjugated antibody. The bright regions indicate the presence of the protein on the ODT area. (a) 30μ stripes of ODT separated by 30μ stripes of PEG. (b) 50μ squares of PEG separated center to center by 50μ with ODT in between them.

the corresponding area also showed no high contrast regions expected of magnetic domains (Fig. 3.8(d)). Sectional analysis was carried out on the AFM images of these surfaces as shown Fig. S3 (b). With Mms6, the surfaces showed retention of the templating pattern, with an average edge-to-edge step height of 28.9 nm (from PEG layer to the magnetite/Mms6/ODT layer) (Fig. 3.8(b),

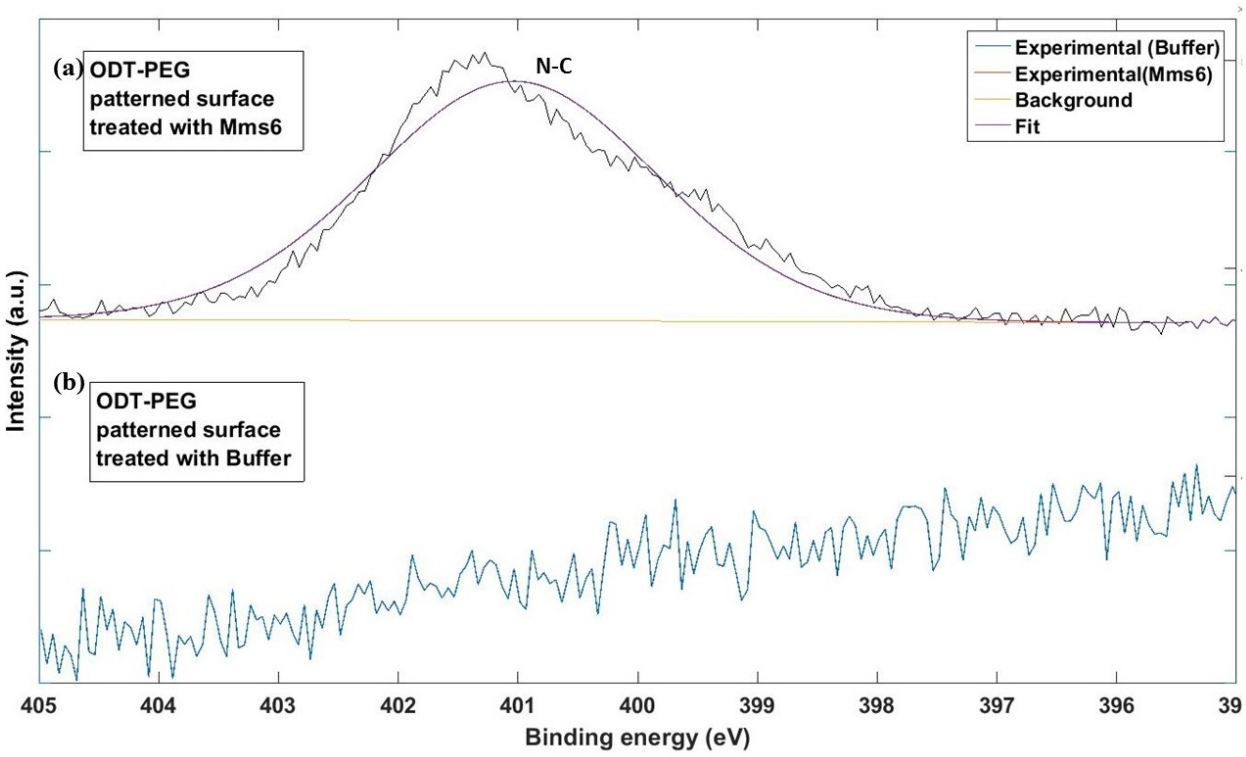

Figure 3.6. N1s peak from XPS for ODT-PEG patterned surface treated with Mms6 (a) and buffer (b). The presence of N1s peak shows the attachment of Mms6 to the ODT-PEG pattern.

and Table 3.1). The magnetic force image pattern corresponds very well with the topographic data (Fig. 3.8(e)). With m2Mms6 on the surface, the observed particles are randomly scattered (Fig. 3.8(c)). The low step size of approximately 12.5 nm (Table 3.1) for these particles suggests that the apparent pattern is mostly due to m2Mms6 on ODT. The corresponding magnetic force microscopy image did not show a contrasting pattern that corresponds to the topographic image (Fig. 3.8(f)) which suggests that the particles formed by RTCP and associated with m2Mms6 are very weakly magnetic. The step height roughly corresponds to the particle size on the ODT layer and the values that we have observed here correspond well with those seen in literature for the RTCP route.[11,12,14,15]

These results show that RTCP results in particles on the ODT-Mms6 areas with some magnetic domains, which are absent in the PEG layer and not found with the functional mutant, m2Mms6. The observation of magnetic nanoparticle production templated by Mms6 but not by m2Mms6 on surfaces is consistent with previous observations of magnetite biomineralization mediated by

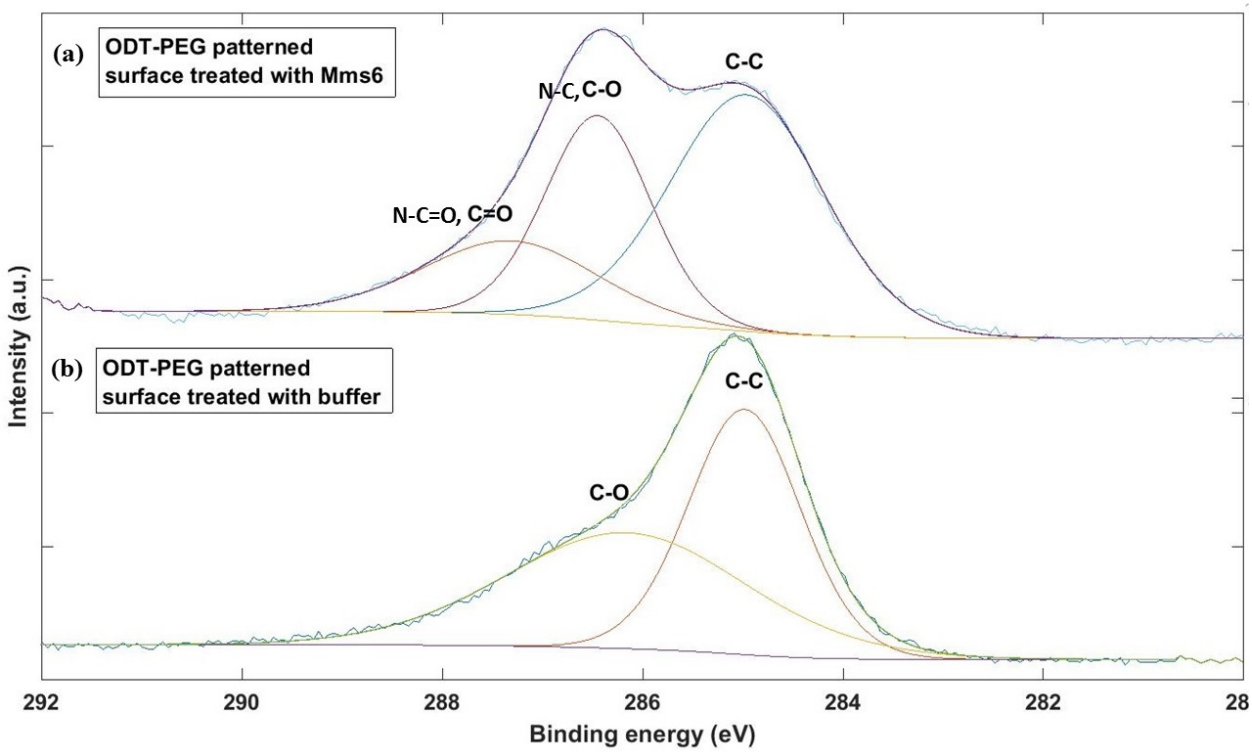

Figure 3.7. C1s peak from XPS for ODT-PEG patterned surface treated with Mms6 (a) and buffer (b). (b) shows fitted peaks corresponding to C-C (285 eV) and C-O (286.2 eV) bonds present in ODT and PEG. (a) shows in addition to the C-C and C-O peaks, fitted peaks corresponding to C=O (287.5 eV) bonds present in Mms6.

Mms6 and m2Mms6 in the bulk.[11] The changes in the C-terminal domain sequence present in m2Mms6 affect its self-assembly into multimeric complexes that are important for Mms6's function as a biomineralization protein.[18,33]

The pattern of nanoparticles grown on the Mms6 surfaces can also be observed by SEM (Fig. 3.9(b)). The ODT-PEG template by itself did not show any contrast in the backscattered electron image (Fig. 3.9(a)). The contrast seen in the presence of Mms6 can be attributed to either the protein or the magnetic nanoparticles. Similar contrast was absent in the BSE image of the surface treated with m2Mms6 (Fig. 3.9 (c)). EDS analysis showed the presence of Fe and O on both ODT layer and PEG layer on the surface treated with Mms6 (Fig. 3.10). Iron salts are expected to be dissolved in the PEG layer which can potentially cause the iron signal even in the absence of Mms6 on PEG. The ODT layer showed a slightly stronger Fe signal than the PEG layers in the EDS area scans, but due to the low thickness of the magnetite layer compared to the penetration

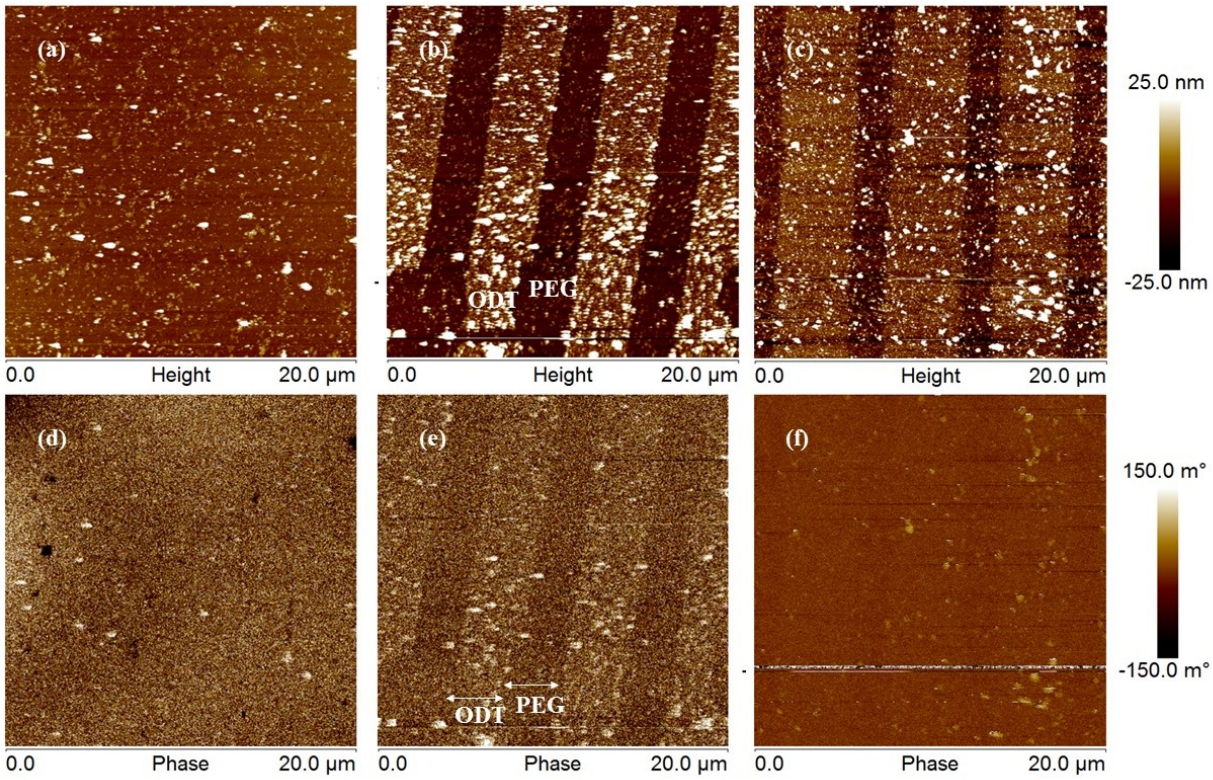

Figure 3.8. Magnetic nanoparticles grown by co-precipitation on surfaces patterned with ODT - PEG and treated with buffer, Mms6 and m2Mms6. Top row (a,b,c) shows the topographic images and the bottom row (d,e,f) shows their corresponding magnetic force microscopy images. Only Mms6 (b,e) shows magnetic contrast corresponding to the topographic image.

depth of the e-beam, the overall Fe signal was weak. Secondary electron images (Fig. 3.10) and the backscattered images (Fig. 3.9(b)) showed many particles on the ODT layer that were rich in Fe and O, while PEG layer had fewer particles rich in Fe and O.

XPS was used for qualitative chemical analysis of the surface. The results, after modelling the data, show Fe^{2+} peaks at 710.7eV ($2p_{3/2}$) and 724.2 eV ($2p_{1/2}$) and Fe^{3+} peaks at 712.9eV ($2p_{3/2}$) and 726.2eV ($2p_{1/2}$) (Fig. 3.11). O1s data also shows the presence of Fe-O bonds with a peak at 530.1eV. Thus, iron is present in both +2 and +3 states on the surface. The modelled data also shows the presence of C-C, C-O, C-N, C=O and N-C=O bonds with peaks in the C1s region and C-N bonds with a peak in N1s region similar to the ones observed in Figure 3.6(a) and Figure 3.7(a).

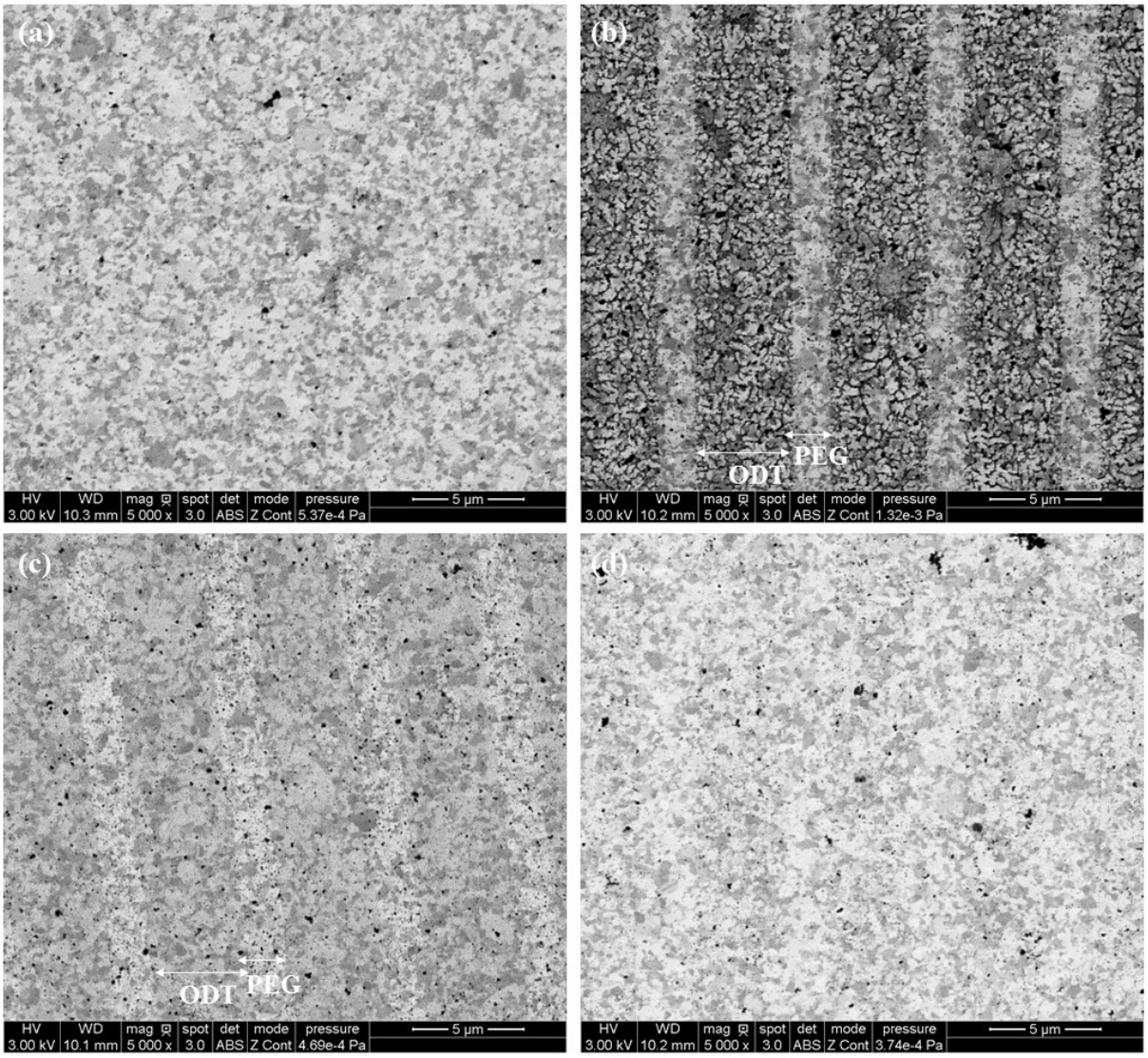

Figure 3.9. Backscattered electron images of magnetite co-precipitated on ODT-PEG patterned surfaces treated with (a) buffer, (b) Mms6, (c) m2Mms6 and (d) BSA.

Results from XPS, EDS and magnetic force microscopy characterization, combined with the fact that RTCP method in the bulk in the presence of Mms6 produces magnetite nanoparticles[12,15] lead to a conclusion that the magnetic nanocrystals on the patterned surfaces are very likely to be magnetite nanocrystals.

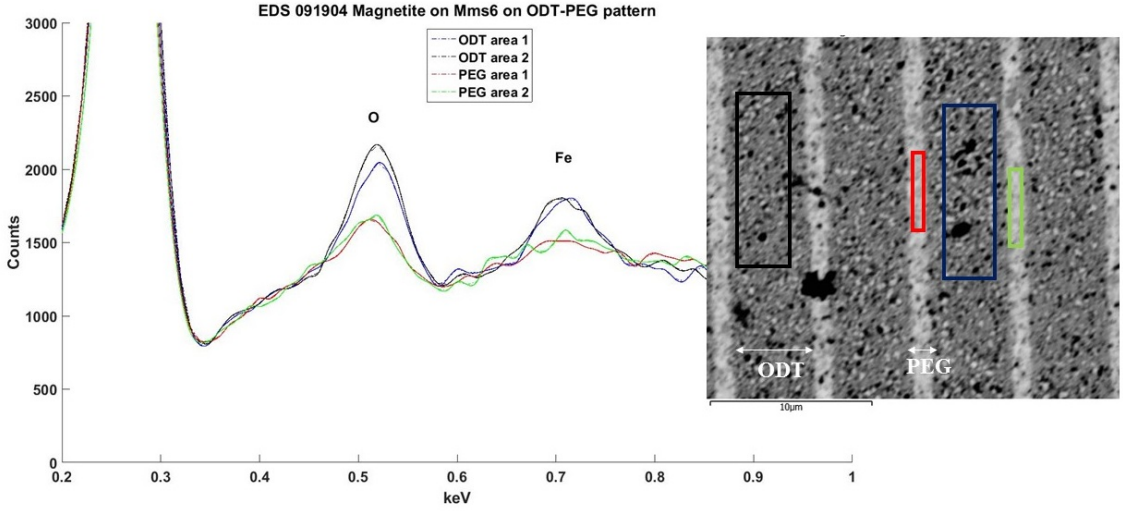

Figure 3.10. EDS data for the corresponding areas on the secondary electron image of ODT-PEG patterned surfaces treated with Mms6 and co-precipitated magnetite.

3.4 Conclusion

In this work, localized deposition of magnetic particles on patterned surfaces was demonstrated by combining the top-down fabrication process of microcontact printing with the bottom-up approach of self-assembly of the biomineralization protein Mms6 and subsequent templating of magnetic nanoparticles by the protein. Its amphiphilic structure is consistent with assembly of Mms6 on hydrophobic surfaces, and the network-like structure of the protein is likely promoted by the self-assembly properties of the C-terminal domain. Both properties of Mms6 contributed to its localization on the ODT regions of the patterned surfaces, and its templating the formation of magnetite nanoparticles selectively on the ODT patterned surfaces. PEG effectively blocked non-specific adsorption of Mms6 and magnetic nanoparticles localized mainly in the ODT regions with Mms6.

The synergistic approach described here can be used to create functionalized surfaces with tunable magnetic properties. Patterns of hydrophobic self-assembled monolayers and protein-resistant layers with smaller dimensions can be created using nanocontact printing[34] or interference lithography.[35] The PEG layer can be further functionalized with different moieties, providing an additional tunable parameter. Magnetic properties of the resulting structures can also be

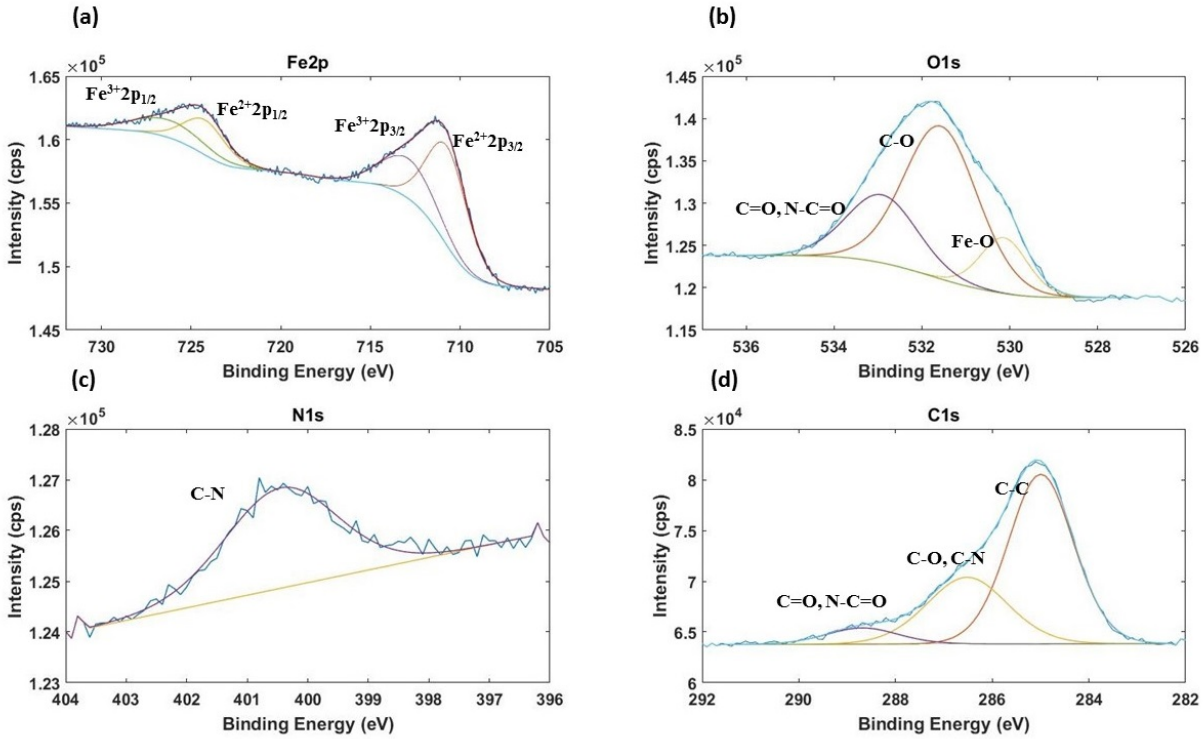

Figure 3.11. XPS peaks with fit models for the patterned surfaces treated with Mms6, after RTCP. Au4f peak at 84.0 eV was used as the reference.

enhanced by doping with a high coercivity ferromagnetic material like cobalt.[13] These functionalized surfaces with arrays and patterns of magnetic nanoparticles can provide tunable magnetic properties and have many applications in high density data storage and sensors.

3.5 Acknowledgements

We thank Dapeng Jing and Warren Straszheim of the Materials Analysis and Research Laboratory, Iowa State University, for helping us collect the XPS data and SEM data respectively, and Zach Njus of the Department of Electrical and Computer Engineering, Iowa State University for helping in making the PDMS stamps. Fluorescence microscopy and AFM were done at Roy J. Carver Laboratory for Ultrahigh Resolution Biological Microscopy, Iowa State University. Research at Ames Laboratory was supported by the U.S. Department of Energy, Office of the Basic Energy Sciences, Division of Materials Sciences and Engineering. Ames Laboratory is operated

for the U.S. Department of Energy by Iowa State University under Contract Number DE-AC02-07CH11358. The use of Magnetic Force Microscopy at the Argonne National Laboratory was supported by the U.S. Department of Energy under Contract Number DE-AC02-06CH11357.

References

[1] Terris, B. D. and Thomson, T. *Journal of Physics D-Applied Physics* **38**(12), R199–R222 (2005).

[2] Huang, H.-T., Lin, Y.-H., Ger, T.-R., and Wei, Z.-H. *Applied Physics Express* **6**(3) (2013).

[3] Shao, I., Chen, M. W., Cammarata, R. C., Searson, P. C., and Prokes, S. M. *Journal of the Electrochemical Society* **154**(11), D572–D576 (2007).

[4] Song, Y., Lu, W., Xu, Y., Shi, J., and Fang, X. *Journal of Alloys and Compounds* **652**, 179–184 (2015).

[5] Pokroy, B., Epstein, A. K., Persson-Gulda, M. C. M., and Aizenberg, J. *Advanced Materials* **21**(4), 463–+ (2009).

[6] Blakemore, R. *Science* **190**(4212), 377–379 (1975).

[7] Faivre, D. and Schuler, D. *Chemical Reviews* **108**(11), 4875–4898 (2008).

[8] Faivre, D. and Godec, T. U. *Angewandte Chemie-International Edition* **54**(16), 4728–4747 (2015).

[9] Arakaki, A., Webb, J., and Matsunaga, T. *The Journal of biological chemistry* **278**(10), 8745 (2003).

[10] Tanaka, M., Mazuyama, E., Arakaki, A., and Matsunaga, T. *Journal of Biological Chemistry* **286**(8), 6386–6392 (2011).

[11] Wang, L., Prozorov, T., Palo, P. E., Liu, X., Vaknin, D., Prozorov, R., Mallapragada, S., and Nilsen-hamilton, M. *Biomacromolecules* **13**(1), 98–105 (2012).

[12] Prozorov, T., Mallapragada, S. K., Narasimhan, B., Wang, L., Palo, P., Nilsen-hamilton, M., Williams, T. J., Bazylinski, D. A., Prozorov, R., and Canfield, P. C. *Advanced Functional Materials* **17**(6), 951–957 (2007).

[13] Prozorov, T., Palo, P., Wang, L., Nilsen-Hamilton, M., Jones, D., Orr, D., Mallapragada, S. K., Narasimhan, B., Canfield, P. C., and Prozorov, R. *Acs Nano* **1**(3), 228–233 (2007).

[14] Amemiya, Y., Arakaki, A., Staniland, S. S., Tanaka, T., and Matsunaga, T. *Biomaterials* **28**(35), 5381–5389 (2007).

[15] Galloway, J. M., Arakaki, A., Masuda, F., Tanaka, T., Matsunaga, T., and Staniland, S. S. *Journal of Materials Chemistry* **21**(39), 15244–15254 (2011).

[16] Oestreicher, Z., Mumper, E., Gassman, C., Bazylinski, D. A., Lower, S. K., and Lower, B. H. *Journal of Materials Research* **31**(5), 527–535 (2016).

[17] Kashyap, S., Woehl, T. J., Liu, X., Mallapragada, S. K., and Prozorov, T. *Acs Nano* **8**(9), 9097–9106 (2014).

[18] Feng, S., Wang, L., Palo, P., Liu, X., Mallapragada, S. K., and Nilsen-Hamilton, M. *International Journal of Molecular Sciences* **14**(7), 14594–14606 (2013).

[19] Liu, X., Zhang, H., Nayak, S., Parada, G., Anderegg, J., Feng, S., Nilsen-Hamilton, M., Akinc, M., and Mallapragada, S. K. *Industrial & Engineering Chemistry Research* **54**(42), 10284–10292 (2015).

[20] Yang, J., Cui, C., Yang, W., Hu, B., and Sun, J. *Journal of Materials Science* **46**(7), 2379–2383 (2011).

[21] Esmaeili, A., Kashi, M. A., Ramazani, A., and Montazer, A. H. *Journal of Magnetism and Magnetic Materials* **397**, 64–72 (2016).

[22] Lamrani, S., Guittoum, A., Schaefer, R., Hemmous, M., Neu, V., Pofahl, S., Hadjersi, T., and Benbrahim, N. *Journal of Magnetism and Magnetic Materials* **396**, 263–267 (2015).

[23] Budevski, E., Staikov, G., and Lorenz, W. J. *Electrochimica Acta* **45**(15-16), 2559–2574 (2000).

[24] Whitesides, G. M., Ostuni, E., Takayama, S., Jiang, X. Y., and Ingber, D. E. *Annual Review of Biomedical Engineering* **3**, 335–373 (2001).

[25] Kane, R. S., Takayama, S., Ostuni, E., Ingber, D. E., and Whitesides, G. M. *Biomaterials* **20**(23-24), 2363–2376 (1999).

[26] Senaratne, W., Andruzzi, L., and Ober, C. K. *Biomacromolecules* **6**(5), 2427–2448 (2005).

[27] Singhvi, R., Kumar, A., Lopez, G. P., Stephanopoulos, G. N., Wang, D. I. C., Whitesides, G. M., and Ingber, D. E. *Science* **264**(5159), 696–698 (1994).

[28] Bird, S. M., Galloway, J. M., Rawlings, A. E., Bramble, J. P., and Staniland, S. S. *Nanoscale* **7**(16), 7340–7351 (2015).

[29] Bird, S. M., El-Zubir, O., Rawlings, A. E., Leggett, G. J., and Staniland, S. S. *J. Mater. Chem. C* , 10.1039.C5TC03895B (2016).

[30] Galloway, J. M., Bramble, J. P., Rawlings, A. E., Burnell, G., Evans, S. D., and Staniland, S. S. *Small* **8**(2), 204–208 (2012).

[31] Qin, D., Xia, Y., and Whitesides, G. M. *Nature Protocols* **5**(3), 491–502 (2010).

[32] Acikgoz, S., Bilen, B., Demir, M. M., Menceloglu, Y. Z., Skarlatos, Y., Aktas, G., and Inci, M. N. *Optical Review* **15**(2), 84–90 (2008).

[33] Zhang, H., Liu, X., Feng, S., Wang, W., Schmidt-Rohr, K., Akinc, M., Nilsen-Hamilton, M., Vaknin, D., and Mallapragada, S. *Langmuir* **31**(9), 2818–2825 (2015). PMID: 25669122.

[34] Li, H. W., Muir, B. V. O., Fichet, G., and Huck, W. T. S. *Langmuir* **19**(6), 1963–1965 (2003).

[35] Mojarad, N., Gobrecht, J., and Ekinci, Y. *Microelectronic Engineering* **143**, 55–63 (2015).

CHAPTER 4. ORDERED NETWORKS OF GOLD NANOPARTICLES CROSSLINKED BY DITHIOL-OLIGOMERS

A paper published in the Journal Particle & Particle Systems Characterization

Srikanth Nayak, Nathan Horst, Honghu Zhang, Wenjie Wang, Surya Mallapragada, Alex Travesset, and David Vaknin [1]

Abstract

Controlled aggregation of nanoparticles into superlattices is a grand challenge in material science, where ligand based self-assembly is the dominant route. Here, we report on the self-assembly of gold nanoparticles (AuNPs) that are crosslinked by water soluble oligo-(ethylene glycol)-dithiol (PEG-dithiol) and determine their three-dimensional (3D) structure by small angle x-ray scattering. Surprisingly, we find a narrow region in the parameter space of dithiol linker-length and nanoparticle size for which the crosslinked networks form short-ranged FCC crystals. Using geometrical considerations and numerical simulations, we evaluate the stability of the formed lattices as a function of dithiol length and the number of connected nearest-neighbors, and provide a phase diagram of superlattice formation. Identifying the narrow parameter space that allows crystallization facilitates focused exploration of linker chemical composition and medium conditions such as thermal annealing, pH and added solutes that may lead to superior and more robust crystals.

4.1 Introduction

Assembling nanoparticles (NPs) into superlattices with specific symmetries is crucial for applications such as catalysis,[1–3] optical devices,[4,5] sensors[6–8] and energy storage.[9] Although there

[1] Author for correspondence

has been considerable progress in assembling two- and three-dimensional (2D and 3D) superlattices of metallic and semiconductor NPs,[10–19] the challenge of up-scaling and stabilizing these crystals still remains.[20] In this regard, self-assembly of NPs driven by inter-particle and thermodynamic forces has proven to be a promising approach for the formation of macroscale ordered assemblies.[21–24]

In solution based methods of NP assembly a surface ligand, covalently bound to a NP, interacts with neighboring ligands via non-covalent interactions such as hydrogen bonding.[1,3,25? ? ,26] While there is a plethora of studies reporting structural properties of NPs by DNA-mediated assembly,[12–14] there is a relative dearth of studies on the structure of NPs networks obtained by covalent crosslinkers, such as dithiol molecules, which are an obvious choice for linking of gold nanoparticles (AuNPs). An advantage of short dithiol ligands (with a length of a few nanometers) over the longer linkers (such as those used in DNA-mediated assembly) is the very short inter-particle distance they accommodate which leads to a higher plasmon coupling and hence has potential applications in plasmonic effective medium metamaterials[27,28] and FRET devices.[29,30] In one of the earliest studies on assembling AuNPs with dithiols, Brust et al.[31] employed the Brust-Schiffrin method of synthesizing AuNPs and used alkyl dithiols instead of monothiols. They obtained super-clusters of NPs by drop-casting on TEM grids. Deffner et al.[32] studied the kinetics of aggregation of AuNPs functionalized with hydrophobic dithiols in water and organic solvents, but did not report on the fine structure of the aggregates. Others have shown the formation of spherical AuNP assemblies with dithiol crosslinkers[33,34] and there has been some effort towards tuning the functional properties of NP assemblies by tuning the length of the dithiol linkers.[35] Dithiols have also been used to crosslink gold nanorods end–to–end and a preferential adsorption of thiols to the end faces of nanorods has been reported.[36,37] Rossner et al.[38] reported the effect of chain length of crosslinking polymer on the formation of NP networks by small angle X-ray scattering (SAXS) studies of the networked NPs with a bifunctional RAFT agent and observed a broad single peak in one experimental condition. They attribute the lack of crystallinity to NP size polydispersity, crosslinking polymer polydispersity and conformational freedom of the crosslinker.

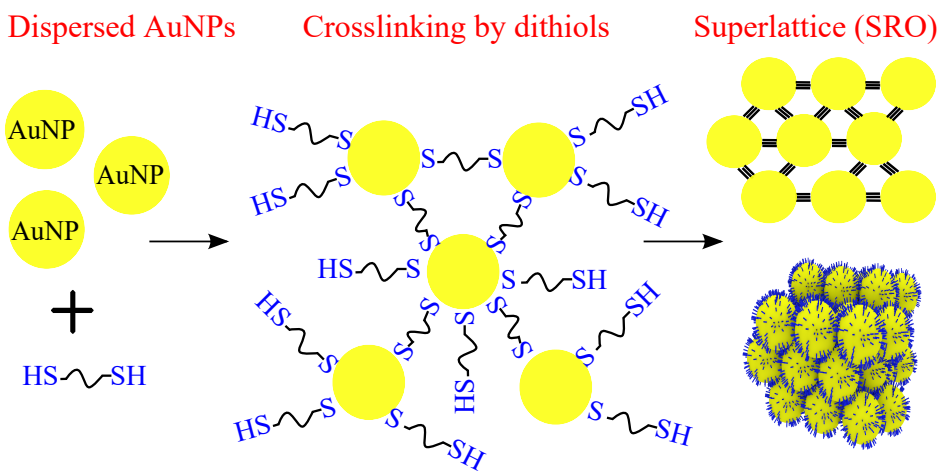

Figure 4.1. Schematic of the procedure to obtain AuNP-dithiol aggregates. AuNPs are cross-linked by short, water soluble dithiols and form superlattices with short-ranged order (SRO).

To address the gap in the existing literature regarding the structure of NP assemblies obtained by covalent crosslinking, we have embarked on a systematic investigation of AuNPs aggregation in the presence of dithiol ligands, using various experimental techniques, computational modeling and theoretical predictions (see schematic illustration in **Figure 4.1**). In particular, we employ synchrotron radiation SAXS to examine the effect that dithiol linker length and the NP size have on the structure of the aggregates. Geometrical considerations of the assembly lead us to provide theoretical predictions on the stability/formation of NP lattices. Furthermore, we evaluate the dependence of lattice quality and stability on the linker length and the connectedness of the nanoparticles by MD simulations.

4.2 Materials and Methods

Reagents and Materials: Aqueous suspension of citrate stabilized gold nanoparticle (AuNP) with a nominal sizes of 5 nm and 10 nm were purchased from Ted Pella Inc. Hexaethylene glycol dithiol (DT6), tetraethylene glycol dithiol (DT4) were purchased from Sigma-Aldrich. Poly(ethylene glycol) dithiol with $M_n \sim 600$ (DT12) and ~ 1000 (DT21) were purchased from CreativePEGWorks.Inc. From the molecular weights, we estimate there are about 12 and 21 ethylene glycol units in DT12 and DT21, respectively.

Synthesis of AuNP aggregates: Schematic of the procedure to obtain aggregates of AuNPs with dithiols by ligand exchange method is presented in Figure 4.1. Aqueous solutions of dithiol (DT) at appropriate concentrations are prepared by dissolving the appropriate amount of dithiols in millipore water at room temperature. To 0.99 ml of AuNP suspension as received, 0.01 ml of the dithiol solution is added under sonication. Final AuNPs concentration in the mixture is estimated at $\sim$ 8.5 nM using the nominal concentrations provided by the manufacturer. The samples are prepared in glass vials with plastic caps and are kept under radial shaking for more than 48 hours. Samples are labeled AuX:DTY (1:r), where X is the nominal size of the AuNPs, Y is the number of ethylene glycol units in the dithiol molecule and r is the molar ratio of dithiol to AuNPs in solution, and characterized by UV/vis absorption spectra.

Characterization methods: UV-vis absorbance spectra are collected with a Malvern Instruments with an optical length of 1 cm in polystyrene cuvettes. Small angle X-ray scattering (SAXS) measurements of the precipitates are conducted at beamline 12-ID of Advanced Photon Source, Argonne National Laboratory. For the SAXS measurements, samples are transferred to quartz capillaries using glass pipettes and the measurements are performed in transmission mode with photon energy, E = 13.3 keV (λ = 0.9322 Å) using 2D Pilatus2m detector at room temperature. SAXS apparatus is calibrated using the diffraction pattern of silver behenate powder standard. The 2D scattering data is circularly averaged and the background scattering from the capillary with blank solution is subtracted.

Aggregates are also studied by transmittance electron microscopy (FEI Tecnai G2-F20) in the transmission mode with an acceleration voltage of 200kV.

Simulation methods: Molecular Dynamics (MD) simulations are executed on graphical processing units using the HOOMD-blue software.[39–41] Nanoparticles are treated as rigid bodies during the simulation, non-bonded interactions with a force-shifted form of the Lennard–Jones potential and bonded interactions through FENE (Finite Extensible Nonlinear Elastic) bond potentials. Simulations are run at the theta-temperature, where polymer coils behave like ideal chains. All simulations are performed in a periodic cell, from an initial configuration of a perfect FCC lattice

using HOODLT? software. Systems are initially equilibrated for 10^5 timesteps, and final statistics are taken from production runs of 10^6 timesteps in length.

4.3 Results and Discussion

4.3.1 Effect of AuNP:dithiol ratio and dithiol-length

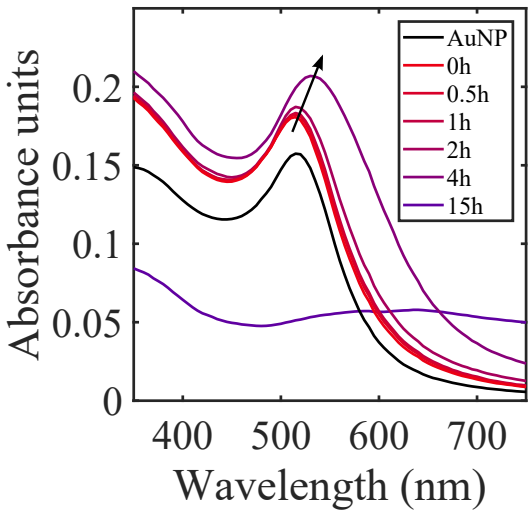

Figure 4.2. Time evolution of UV-vis absorbance spectra of Au10:DT6 (1:850) mixture indicated by arrow. Initially, the LSPR peak of AuNPs shifts to longer wavelengths consistent with the formation of large aggregates, and vanishes as precipitates of crosslinked AuNPs are formed and move away from the UV-illuminated volume.

Upon addition of dithiols to the suspension, gold nanoparticles aggregate, as visually observed and also as recorded by UV-vis absorbance spectra. **Figure 4.2**(a) shows that the localized surface plasmon resonance (LSPR) peak of AuNPs UV-vis shifts to longer wavelengths indicating aggregation after adding DT6. Initially, the LSPR peak intensity increases, and after sufficiently long time, aggregates precipitate out of the illuminated volume of the suspension leading to a flat line in the absorbance spectrum. **Figure 4.3** shows TEM images of AuNPs aggregates, obtained 4 hours after adding DT6 to bare AuNP suspensions, and spread on carbon coated TEM grid. Compared to dispersed bare AuNPs (Figure 4.3a), the aggregates with DT6 are more tightly packed and display features that suggest the formation of multilayers in some regions. We emphasize that the individual identity of each AuNP upon addition of DT6 is preserved indicating that linked AuNPs do not

coalesce into a larger Au particle. Such a separation among nearest-neighbors (NN) is achieved by virtue of the steric hindrance that the PEG linker provides. SAXS measurements, discussed below, corroborate the correlated aggregation seen in the TEM and provide more detailed averaged insight of the aggregation.

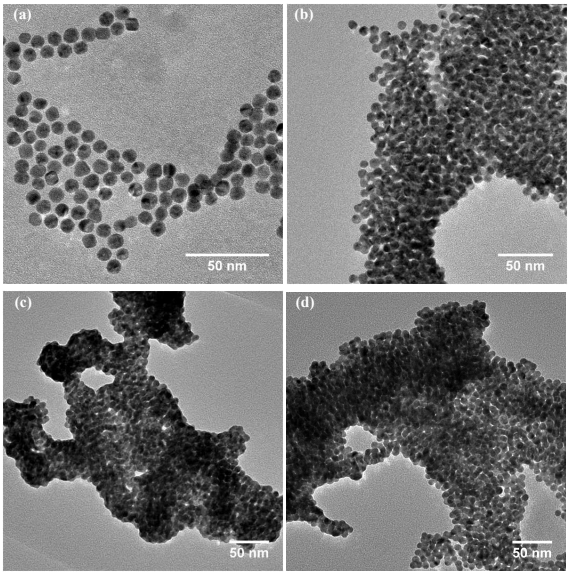

Figure 4.3. TEM images of dried 10 nm AuNPs mixed with hexa-ethylene-glycol (Au10-DT6) on carbon-coated copper grids at a molar ratio of Au10:DT6 (a) 1:0 (bare AuNPs), (b), 1:850 (c), 1:8500, and (d) 1:85000. Images are taken for samples that are mixed for 4 hours. While (a) shows dispersed particles, (b), (c) and, (d) show closely packed particles, and as the Au10:DT6 increases, darker regions appear indicating multilayer formation.

Figure 4.4(a) and (b) show structure factor patterns as a function of momentum transfer ($S(q)$) for precipitates of nominal 5 and 10 nm AuNPs that are mixed with DT6 at various ratios of AuNP:DT6, r. The $S(q)$ is obtained from averaged SAXS data ($I(q)$) after normalization by the measured form-factor of AuNP ($F(q)$); such that $S(q) \propto I(q)/|F(q)|^2$ (see details on data reduction in the Supporting Information). The $F(q)$ is determined by fitting SAXS intensity of as-purchased AuNPs suspensions to a theoretical scattering profile of non-interacting spherical particles with a Gaussian size-distribution that yields $D_0 = 6.3 \pm 0.9$ and 8.9 ± 0.8 nm for the nominal 5 and 10 nm diameter AuNP, respectively. Both Figure 4.4(a) and (b) exhibit clear interference patterns that indicates a relatively high degree of ordering in the aggregated clusters in the presence of DT6. Inspection of the interference pattern shows that the lowest order interference peak is superimposed with an adjacent peak that shows up as a shoulder or making the lineshape asymmetric.

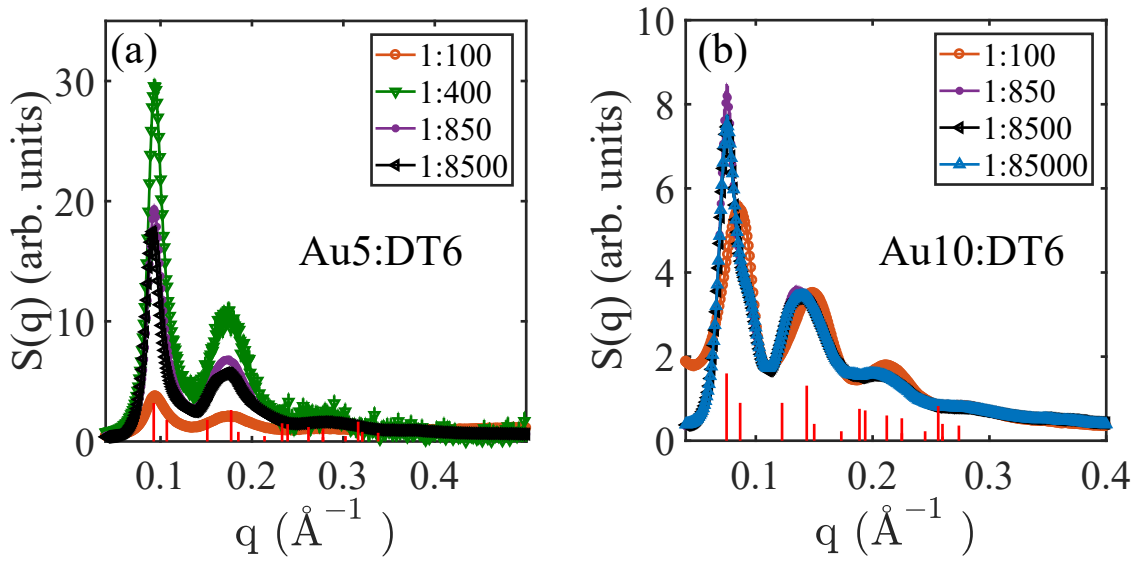

Figure 4.4. (a) Structure factor obtained from SAXS data for (a) Au5:DT6 with $r = 1:100$, 1:850, 1:8500, and 1:85000, and (b) Au10:DT6 with $r = 1:100$, 1:850, 1:8500, and 1:85000. The shift in and narrowing of the primary peak as the ratio of AuNP to DT6 is changed from 100 to 850 k indicate improved crystallinity with increased DT6. Vertical lines in both (a) and (b) are calculated positions (and relative intensities) of structure factor peaks for a perfect FCC crystal assuming lattice constants $a = 11.5$ and 14 nm, respectively.

The proximity of the two peaks is qualitatively consistent with the preferential formation of FCC short-range-order (SRO) over the competing HCP with a second distant peak that could be resolved in our set-up. Whereas varying the ratio Au5:DT6 (r) gradually affects the intensity it does not significantly affect the peak position, namely, the lattice constant is robust. For the Au10:DT6, on the other hand, for $r = 100$ the peak shifts to larger q and is broadened, indicating a shorter NN characteristic length scale and inferior crystal quality.

To model the observed structure factors, we base our analysis on a theoretical framework proposed recently.[14,42,43] Observed structure factor, $S(q)$ is fit to $S_{Mod}(q)$ from Equation **6.2**(a) using the linear least squares method assuming the peaks lineshape are Lorentzian-like. We find that the FCC lattice is the best match for the observed structure factor as shown in **Figure 4.10**(b). The fitted curves reasonably match the observed structure factor, especially the primary peak which in the model appears as a superposition of (111) and (200) FCC peaks. Results of the fit model are presented in Table **6.3** and Figure 4.10(b). Values obtained for σ_d (related to the Lindemann ratio, see definition below and in the SI) from the fitting match well with those reported in the literature

for similar systems.[44] The average lattice constants for Au5:DT6 and Au10:DT6 are $a \approx 11.5$ and ≈ 14 nm, respectively, with corresponding NN distances for FCC structure $D_n = a/\sqrt{2} \approx 8$ and ≈ 10 nm. Since $D_n < L_{contur} + D_0$, where $L_{contur} \approx 2.3$ nm is the contour length of DT6, we propose that the linking of two neighboring particles is achieved primarily by dithiols that are residing away from the line that connects the center of NN AuNPs and with insignificant indirect bridges of two diothiols that form disulfide bonds (see **Figure 4.9**). Similar arguments hold for the other systems namely Au5:DT4, Au5:DT6, and Au10:DT4. This argument is based on the assumption that the short dithiols DT6 and DT4 are relatively rigid. Based on the extracted linewidths we estimate that the average FCC aggregate consists of nearly 500 NPs per crystallite. We also employ a second model where the peak positions of the lattice are maintained but the intensities of the FCC are allowed to vary slightly from their calculated structure factor to account for poor crystallinity.

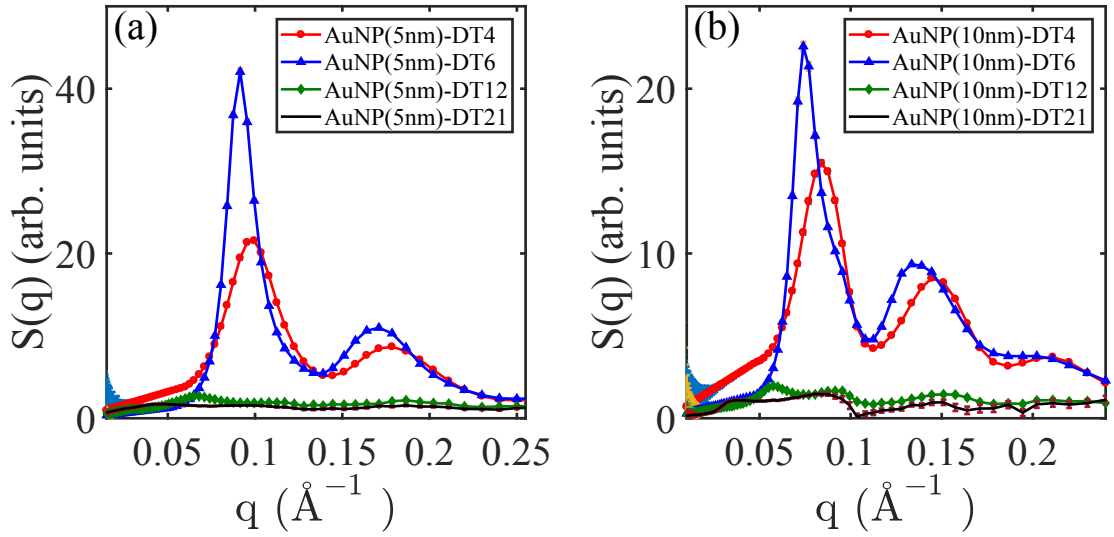

Figure 4.5. Structure factor curves obtained for (a) Au5:DT4, Au5:DT6, Au5:DT12, and Au5:DT21, and (b) Au10:DT4, Au10:DT6, Au10:DT12, and Au10:DT21, both at $r = 8500$. The data is binned on a logarithmic scale for better presentation preserving results integrity. The first peak in $S(q)$ shifts to lower q values by increasing dithiol linker length indicating increase in inter-particle distance in the assemblies.

To examine the role of dithiol linker length on crystal quality, we examine a few unique dithiols varying in PEG lengths as they are mixed with AuNPs. While samples with DT4 and DT6 lead

to quantitative precipitation of nanoparticles, those with DT12 and DT21 showed only a change in color, from dark red to pale pink, indicating nanoparticle aggregation. Even two weeks after sample preparation, we do not observe precipitates in these samples. **Figure 4.5** shows the structure factor ($S(q)$) obtained for the precipitates of Au10:DT4, Au10:DT6, Au10:DT12, Au10:DT21, (b) Au5:DT4, Au5:DT6, Au5:DT12 and Au5:DT21 at a fixed $r = 8500$. Whereas DT4 and DT6 show clear and prominent diffraction signals, DT12 and DT24 exhibit much weaker and broader signals. In fact, for both 5 and 10 nm linked particles DT6 seems to yield the better crystalline structure. **Figure 4.6** shows the nearest-neighbor (NN) distance (D_n) calculated from the position of the first peak in the structure factor (assuming an FCC lattice) as a function of the contour length of dithiol (i.e., stretched length) indicating a linear relationship at small values of contour lengths that deviates significantly at longer lengths. As we show below, there are some geometrical constraints imposed on the system when considering NP size and linker length that limit how crystallinity can be achieved through self-assembly.

4.3.2 Geometrical and stability considerations

Below we examine crosslinking assembly conditions that reinforce ordered rather than amorphous states. We specifically focus on two main sources for increased disorder that work against superlattice formation: 1. A broad or random distribution of binding dithiol sites between neighboring NPs and 2. The effect of defects (i.e., missing or misplaced particles on a lattice) due to weak or insufficient number of dithiol bonds on the stability of an ordered state. The first source has to do with random linking NPs such that NN distances are broadly distributed, resulting in an amorphous state, as is typical of glasses. In the limit of long linkers, dithiols no longer work as tethers and the system would exhibit fluid properties. We note that the dithiol bridges are flexible (especially with longer PEGs) implying that there is some leverage on the location of the binding sites. The second source for disorder pertains to the overall stability of an ordered crystal as more and more symmetry sites become unoccupied. In an FCC lattice, for example, although each NP has twelve NNs, we expect that the assembly can be stable even when all the NNs are not connected. We address these two issues in turn.

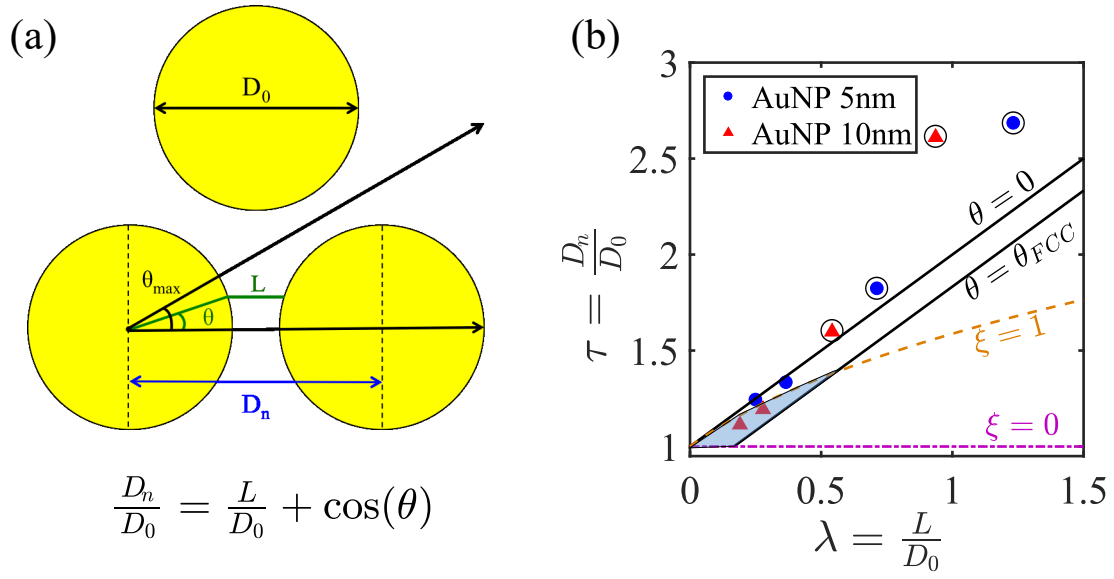

$$\frac{D_n}{D_0} = \frac{L}{D_0} + \cos(\theta)$$

Figure 4.6. (a) Geometric considerations in AuNP assembly with dithiols. D_0, D_n, and L are AuNP diameter, NN distance, and dithiol linker length, respectively. All binding sites must be contained within the conical volume defined by θ_{FCC} to obtain a stable FCC lattice. (b) Variation of dimensionless nearest neighbor distance (τ) versus the dimensionless contour length of dithiol (λ) for 5 and 10 nm AuNPs as indicated in the Figure. Data points outlined by empty circles represent the experimental conditions for which precipitation of AuNPs is not observed. Solid lines, corresponding to $\theta = 0$ and $\theta = \theta_{FCC}$, impose restrictions on the allowed values for τ for a given λ as determined by the geometric considerations discussed in the text. Dotted and dashed (magenta and orange) curves are predictions from OPM for $\xi = 0$ and $\xi = 1$, respectively. Shaded region (blue) is the overlap of the predictions from OPM and the geometrical constraints is the identified phase space to obtain FCC NPs crystals.

To correlate AuNP NN distance with the dithiol length, we consider simple geometrical requirements for the assembly as depicted in Figure 4.6(a). We assume that NPs are bridged by a bundle of dithiols coaxial to the line joining the NP centers and consider one of these bridges represented by a general straight line (colored green). The dithiol ligand can bridge two NPs along a straight line that connects the center of two NPs or it can be at a position corresponding to θ, the subtended angle. To satisfy the first condition for the formation of superlattice, that of the narrow distribution of binding sites, θ should be within the range from 0 to θ_{max}. θ_{max} for different crystal lattices can be determined by using the solid angle based nearest neighbor method (SANN) , which follows from the equation[45]

$$4\pi = \sum_{j=1}^{m} 2\pi[1 - \cos(\theta_{i,j})] \tag{4.1}$$

For a perfect FCC crystal, this equation yields an angle of $\theta_{max} = \theta_{FCC}$ = 33.55°where as for a perfect BCC crystal it is $\theta_{max} = \theta_{BCC}$ = 41.41°. θ_{FCC} (see Figure 4.6(a)), is the semi–apex angle that

defines the cone associated with each NN in the FCC lattice. Assuming that the dithiol molecule is completely stretched so that the length of the dithiol bridge is equal to the contour length of dithiol, we obtain bounds for the nearest neighbor distance in an FCC lattice as follows

$$\tau = \lambda + \cos(\theta), 0 < \theta < \theta_{FCC};\ \tau = \frac{D_n}{D_0},\ \lambda = \frac{L}{D_0} \tag{4.2}$$

Experimentally obtained τ and λ for different lengths of dithiols is plotted in Fig.4.6(b) for 5 and 10 nm nanoparticles along with the bounds using **Equation 4.2**. As seen from this figure, D_{NN} for DT12 and DT21 ($\lambda > 0.5$ in this study) appears outside the bounds, consistent with our observation that these two systems behave substantially different from the other two (with DT4 and DT6) displaying weak inter-particle correlations (fig. 4.11). In addition to these geometrical constraints, more detailed models such as, OPM,[46] OCM[47] and OTM[48,49] can provide upper and lower bounds to the NN distances. Here we consider the OPM and OCM as follows,

$$\tau_{OPM} = (1 + 3\lambda\xi)^{\frac{1}{3}}, \tag{4.3}$$

$$\tau_{OCM} = -\frac{1+\lambda}{2} + \sqrt{\left(\frac{1+\lambda}{2}\right)^2 + \frac{6\xi\lambda + 2}{1+\lambda}}, \tag{4.4}$$

where the parameter $\xi = \frac{A_0}{A}$ is a relative measure of grafting density, A_0 is the smallest possible molecular area, and A is the actual molecular area. Using the aforementioned models, we can predict where we would expect to find ordered structures experimentally. First, we note that geometrical considerations restrict the phase diagram into a narrow strip. We can then add the bounds given by the OPM and OCM models and the phase diagram is now restricted to a small region that satisfies both the geometry and the nanoparticle interaction models. In Figure 4.6, we shade the entire expected region predicted in this way, considering the full range of ξ as the grafting density of this system is yet unknown. We clearly predict the experimental results, where ordered structures fall in or near the prediction and experimental cases that did not result in order are far from our prediction.

Having shown that the distribution of dithiol binding sites is sufficiently narrow, we now proceed to analyze the stability of the lattice as a function of number connected NNs and chain length.

Here, we present MD simulations (see simulation methods for details) where we start with a perfect FCC lattice of NPs, each tethered to its NN by a flexible, coarse grained polymer chain. We analyze the effect of dithiol–lengths and the number of connected NNs on the mean squared displacement (MSD; $\langle \Delta r^2 \rangle$) of a particle center of mass from its ideal position in the lattice.[50] and determine the Lindemann ratio $f_L = \frac{\sqrt{\langle \Delta r^2 \rangle}}{D_n}$. We note that for $f_L \geq 0.13$ the lattice becomes disordered in a liquid-like state.[51] We define the average number of connected NNs per nanoparticle to be $2k$. In a fully connected FCC lattice $k = 6$ as there are 12 NNs per lattice point. From the plots for f_L versus k from the MD simulations (**Figure 4.7**) it can be observed that $k_{critical}$ at which $f_L = 0.13$ is ~2.5 meaning that on an average nanoparticles should be connected to at least 5 NNs to induce lattice stability. Further, as shown in the inlaid plot in Figure.4.7, f_L increases with the tether length (number of monomers) indicating decreasing crystal quality with longer tethers. Snapshots from these MD simulations are presented in **Figure 4.12,** and **4.13** in the SI.

In our analysis we assume the NPs to be perfect spheres which is a reasonable approximation considering SAXS and TEM results of the bare NPs and also geometrical packing of Au atoms into large clusters ($D \geq 4$ nm) appear more spherical.[52] For non-spherical particles (such as, smaller gold clusters) there necessarily exists a regime where NP geometry affects the equilibrium structure, particularly at low values of the parameter λ. Specifically, we expect that as the NP becomes less spherical, the number of geometrically allowed bridges in the network can vary. This is certainly an issue that requires further investigation, but we expect that the effect of NP geometry in our system is small for the values of λ studied.[49] Furthermore, because our results indicate robust lattice stability with decreasing connection number, these effects are insignificant for sufficiently spherical NPs.

4.4 Conclusions

Using a slew of experimental techniques, geometrical considerations and MD simulations, we explore routes to improve crystal quality of crossed-linked AuNPs with dithiol oligo-ethyleneglycol linkers. SAXS experiments of the crosslinked AuNPs precipitates in aqueous suspensions show formation of close-packed structures. Our analysis of the SAXS data shows the aggregates are bet-

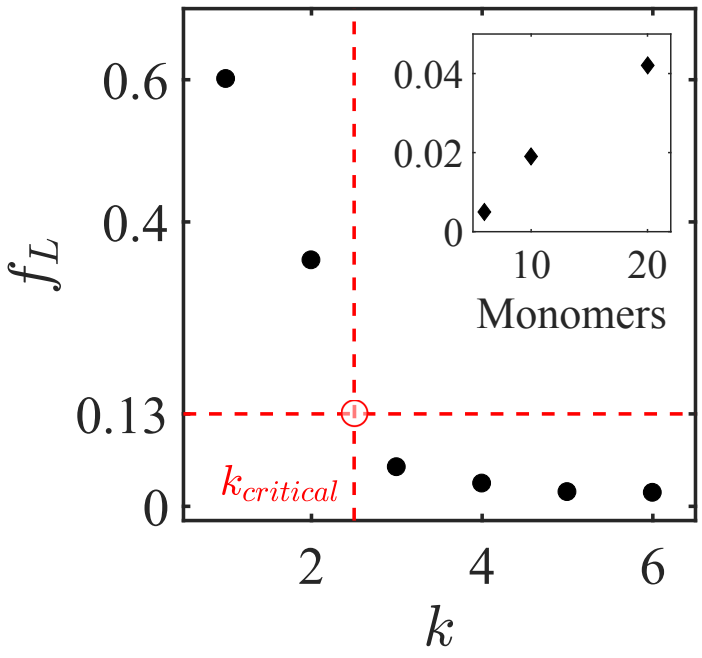

Figure 4.7. Variation of the Lindemann ratio (f_L), obtained from the results of MD simulations, with k (defined in text). For $k <\sim 2.5$, for which $f_L > 0.13$, the system is in a liquid-like state. The inset plot shows the variation of f_L with the number of monomers in the tether which is proportional to the stretched length of the tether.

ter modeled in FCC symmetry, albeit short-ranged-order. The characteristic length scale between nearest neighbors in the aggregates is found to increase with the length of the dithiol linker and hence offer tunable control in inter-particle distances. Based on experimental results, geometrical considerations and numerical simulations, we identify a narrow region in the parameter space of dithiol linker-length and particle diameter that favors superstructure formation. Narrowing the phase space that allows crystallization enables future research to be focused on exploring other parameters that can improve crystal quality and process robustness. These can include varying linker chemical composition, medium and medium conditions such as, thermal annealing, pH and added solutes that can potentially lead to superior and more robust crystals. For instance, with the use of aromatic conducting crosslinkers, such superlattices can exhibit unique plasmonic properties suitable for photonics and metamaterials.

4.5 Acknowledgement

Research was supported by the U.S. Department of Energy (U.S. DOE), Office of Basic Energy Sciences, Division of Materials Sciences and Engineering. Ames Laboratory is operated for the U.S. DOE by Iowa State University under Contract No. DE-AC02-07CH11358. Use of the Advanced Photon Source, an Office of Science User Facility operated for the U.S. DOE Office of Science by Argonne National Laboratory, was supported by the U.S. DOE under Contract No. DE-AC02-06CH11357.

This work used the Extreme Science and Engineering Discovery Environment (XSEDE), which is supported by National Science Foundation grant number ACI-1548562. Our project within XSEDE is supported by grant TG-MCB14007

4.6 Supporting Information

4.6.1 Complementary experiments

Dynamic light scattering (DLS) experiments (uisng with Zetasizer Nano at a wavelength of 633 nm and forward scattering angle of 90 were conducted 4 hours after mixing gold nanoparticles with various dithiols. Aggregates with DT6 showed quantitative precipitation after 2 days whereas DT12 did not induce quantitative precipitation of the nanoparticles. With DT6 and DT12 there are larger aggregates formed with hydrodynamic size centered at $\sim$ 400 nm, as shown in Fig. 4.8. We note that the aggregate-size for DT6 is larger than the estimated crystal size from SAXS measurements. Aggregates with DT21 formed only small aggregates with hydrodynamic size $\sim$ 25 nm and in fact this value did not change significantly even after 2 days indicating oligomerization. This is consistent with inter-particle correlation length (20 nm)for DT21 extracted from SAXS.

X-ray photoelectron spectroscopy (XPS) surface analysis was performed with a PHI 5500 spectrometer using Al-Kα1 radiation with a 45 electron collection angle, corresponding to the maximal penetration depth of about 10 nm. Au4f7/2 peak (84 eV) was used to calibrate the data and CasaXPS was used for fitting the models. The precipitates were collected and analyzed with XPS

to study the nature of chemical bonds (Fig. 4.8(b)). S2p region showed two components: a S-Au component centered at 162.5 eV and S-C component centered at 164 eV. Since -C-S-S-C- and -C-S-H have similar bond energies it is difficult to ascertain the presence or absence of disulfide bridges in the precipitates.

In addition to direct crosslinking AuNPs by dithiol, there exists another linking route where a bound dithiol to a AuNP forms a disulfide bridge with a similar dithiol that is bound to a neighboring AuNP (see schematic Figure 4.9(a) and 4.9(b)). However, as we argue below such indirect bridging is less plausible, in particular for the short chains dithiols. Indeed, the obtained NN distances for DT4 and DT6 are too short to be rationalized with indirect disulfide bridging, as discussed in the manuscript. Furthermore, the disulfide bridges are energetically weaker compared to the Au-thiol bond. Also, the cross section for a bound dithiol impinging on to another dithiol is much smaller than compared to a bare surface of a AuNP even after the binding of a few dithiols on it. We note that XPS results of these samples could not distinguish between these mechanisms as explained in the SI (Figure 4.8(a)).

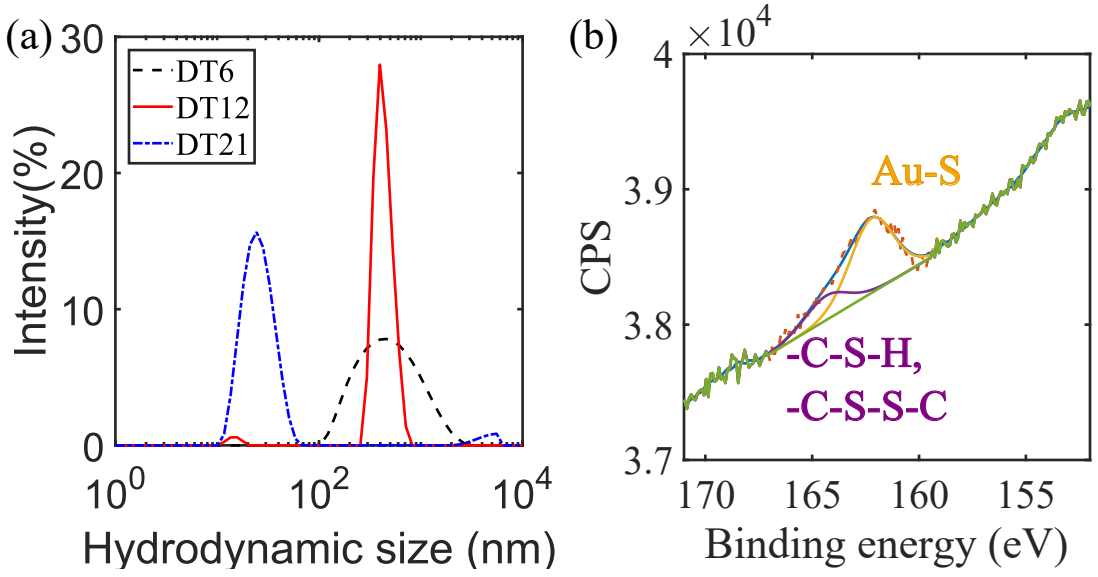

Figure 4.8. (a) Dynamic light scattering from gold nanoparticle aggregates upon addition of DT6, after 4 hours. (b) XPS results obtained with AuNP-DT6 aggregates spread on a a silicon waffer substrate. There are two components in the S2p region of the spectrum corresponding to Au-S and -C-S bonds. We note that the peaks from C-S-S-C and C-S-H bonds cannot be resolved with our apparatus.

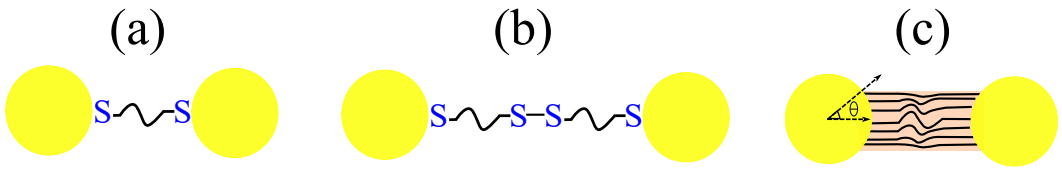

Figure 4.9. (a) NPs crosslinked *directly* by a dithiol molecule, (b) NPs crosslinked by two dithiols via a *disulfide bridge*. In this study, primarily for DT4 and DT6, *direct* crosslinking is expected to be prevalent as explained in the manuscript and the SI text, as depicted in (c). For a given D_n and D_0, θ is limited by the geometrical constraints as explained in the main text.

4.6.2 SAXS data reduction and fitting

The precipitates and aggregates are analyzed in their native environment by standard reduction of SAXS data as plotted in Figure 4.10(a). We recall that the scattering intensity ($I(q)$) is given by $I(q) = A|F(q)|^2 S(q)$, where $I(q)$ is the observed intensity after standard data reduction (from 2D area image to 1D curve and background subtraction), A is a scaling constant that depends on the number of particles, $|F(q)|$ is the form factor of the NPs and $S(q)$ is the experimentally observed structure factor. A representative figure showing the SAXS intensity profile after background subtraction is shown in Fig. 4.10(a), along with the form factor.

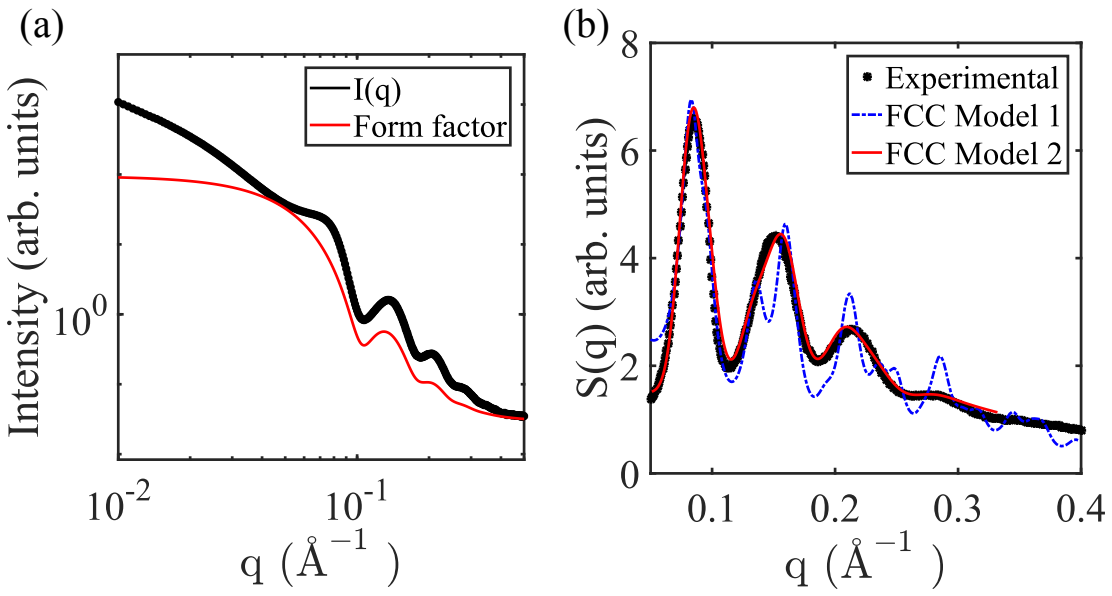

Figure 4.10. (a) SAXS intensity from AuNP-dithiol assemblies at $r = 8500$ for Au10:DT4, and the average form factor (solid line in red) based on AuNPs size distribution. (b) $S(q)$ obtained from (a) including two fit-models as described in the text.

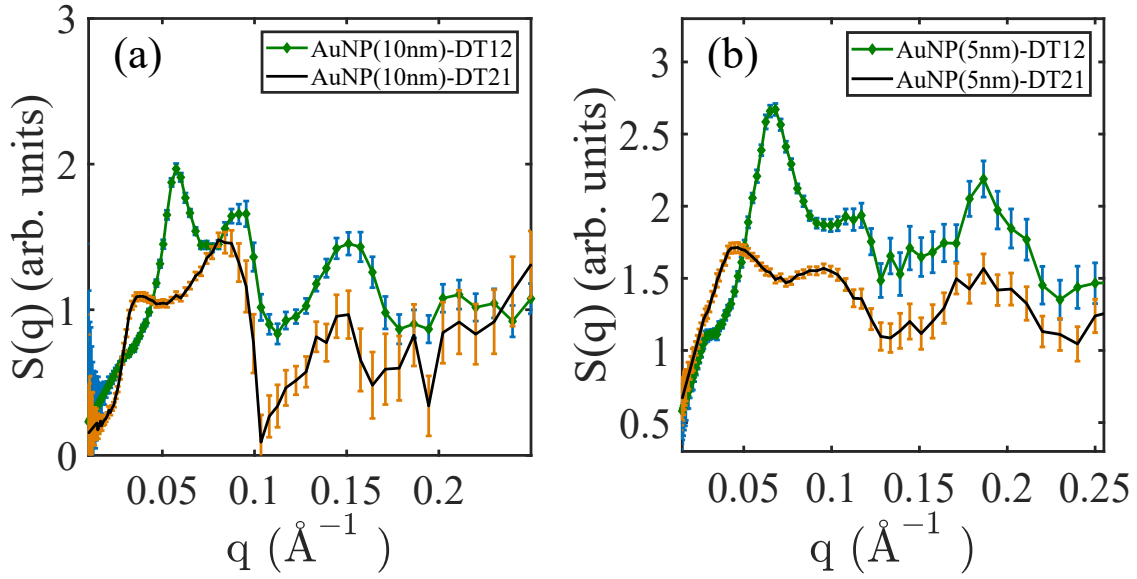

Figure 4.11. Structure factor curves for (a) Au10:DT12, Au10:DT21, (b) Au5:DT12 and Au5:DT21 at r = 8500. The data has been binned on a logarithmic scale in q for better presentation. Due to the relatively large error bars at high q, only primary peak has been considered to draw inferences on the structure of the assemblies. Unlike the structure factors for DT4 and DT6 systems, these do not show much semblance to FCC lattice structure factors.

4.6.2.1 Structure factor model 1

$$S_{Mod}(q) = A_0 \sum_{hkl} S(q : q_{hkl}) \tag{4.5a}$$

$$S(q : q_{hkl}) = 1 + G(q_{hkl}) \left[\beta(q) Z_0(q_{hkl}) L(q : q_{hkl}, \sigma) - 1\right] \tag{4.5b}$$

$$\beta(q) = 1(Assumption) \tag{4.5c}$$

$$Z_0(q_{hkl}) = \frac{m_{hkl}}{q_{hkl}^2} \tag{4.5d}$$

$$G(q) = \exp\left(-\sigma_D^2 D_n^2 q_{hkl}^2\right) \tag{4.5e}$$

$$L(q : q_{hkl}, \sigma) = \frac{\sigma}{2\pi} \frac{1}{(q - q_{hkl})^2 + (\frac{\sigma}{2})^2} \tag{4.5f}$$

$$C_{FCC} = \frac{K\lambda}{\beta cos\theta} \tag{4.6}$$

In this model, A_0 is a constant, free parameter; $\beta(q)$ corrects for particle size polydispersity and orientational disorders;[43] $G(q_{hkl})$ is the Debye Waller factor that allows for translational disorders

in the lattice;[42,43] σ_D is related to the Lindemann ratio as $f_L = \sqrt{(3)}\sigma_D$ $Z_0(q_{hkl})$ is the structure factor for an ideal crystal; $L(q : q_{hkl}$ is the shape function (we use Lorentzian shape function) arising due to the finite size of the crystals; and D_n is the nearest neighbor distance. For model simplicity we have assumed the polydispersity of nanoparticle size to have no effect on the structure factor (β(q) = 1). Crystallite sizes (C_{FCC}) were calculated using the Scherrer equation (Eq.6.3). Results from this model are tabulated in Table 6.3 and a representative fit is shown in Figure 4.10(b). Nearest neighbor distances for FCC used in Figure 4.6 are obtained from fits to this model as $D_n = \frac{\sqrt{6}\pi}{q_{111}}$. Since SAXS results from DT12 and DT21 systems could not be fit to scattering from any standard lattice, the first peak in S(q) was used as q_{111}.

4.6.2.2 Structure factor model 2

$$S_{Total}(q) = A_o \sum_{hkl} S(q : q_{hkl}) \tag{4.7a}$$

$$S(q : q_{hkl}) = h_{hkl} * \mathcal{N}(q : q_{hkl}, \sigma_{hkl}) \tag{4.7b}$$

$$\sigma_{hkl} = \sigma_{111}(1 + \alpha(q_{111} - q_{hkl})) \tag{4.7c}$$

This model relaxes the constraints on relative peak intensities which are fixed by the peak multiplicities, the Lorentz factor and the Debye-Waller factor in model 1. Due to this relaxation of constraints, this model shows a better fit to the experimentally observed scattering. h_{hkl} is the relative peak height for the peak corresponding to {hkl} reflections. Peak width (σ_{hkl}) is allowed to increase linearly with q_{hkl} as a first order approximation.

4.6.3 Contour length of dithiols

In order to relate the geometrical quantities to the properties of the dithiol chains, we need to compute their maximum extended (all trans) length, sometimes called the contour length $L_{contour}$. We use the results from our previous papers [18,19] and simulations[49] and derive Equation 4.8 and

Table 4.1. Lattice constant, nearest neighbor distance $D_{n,FCC}$, crystallite size C_{FCC}, and Debye-Waller factor σ_d obtained from structure factor fit to assuming FCC superlattice (model 1).

AuX:DTY (1:r)	Lattice constant (Å)	$D_{n,FCC}$ (Å)	C_{FCC} (Å)	σ_d
Au5:DT4 (1:100)	105.0	74.3	549	0.03
Au5:DT4 (1:400)	106.2	75.1	545	0.032
Au5:DT4 (1:850)	107.2	75.8	553	0.032
Au5:DT4 (1:8500)	110.7	78.3	546	0.031
Au5:DT6 (1:100)	114.3	80.8	586	0.019
Au5:DT6 (1:400)	115.8	81.9	806	0.038
Au5:DT6 (1:850)	116.4	82.3	806	0.037
Au5:DT6 (1:8500)	118.8	84.0	814	0.036
Au10:DT4 (1:400)	128.8	91.1	616	0.019
Au10:DT4 (1:850)	130.7	92.4	640	0.021
Au10:DT4 (1:8500)	130.7	92.4	616	0.021
Au10:DT6 (1:100)	131.6	93.1	541	0.026
Au10:DT6 (1:850)	141.1	99.8	767	0.027
Au10:DT6 (1:8500)	140.1	99.0	732	0.027
Au10:DT6 (1:85000)	140.4	99.3	728	0.027

Table 4.2. Relevant values that describe the backbone length of the dithiol chain.

	l(nm)	θ
C - *O*	0.143	68°
C - *C*	0.153	68°
S - *C*	0.182	unrestricted

its accompanying table (Table 4.2)

$$\begin{aligned} L_{contour} &= L_{PEG} + L_{ends} \\ &= (2l_{CO} + l_{CC})cos(\frac{\theta}{2})n + L_{ends} \\ &= .364n + L_{ends} \\ &= .364n + 2[l_{SC} + l_{CC}cos(\frac{\theta_{CC}}{2}) + l_{CO}cos(\frac{\theta_{CO}}{2})] \\ &= .364n + 0.855. \end{aligned} \tag{4.8}$$

In this work, $n = 2, 4, 10, 19$ corresponding to DT4, DT6, DT12 and DT21, respectively.

4.6.4 MD simulations for lattice stability

Snapshots from MD simulations illustrate the results of Fig. 4.7 from the main text. Overall lattice quality relies heavily on the connectedness of the lattice, as is evident in Fig. 4.12. Due to the random distribution of bridges in the lattice, we see regions of high relative order and

(a) 6N Connected Lattice (b) 1N Connected Lattice

Figure 4.12. Snapshot from MD simulations illustrating lattice quality is noticeably worsened as the number of connected NNs decreases. (a) FCC structure is retained for 6N connections, but (b) is dissolved at 1N connections. Our results show in Fig. 4.7 that at 5 connected nearest neighbors ($k \approx 2.5$) are necessary to stabilize the FCC lattice.

connectivity (Fig. 4.13(a)), as well as local regions where relative connectivity is low and local order is not present (Fig. 4.13(b)).

Figure 4.13. Snapshot of MD simulations for 2N connected lattice where the examined particle is shown in blue and is connected particles in yellow and other non-connected particles in transparent gray. (a) Local order emerges due to clusters of higher order bridging, created by the random selection of bridges. (b) This order dissolves as connection number decreases to allow particle diffusion about the lattice.

References

[1] Prasad, B. L. V., Sorensen, C. M., and Klabunde, K. J. *Chemical Society Reviews* **37**(9), 1871–1883 (2008).

[2] Auyeung, E., Morris, W., Mondloch, J. E., Hupp, J. T., Farha, O. K., and Mirkin, C. A. *Journal of the American Chemical Society* **137**(4), 1658–1662 (2015).

[3] Gerth, M. and Voets, I. K. *Chem. Commun.* **53**(32), 4414–4428 (2017).

[4] Talapin, D. V., Lee, J. S., Kovalenko, M. V., and Shevchenko, E. V. *Chemical Reviews* **110**(1), 389–458 (2010).

[5] Klinkova, A., Choueiri, R. M., and Kumacheva, E. *Chemical Society Reviews* **43**(11), 3976–3991 (2014).

[6] Zabet-Khosousi, A. and Dhirani, A.-A. *Chemical Reviews* **108**(10), 4072–4124 (2008).

[7] Liu, S. Q. and Tang, Z. Y. *Journal of Materials Chemistry* **20**(1), 24–35 (2010).

[8] Nie, Z. H., Petukhova, A., and Kumacheva, E. *Nature Nanotechnology* **5**(1), 15–25 (2010).

[9] Li, J., Yiliguma, Y., Wang, G., and Zheng, G. *Nanoscale* **8**(30), 14359–14368 (2016).

[10] Park, S. Y., Lytton-Jean, A. K. R., Lee, B., Weigand, S., Schatz, G. C., and Mirkin, C. A. *Nature* **451**, 553 (2008).

[11] Nykypanchuk, D., Maye, M. M., van der Lelie, D., and Gang, O. *Nature* **451**(7178), 549–552 (2008).

[12] Jones, M. R., Macfarlane, R. J., Lee, B., Zhang, J., Young, K. L., Senesi, A. J., and Mirkin, C. A. *Nature Materials* **9**(11), 913–917 (2010).

[13] Macfarlane, R. J., Jones, M. R., Senesi, A. J., Young, K. L., Lee, B., Wu, J., and Mirkin, C. A. *Angewandte Chemie (International ed. in English)* **49**(27), 4589 (2010).

[14] Macfarlane, R. J., Lee, B., Jones, M. R., Harris, N., Schatz, G. C., and Mirkin, C. A. *Science* **334**(6053), 204–208 (2011).

[15] Campolongo, M. J., Tan, S. J., Smilgies, D.-M., Zhao, M., Chen, Y., Xhangolli, I., Cheng, W., and Luo, D. *ACS nano* **5**(10), 7978 (2011).

[16] Tan, S. J., Kahn, J. S., Derrien, T. L., Campolongo, M. J., Zhao, M., Smilgies, D.-M., and Luo, D. *Angewandte Chemie International Edition* **53**(5), 1316–1319 (2013).

[17] Srivastava, S., Nykypanchuk, D., Fukuto, M., Halverson, J. D., Tkachenko, A. V., Yager, K. G., and Gang, O. *Journal of the American Chemical Society* **136**(23), 8323–8332 (2014).

[18] Zhang, H., Wang, W., Mallapragada, S., Travesset, A., and Vaknin, D. *Nanoscale* **9**(1), 164–171 (2016).

[19] Zhang, H., Wang, W., Akinc, M., Mallapragada, S., Travesset, A., and Vaknin, D. *Nanoscale* **9**(25), 8710–8715 (2017).

[20] Si Kae, J., Chen, Y., Shi, Q., and Cheng, W. *Advanced Science* **5**(1), 1700179 (2018).

[21] Whitesides, G. M. and Grzybowski, B. *Science* **295**(5564), 2418–2421 (2002).

[22] Grzelczak, M., Vermant, J., Furst, E. M., and Liz-Marzan, L. M. *Acs Nano* **4**(7), 3591–3605 (2010).

[23] Luo, D., Yan, C., and Wang, T. *Small* **11**(45), 5984–6008 (2015).

[24] Boles, M. A., Engel, M., and Talapin, D. V. *Chemical Reviews* **116**(18), 11220–11289 (2016).

[25] Mirkin, C. A., Letsinger, R. L., Mucic, R. C., and Storhoff, J. J. *Nature* **382**(6592), 607–609 (1996).

[26] Boal, A. K., Ilhan, F., DeRouchey, J. E., Thurn-Albrecht, T., Russell, T. P., and Rotello, V. M. *Nature* **404**(6779), 746–748 (2000).

[27] Baron, A., Aradian, A., Ponsinet, V., and Barois, P. *Optics and Laser Technology* **82**, 94–100 (2016).

[28] Yoon, G., Kim, I., and Rho, J. *Microelectronic Engineering* **163**, 7–20 (2016).

[29] Ray, P. C., Darbha, G. K., Ray, A., Walker, J., and Hardy, W. *Plasmonics* **2**(4), 173–183 (2007).

[30] Yue, M., Li, Y., Hou, Y., Cao, W., Zhu, J., Han, J., Lu, Z., and Yang, M. *ACS nano* **9**(6), 5807 (2015).

[31] Brust, M., Bethell, D., Schiffrin, D. J., and Kiely, C. J. *Advanced Materials* **7**(9), 795–& (1995).

[32] Deffner, M., Schulz, F., and Lange, H. *Zeitschrift Fur Physikalische Chemie-International Journal of Research in Physical Chemistry & Chemical Physics* **231**(1), 19–31 (2017).

[33] Lin, G. Y., Wang, Y., Zhang, Q. J., Zhang, X. X., Ji, G., and Ba, L. *Nanoscale* **3**(11), 4567–4570 (2011).

[34] Hussain, I., Wang, Z. X., Cooper, A. I., and Brust, M. *Langmuir* **22**(7), 2938–2941 (2006).

[35] Sugata, E. and Kobatake, S. *Rsc Advances* **5**(44), 34704–34708 (2015).

[36] Joseph, S. T. S., Ipe, B. I., Pramod, P., and Thomas, K. G. *Journal of Physical Chemistry B* **110**(1), 150–157 (2006).

[37] Ferrier, Robert C., J., Lee, H.-S., Hore, M. J. A., Caporizzo, M., Eckmann, D. M., and Composto, R. J. *Langmuir* **30**(7), 1906–1914 (2014).

[38] Rossner, C., Glatter, O., Saldanha, O., Koster, S., and Vana, P. *Langmuir* **31**(38), 10573–10582 (2015).

[39] Anderson, J. A., Lorenz, C. D., and Travesset, A. *Journal of Computational Physics* **227**(10), 5342–5359 (2008).

[40] Nguyen, T. D., Phillips, C. L., Anderson, J. A., and Glotzer, S. C. *Computer Physics Communications* **182**(11), 2307–2313 (2011).

[41] Glaser, J., Nguyen, T. D., Anderson, J. A., Lui, P., Spiga, F., Millan, J. A., Morse, D. C., and Glotzer, S. C. *Computer Physics Communications* **192**, 97–107 (2015).

[42] Forster, S., Timmann, A., Konrad, M., Schellbach, C., Meyer, A., Funari, S. S., Mulvaney, P., and Knott, R. *Journal of Physical Chemistry B* **109**(4), 1347–1360 (2005).

[43] Senesi, A. J. and Lee, B. *Journal of Applied Crystallography* **48**, 1172–1182 (2015).

[44] Kewalramani, S., Guerrero-Garcia, G. I., Moreau, L. M., Zwanikken, J. W., Mirkin, C. A., de la Cruz, M. O., and Bedzyk, M. J. *Acs Central Science* **2**(4), 219–224 (2016).

[45] van Meel, J. A., Filion, L., Valeriani, C., and Frenkel, D. *Journal of Chemical Physics* **136**(23) (2012).

[46] Landman, U. and Luedtke, W. D. *Faraday Discussions* **125**, 1–22 (2004).

[47] Schapotschnikow, P. and Vlugt, T. J. H. *The Journal of Chemical Physics* **131**(12) (2009).

[48] Travesset, A. *Soft Matter* **13**(1), 147–157 (2017).

[49] Waltmann, C., Horst, N., and Travesset, A. *ACS nano* **11**(11) (2017).

[50] Anderson, J. A., Lorenz, C. D., and Travesset, A. *Journal of Chemical Physics* **128**(18) (2008).

[51] Hansen, J.-P. *Theory of simple liquids Jean-Pierre Hansen, Ian R. McDonald*. Amsterdam : Elsevier, Amsterdam, 3rd ed.. edition, (2006).

[52] Mori, T. and Hegmann, T. *Journal of Nanoparticle Research* **18**(10), 295 (2016).

CHAPTER 5. EFFECT OF (POLY)ELECTROLYTES ON THE INTERFACIAL ASSEMBLY OF PEG FUNCTIONALIZED GOLD NANOPARTICLES

A paper submitted to the Journal Langmuir

Srikanth Nayak, Max Fieg, Wenjie Wang, Wei Bu, Surya Mallapragada, and David Vaknin [1]

Abstract

We report on the effect of interpolymer complexes (IPCs) of poly(acrylic acid) (PAA) with poly(ethylene glycol) functionalized Au nanoparticles (PEG-AuNPs) as they assemble at the vapor-liquid interface, using surface sensitive synchrotron X-ray scattering techniques. Depending on the suspension pH, PAA functions both as a weak polyelectrolyte and a hydrogen bond donor, and these two roles affect the interfacial assembly of PEG-AuNPs differently. Above its isoelectric point, we find that PAA leads to the formation of a PEG-AuNPs monolayer at the interface with hexagonal structure. In the presence of high concentration of HCl (i.e., below the isoelectric point), at which PAA forms IPCs with PEG, the hexagonal structure at the interface appears to deteriorate, concurrent with aggregation in the bulk. Thus, while electrolytic behavior of PAA induces interfacial assembly, hydrogen bonding behavior, as PAA becomes neutral, favors the formation of 3D assemblies. For comparison, we also report on the formation of PEG-AuNPs monolayers (in the absence of PAA) with strong electrolytes such as HCl, H_2SO_4 and NaOH that lead to a high degree of crystallinity.

5.1 Introduction

Arrays of nanoparticles (NPs) with long range order in two and three dimensions, referred to as NP superlattices, can be self-assembled from colloidal suspensions of NPs. Such NP superlattices are of significant research interest due to their potential applications in fields such as

[1] Author for correspondence

plasmonics, sensing, catalysis etc.[1–3] Interfacial assembly of NPs is of particular interest by virtue of its relevance to biological systems and its applications in device fabrication.[4] Earliest examples of NP superlattice formation have been demonstrated with evaporation induced assembly of NPs at the solid-air interface.[5] Similar strategy has later been extended to air-liquid interface by spreading a NP suspension on an immiscible liquid surface to obtain a monolayer of two-dimensional (2D) superlattice.[6] Charged Langmuir monolayers have been used as templates for the formation of stimuli-responsive assemblies of DNA-functionalized NPs.[7–9]

Nanoparticles functionalized with various polymers such as single stranded DNA (ssDNA),[10,11] poly(ethylene glycol) (PEG),[12–15] and poly(N-isopropylacrylamide) (PNIPAM)[16] have been shown to form salt responsive Gibbs monolayer assemblies with high degree of two-dimensional (2D) crystallinity at the vapor-liquid interface. Charge neutralization and the hydrophobicity of the alkyl thiol linker were hypothesized to be the driving factors for the salt-responsive assembly of ssDNA functionalized AuNPs.[11] When the ssDNA have "sticky ends" that can hybridize, the apparent order at the interface worsens and aggregation is observed in bulk.[11] In the case of PEG-AuNPs, the addition of ions causes decrease in solvent quality for the polymers leading to phase separation and nanoparticle self-assembly, where the specific effect of ions follows the Hofmeister series.[12,14] Similarly, PNIPAM-AuNPs also show salt responsive 2D assembly due to lowering of lower critical solution temperature (LCST) of PNIPAM by salt. In all the above cases, a hexagonal packing at the interface is observed at appropriate salt concentrations. In contrast, AuNPs functionalized with alkyl thiol terminated poly(acrylic acid) (PAA) form a dense monolayer at vapor-liquid interface with 1D chain-like order upon lowering the pH, driven by inter-particle hydrogen bonds.[17] Thus, there are apparent differences in the formation of assemblies mediated by ions and hydrogen bonds. The basic mechanism of formation of these assemblies needs to be understood so that the crystal symmetry can be controlled for specific applications.

One phenomenon where both ionic and hydrogen bonding interactions play a role is the formation of interpolymer complexes (IPCs). IPCs are formed when two distinct polymers interact with each other along their respective chains via non-covalent interactions such as hydrogen bonds. Formation of hydrogen bonded IPCs has been shown with a variety of polymers, most

commonly with a poly(acid) such as PAA and a poly(base) such as PEG.[18,19] Since the formation of stable hydrogen bonds requires the poly(acid) to be protonated, there exists a critical pH above which the IPCs dissociate. Here, we explore the effect of formation of IPCs at low and high PAA concentrations on the interfacial assembly of PEG-AuNPs using liquid surface X-ray scattering (schematic shown in Fig. 6.1).

To unravel the effect of interpolymer complexation on the 2D assembly of PEG-AuNPs in the presence of PAA we also study the effect of HCl alone on PEG-AuNPs assembly as a control system. Previous studies have already established that electrolytes such as NaCl cause 2D interfacial assembly, but the specific ion effects are not yet understood.[14] Anions have a pronounced effect on the inter-particle distances in the assemblies compared to the cations. Distribution of ions in these monolayers is still an outstanding question. In the case of assemblies obtained with Cs_2SO_4, an interfacial depletion of the cation Cs^+ has been reported.[13] This makes the effect of strong acids on the assembly particularly interesting as the hydronium ions are expected to preferentially adsorb at the air-water interface.[20,21] This anomalous behavior of hydronium ions has been hypothesized to be the cause of decrease in interfacial tension in the presence of high concentration of strong acids, which is in contrast to the increase in interfacial tension in the presence of salts. So, to explore the effects of different ions on the interfacial assembly of PEG-AuNPs, we used NaCl, PAA (by itself and with HCl), HCl, H_2SO_4 and NaOH at different concentrations. Remarkably, we find that all the electrolytes lead to interfacial assembly of a monolayer of PEG-AuNPs, where the strong electrolytes lead to better crystallinity compared to PAA.

5.2 Materials and Methods

Reagents and Materials

Citrate stabilized gold nanoparticles with 10 nm nominal diameter (referred to as AuNP) were purchased from Ted Pella Inc. Poly(ethylene glycol) methyl ether thiol of average molecular weight (M_n) of $\sim$ 2000Da and Poly(acrylic acid) of $M_n \sim$ 2000Da (referred to as PEG2k and PAA2k, respectively) were purchased from Sigma Aldrich. Poly(ethylene glycol) methyl ether

thiol of $M_n \sim 5000$Da (referred to as PEG5k) was purchased from CreativePEGWorks Inc. All the chemicals were used as obtained from the manufacturer, without any purification.

Poly(ethylene glycol) functionalized AuNPs (referred to as PEG2k-AuNP or PEG5k-AuNP) were prepared by a simple ligand exchange. AuNPs and aqueous solutions of PEG2k or PEG5k were mixed at a molar ratio of 1:25000, under roto-shaking for 2 days. The solution was then purified by centrifuging the mixture for 1.5 hours, over 4 cycles to remove unbound PEG and the PEG-AuNPs were redispersed in millipore water. Concentration of PEG-AuNPs was estimated from the extinction value of the suspension at 520 nm, using UV-vis absorption spectra (Molecular Devices SpectraMax). Hydrodynamic sizes of the NPs were measured by Dynamic Light Scattering (Malvern Zetasizer Nano-ZS90 (HeNe laser, wavelength =633 nm, 90^o scattering angle).

Experimental Setup

Grazing incidence - small angle X-ray scattering (GI-SAXS) and specular X-ray reflectivity (XRR) measurements were taken at Argonne National Laboratory on beamline 15 ID-C at APS using liquid surface x-ray scattering with X-ray energy, E = 10 keV, and $\lambda = 1.24$Å. We used a set-up described elsewhere.[16] Briefly, 1.5 mL of ~ 14nM PEG-AuNPs were spread on a stainless steel trough (approximate dimensions 20 × 100 × 0.3 mm^3) and the trough was placed in an air-tight chamber that is continuously flushed with water-saturated Helium. To observe the interfacial behavior of PEG-AuNPs upon addition of various electrolytes (HCl, H_2SO_4, PAA2k etc., and water for control) appropriate amounts of aqueous solutions of electrolytes were added to the trough and mixed well. GI-SAXS and XRR data were measured and analyzed as described earlier.[16] Note that all GI-SAXS graphs are displayed as an integration across the area detector (Pilatus 100K) from a Q_z range of $[0.02 : 0.1]$Å^{-1}. All the measurements were conducted at room temperature.

5.3 Results and Discussion

To ensure colloidal stability of PEG-AuNPs that are synthesized by ligand exchange method, we use dynamic light scattering (DLS). As expected, the hydrodynamic size of the particles increases with molecular weight of the PEG used in this study, as shown in Figure 5.10. For the

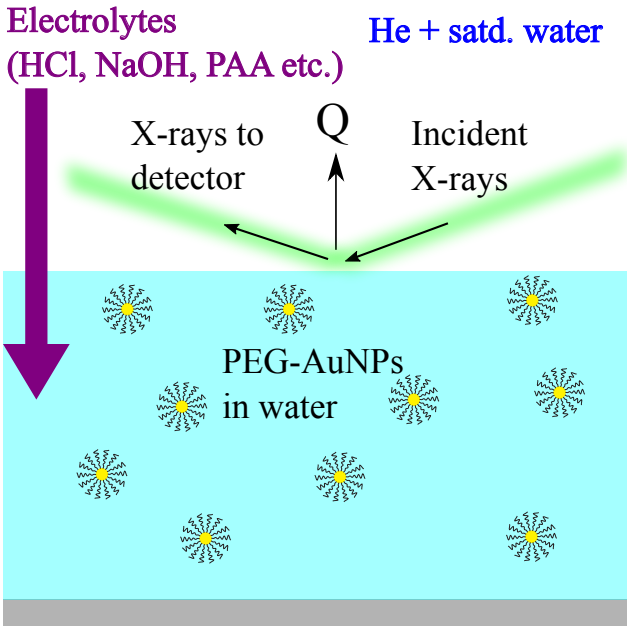

Figure 5.1. Schematic of the experimental set-up. A suspension of PEG-AuNPs is contained in a trough that is placed in a chamber flushed with water saturated helium gas. Electrolytes, such as HCl, are added to the suspension and mixed thoroughly. X-rays are incident on the vapor-liquid surface and the scattered rays (in terms of scattering vector, **Q**) are collected in X-ray reflectivity (XRR) and grazing incidence small angle X-ray scattering (GI-SAXS) modes to provide the interfacial structural information.

x-ray measurements, the NP suspensions are placed in a trough which is enclosed in an air-tight chamber that is constantly flushed with water-saturated helium.

5.3.1 Effect of electrolytes

First, we focus on the effect of strong electrolytes (NaCl, HCl, H_2SO_4 and NaOH) on the assembly of PEG5k-AuNPs and PEG2k-AuNPs. It has been shown that assembly and crystallization occurs in the presence of ions at neutral and basic conditions,[14] and here we further explore the effect of acids. The concentration of electrolytes is raised sequentially by additions of concentrated aqueous solutions to the same sample. At each addition (sample condition) the sample is let to equilibrate for ~ 30 minutes, and then GI-SAXS and XRR are measured.

Figure 5.2 (a) shows 2D (Q_{xy},Q_z) GI-SAXS patterns of PEG-AuNPs in the presence of HCl, demonstrating acids also induce assembly and crystallization of the NPs at the interface, as also shown in the SI for sulfuric acid. In the absence of HCl the pattern in Fig. 5.2 (a) shows a form

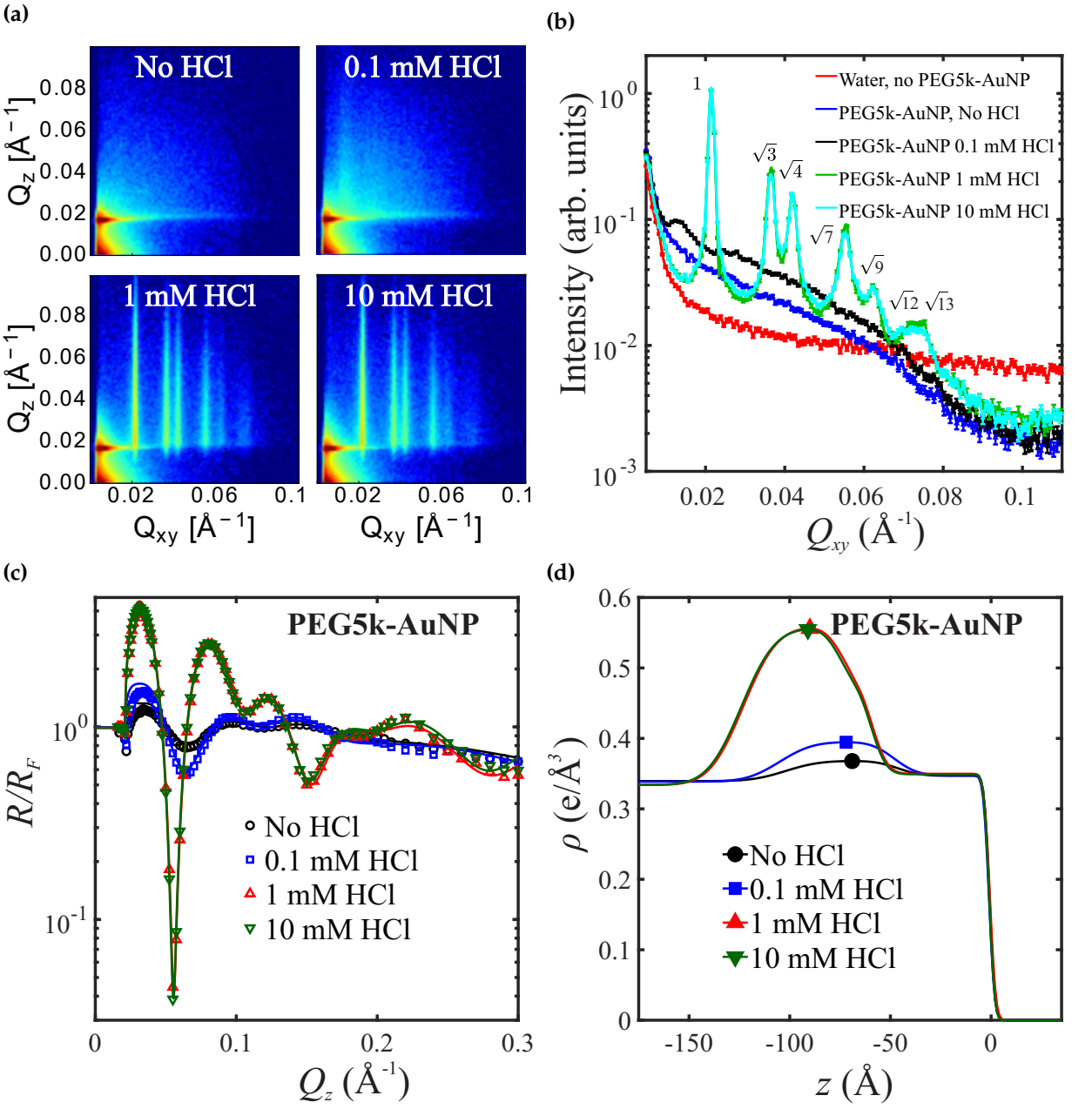

Figure 5.2. HCl induces the formation of hexagonally ordered monolayers of PEG5k-AuNPs at the air-water interface. (a) Raw GI-SAXS patterns for PEG5k-AuNPs with increasing HCl concentrations. Intensities are shown on a logarithmic scale. In the absence of HCl, the GI-SAXS pattern shows the form factor, indicating presence of PEG5k-AuNPs at the interface in a dispersed state. At 0.1 mM of HCl the GI-SAXS pattern shows a broad peak at $\sim 0.012\text{Å}^{-1}$ along with diffuse scattering, indicating the emergence of correlations among nanoparticles at the interface. At 1 and 10 mM of HCl, there are clear diffraction rods from the 2D crystalline structures at the interface. (b) Q_z line-cuts from (a) integrated from $Q_z = 0.02\text{Å}^{-1}$ to 0.1Å^{-1}. At 1 and 10 mM of HCl, diffraction peaks can be indexed to hexagonal structure with $a_L \simeq 33.5$ nm. The plots are vertically shifted for clarity. (c) Normalized X-ray reflectivities show the evolution of surface-normal structure with increasing HCl concentration. (d) Electron density fits obtained from box model corresponding to the normalized reflectivities observed in (c). Best fits for reflectivities are shown as solid lines in (c).

factor-like feature that can be associated with PEG5k-AuNPs, indicating that some of the grafted NPs spontaneously populate the interface without any inter-particle correlations. The corresponding XRR shows some modest oscillations (Fig. 5.2c). This is likely due to the the weak amphiphilic property of PEG chains in water. At 0.1 mM the GISAXS pattern shows two broad peaks at $\sim 0.012\text{Å}^{-1}$ and $\sim 0.025\text{Å}^{-1}$ consistent with the emergence of developing correlations among the PEG-AuNPs. There are prominent oscillations in the XRR and a slight increase in the ED (Fig. 5.2d) compared to that without HCl, indicating higher tendency for the PEG5k-AuNPs to populate the interface in the presence of 0.1 mM of HCl. At and above 1 mM of HCl, crystalline assemblies of PEG5k-AuNPs form at the vapor-liquid interface with HCl (Fig. 5.2) similar to those obtained with NaCl (Fig. 5.11). Sharp diffraction peaks are observed in the GI-SAXS results, and the relative peak positions Q^i_{xy}/Q^1_{xy} = 1, $\sqrt{3}, \sqrt{4}, \sqrt{7}$... (where Q^1_{xy} is the primary peak position corresponding to (1 0) two-dimensional (2D) Bragg reflection, and i indexes the diffraction peaks with $i = 1, 2, 3, 4$..) show the formation of hexagonal structure (Fig. 5.2a and 5.2b). Peak positions, and widths are obtained by a Lorentz shape function fit to each diffraction peak. For example, at 10 mM HCl we obtain a lattice constant, $a_L \simeq 33.5$ nm, and a full-width at half maximum (FWHM) of the primary peak is $\simeq 0.0015\text{Å}^{-1}$ corresponding to an average crystal size of $\frac{2\pi}{FWHM} \sim 400$ nm. Strong oscillations in the XRR profile and the extracted electron density (ED) profile for PEG5k-AuNP in the presence of 1 mM HCl show the formation of monolayer at the interface (Fig. 5.2c and 5.2d). The extent of population of the interface by PEG-AuNPs can be qualitatively gauged by the height of the ED profile. Maximum electron density of the 2D assembly is $\sim 0.55e/\text{Å}^3$ (Fig. 5.2d), whereas the electron density of bulk water and gold are $\sim 0.33e/\text{Å}^3$ and $\sim 4.67e/\text{Å}^3$, respectively. XRR and the fit ED profile show that the assembly is approximately one nanoparticle thick (Fig. 5.2c, and 5.2d). There is no significant change in XRR when the HCl concentration is increased from 1 mM to 10 mM showing saturation of the monolayer at the interface at $\sim$ 1 mM HCl.

Similar trends are obtained using H_2SO_4 instead of HCl while maintaining same pH (Fig. 5.12 a-c). Parameters concerning GI-SAXS peak shapes and ED profiles can be found in Table. 5.1. While the pH of the corresponding samples with HCl and H_2SO_4 at similar values, the ionic nature

of each solution is markedly different (Cl^- compared to $SO_4{}^{2-}$). This change in ionic environment has no appreciable difference on the accumulation of particles at the surface, nor on the formation of the 2D superlattice, except for small differences in lattice constant.

For comparison, we also examine the effect of adding a strong base to the suspension. Interestingly, while 1 mM of HCl induces the formation of highly crystalline hexagonal structure, 1 mM NaOH induces only short range order (Fig. 5.12d). Further concentration increase of NaOH to 10 mM improves significantly the crystallinity. The surface accumulation of PEG5k-AuNPs at 10 mM of NaOH is comparable in magnitude ($\rho_{max} \approx 0.58$ e/Å^3) to the same in acidic environment. Results from GI-SAXS and XRR for PEG5k-AuNPs with the strong electrolytes are summarized in Table 5.1. With all the salts, lattice constant of the assemblies either remains constant or decreases with increasing salt concentration. The variation of lattice constants for different anions is in correspondence with results reported earlier.[14] However, the difference in lattice constants observed for HCl and H_2SO_4 (< 1nm) is much smaller than the values reported for KCl and K_2SO_4 (~ 7 nm).[14]

$$\rho_{2D} = \int_{-\infty}^{0} (\rho(z) - \rho_{water})\, dz \tag{5.1}$$

We examine the effect of PEG chain length by conducting similar experiments with PEG2k-AuNP. Figure 5.3 shows that PEG2k-AuNPs under appropriate electrolyte conditions forms crystalline assemblies similar to PEG5k-AuNPs, albeit with a smaller unit cell. GI-SAXS at 1 and 10 mM of HCl show good hexagonal crystallinity and unlike PEG5k-AuNPs, the unit cell can be controlled by HCl concentration. Based on GI-SAXS, we find that the lattice constant is ~ 20.2 nm and 19.0 nm at 1 and 10 mM of HCl, respectively. Thus, the lattice constant in the interfacial assembly can be tuned by the length of PEG chains on nanoparticles. XRR and the extracted ED (Fig. 5.3d) are consistent with the smaller unit cell that lead to much higher EDs than those observed for PEG5k-AuNPs. Furthermore, the monolayer is brought closer to the surface; this indicates that the proximity of the monolayer to the surface is directly influenced by the length of the polymer. More details and comparisons are provided in Table, 5.1 and in Fig. 5.13. For comparing the extent of interfacial accumulation of AuNPs, we define electron surface-excess, ρ_{2D}, as

the integration of $\rho(z)$ across the z direction, after subtracting off the ED of water (Equation 5.1). In general, ρ_{2D} increases with increasing ion concentration and is higher for PEG2k-AuNPs than that for PEG5k-AuNPs, consistent with the shorter inter-particle distances in PEG2k-AuNP crystals.

Table 5.1. Summary of GI-SAXS and X-ray reflectivity results for PEG5k-AuNPs and PEG2k-AuNPs with different electrolytes (PAA, HCl, NaOH and H_2SO_4). Q_1 and FWHM are the position and the full width at half maximum of the primary peak in GI-SAXS curves. c is the concentration of the electrolyte, Q_1 is the position of the primary peak in GI-SAXS curves, a_L is the lattice constant of the hexagonal lattice, $a_L = \frac{4\pi}{\sqrt{3}Q_1}$, FWHM is the full-width at half-maximum of the primary peak in GI-SAXS curves, Q_1/FWHM is proportional to the number pf unit cells in a crystallite, and ρ_{2D} is the electron surface-excess, obtained by integrating the electron density with height according to Equation 5.1. Values in the parenthesis indicate the error on the last significant digit.

Electrolyte	c (mM)	Q_1 (Å^{-1})	a_L (nm)	FWHM (Å^{-1}) $\times 10^2$	Q_1/FWHM	ρ_{2D} ($e\text{Å}^{-2}$)
		PEG5k-AuNP				
None	0	-	-	-	-	-
NaCl	500	0.0203(1)	35.7(1)	0.10(1)	20(2)	0.54
HCl	0.1	-	-	-	-	4.52
HCl	1	0.0215(1)	33.7(2)	0.10(3)	21(6)	14.03
HCl	10	0.0215(1)	33.7(2)	0.10(2)	23(6)	13.92
H_2SO_4	0.05	-	-	-	-	4.71
H_2SO_4	0.5	0.0218(1)	33.3(2)	0.10(2)	30(9)	14.39
H_2SO_4	5	0.0220(1)	33.0(2)	0.10(2)	18(3)	14.72
NaOH	0.1	-	-	-	-	3.13
NaOH	1	0.0183(1)	39.6(2)	0.30(4)	5(1)	15.78
NaOH	10	0.0198(1)	36.6(2)	0.10(1)	17(2)	17.61
		PEG2k-AuNP				
None	0	-	-	-	-	-
NaCl	500	0.0365(1)	19.8(1)	0.10(1)	37(4)	0.87
HCl	0.1	-	-	-	-	2.70
HCl	1	0.0359(1)	20.2(1)	0.12(1)	32(4)	31.76
HCl	10	0.0382(1)	19.0(1)	0.11(1)	35(4)	37.00
H_2SO_4	0.05	-	-	-	-	-
H_2SO_4	0.5	0.0345(1)	21.0(1)	0.19(1)	19(1)	28.31
H_2SO_4	5	0.0368(1)	19.7(1)	0.12(2)	31(4)	35.04
NaOH	0.1	-	-	-	-	3.41
NaOH	1	0.027(4)	26.9(4)	1.3(4)	2(1)	14.25
NaOH	10	0.0352(1)	20.6(1)	0.11(1)	32(3)	30.84

In summary, all the tested electrolytes (strong/weak, acidic/basic/neutral) cause interfacial assembly of PEG-AuNPs in a concentration dependent fashion, as schematically depicted in Figure 5.4. The assemblies are formed in the presence of sufficient concentration of ions, irrespective of the solution pH. Previous studies have hypothesized that the ion induced assembly of PEG-

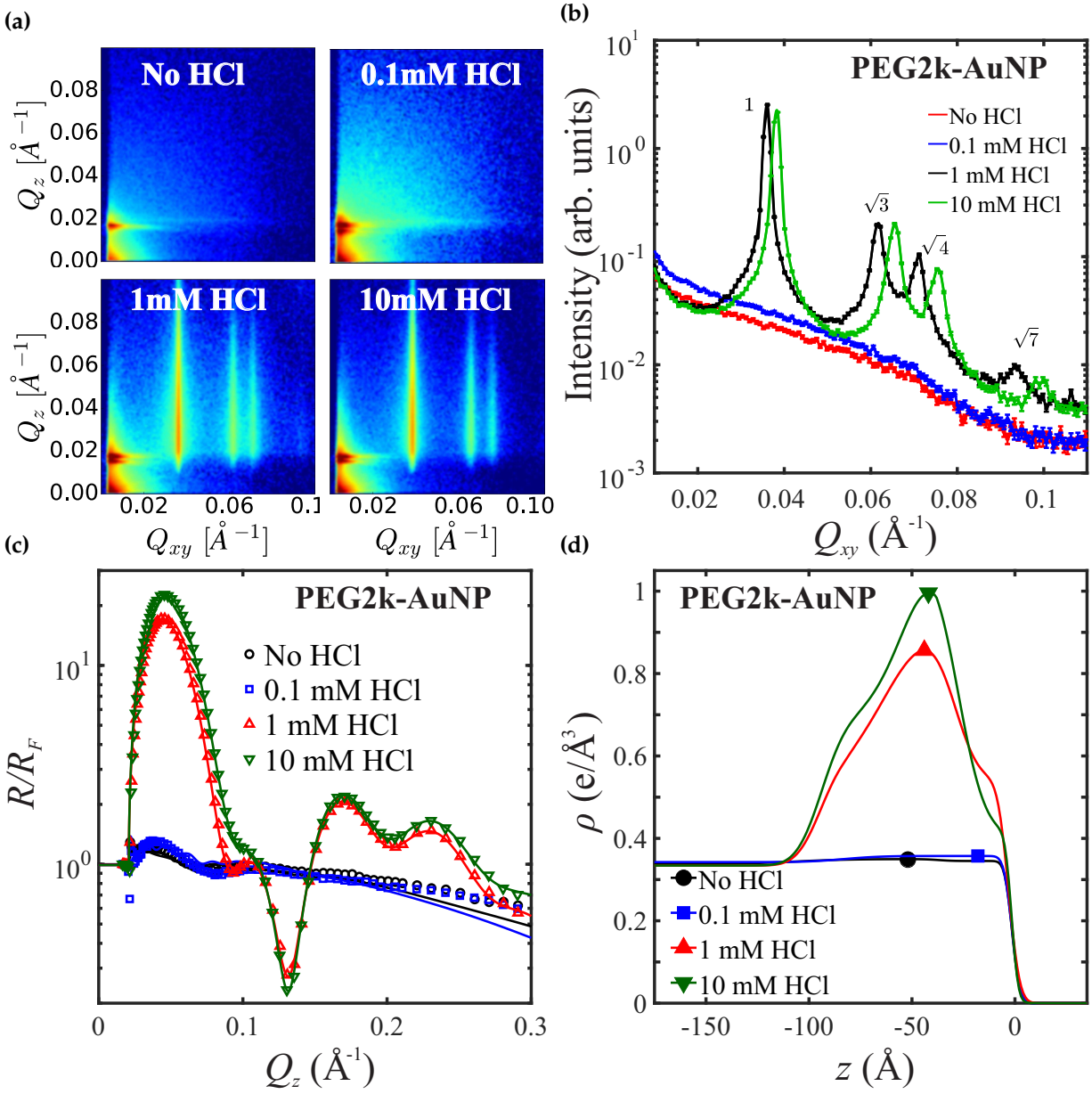

Figure 5.3. GI-SAXS and X-ray reflectivity results for PEG2k-AuNPs with increasing concentrations of HCl. Details of the various figures (a)-(d) are similar to those provided for Fig. 5.2. Note that inter-particle spacing in the lattice decreases for the PEG-2k compared to the PEG-5k shown in Fig 5.2. Also, the electron density for the PEG2k-AuNPs shown (d) is larger than that for PEG5k-AuNPs as the density of AuNPs is higher.

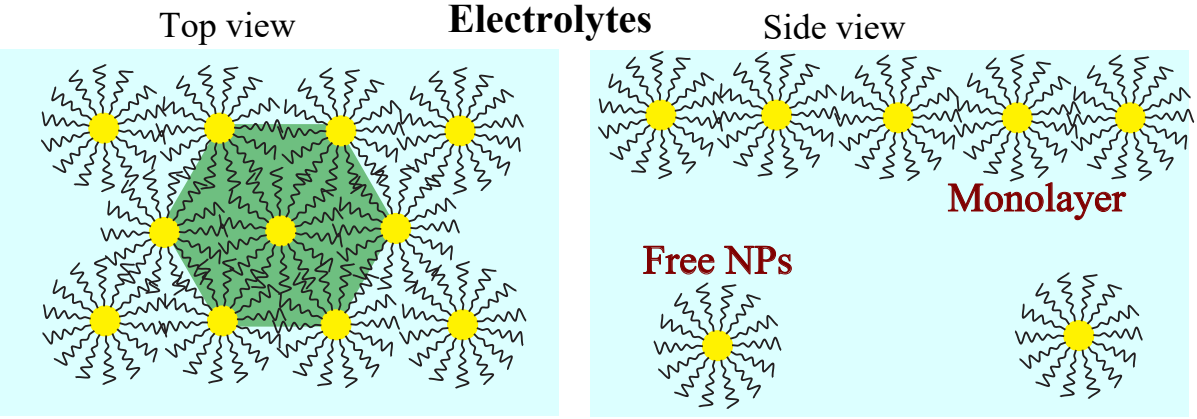

Figure 5.4. Schematic representation of the effect of electrolytes on the assembly of PEG-AuNPs at the vapor-liquid interface and in bulk. In electrolytic conditions, a monolayer of PEG-AuNPs with hexagonal in-plane structure forms at the interface without particle aggregation in the bulk. This phenomena is observed in the presence of ions despite the solution pH being acidic, basic or neutral.

AuNPs is driven by the reduction in interfacial tension "experienced" by PEG at the air-water interface as opposed to that in bulk electrolyte solution.[12] Furthermore, it has been demonstrated that the ion specificity (which follows the Hofmeister series in anions) of the lattice parameters is correlated with the specific ion effect on the bulk viscosity of electrolyte solutions via the Jones-Dole viscosity B coefficient (JDC).[14] In fact, air-water interfacial adsorption of ions and hence the interfacial tension have been found to be strongly correlated with JDC.[22] Namely, an ion with positive JDC (kosmotrope) is repelled from the interface and thus leads to increase in interfacial tension, whereas the increase is positively correlated with the magnitude of JDC. Ions with negative JDC are found to adsorb to the air-water interface. However, for H^+ ions, which adsorb to the interface, JDC is positive,[23] and this correlation between interfacial and bulk properties appears to break down. Under the assumption that the effect of ions on air-water interface is qualitatively similar to that on the PEG-water interface, we expect JDC to be well correlated with ion-induced assembly of PEG-AuNPs. Thus, the formation of 2D assemblies with HCl is particularly interesting as both H^+ and Cl^- are expected to adsorb to the interface (JDC for Cl^- is just below zero, indicating weak interfacial adsorption) i.e., act as chaotropes and not cause the dehydration of PEG chains. In fact, the effect of acids on PEG corona is still debated. For example, in the case of Pluronic block copolymers, which are analogous to spherical NPs with PEG corona, SANS results

show no significant dehydration of PEG corona ("salting out"), even at high HCl concentrations.[24] In addition, DSC and FTIR of the same polymer shows an increase in Critical Micellization Temperature (CMT) with the addition of HCl.[24,25] This increase in CMT was attributed to the enhanced interactions between the ether groups and water,[25] and it is consistent with the expected chaotrope nature of HCl. Our results however indicate the kosmotropic/"salting out" effect of HCl. Other ions that we studied (Na^+, SO_4^{2-} and OH^-) have positive JDC and show behavior consistent with kosmotropes, having positive JDC ("salting out").

5.3.2 Effect of PAA on PEG-AuNPs

The effect of PAA, a weak polyelectrolyte, on the assembly of PEG-AuNPs is shown in Fig. 7.3 and Table 5.2. At 0.001 mM of PAA, GI-SAXS results shows a broad shoulder at 0.012Å^{-1} indicating weak correlations among the NPs. As the concentration of PAA in the suspension increases, the in-plane order of PEG5k-AuNPs increases as shown by the appearance of Bragg peaks (Fig. 5.5b). The position of the primary peak, Q_1 appears at 0.018Å^{-1} and 0.017Å^{-1} for 0.01 mM and 0.1 mM of PAA, respectively. The corresponding XRR and ED profiles show the formation of dense NP monolayer at the interface with increasing PAA concentration in the suspension (Fig. 5.5c and 5.5d). There is significant rearrangement of the NPs at the interface as the PAA concentration is increased from 0.01mM to 0.1 mM, as evidenced by the interference in the diffraction pattern. At 1 mM of PAA, the interference in the diffraction pattern appears to deteriorate. For 0.1 and 1 mM of PAA, the GI-SAXS curve is a combination of form factor and structure factor, and the higher order peaks are not well defined, indicating poor crystallinity. Although PAA can bring nanoparticles to the surface to a somewhat comparable degree ($\rho_{max} \approx 0.45\ e/^3$) as HCl, the in-plane structure is not as well ordered ($FWHM^{(1\ 0)} = 0.01\text{Å}^{-1}$). We note that PAA is a weak electrolyte and is partially ionized in water, leading to a drop in pH of the suspension. At 1 mM of PAA, the pH is nearly 3, making it similar to 1 mM of HCl in terms of proton concentration. However, the crystal quality is significantly better with 1 mM of HCl than that with 1 mM of PAA indicating the adverse effect of polyelectrolytic nature of PAA. Table. 5.2 shows the results from GI-SAXS and XRR data for different PAA concentrations. Due to the polymeric nature of PAA, it is not clear

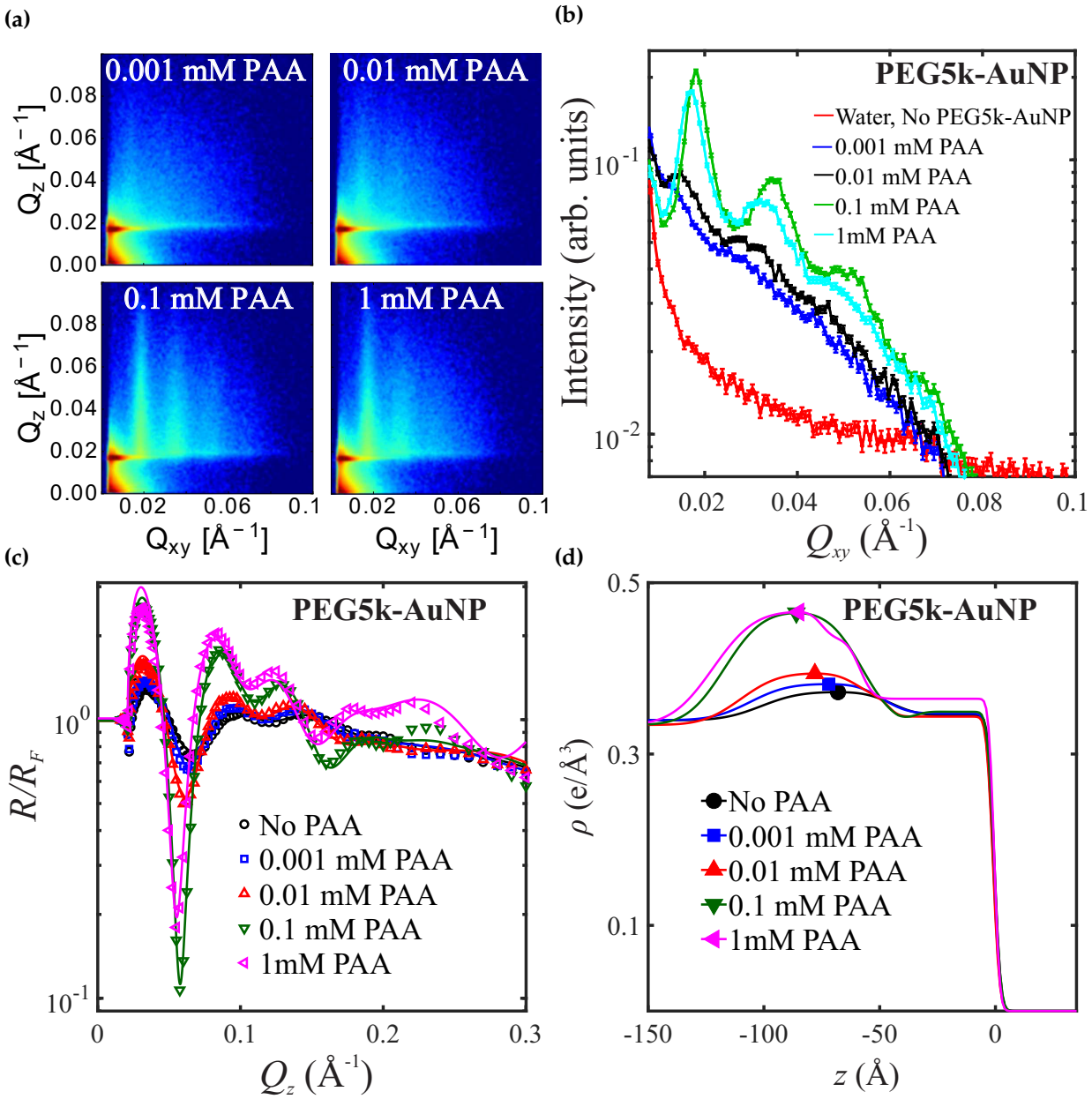

Figure 5.5. Poly(acrylic acid) (PAA) also induces the formation of a monolayer of PEG-AuNPs at the interface. (a) GI-SAXS pattern show the evolution of 2D structure with increasing PAA concentration. (b) Line-cuts from (a) - Peaks can be indexed to a 2D hexagonal structure. (c) Oscillations in normalized reflectivity (colored markers) show the presence of a layered structure at the interface. Results from fits to a monolayer structure of PEG-AuNPs is shown as colored solid lines. (d) Electron density fits obtained from X-ray reflectivity data. The film thickness is commensurate with the core size of PEG-AuNPs.

whether the JDC concept can be extended to the PAA case. Considering PAA to be a collection of propionic acid molecules, the interfacial assembly is consistent with the positive JDC of propionic acid anion.[23] Interestingly, in the presence of PAA GI-SAXS results show poorer crystallinity for PEG2k-AuNPs compared to PEG5k-AuNPs (Fig. 5.14).

Table 5.2. Summary of GI-SAXS and X-ray reflectivity results for PEG5k-AuNPs with PAA. Symbols have the same meaning as defined in Table. 5.1

Electrolyte	c (mM)	Q_1 (Å^{-1})	a_L (nm)	FWHM (Å^{-1}) $\times 10^2$	Q_1/FWHM	ρ_{2D} ($e\text{Å}^{-2}$)
		PEG5k-AuNP				
PAA	0.001	-	-	-	-	3.79
PAA	0.01	-	-	-	-	3.86
PAA	0.1	0.0181(1)	40(2)	0.6(1)	2.9(6)	8.30
PAA	1	0.0171(1)	42(3)	0.7(2)	2.3(6)	9.56
		PEG2k-AuNP				
PAA	0.001	-	-	-	-	3.43
PAA	0.01	-	-	-	-	2.95
PAA	0.1	0.025(2)	29.0(2)	2.1(6)	1.2(3)	10.33
PAA	1	0.0264(3)	28(3)	1.9(6)	1.4(4)	15.81

5.3.2.1 Effect of neutral PAA (inter-polymer complexation)

To test the effect of formation of IPCs via the hydrogen bonds on the 2D assembly of PEG-AuNPs, we systematically vary the concentration of HCl in the suspension so that PAA is increasingly becoming charge neutral. For each PAA concentration, we add HCl serially to the sample to obtain different sample conditions (fresh NPs are used for each level of PAA). The results are shown in Figure 5.6, 5.15, 5.16, and Table 5.3. In all the tested conditions, whenever a crystalline structure is observed, the lattice is found to be hexagonal and is also one NP thick monolayer. So, for brevity, we show the variation of fit parameters namely, the lattice constant of the hexagonal lattice, FWHM from the primary GI-SAXS peak, and ρ_{2D} from ED fits to XRR data in Figure 5.7. As shown in Figure 5.7a, at all PAA concentrations, the lattice constant is observed to show a decreasing trend with increasing [HCl]. As [HCl] is increased, at a given [PAA], the formation of IPCs is enhanced due to higher protonation of PAA. In fact, the critical pH below which stable IPCs are formed is ~ 3 for PEG-PAA IPCs.[26] Further, the formation of IPCs increases the hydrophobic in-

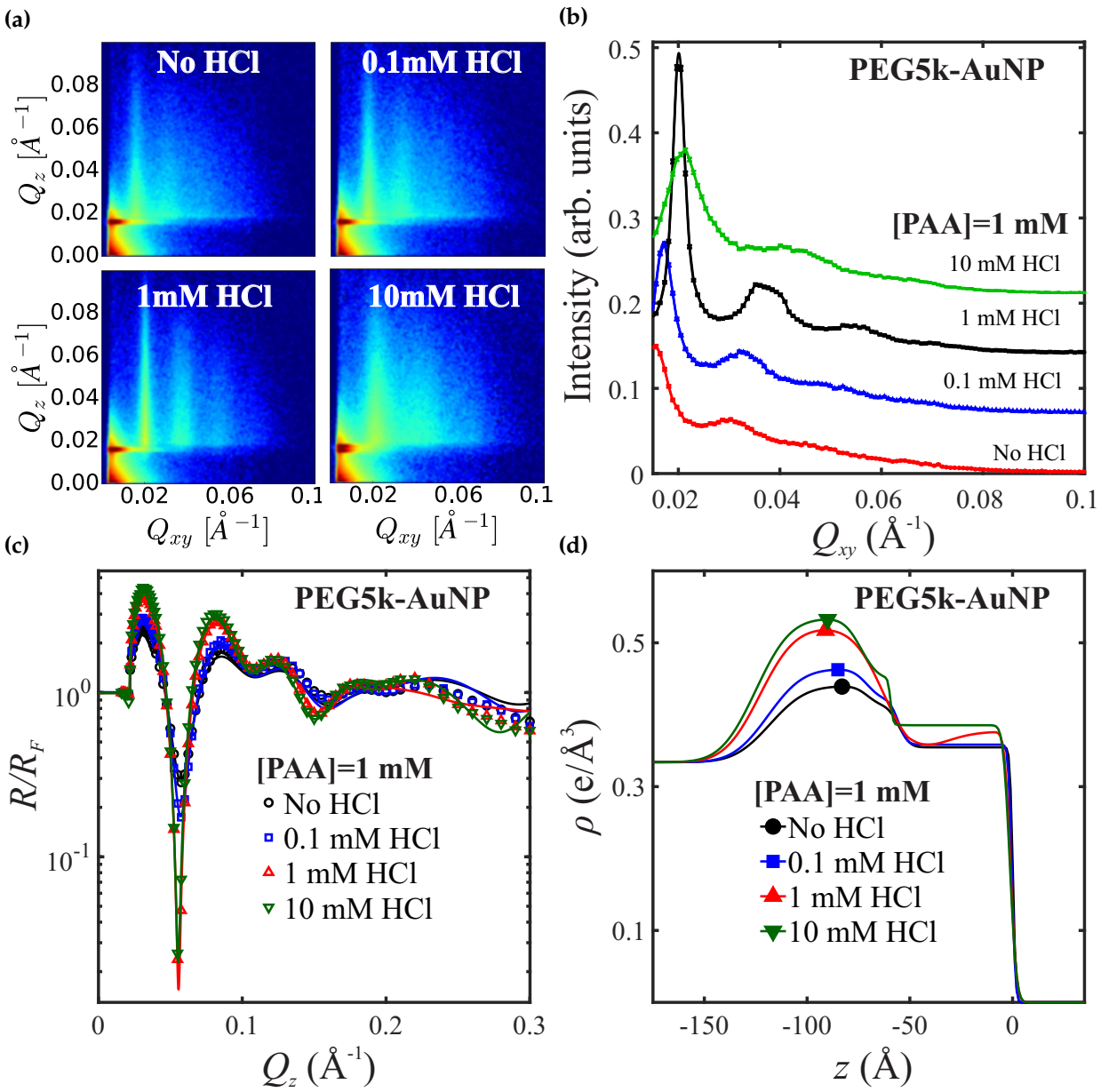

Figure 5.6. GI-SAXS and X-ray reflectivity results for PEG5k-AuNPs with 1mM PAA and increasing concentrations of HCl. Details of (a)-(d) are similar to those provided for Fig. 7.3. Note that the crystallinity improves with the increase of HCl up to 1 mM and deteriorates for higher HCl concentrations as precipitates are formed after a long incubation time.

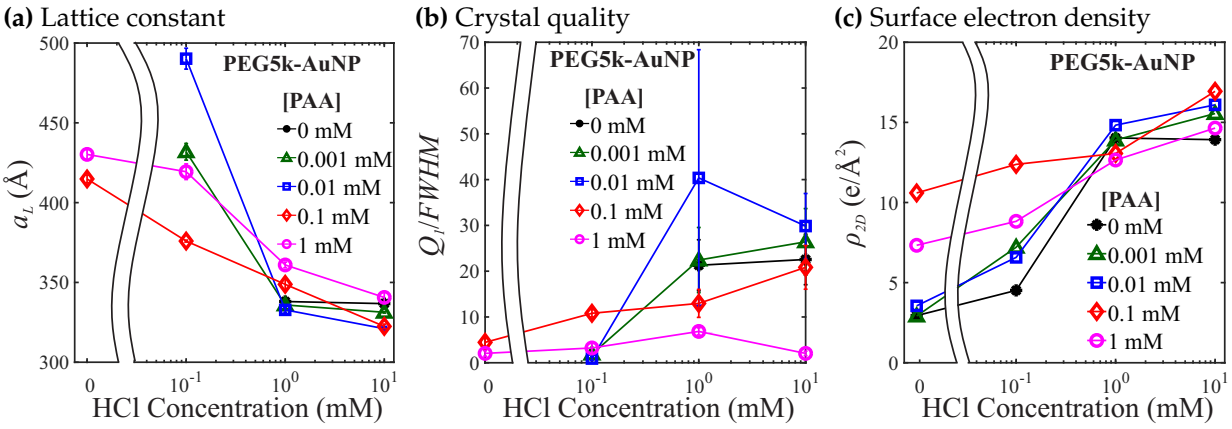

Figure 5.7. Parameters obtained from fits to GI-SAXS and X-ray reflectivity data for assemblies of PEG-AuNPs in the presence of PAA and HCl. (a) Lattice constant ($a_L = 4\pi/\sqrt{3}Q_1$) of the assemblies shows a decreasing trend with increasing [HCl] at all [PAA], consistent with the increasing hydrophobicity of the formed IPCs. (b) Crystal quality of the assemblies as measured by the ratio of position of the primary GI-SAXS peak to its full width at half maximum (FWHM). This ratio is proportional to the number of unit cells in a crystallite. In general crystal quality increases with [HCl] consistent with increasing ion concentration in the suspension. At 1mM of PAA however, best crystals are formed at 1 mM rather than 10 mM of HCl. (c) Surface electron density (ρ_{2D}) increases with [HCl], but decreases with increasing [PAA]. In all the three figures error-bars represent 95% confidence intervals.

teractions[27] which could cause contraction of PEG chains on the NPs and hence a decrease in the lattice constant. In the absence of PAA (blue circles), 0.1 mM of HCl does not show any GI-SAXS peaks, while there is no significant difference in the lattice constant of the assemblies obtained at 1 and 10 mM of HCl. Formation of 2D assemblies with PAA and 0.1 mM of HCl can be attributed to the polyelectrolyte behavior of PAA, especially at low [HCl], where in IPC formation is suppressed due to insufficient protonation. At 1 mM of PAA and 10 mM of HCl, the lattice constant is larger compared to 0.1 mM (or less) PAA and 10 mM of HCl. This is likely due to the incorporation of more and more PAA into the superlattice via the formation of IPCs.

Crystalline quality of the assemblies can be quantified by the ratio of primary peak position in GI-SAXS to its FWHM ($Q_1/FWHM$) as crystal imperfections lead to widening of the peaks. Figure 5.7b shows the variation of this ratio at different levels of PAA and HCl. At low [PAA] concentrations the crystal quality increases with [HCl], whereas at high [PAA] concentration, it decreases above 1 mM of HCl. At 1 mM of PAA, the crystal quality is significantly diminished

at 10 mM of HCl, although the monolayer is still maintained (Fig. 5.6). We hypothesize that at low [PAA] the electrolyte induced assembly is the dominating mechanism, whereas at high [PAA] and high [HCl], IPCs play a significant role in altering the assembly structures. In fact, when the sample corresponding to 1 mM PAA and 10 mM HCl is collected from the trough and left to stand for more than two days, aggregation of nanoparticles in the bulk is clearly observed. Electron surface-excess shows an increasing trend with [HCl] (Fig. 5.7c)and appears to be inversely related to the corresponding lattice constants, which is consistent with the decreasing NP density at higher inter-particle spacing.

Table 5.3. Summary of GISAXS and X-ray reflectivity results for PEG5k-AuNPs with PAA and HCl. Symbols have the same meaning as defined in Table. 5.1.

[PAA] (mM)	[HCl] (mM)	Q_1 (Å^{-1})	a_L (nm)	FWHM ($\text{Å}^{-1} \times 10^2$)	Q_1/FWHM	ρ_{2D} (e Å^{-3})
0	0	-	-	-		-
0	0.1	-	-	-	-	-
0	1	0.0215(1)	33.7(2)	0.1	21(6)	14.03
0	10	0.0215(1)	33.7(2)	0.1	23(6)	13.92
0.001	0	-	-	-	-	-
0.001	0.1	0.0168(2)	43.2(5)	0.9(3)	2(1)	7.21
0.001	1	0.0216(1)	33.6(2)	0.10(3)	22(7)	13.89
0.001	10	0.0219(1)	33.1(2)	0.10(2)	26(7)	14.78
0.01	0	-	-	-	-	-
0.01	0.1	0.0148(2)	49.0(7)	1.6(7)	1.0(4)	6.57
0.01	1	0.0218(1)	33.2(2)	0.05(3)	40(28)	14.83
0.01	10	0.0226(1)	32.1(1)	0.07(1)	30(7)	16.09
0.1	0	-	-	-	-	-
0.1	0.1	0.0193(1)	37.6(1)	0.18(1)	11(1)	12.38
0.1	1	0.0208(2)	34.9(3)	0.16(4)	13(3)	13.06
0.1	10	0.0225(1)	32.2(1)	0.11(2)	21(5)	16.94
1	0	-	-	-	-	-
1	0.1	0.0173(2)	41.9(5)	0.5(2)	3(1)	8.83
1	1	0.0201(1)	36.1(2)	0.29(3)	7(1)	12.65
1	10	0.0213(2)	34.1(3)	1.1(2)	2(1)	14.64

In order to study the effect of molecular weight of PAA, we examine the formation of assemblies with PAA of $M_n \sim 100$ kDa at 20μM, which has the same monomer concentration as 1mM of 2kDa PAA. Firstly, PAA100kDa in the absence of HCl does not lead to any ordered assembly at the

interface (Fig. 5.17). Further, PAA100kDa suppresses the lateral ordering of PEG5k-AuNPs in the presence of 1 and 10 mM HCl. XRR results and the corresponding ED fits show that addition of HCl to PEG5k-AuNPs in the presence of PAA100kDa does not lead to population of the interface by the NPs until [HCl] is 10 mM. At 10mM of HCl and 20 μM PAA100kDa the maxima of the ED is slightly lower compared to the corresponding value for 10 mM HCl alone, and 10 mM HCl and 1mM PAA2kDa. These results show that longer PAA lengths have an adverse effect on both the formation of the monolayer and the 2D order in the formed monolayers. IPCs are formed more readily with longer polymers, and the critical pH required for the formation of the assemblies increases with increasing molecular weight of the polymers.[19,26]

In summary, conditions that favor the formation of IPCs (high concentrations of HCl and PAA) cause compaction of the 2D lattice with apparent deterioration in crystal quality and slow aggregation in bulk as depicted in Figure. 5.8. We propose that at low [HCl], the mixture of PAA and HCl mainly show electrolytic behavior and hence electrolyte induced assembly is observed. This explains the improvement in crystal quality obtained at 1 mM of HCl. At high [HCl] however, the IPC formation is favored as the PAA is mostly in protonated state. These assembly features are shown in schematic (Fig. 5.4) and qualitatively in the phase diagram (Fig. 5.9). The reduction in crystal quality at high pH suggests that the mechanism through which IPC-mediated 3D assemblies form is different from the electrolyte induced 2D assembly. Superficially, both the phenomena are expected to cause dehydration of PEG-AuNPs, and hence form assemblies due to hydrophobic effect and van der Waal's (vdW) forces. However, as our results show, there are differences in assembly due to ions and due to IPCs and thus the exact mechanisms through which the assemblies form need further research.

5.4 Conclusions

Here, we have expanded the library of electrolytes that induce 2D interfacial assembly of PEG-AuNPs to include strong acids and bases, and also a weak polyelectrolyte. Similar to salts, HCl, H_2SO_4 and NaOH induce the formation of a monolayer of PEG-AuNPs with hexagonal in-plain order. Poly(acrylic acid), a weak polyelectrolyte also induces 2D assembly, although the in-plane

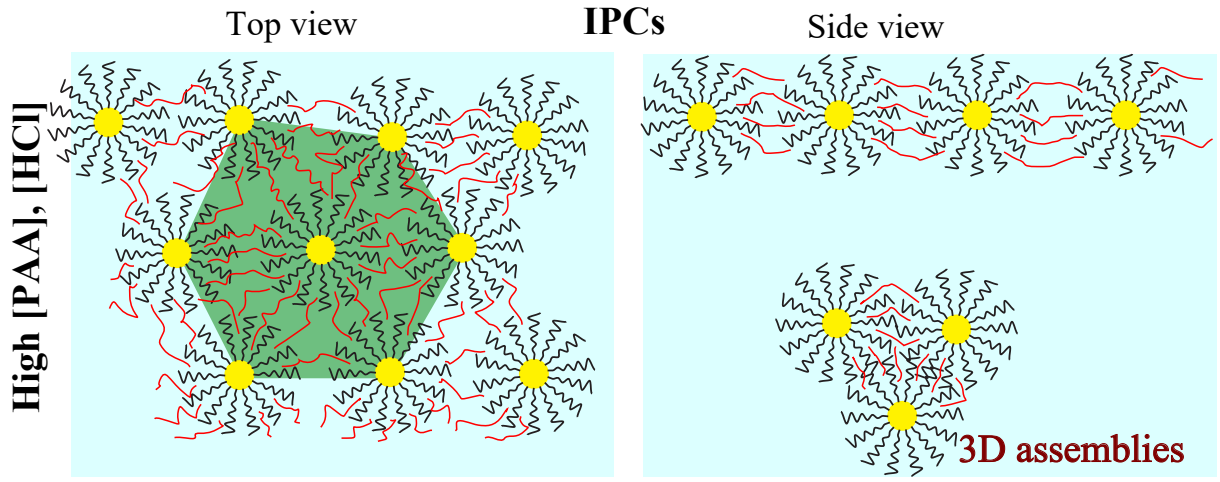

Figure 5.8. Schematic representation of the effect of PAA and HCl on the assembly of PEG-AuNPs at the vapor-liquid interface and in bulk. In interpolymer complexation (IPC) favoring conditions (high [PAA] and high [HCl]), aggregation is observed in the bulk, indicating the initiation of 3D assembly. The structure at the interface appears to deteriorate when IPCs are formed.

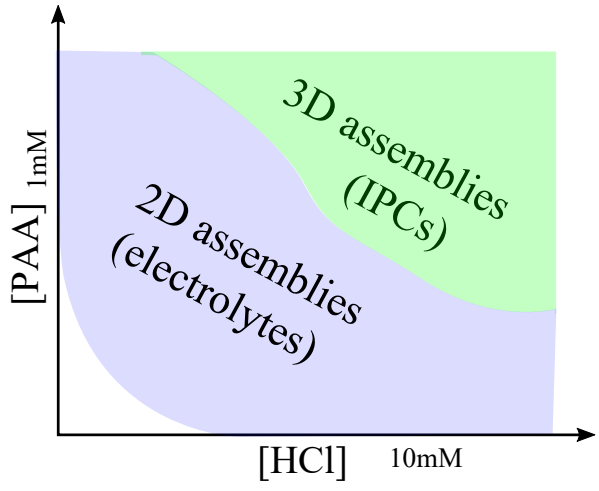

Figure 5.9. Qualitative phase diagram depicting the effect of PAA and HCl on the assembly of PEG-AuNPs.

order in the assemblies is poor compared to that obtained with strong electrolytes. These results show that the presence of ions in a sufficient concentration leads to the formation of a crystalline monolayer of PEG-AuNPs at the vapor-liquid interface, irrespective of the solution pH. In the presence of both PAA and HCl, conditions that favor the formation of IPCs lead to deterioration in the crystal quality. Thus, there are different assembly mechanisms at play with ion-induced interfacial assembly and IPC-mediated assembly. This behavior of PEG-AuNPs is analogous to those shown by DNA functionalized AuNPs.[11] With non-base pairing ssDNA, AuNPs show salt responsive formation of interfacial assemblies. When the ssDNA chains have a sticky end so that they can hybridize, interfacial assembly appears to deteriorate concurrent with aggregation of AuNPs in the bulk.[11] Thus, by this analogy, IPC mediated assembly is a potential path for 3D assembly of nanoparticles.

5.5 Acknowledgement

Research was supported by the U.S. Department of Energy (U.S. DOE), Office of Basic Energy Sciences, Division of Materials Sciences and Engineering. Ames Laboratory is operated for the U.S. DOE by Iowa State University under Contract No. DE-AC02-07CH11358. Use of the Advanced Photon Source, an Office of Science User Facility operated for the U.S. Department of Energy (DOE) Office of Science by Argonne National Laboratory, was supported by the U.S. DOE under Contract No. DE-AC02-06CH11357. NSF's ChemMatCARS Sector 15 is principally supported by the Divisions of Chemistry (CHE) and Materials Research (DMR), National Science Foundation, under grant number NSF/CHE-1346572.

5.6 Supporting Information

5.6.1 Complementary experiments

Dynamic light scattering results show that the electrolytes do not affect the brush height of PEG chains (Fig. 5.10b, and Fig. 5.10c). These results are consistent with the results obtained with K_2CO_3.[12]

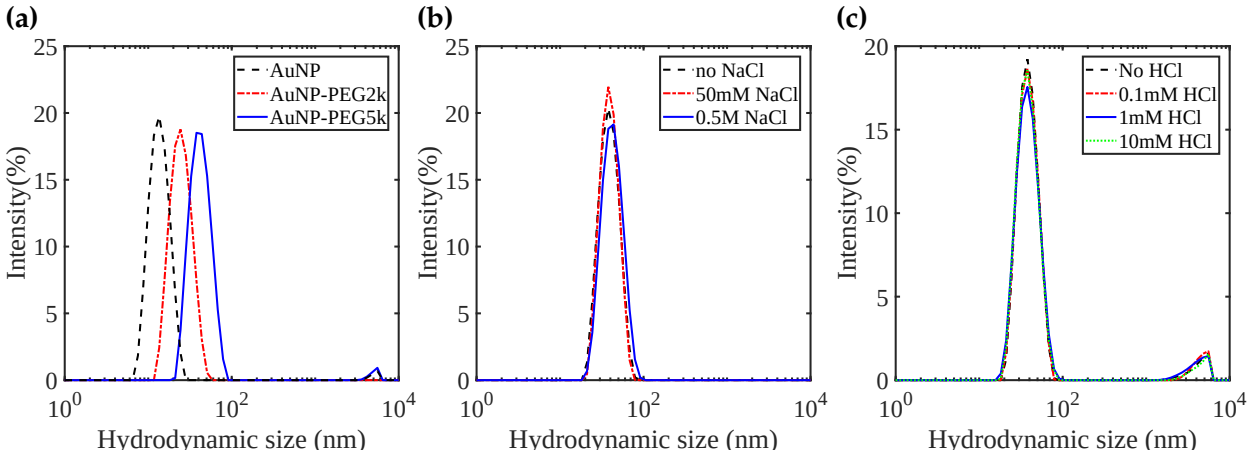

Figure 5.10. Dynamic light scattering results for (a) AuNPs functionalized with PEG5k and PEG2k, (b) PEG5k-AuNPs in the presence of NaCl, and (c) PEG5k-AuNPs in the presence of HCl. There is no apparent effect of electrolytes on the hydrodynamic size of PEG5k-AuNPs in bulk.

5.6.2 Effect of electrolytes

PEG5k-AuNPs were found to form salt-responsive, crystalline Gibbs monolayers at the vapor-liquid interface (Fig. 5.11) as reported earlier.[14] Here we find that in the presence of 0.5 M NaCl, PEG5k-AuNP shows a hexagonal lattice with a lattice constant ($a_L = 4\pi/\sqrt{3}Q^1_{xy}$) of 35.9 nm ($Q^1_{xy} = 0.02\text{Å}^{-1}$)(Fig. 5.11b). In the earlier report, hexagonal structures obtained with PEG6k-AuNP in the presence of 0.5M NaCl were found to have $a_L = 33.4 \pm 0.4$ nm.[14] This slight discrepancy in the lattice constants for PEG5k and PEG6k can be explained by the differences in PEG grafting procedures in both the studies. Differences in grafting density effects the packing behavior of NPs and hence the lattice constant. More importantly, the characteristic features of the system, mainly, the salt responsive behavior and the formation of a monolayer with hexagonal packing are maintained. In the presence of 0.5 M NaCl, PEG2k-AuNPs form a monolayer with in-plain hexagonal structure with $a_L = 19.8$ nm (Fig. 5.11b).

5.6.3 Effect of IPCs

Interestingly, in the presence of 1 μM of PAA and 0.1 mM HCl, there are some diffraction peaks which are not seen with either 1 μM of PAA or 0.1 mM HCl alone (Fig. 5.15a). The primary peak is at $\sim 0.017\text{Å}^{-1}$. With increasing HCl concentration, the GI-SAXS profiles look similar

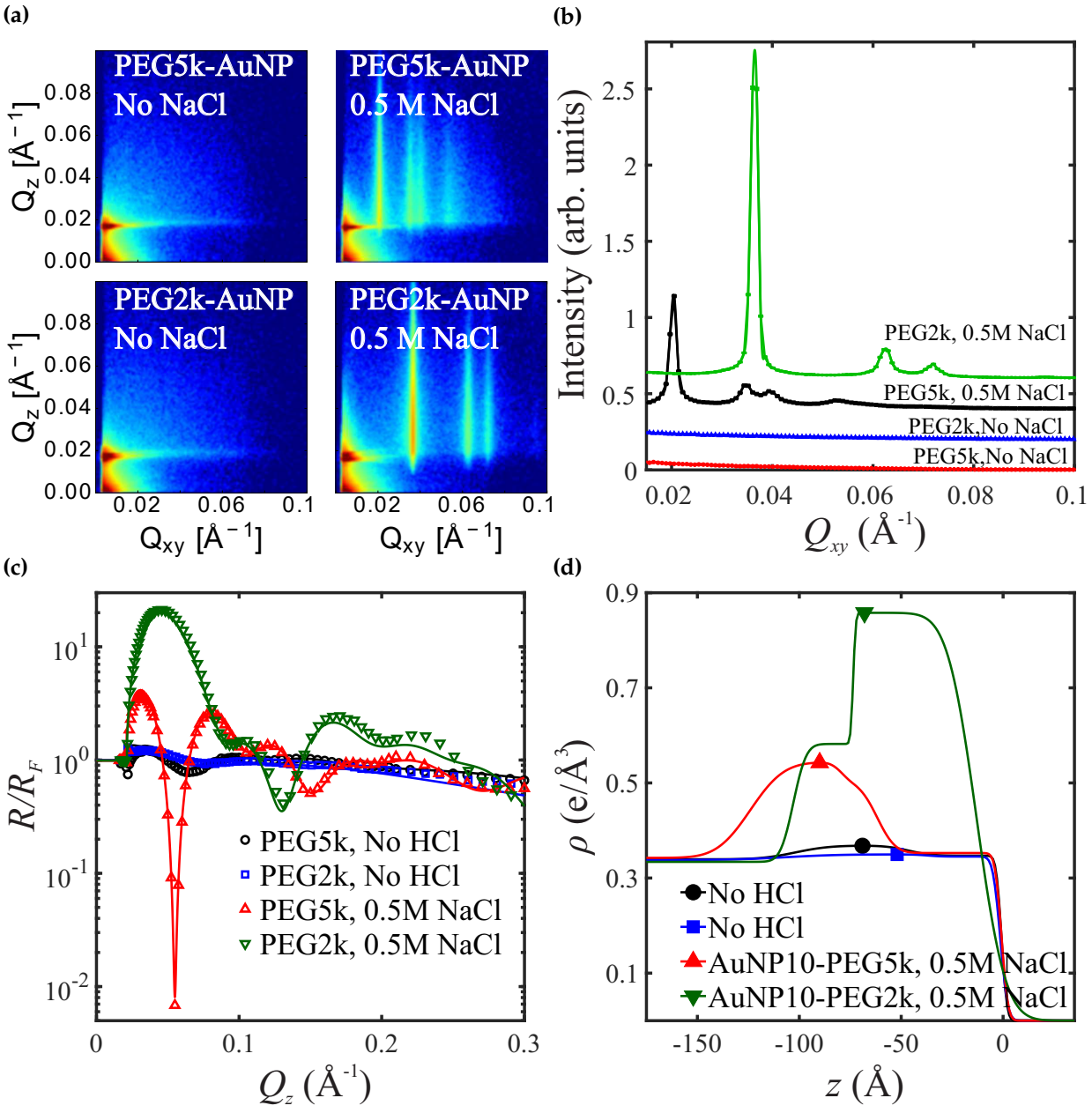

Figure 5.11. GI-SAXS and X-ray reflectivity results for PEG5k-AuNPs and PEG2k-AuNPs with and without NaCl. Both the nanoparticles show the formation of a monolayer with hexagonal order in the presence of NaCl.

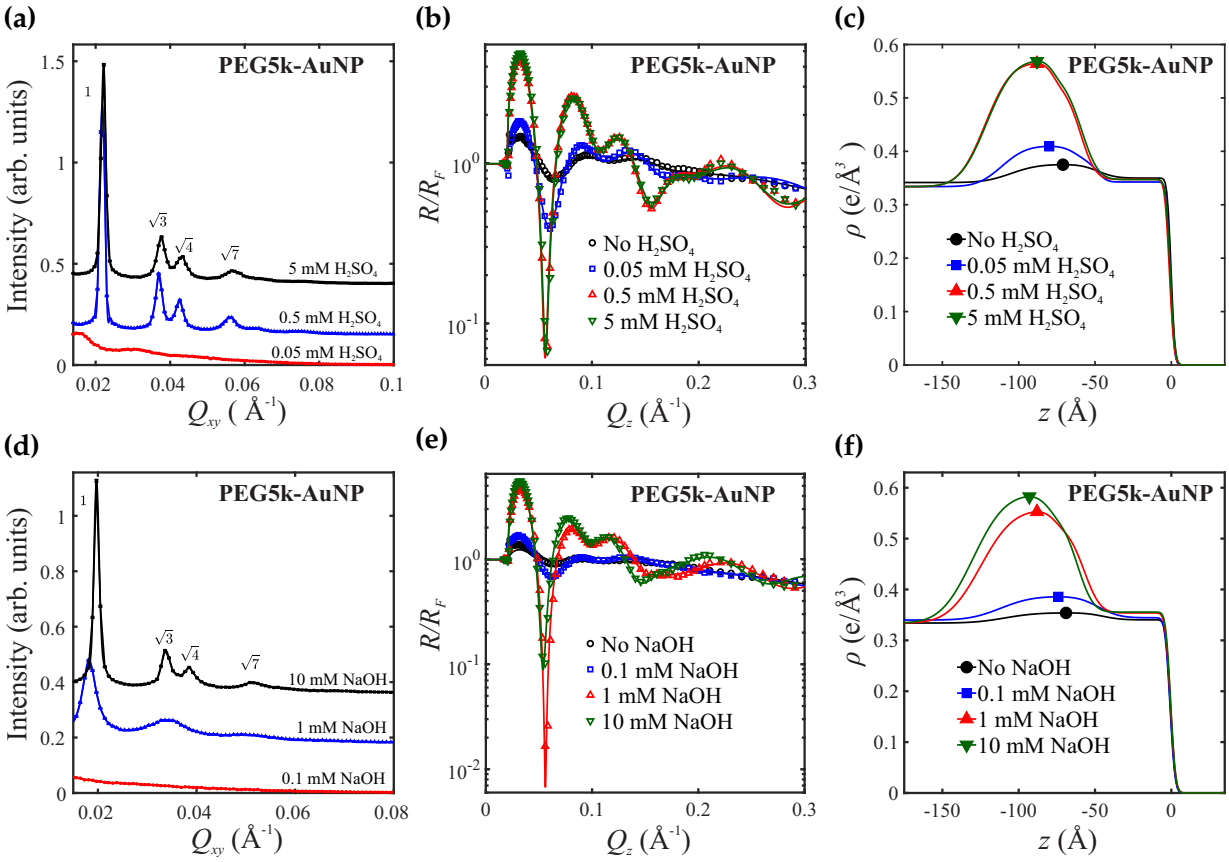

Figure 5.12. GI-SAXS and X-ray reflectivity results for PEG5k-AuNPs with increasing concentrations of H_2SO_4(a-c) and NaOH (d-f).

to ones observed at the same HCl levels, but without PAA. This indicates that the contribution of HCl dominates the assembly at $\geq$ 1 mM HCl. There is a slight shift in the primary peak position when HCl concentration is increased from 1 mM to 10 mM. Same trend is also obtained in the presence of 10 μM of PAA. At 0.1 mM of PAA interesting trends in GI-SAXS curves can be observed(Fig. 5.16a). As [HCl] is increased, the diffraction peaks appear more well defined and Q_1 progressively increases from 0.017Å^{-1} to 0.022Å^{-1}. This indicates that in the presence of 0.1mM PAA, increasing [HCl] decreases the inter-particle distance. Decreasing inter-particle distance with increasing [HCl] is consistent with the formation of IPCs which have a hydrophobic character and hence water is expelled from the lattice. Quality of the crystalline order in the assemblies as quantified by the FWHM however is maximum at the intermediate [HCl] of 1 mM.

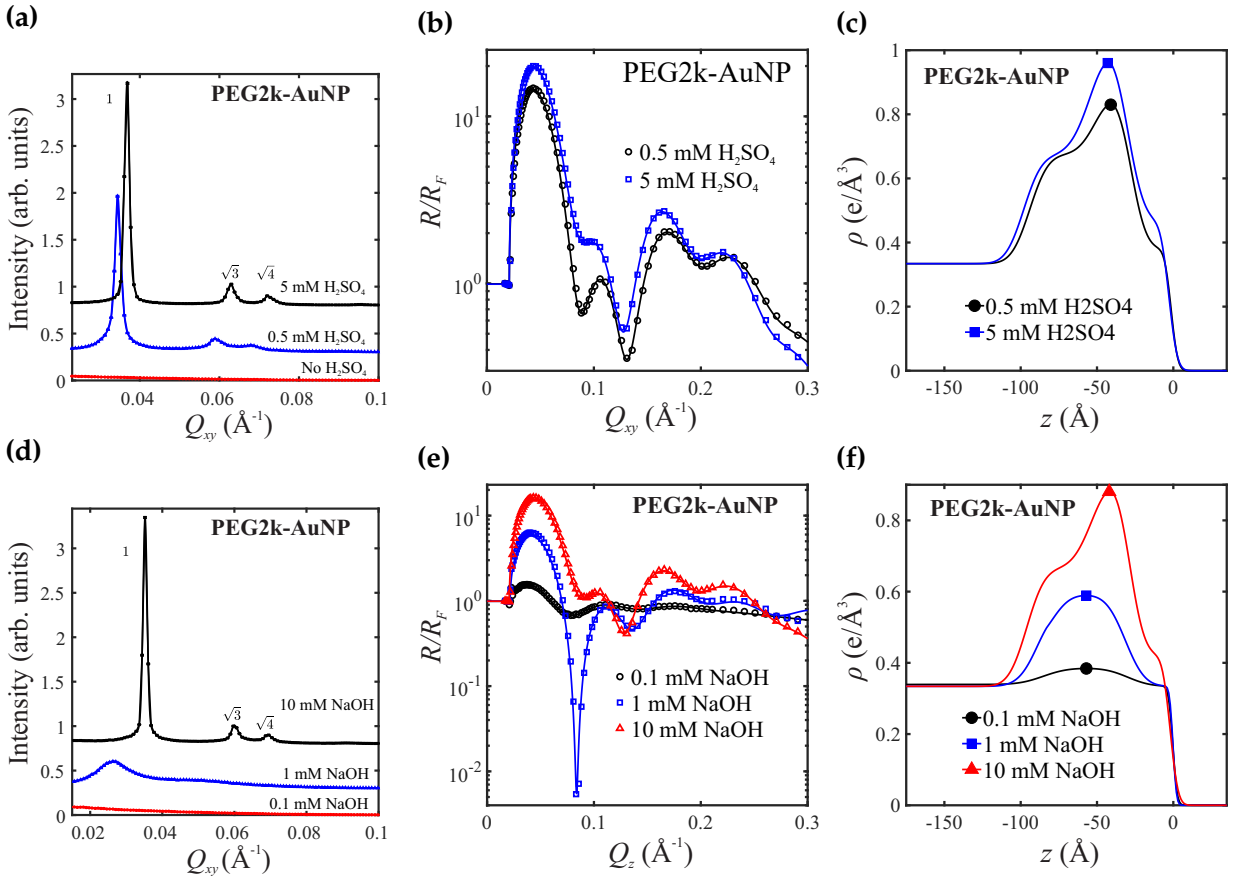

Figure 5.13. GI-SAXS and X-ray reflectivity results for PEG2k-AuNPs with increasing concentrations of H_2SO_4(a-c) and NaOH (b-d).

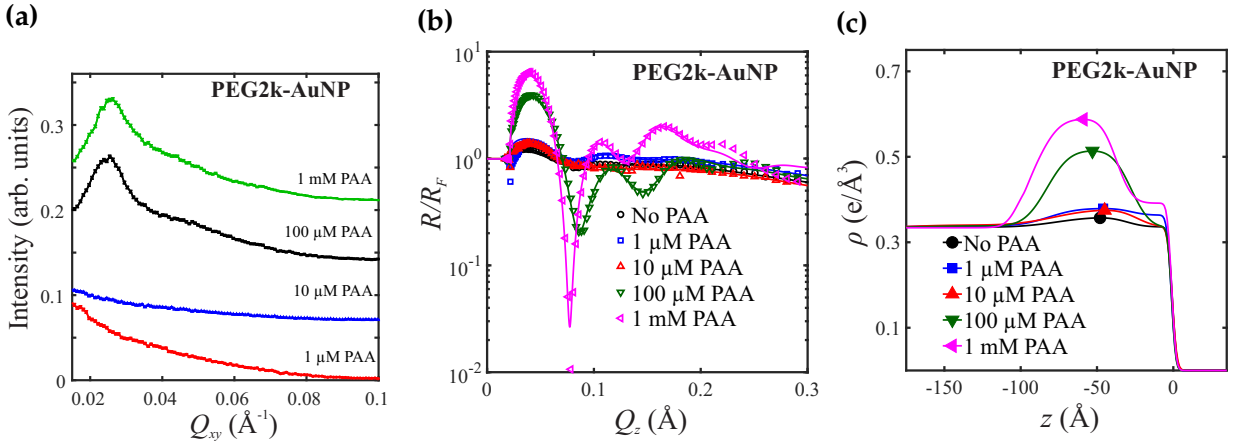

Figure 5.14. GI-SAXS and X-ray reflectivity results for PEG2k-AuNPs with increasing concentrations of PAA.

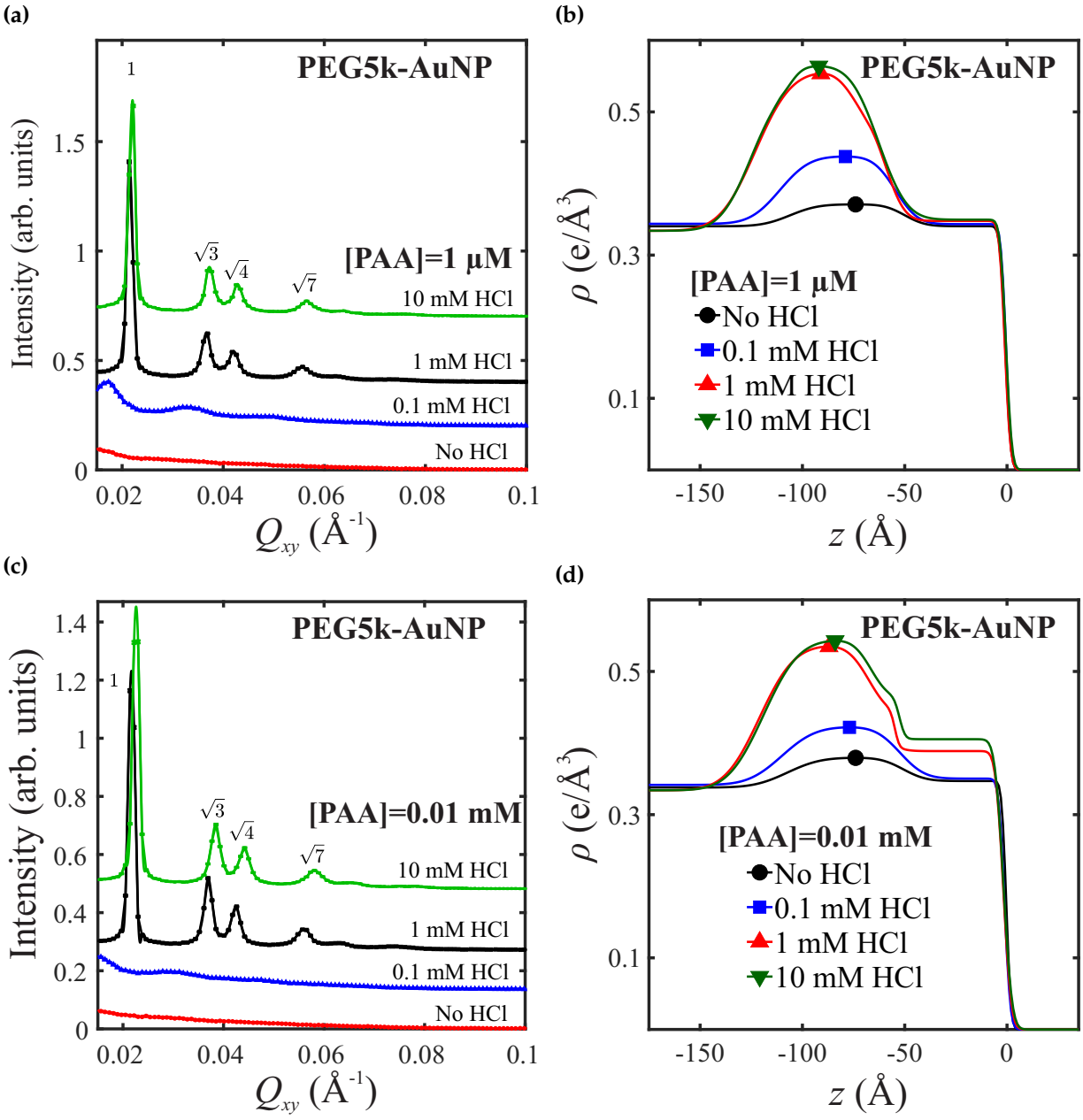

Figure 5.15. GI-SAXS (a,c) and electron density fits (b,d) for PEG5k-AuNPs with 1μ M and 0.01 mM of PAA respectively.

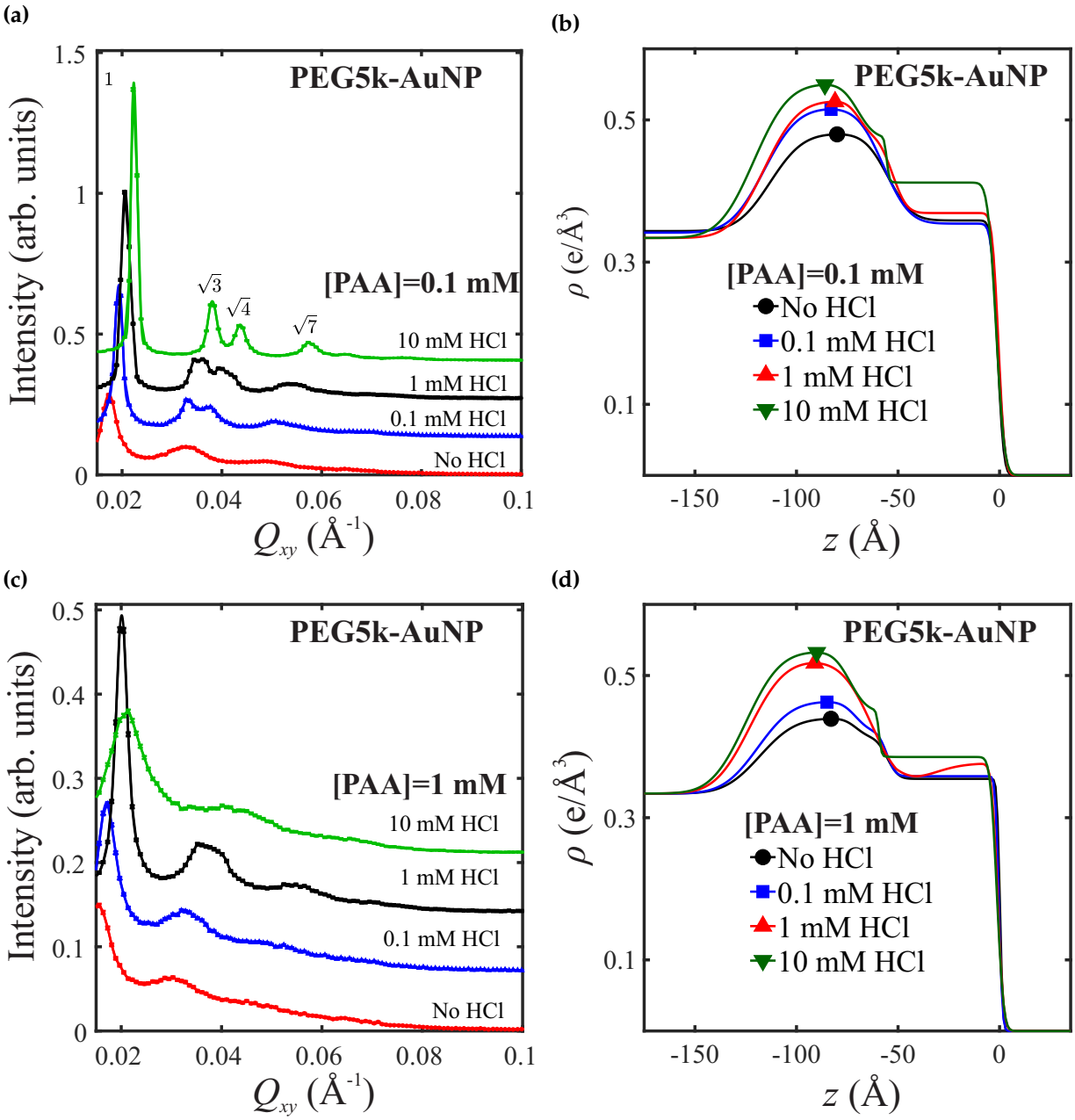

Figure 5.16. GI-SAXS (a,c) and electron density (b,d) fits for PEG5k-AuNPs with 0.1 mM and 1 mM of PAA respectively.

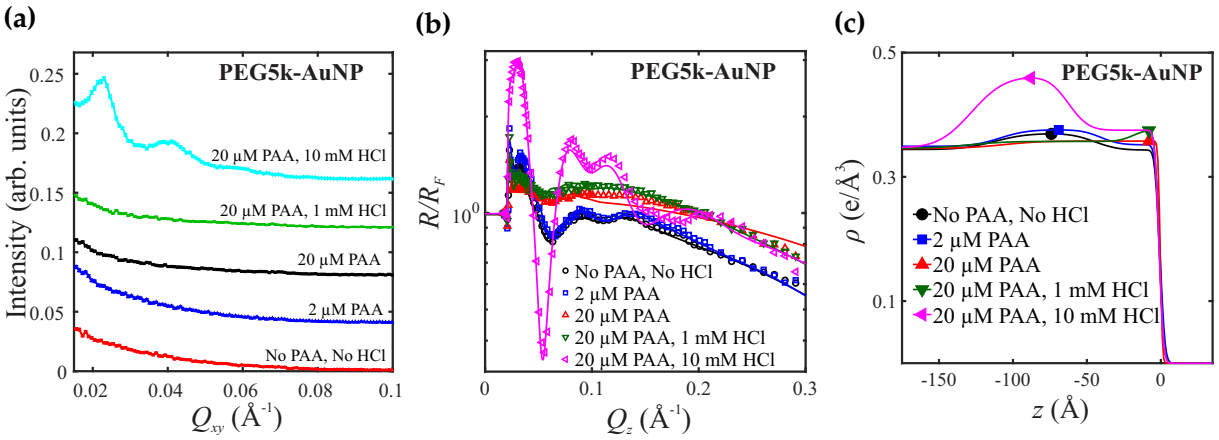

Figure 5.17. GI-SAXS (a), X-ray reflectivity (b) and electron density fits (c) for PEG5k-AuNPs with increasing concentrations of PAA100kDa.

At 1 mM of PAA, a trend similar to one with 0.1 mM PAA is observed, although the effect of IPC formation, as evidenced by the deterioration in the crystal quality are more apparent. We note that at 1 mM PAA and 10 mM HCl, 3D assemblies are observed. These results indicate that the formation of IPCs reduce the crystallinity of 2D assemblies. The corresponding ED fits obtained from the XRR data do not show any significant difference between the samples with only HCl, and samples with PAA at different concentrations and corresponding HCl concentrations. Thus, in IPC forming conditions (relatively high [HCl]), PAA seems to affect the in-plain structure of the assemblies whereas the structure in the surface normal direction (monolayer) is left intact.

References

[1] Nie, Z. H., Petukhova, A., and Kumacheva, E. *Nature Nanotechnology* **5**(1), 15–25 (2010).

[2] Talapin, D. V., Lee, J. S., Kovalenko, M. V., and Shevchenko, E. V. *Chemical Reviews* **110**(1), 389–458 (2010).

[3] Henry, C. R. *Catalysis Letters* **145**(3), 731–749 (2015).

[4] Roldughin, V. I. *Russian Chemical Reviews* **73**(2), 115–145 (2004).

[5] Sun, S. and Murray, C. B. *Journal of Applied Physics* **85**(8), 4325–4330 (1999).

[6] Dong, A., Ye, X., Chen, J., and Murray, C. B. *Nano Letters* **11**(4), 1804–1809 (2011).

[7] Srivastava, S., Nykypanchuk, D., Fukuto, M., and Gang, O. *Acs Nano* **8**(10), 9857–9866 (2014).

[8] Srivastava, S., Nykypanchuk, D., Fukuto, M., Halverson, J. D., Tkachenko, A. V., Yager, K. G., and Gang, O. *Journal of the American Chemical Society* **136**(23), 8323–8332 (2014).

[9] Srivastava, S., Fukuto, M., and Gang, O. *Soft Matter* **14**(19), 3929–3934 (2018).

[10] Tan, S. J., Kahn, J. S., Derrien, T. L., Campolongo, M. J., Zhao, M., Smilgies, D.-M., and Luo, D. *Angewandte Chemie International Edition* **53**(5), 1316–1319 (2013).

[11] Zhang, H. H., Wang, W. J., Hagen, N., Kuzmenko, I., Akinc, M., Travesset, A., Mallapragada, S., and Vaknin, D. *Advanced Materials Interfaces* **3**(16) (2016).

[12] Zhang, H., Wang, W., Mallapragada, S., Travesset, A., and Vaknin, D. *Nanoscale* **9**(1), 164–171 (2016).

[13] Wang, W., Zhang, H., Mallapragada, S., Travesset, A., and Vaknin, D. *Phys. Rev. Materials* **1**(7) (2017).

[14] Zhang, H., Wang, W., Mallapragada, S. K., Travesset, A., and Vaknin, D. *The Journal of Physical Chemistry C* (2017).

[15] Vaknin, D., Wang, W., Islam, F., and Zhang, H. *Advanced Materials Interfaces* **5**(6), 1701149 (2018).

[16] Wang, W., Lawrence, J. J., Bu, W., Zhang, H., and Vaknin, D. *Langmuir* **34**(28), 8374–8378 (2018).

[17] Zhang, H., Nayak, S., Wang, W., Mallapragada, S., and Vaknin, D. *Langmuir* (2017).

[18] Kabanov, V. A. and Papisov, I. M. *Vysokomolekulyarnye Soedineniya Seriya A* **21**(2), 243–281 (1979).

[19] Khutoryanskiy, V. V. and Staikos, G. *Hydrogen-bonded interpolymer complexes : formation, structure and applications / editors, Vitaliy V. Khutoryanskiy, Georgios Staikos*. Singapore ; Hackensack, NJ : World Scientific, Singapore ; Hackensack, NJ, (2009).

[20] Jungwirth, P. and Winter, B. *Annual Review of Physical Chemistry* **59**(1), 343–366 (2008). PMID: 18031215.

[21] Bera, M. K. and Antonio, M. R. *ChemistrySelect* **1**(10), 2107–2112 (2016).

[22] dos Santos, A. P. and Levin, Y. *Faraday Discussions* **160**(0), 75–87 (2013).

[23] Jenkins, H. D. B. and Marcus, Y. *Chemical Reviews* **95**(8), 2695–2724 (1995).

[24] Manet, S., Lecchi, A., Impéror-Clerc, M., Zholobenko, V., Durand, D., Oliveira, C. L. P., Pedersen, J. S., Grillo, I., Meneau, F., and Rochas, C. *The Journal of Physical Chemistry B* **115**(39), 11318–11329 (2011).

[25] Yang, B., Guo, C., Chen, S., Ma, J., Wang, J., Liang, X., Zheng, L., and Liu, H. *The Journal of Physical Chemistry B* **110**(46), 23068–23074 (2006).

[26] Khutoryanskiy, V. V., Dubolazov, A. V., Nurkeeva, Z. S., and Mun, G. A. *Langmuir* **20**(9), 3785–3790 (2004).

[27] Koussathana, M., Lianos, P., and Staikos, G. *Macromolecules* **30**(25), 7798–7802 (1997).

CHAPTER 6. INTERPOLYMER COMPLEXATION AS A STRATEGY FOR NANOPARTICLE ASSEMBLY AND CRYSTALLIZATION

A paper submitted to the Journal of Physical Chemistry C

Srikanth Nayak, Nathan Horst, Honghu Zhang, Wenjie Wang, Surya Mallapragada, Alex Travesset[1], and David Vaknin[2]

Abstract

Controlled self-assembly of nanoparticles into ordered structures is a major step in fabricating nanotechnology based devices. Here, we report on the self-assembly of high quality superlattices of nanoparticles in aqueous suspensions induced via interpolymer complexation. Using small angle X-ray scattering, we demonstrate that the NPs crystallize into superlattices of FCC symmetry, initially driven by hydrogen bonding and subsequently by van der Waals forces between the complexed coronas of hydrogen-bonded polymers. We show that the lattice constant and crystal quality can be tuned by polymer concentration, suspension pH and the length of polymer chains. Interpolymer complexation to assemble nanoparticles is scalable, inexpensive, versatile and general.

6.1 Introduction

Assembling nanoparticles into ordered structures is essential for applications in photonics, magnetic storage, spintronics, and other applications.[1–3] Thus, self-assembly of nanoparticles into ordered lattices (superlattices), where large scale ordered structures can be realized, has been the focus of research across multiple disciplines.[2,4] Specifically, self-assembly of metallic nanoparticles and quantum dots have been explored to obtain tunable optical properties.[5,6] A few approaches

[1]Author for correspondence
[2]Author for correspondence

to achieving ordered structures have been developed including, solvent evaporation,[1] DNA base-pairing,[7] biphasic-separation of water soluble polymers,[8,9] and covalent crosslinking with small molecules.[10] Among these, two of the illustrative approaches for 3D assembly of nanoparticles into superlattices are 1) solvent evaporation induced assembly and 2) DNA-mediated assembly. Both methods have led to the formation of exquisite superlattices by engineering the core sizes, shapes and ligand structure.[11–14] While solvent evaporation based assembly is driven mainly by ligand-entropy and van der Waals forces (vdW),[13,15] DNA-mediated assembly is driven by maximizing Watson-Crick base-pairing.[7]

Various water soluble polymers (charged or neutral) are commonly used as nanoparticle stabilizers and surface modifiers that enable tunable interactions.[16] Recently, we have shown that poly(ethylene glycol) functionalized gold nanoparticles (AuNP-PEG) dispersed in aqueous solutions can be assembled into 2D and 3D superlattices by controlling ionic strength.[8,9] Extending this approach to tune the interactions among the functionalized NPs may be achieved by introducing other polymers that can form inter-polymer complexes (IPCs). Inter-polymer complexes consist of two distinct polymers that interact by non-covalent interactions, such as hydrogen bonds, and have been studied extensively,[17] especially for pharmaceutical applications.[18]

It has been long recognized that IPCs show recognition properties similar to DNA strands.[19] There is a very large family of polymers that can form IPCs, but whether they can be used for nanoparticle superlattice engineering remains an outstanding question. Despite some efforts to leverage IPCs to assemble nanoparticles,[20,21] as per our knowledge, no examples of long-range structures have been reported. Here, we show that AuNP-PEG in the presence of poly(acrylic acid) (PAA) self-assembles into 3D superlattices (the concept is depicted in Fig. 6.1). We conduct small angle X-ray scattering (SAXS) and systematically vary the PEG chain length and nanoparticle core size.

6.2 Materials and Methods

Materials: Gold nanoparticles (AuNPs) of 5 and 10 nm nominal diameters, referred to as AuNP5 and AuNP10 respectively, were purchased from Ted Pella Inc. Poly(ethylene glycol)

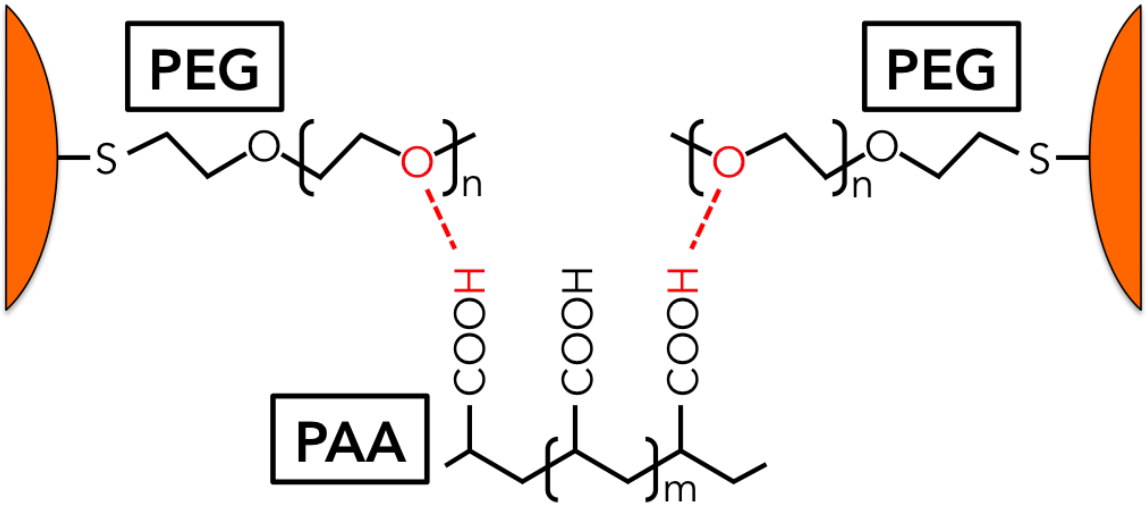

Figure 6.1. (a) Depiction of inter-polymer complexes between the end tethered PEG chains and free PAA leading to self-assembly of nanoparticles into superlattices.

methyl ether thiol (mPEG-SH) with molecular weight (M_n) of $\sim$ 800 Da and $\sim$ 2000 Da (referred to as PEG800 and PEG2000, respectively) and poly(acrylic acid), $M_n \sim$ 2000 Da, 50 wt$\%$ in water (PAA2000) were purchased from Sigma Aldrich. Poly(ethylene glycol) methyl ether thiol with M_n of $\sim$ 5000 Da (PEG5000) was purchased from CreativePEGWorks Inc.

Synthesis of assemblies Gold nanoparticles were functionalized with mPEG-SH using the ligand exchange method. Gold nanoparticles were mixed with aqueous solutions of mPEG-SH such that molar ratio of nanoparticles to mPEG-SH is 1:25000 and the mixture was incubated in dark under rotoshaking for $\sim$ 48 hours. Unbound mPEG-SH was separated by dialysis against water for 48 hours using Slide-a-lyzer dialyser cassettes (10000 MWCO). To 0.98 ml of the functionalized nanoparticles, 10 μL of PAA at appropriate concentrations were added and mixed by vortex mixing. After 1 minute of addition of PAA, 10 μL of hydrochloric acid (HCl) at appropriate concentrations were added and mixed again by vortex mixing. The solution was left to stand at room temperature for more than 3 days. The samples are labeled as AuNPx-PEGy, a mM PAA2000, b mM HCl, where x = nominal nanoparticle core diameter in nm, y = M_n of PEG, a = concentration of PAA2000, and b = concentration of HCl.

Characterization methods: Small angle X-ray scattering (SAXS) measurements of the precipitates were conducted at beamline 12-ID-B of Advanced Photon Source, Argonne National Lab-

oratory. Samples were transferred to 2mm OD quartz capillaries using glass pipettes and the measurements were done at room temperature. Measurements were made in transmission mode with photon energy, $E = 13.3$ keV ($\lambda = 0.9322$ Å) using 2D Pilatus2m detector. Scattering angle was calibrated with silver behenate powder standard.

To test the stability of the assemblies in the absence of solvent (under dry conditions), AuNP10-PEG5000, 1mM PAA2000, 10mM HCl assemblies were collected along with $\sim 100\mu$L of mother liquor and dropped on a kapton tape and left to dry for several hours. SAXS results show that the FCC structure is maintained in the dry state, albeit with a different lattice constant compared precipitates in capillaries.

UV-vis absorbance spectra of the suspensions were measured with Molecular Devices SpectraMax spectrometer, using polystyrene cuvettes. Dynamic light scattering (DLS) measurements were conducted with Malvern Zetasizer Nano-ZS90 (HeNe laser, wavelength = 633 nm, 90^o scattering angle).

6.3 Results and Discussions

We find that nanoparticle assemblies are formed by the addition of PAA and HCl to the AuNP-PEG suspensions. At varying concentrations of each constituent, color change and aggregation are visible, followed by precipitation. Samples are collected from this mixture and transferred to quartz capillaries for SAXS measurements (more details are found in the Experimental Section, and the Supporting Information). Nanoparticles are labeled as AuNPx-PEGy, where x refers to the nominal core diameter of the nanoparticle in nanometers, and y refers to the molecular weight of poly(ethylene glycol) used to functionalize the nanoparticles. Assembly conditions are indicated with the concentrations of PAA and HCl in the final solution. More details about sample preparation can be found in the Supporting Information.

SAXS characterization of the assemblies shows the emergence of crystalline structure in the assemblies that can be tuned by the length of the PEG chains. Figure 6.2(a) shows the structure factor obtained by standard data reduction of SAXS patterns (as the one shown in the inset) for

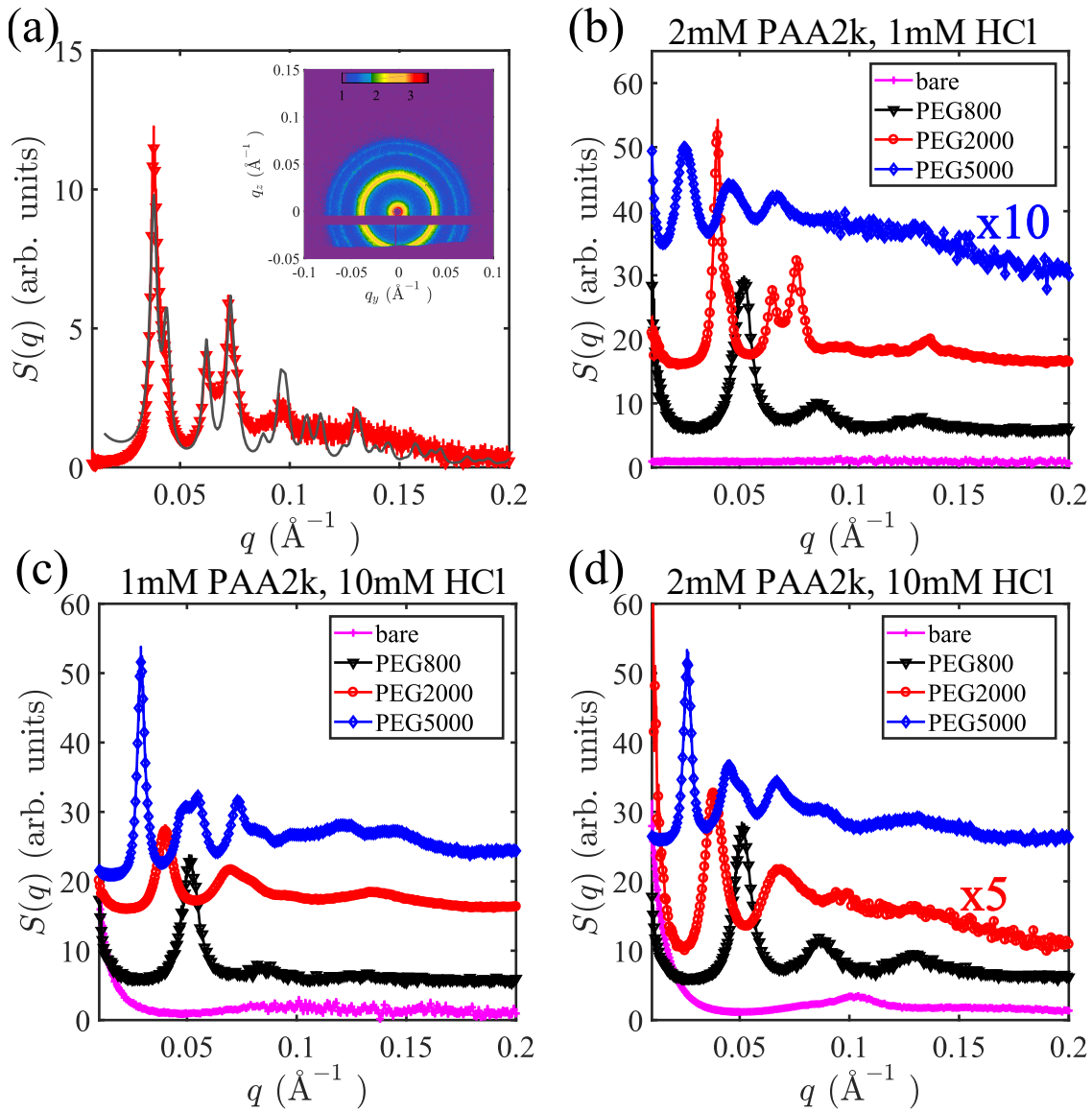

Figure 6.2. (a) Structure factor curve for AuNP10-PEG2000, 2mM PAA2000, 1mM HCl (red symbols) and the model fit (solid line) for an FCC lattice. (inset) Raw SAXS data shown here with scattering intensity shown on a logarithmic color scale. Structure factor curves obtained from the SAXS data for gold nanoparticles coated with different lengths of PEG-thiol at (b) 2mM PAA2000 and 1mM HCl, (c) 1mM PAA2000 and 10mM HCl, and (d) 2mM PAA2000 and 10mM HCl. Curves are vertically shifted for clarity. Structure factor for AuNP10-PEG2000 in (b) and AuNP10-PEG5000 in (c) are characterized as FCC, while the other diffraction profiles are consistent with FCC structure with stacking faults along the (111) planes.

assemblies formed with AuNP10-PEG2000 at 2 mM PAA and 1 mM HCl. Clear diffraction rings in the 2D pattern with distinct peaks in the structure factor emerge, indicating a crystalline structure. To analyze the diffraction pattern, we use a model structure factor[22] as used in an earlier work on

crosslinked AuNP assemblies using dithiol chains.[10] The best fit model to the diffraction pattern both in terms of peak positions and intensities is a face-centered-cubic (FCC) lattice with a primary peak at $q_0 \simeq 0.038$ Å^{-1}, and a lattice constant $a \simeq 286$ Å. The nearest neighbor (NN) distance is thus $\frac{\sqrt{6}\pi}{q_0} \simeq 203$ Å. From the full width at half maximum of the Lorentzian shaped peaks used in the fit, we obtain an average crystallite size using Scherrer equation to be ~ 2900 Å.

Assemblies are also obtained with nanoparticles functionalized with shorter PEG (PEG800) and longer PEG (PEG5000) for which the position of the primary peak (q_0) decreases with the length of the PEG chains as shown in Figure 6.2(b-d). Further, the quality of the crystal is found to depend on the concentration of PAA and HCl in the suspension. Table 6.1 shows characteristic length scales of unit cells under close to optimal crystallization conditions. A full list of conditions explored and the obtained results are presented in Table 6.3 and Table 6.4. All structure factors for PEG-AuNPs assemblies shown in Figure 2 display Bragg-like reflection peaks indicating 3D superlattice formation. By increasing PEG length alone under otherwise identical PAA and HCl concentrations, the resulting superlattice diffraction profiles become more well defined and can be clearly indexed as FCC under favorable conditions (see Fig2.(b) and (c)). In all the cases, the relative peak positions are consistent with FCC structure, although in some cases they are not very well defined indicating poor crystallinity, possibly due to stacking faults. For 10 nm nominal AuNPs the center-to-center inter-particle distance ranges from ~ 15 nm to ~ 27 nm with different PEG chain lengths.

Table 6.1. Lattice constant a, and nearest neighbor (D_n) with 95% confidence intervals, extracted from SAXS for AuNP-PEG of different PEG lengths obtained in the presence of 1 mM PAA2000 at 10 mM HCl. The hydrodynamic radius D_H obtained from DLS is obtained without PAA and HCl. The values in parentheses represent the distribution of hydrodynamic size of the grafted particles. Actual diameter of the nominal 10 and 5 nm AuNP obtained from SAXS are AuNP diameter $D = 8.8 \pm 0.8$ and 6.3 ± 0.9 nm respectively.

Nanoparticle	a (Å)	D_n (Å)	D_H (Å)
AuNP10	-	-	139(37)
AuNP10-PEG800	214 ± 1	151 ± 1	186(48)
AuNP10-PEG2000	272 ± 2	192 ± 1	249(63)
AuNP10-PEG5000	376 ± 1	266 ± 1	408(121)
AuNP5-PEG2000	225 ± 1	159 ± 1	205(35)

To gain insight into the assembly mechanism, we determine the variation of NN distances in the assembly as a function of PEG chain length experimentally and compare the results with

expected trends for vdW and hydrogen bonding dominated assemblies. For structures with local coordination larger than 6, such as FCC, the orbifold topological model (OTM)[23] predicts that the dimensionless NN distance, τ_{OPM} (D_n/D) is given by optimal packing model (OPM)[24]

$$\tau_{OPM} = (3\xi\lambda + 1)^{\frac{1}{3}}, \tag{6.1}$$

where, $\xi = \frac{A_0}{A} \approx 1$ (A_0 is the cross section of the polymer ≈ 20 Å^2 and A is actual area occupied by a bound polymer to the NP surface; $1/\xi =$ dimensionless grafting density) and $\lambda = 2L/D$ (L is the polymer contour length and D is the NP diameter). The $1/3$ exponent reflects the optimization of the packing fraction that follows from vdW attractive forces. In contrast, in DNA-mediated assembly where the structure is stabilized by hydrogen bonds, the NN distances are found to be linearly dependent on the DNA length.[25,26]

Figure 6.3 shows SAXS extracted NN-distances *versus* PEG contour-length (both normalized to the core-particle diameter) and the theoretical OTM/OPM curve (Eq. (6.1)) with no fitting parameters. The $\tau = 1+\lambda$ line refers to the NN-distance assuming the PEG chains are fully stretched and there is no overlap of PEG coronas, and hence is the maximum distance between NPs. The close match between the experimentally observed NN distances and the predictions from OTM/OPM suggests that the dominant forces in the assembly are vdW as it is found in solvent evaporated assembly.[23] In Fig. 6.3 data from assemblies obtained by solvent evaporation in polystyrene functionalized gold nanoparticles[13] also follow the OTM/OPM curve.[23] This, combined with the need for low pH for the formation of assemblies, indicate that the assembly is initially driven by hydrogen bonds, and as the aggregates become solvent free, vdW forces establish a close to optimal packing FCC structure. Our results contrast with those of DNA mediated assemblies, where NN distance is much larger than that predicted by OPM (blue line in Fig. 6.3, obtained from Hill et al.[25]) as it is known that the superlattice is swollen with more than 90% interstitial water.[12]

Our results show that the formation of ordered assemblies depends on all the tested parameters, namely, molecular weight of PEG, concentration of PAA and HCl. The critical pH, at which IPCs formed by linear chains of PAA and PEG phase separate, depends on the molecular weight and concentration of the polymers.[27] Although there are qualitative similarities in the formation of IPCs in both scenarios (i.e., with linear PAA and PEG in bulk, versus grafted PEG on NPs with

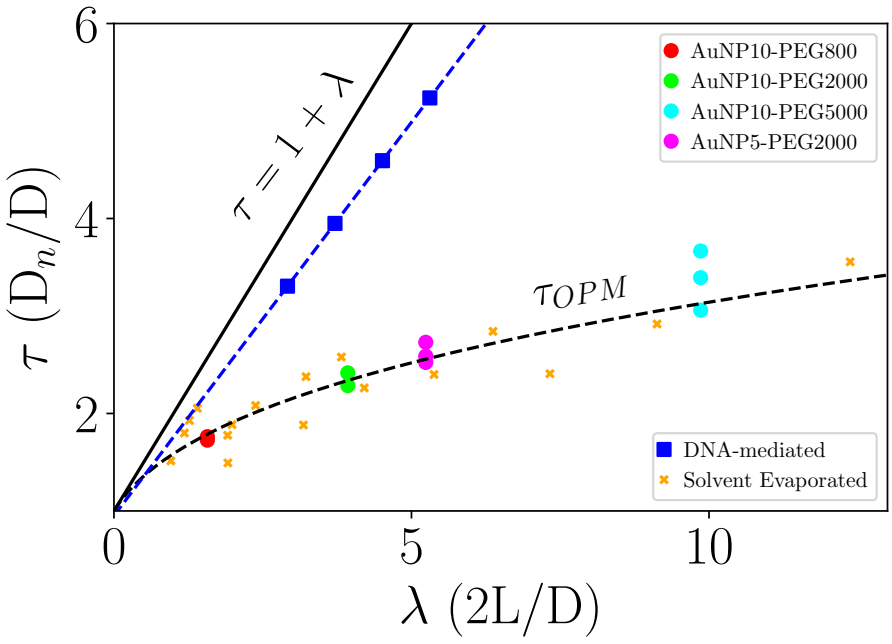

Figure 6.3. Dimensionless nearest neighbor distances (τ) plotted against dimensionless contour length of PEG (λ). We plot the result of the OTM/OPM model (Eq. 6.1) to show that our data agrees without the use of any fitting parameters. Solid black line refers to the maximum possible distance between the nanoparticles. Red, green, magenta and turquoise circles are the experimentally obtained points for AuNP10-PEG800, AuNP10-PEG2000, AuNP10-PEG5000, and AuNP5-PEG2000 respectively. The black dashed line is the prediction from OTM/OPM. The blue dashed line is the variation of NN distance with the DNA linker length in DNA-mediated assemblies, obtained by using equation (2) provided in reference.[25] The orange xs refer to the data points obtained from reference[13] for the solvent evaporation system with poly(styrene) functionalized AuNPs. Despite the fundamental role played by hydrogen bonds, the nearest neighbor distances are typical of vdW driven systems, as it is the case with superlattices obtained from solvent evaporation.

PAA) there are some notable differences. For PAA/PEG IPCs in bulk, at a fixed monomer concentration and PAA length, there is a minimum molecular weight of $\sim$ 6000Da of PEG required to form IPCs.[17,28] This dependence on molecular weight has been attributed to the higher loss of translational entropy for the shorter polymers and the co-operative behavior of hydrogen bond formation in the complexes.[29,30] In contrast, we find that assemblies are formed even with 800 Da AuNP-PEG. Although not forming superlattices, even shorter (3 or 6-mer) AuNP-oligoEG show pH-responsive assembly in the presence of PAA.[21] Further, an excess of PAA (in base-moles) is required for the formation of NP assembly (Table.6.5), as opposed to the equimolar proportions required in the formation of IPCs of PAA /PEG in bulk solution.[18]

6.4 Conclusion

In this work, we have demonstrated the formation of FCC crystals of AuNPs functionalized with PEG via interpolymer complexes with PAA. The NN distances in the superlattices primarily depend on the length/molecular-weight of PEG and hence are tunable. Further, the conditions (pH and PAA concentration) for the formation of the assemblies depend on the PEG molecular weight. Theoretical considerations of the dependence of NN distance on the PEG chain length suggest that van der Waals forces that arise due to the formation of IPCs play a significant role in the stability of the assemblies. IPCs have been shown to form with several polymers such as poly(N-isopropylacrylamide), poly(N-vinylpyrrolidone), and polysaccharides.[18] Since these polymers are commonly used in NP functionalization and stabilization, our results open a potential route for the assembly of a wide variety of NPs. These results also raise several possibilities such as obtaining binary superlattices using different cores and ligands, and using block copolymers instead of PAA homopolymers. Thus, this work brings new tools for controlling and directing the self-assembly of nanoparticles.

6.5 Acknowledgement

We thank Dr. Xiaobing Zuo for technical support with the SAXS measurements. Research was supported by the U.S. Department of Energy (U.S. DOE), Office of Basic Energy Sciences, Division of Materials Sciences and Engineering. Ames Laboratory is operated for the U.S. DOE by Iowa State University under Contract No. DE-AC02-07CH11358. Use of the Advanced Photon Source, an Office of Science User Facility operated for the U.S. DOE Office of Science by Argonne National Laboratory, was supported by the U.S. DOE under Contract No. DE-AC02-06CH11357.

6.6 Supporting information

6.6.1 Complementary experiments

We estimate the core size of the AuNPs from SAXS of the suspension. The form factor of the nanoparticles was obtained by fitting SAXS results from nanoparticle suspension to theoretical

scattering from a population of spheres with Gaussian size distribution (Figure 6.4(a))and it resulted in $R_0 \sim \mathcal{N}(42\ \text{Å}, 4.0^{2\ 2})$. We functionalized the gold nanoparticles with thiol terminated PEG using ligand exchange method and obtained the nanoparticle concentration and the hydrodynamic size using UV-vis spectroscopy (extinction at 520 nm) and dynamic light scattering respectively. The results are listed in Table.6.2. The hydrodynamic size of the AuNPs increased with increasing PEG chain length upon functionalization as shown in Figure 6.4(b)).

Table 6.2. Concentrations of nanoparticles from absorbance value at 520 nm and the hydrodynamic size for gold nanoparticles grafted with different mPEG-SH chains.

Nanoparticle	Concentration, nM	D_H, nm	PEG chain length, nm
AuNP10	9.3	13.9 ± 3.7	-
AuNP10-PEG800	6.2	18.6 ± 4.8	6.6
AuNP10-PEG2000	6.2	24.9 ± 6.3	16.5
AuNP10-PEG5000	5.8	40.8 ± 12.1	41.4
AuNP5-PEG2000	66	20.5 ± 3.5	16.5

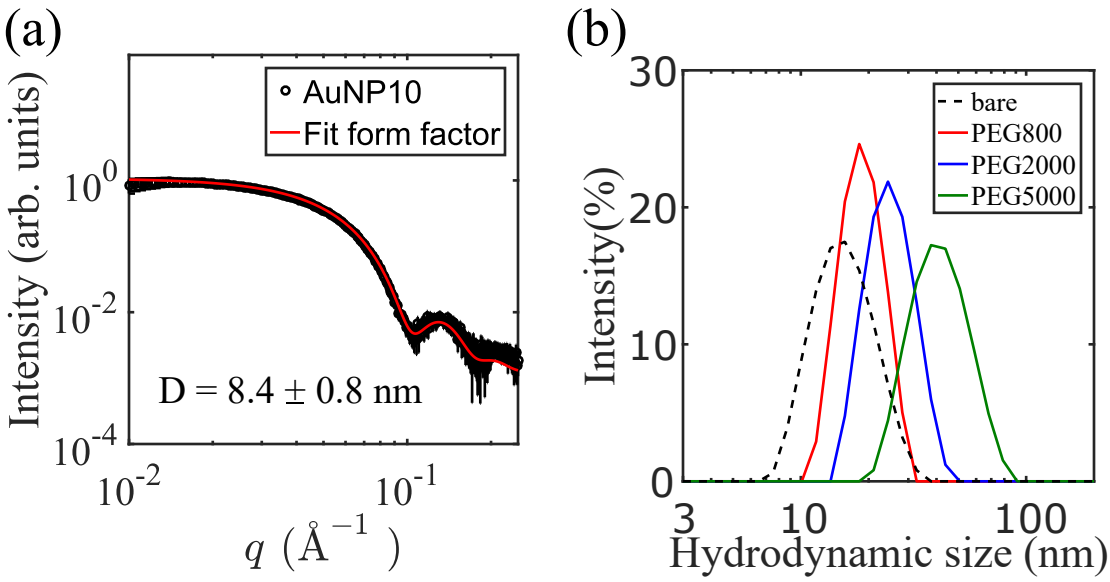

Figure 6.4. (a) SAXS results for bare AuNPs with nominal diameter of 10 nm after standard data reduction (shown in black circles with error bars) and the form factor fit (solid red line) showing a normal distribution with mean particle diameter, $D = 8.4$nm and standard deviation = 0.8 nm. For AuNPs with 5 nm nominal diameter the form factor fit results in mean diameter, $D = 6.3$nm and standard deviation of 0.9 nm.(b) Dynamic light scattering results for bare gold nanoparticles with nominal diameter of 10 nm and the same gold nanoparticles after being functionalized with PEG-thiol of Mn ∼800 Da, ∼2000 Da and ∼5000 Da.

PEG brush height on the gold nanoparticles are found by subtracting the gold nanoparticle core size from the hydrodynamic size of the functionalized nanoparticles. Figure 6.5(a) shows the

variation of brush height with number of monomers in PEG. The trend can be approximated by a scaling law with a scaling exponent of ~ 0.6, which indicates that the brushes are in semi-dilute polymer brush regime.[31]

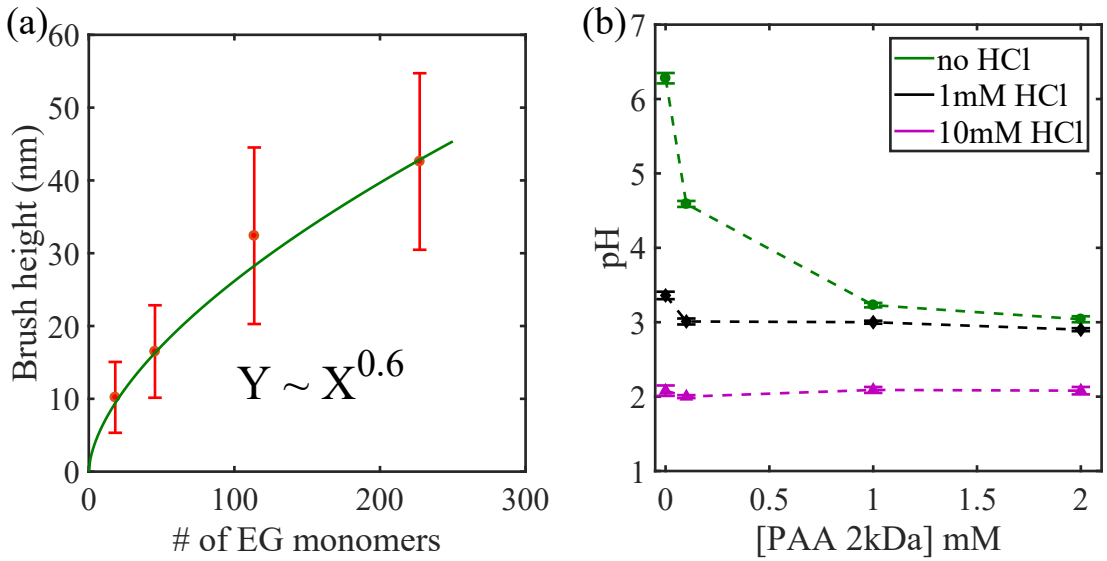

Figure 6.5. (a) Brush height of PEG chains on gold nanoparticles obtained from hydrodynamic sizes plotted against number of EG monomers in the chain (red circles with error bars). The trend (green line)shows a scaling law behavior with a scaling exponent of ~ 0.6 indicating that the brushes are in semi-dilute polymer brush (SDPB) regime. PEG10000 shown in these results were not used for the experiment. (b) pH change with increasing concentration of PAA2000 and hydrochloric acid in solution. The dashed lines are to guide the eye. It can be seen from the above plot that at high concentration of HCl, PAA does not affect the pH. Thus, in the presence of HCl, increasing the PAA concentration does not affect the degree of protonation of PAA. Measurements of pH were made in aqueous solutions without nanoparticles.

6.6.2 SAXS data reduction and summary of results

SAXS data are reduced according to techniques as shown in Figure 6.6. In the absence of PAA, addition of HCl causes precipitation of non-functionalized AuNPs, but does not affect the PEG functionalized AuNPs, indicating good colloidal stability upon PEG functionalization. (Table 6.3 and Figure 6.7) Further, the PEG functionalized AuNPs showed varying assembly behavior at different PAA and HCl concentrations.

Since the molecular area of a thiol bond on gold is $\simeq 0.25\,\mathrm{nm}^2$,[32] we estimate that the maximum number of PEG chains on 10 nm AuNPs to be ~ 900/nanoparticle and that for 5 nm AuNPs to be ~ 500/nanoparticle. Concentration of acrylic acid monomers in PAA2000 solutions is ~ 27.7

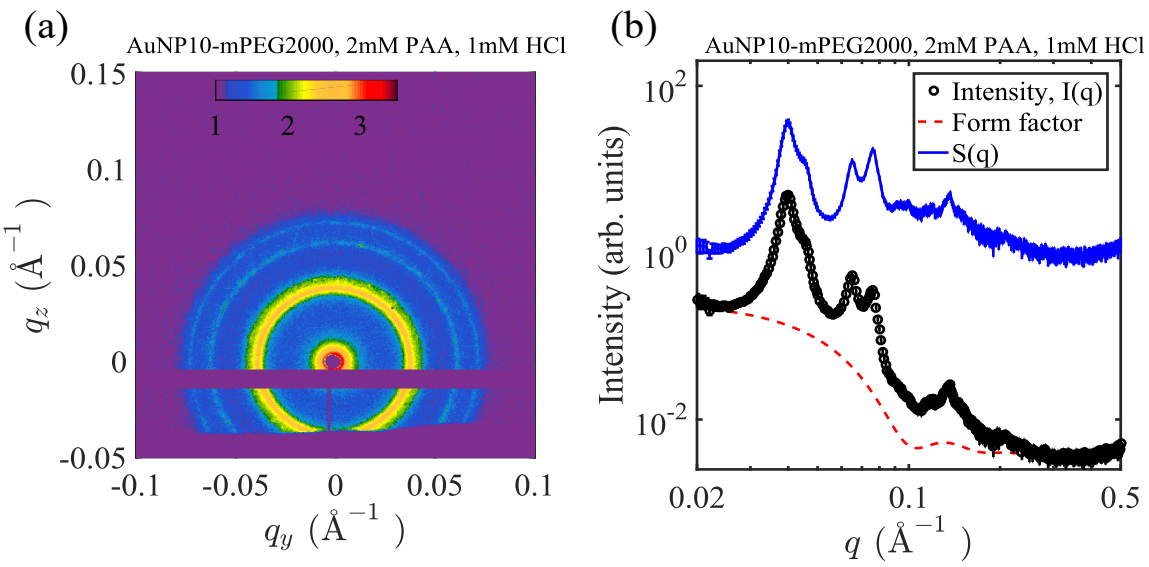

Figure 6.6. (a) Raw SAXS intensity shown on a logarithmic scale. Standard data reduction techniques to obtain 1D SAXS results were applied on this 2D data. Rings can be clearly seen showing the crystalline nature of the sample. (b) Structure factor S(q) is obtained by removing the form factor from background subtracted intensity data for a sample. Here the procedure is illustrated for sample with AuNP10-PEG2000, 2mM PAA2000 and 1mM HCl.

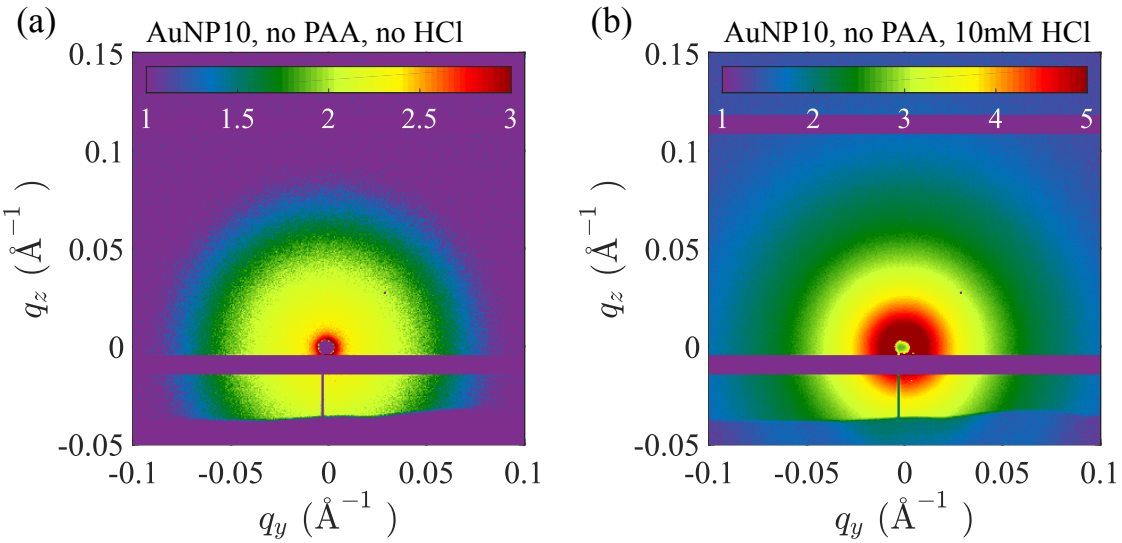

Figure 6.7. Raw SAXS intensity shown on a logarithmic scale for (a) gold nanoparticles dispersed in suspension (indicated as S in Table 6.3) and (b) amorphous aggregates (indicated as A in Table 6.3)

times the concentration of PAA2000 polymer. Table.6.5 shows the estimated ethylene glycol (EG) concentration in the nanoparticle suspensions. Given that 0.1 mM of PAA2000 (2.7mM of AA) was not sufficient in most cases for the assemblies to form, an excess of AA per EG appears necessary.

Table 6.3. Summary of results for different experimental conditions. Values in the table are the positions of the primary peak in the structure factor curves given in $Å^{-1}$ units. Letters 'A' indicates that the aggregates showed an amorphous structure while 'S' indicates that the nanoparticles did not aggregate and a stable suspension was observed.

Nanoparticle	[PAA2000] (mM)	0 M	1 mM	10 mM
AuNP10	0	S	S	A
AuNP10	0.1	S	S	A
AuNP10	1	S	S	A
AuNP10	2	S	S	A
AuNP10-PEG800	0	S	S	S
AuNP10-PEG800	0.1	S	S	0.051
AuNP10-PEG800	1	0.051	0.051	0.051
AuNP10-PEG800	2	0.051	0.051	0.051
AuNP10-PEG2000	0	S	S	S
AuNP10-PEG2000	0.1	S	S	S
AuNP10-PEG2000	1	S	S	0.04
AuNP10-PEG2000	2	S	0.038	0.038
AuNP10-PEG5000	0	S	S	S
AuNP10-PEG5000	0.1	S	S	S
AuNP10-mEG5000	1	S	S	0.029
AuNP10-PEG5000	2	S	0.027	0.026
AuNP5	1	–	–	A
AuNP5	2	–	–	A
AuNP5-PEG2000	1	S	S	0.048
AuNP5-PEG2000	2	S	0.045	0.047

6.6.3 Structure factor model

In this model, A_0 is a constant, free parameter; $\beta(q)$ corrects for particle size polydispersity and orientational disorders;[22] $G(q_{hkl})$ is the Debye Waller factor that allows for translational disorders in the lattice;[22] $Z_0(q_{hkl})$ is the structure factor for an ideal crystal; $L(q : q_{hkl}$ is the shape function (we use Lorentzian shape function) arising due to the finite size of the crystals; and D_n is the nearest neighbor distance. For model simplicity we have assumed the polydispersity of nanoparticle size to have no effect on the structure factor (β(q) = 1). Crystallite sizes (C_{FCC}) were calculated using the Scherrer equation (Eq.6.3).

Table 6.4. Summary of structure factors obtained for AuNP-PEG systems when a diffraction pattern is observed. PEG length refers to the contour length of the PEG-thiols. D_n is the nearest neighbor distance in the FCC crystal obtained from the position of the primary peak in the structure factor curve. Crystallite size is obtained from the Scherrer equation.

Nanoparticle	PAA2000 (mM)	HCl	PEG length (nm)	$D_n(nm)$	Crystallite size (nm)
AuNP10-PEG800	0.1	10	6.6	15.0	171
AuNP10-PEG800	1	0	6.6	15.1	177
AuNP10-PEG800	1	1	6.6	15.1	172
AuNP10-PEG800	1	10	6.6	15.1	172
AuNP10-PEG800	2	0	6.6	15.1	168
AuNP10-PEG800	2	1	6.6	15.1	164
AuNP10-PEG800	2	10	6.6	15.1	175
AuNP10-PEG2000	1	10	16.5	19.2	191
AuNP10-PEG2000	2	1	16.5	20.3	289
AuNP10-PEG2000	2	10	16.5	20.3	148
AuNP10-PEG5000	1	10	41.4	26.6	300
AuNP10-PEG5000	2	1	41.4	29	159
AuNP10-PEG5000	2	10	41.4	29.6	289
AuNP5-PEG2000	1	10	16.5	15.9	159
AuNP5-PEG2000	2	1	16.5	17.2	-
AuNP5-PEG2000	2	10	16.5	16.4	159

Table 6.5. Concentration of ethylene glycol (EG) in the nanoparticle assemblies estimated at highest grafting density.

Nanoparticle	[EG] estimated (mM)
AuNP10-PEG800	0.1
AuNP10-PEG2000	0.25
AuNP10-PEG5000	0.6
AuNP5-PEG2000	1.5

$$S_{Mod}(q) = A_0 \sum_{hkl} S(q : q_{hkl}) \tag{6.2a}$$

$$S(q : q_{hkl}) = 1 + G(q_{hkl}) \left[\beta(q) Z_0(q_{hkl}) L(q : q_{hkl}, \sigma) - 1\right] \tag{6.2b}$$

$$\beta(q) = 1(Assumption) \tag{6.2c}$$

$$Z_0(q_{hkl}) = \frac{m_{hkl}}{q_{hkl}^2} \tag{6.2d}$$

$$G(q) = \exp\left(-\sigma_D^2 D_n^2 q_{hkl}^2\right) \tag{6.2e}$$

$$L(q : q_{hkl}, \sigma) = \frac{\sigma}{2\pi} \frac{1}{(q - q_{hkl})^2 + (\frac{\sigma}{2})^2} \tag{6.2f}$$

And the particle size or correlation length is given by the Scherrer formula using the constant $K \approx 0.9$

$$C_{FCC} = \frac{4\pi K}{\sigma} \tag{6.3}$$

6.6.4 OTM model as applied to IPC mediated assembly

We see that in all cases, the maximum grafting density ($\xi = 1$) is the a better predictor than smaller values of ξ, which prompts us to realize the different possibilities for inter-particle linkage (IPL) as shown in Fig. 6.8.

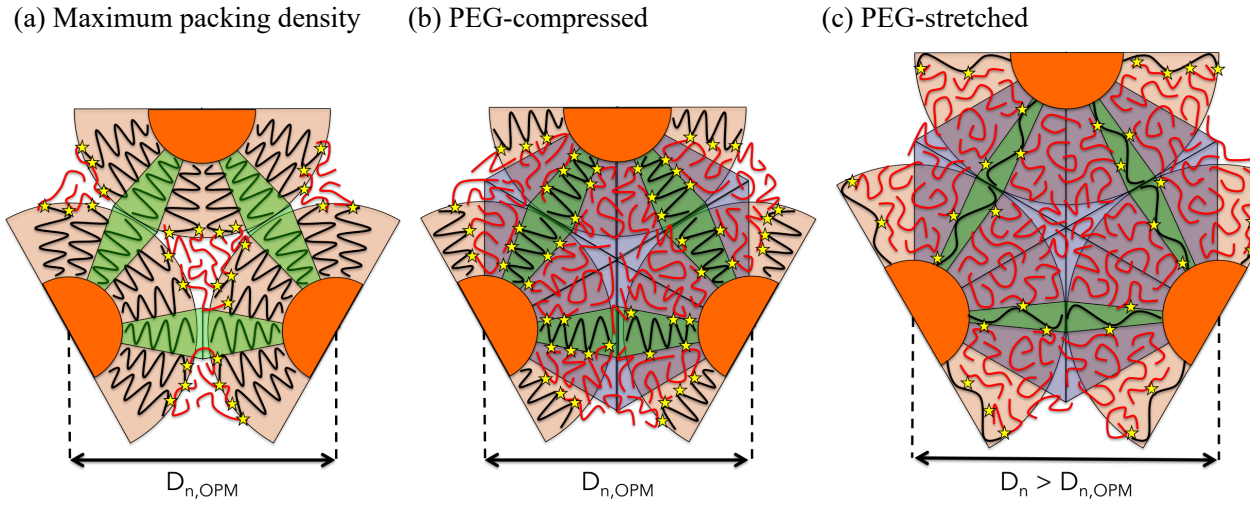

Figure 6.8. Possible mechanisms of inter-particle linkage (IPL) mediated by direct PAA bridging. The case of maximum grafting density (a) shows PAA chains forming bridges between nanoparticles, but at lower grafting densities, PAA fills unoccupied space, leading to a range of possible D_n values (b,c).

We speculate possible structure of the IPCs in the assemblies as shown in Figure.6.8. Figure.6.8(a) shows the formation of IPCs when the PEG chains are in the concentrated brush regime (maximum packing density of PEG chains on the AuNPs) where the PAA chains cannot permeate into the corona and the IPCs are at the edges of the PEG corona. When the PEG chains are less densely packed on the AuNPs, PAA chains can permeate and form IPCs within the corona (Fig.6.8(b) and (c). Since the tethered PEG chains are in SDPB regime, PAA chains can permeate the PEG corona of the nanoparticles and the PEG chains in the IPCs can be either compressed (Fig.6.8(b))or extended (Fig.6.8(c)).

References

[1] Talapin, D. V., Lee, J.-S., Kovalenko, M. V., and Shevchenko, E. V. *Chemical Reviews* **110**(1), 389–458 (2010).

[2] Boles, M. A., Engel, M., and Talapin, D. V. *Chemical Reviews* **116**(18), 11220–11289 (2016).

[3] Sun, L., Lin, H., Kohlstedt, K. L., Schatz, G. C., and Mirkin, C. A. *Proceedings of the National Academy of Sciences of the United States of America* **115**(28), 7242 (2018).

[4] Nie, Z. H., Petukhova, A., and Kumacheva, E. *Nature Nanotechnology* **5**(1), 15–25 (2010).

[5] Ross, M. B., Ku, J. C., Lee, B., Mirkin, C. A., and Schatz, G. C. *Advanced Materials* **28**, 2790–2794 (2016).

[6] Sun, L., Lin, H., Park, D. J., Bourgeois, M. R., Ross, M. B., Ku, J. C., Schatz, G. C., and Mirkin, C. A. *Nano Letters* **17**(4), 2313–2318 (2017).

[7] Macfarlane, R. J., Lee, B., Jones, M. R., Harris, N., Schatz, G. C., and Mirkin, C. A. *Science* **334**(6053), 204–208 (2011).

[8] Zhang, H., Wang, W., Mallapragada, S., Travesset, A., and Vaknin, D. *Nanoscale* **9**(1), 164–171 (2016).

[9] Zhang, H., Wang, W., Akinc, M., Mallapragada, S., Travesset, A., and Vaknin, D. *Nanoscale* **9**(25), 8710–8715 (2017).

[10] Nayak, S., Horst, N., Zhang, H., Wang, W., Mallapragada, S., Travesset, A., and Vaknin, D. *Particle & Particle Systems Characterization* **0**(0), 1800097 (2018).

[11] Park, S. Y., Lytton-Jean, A. K. R., Lee, B., Weigand, S., Schatz, G. C., and Mirkin, C. A. *Nature* **451**, 553 (2008).

[12] Nykypanchuk, D., Maye, M. M., van der Lelie, D., and Gang, O. *Nature* **451**(7178), 549–552 (2008).

[13] Ye, X. C., Zhu, C. H., Ercius, P., Raja, S. N., He, B., Jones, M. R., Hauwiller, M. R., Liu, Y., Xu, T., and Alivisatos, A. P. *Nature Communications* **6** (2015).

[14] Tian, Y., Zhang, Y., Wang, T., Xin, H., Li, H. L., and Gang, O. *Nat. Mater.* **15**(6), 654–+ (2016).

[15] Bodnarchuk, M. I., Kovalenko, M. V., Heiss, W., and Talapin, D. V. *Journal of the American Chemical Society* **132**(34), 11967–11977 (2010).

[16] Si Kae, J., Chen, Y., Shi, Q., and Cheng, W. *Advanced Science* **5**(1), 1700179 (2018).

[17] Kabanov, V. A. and Papisov, I. M. *Vysokomolekulyarnye Soedineniya Seriya A* **21**(2), 243–281 (1979).

[18] Khutoryanskiy, V. V. and Staikos, G. *Hydrogen-bonded interpolymer complexes : formation, structure and applications / editors, Vitaliy V. Khutoryanskiy, Georgios Staikos*. Singapore ; Hackensack, NJ : World Scientific, Singapore ; Hackensack, NJ, (2009).

[19] Litmanovich, A. A., Papisov, I. M., and Kabanov, V. A. *European Polymer Journal* **17**(9), 981–988 (1981).

[20] Irmukhametova, G. S., Fraser, B. J., Keddie, J. L., Mun, G. A., and Khutoryanskiy, V. V. *Langmuir* **28**(1), 299–306 (2012).

[21] Torii, Y., Sugimura, N., Mitomo, H., Niikura, K., and Ijiro, K. *Langmuir : the ACS journal of surfaces and colloids* **33**(22), 5537 (2017).

[22] Senesi, A. J. and Lee, B. *Journal of Applied Crystallography* **48**, 1172–1182 (2015).

[23] Travesset, A. *Soft Matter* **13**(1), 147–157 (2017).

[24] Landman, U. and Luedtke, W. D. *Faraday Discussions* **125**, 1–22 (2004).

[25] Hill, H. D., Macfarlane, R. J., Senesi, A. J., Lee, B., Park, S. Y., and Mirkin, C. A. *Nano Letters* **8**(8), 2341–2344 (2008).

[26] Knorowski, C., Burleigh, S., and Travesset, A. *Phys. Rev. Lett.* **106**, 215501 May (2011).

[27] Khutoryanskiy, V. V., Mun, G. A., Nurkeeva, Z. S., and Dubolazov, A. V. *Polymer International* **53**, 1382–1387 (2004).

[28] Antipina, A. D., Baranovskii, V. Y., Papisov, I. M., and Kabanov, V. A. *Polymer Science U.S.S.R.* **14**(4), 1047–1057 (1972).

[29] Pradip, Maltesh, C., Somasundaran, P., Kulkarni, R., and Gundiah, S. *Langmuir* **7**(10), 2108–2111 (1991).

[30] Hao, J., Yuan, G., He, W., Cheng, H., Han, C., and Wu, C. *Macromolecules* **43**(4), 2002–2008 (2010).

[31] Dukes, D., Li, Y., Lewis, S., Benicewicz, B., Schadler, L., and Kumar, S. K. *Macromolecules* **43**(3), 1564–1570 (2010).

[32] Love, J. C., Estroff, L. A., Kriebel, J. K., Nuzzo, R. G., and Whitesides, G. M. *Chemical Reviews* **105**(4), 1103–1170 (2005).

CHAPTER 7. CONCLUSIONS AND FUTURE WORK

7.1 Conclusions

In this work, we have demonstrated various strategies using bottom-up approaches for fabricating ordered assemblies of nanoparticles. Using bioinspired approaches, we have used natural and synthetic macromolecules as templates for the synthesis and assembly of inorganic nanoparticles. All the synthesis and assembly processes have been conducted under ambient conditions and in aqueous media, without the need for hazardous chemicals, and thus paving the way for scalable fabrication of nanoparticle assemblies. The fabricated assemblies have been characterized using standard materials characterization techniques such as atomic force microscopy, electron microscopy, and X-ray scattering analysis.

Based on the previous research showing the effect of surface hydrophobicity on the self-assembly of Mms6,[1] we devised a method to obtain arrays of magnetic nanoparticle assemblies on solid substrates. It is demonstrated that non-covalent immobilization of a biomineralization protein, Mms6, on hydrophobic surfaces can be used to create functional protein arrays. The advantage of non-covalent immobilization is in the orientation of immobilized protein on the surface that is favorable to its templating action. The immobilized protein arrays are used to template the formation of magnetic nanoparticle arrays. Thus synthesis and assembly of magnetic nanoparticles on a using a synergistic combination of self-assembly and top-down approach is demonstrated.

Thiol groups have high affinity to noble metals like gold and this has been utilized to assemble spherical clusters and multilayers of gold nanoparticles with α-ω dithiol linkers. We studied the self assembly of citrate stabilized gold nanoparticles in the presence of oligo(ethylene glycol) dithiol chains. Short (4-mer or 6-mer) dithiol chains cause quantitative precipitation of the nanoparticles with short-ranged order in the assemblies. Inter-particle distance is a function of dithiol chain length, however longer chains (more than 12-mer) show only weak inter-particle correlations, akin to dimers. Geometrical constraints and molecular dynamics simulation show the

bounds on the chain length relative to the nanoparticle diameter, and the number of connected nearest neighbors to obtain a stable lattice.

Previous research shows that poly(ethylene glycol) (PEG) functionalized nanoparticles form two and three dimensional assemblies in the presence of strong electrolytes.[2] Nanoparticles functionalized with polymers and DNA that are capable forming inter-chain hydrogen bonds also form assemblies in appropriate medium conditions.[3–5] We studied the effect of a weak polyelectrolyte, poly(acrylic acid) (PAA), on the assembly of PEG functionalized nanoparticles. A monolayer of nanoparticles with hexagonal in-plane order forms at the liquid-vapor interface at sufficiently high PAA concentrations. Further, with neutralized PAA (at low pH), the crystallinity of the 2D assemblies deteriorates with concurrent aggregation of the nanoparticles in the bulk. Surprisingly, PEG functionalized nanoparticles are found to form 2D assemblies at the liquid-vapor interface in the presence of sufficient concentration of ions, irrespective of the solution pH.

Poly(acids) such as poly(acrylic acid) form inter-polymer complexes (IPCs) with other polymers with electron-donating groups by hydrogen bonding interactions. We explored the analogy of this phenomenon to the hybridization of DNA chains, in the context of nanoparticle self-assembly. Nanoparticles functionalized with PEG form crystals with FCC structure in the presence of a high concentration of neutralized PAA (at low pH). Inter-particle distances in these assemblies follow the Optimal Packing Model (OPM), meaning that the assemblies are nearly dehydrated, resembling the assemblies obtained by solvent-evaporation. This is in contrast to the DNA-mediated assemblies where the assemblies have high water content and are unstable in dry conditions. We hypothesize that the van der Waal's forces play the dominant role in assembly stability in the IPC-mediated case.

In keeping with the objectives of this work, we have -

1. leveraged the self-assembly of a biomineralization protein on hydrophobic surfaces to obtain patterns of magnetic nanoparticles on the surface, using patterns obtained by top-down approach (soft lithography),

2. developed self-assembly procedures to obtain 2D and 3D superlattice of nanoparticles using electrolytes, inter-polymer complexation, and crosslinking dithiols, and

3. evaluated the effect of medium conditions on the structural properties of the assemblies and correlated the results with theoretical predictions.

Based on the above results, new avenues for research have been identified and preliminary studied have been conducted to test their viability as detailed below.

7.2 Future Work

7.2.1 Electrolytes and polyelectrolytes for the assembly of polymer functionalized nanoparticles

In realizing functional nanomaterials, there are several outstanding challenges with regards to their fabrication or assembly. Once the challenges of synthesizing complex shaped nanoparticles such as split-rings are overcome, self-assembly techniques developed in this dissertation can be employed obtain ordered assemblies. However, controlling the crystal dimensions (inter-particle distances) and symmetries (cubic, monoclinic etc) with arbitrary morphology of inorganic core remains to be explored. In this work we have focused on the assembly of spherical, metallic nanoparticles of 5 - 20 nm diameter into close-packed structures and these nanoparticles/assemblies do not always meet the desired criteria for functionalities.

7.2.1.1 Extension of the assembly processes to anisotropic nanoparticles

First, we discuss the possible challenges in controlling the inter-particle distances in the assemblies. Although, our major findings on the structural properties of the assemblies are in non-dimensional units, meaning that they are expected to be applicable to a range of sizes, there are other practical considerations for extending these principles. For example, with larger nanoparticle cores and longer functionalizing polymers, the polymer grafting density reduces, and thus the inter-particle distance can also be reduced. Further, for anisotropic particles like nanoprisms or discs, polymer grafting can be anisotropic due to preferential binding of the polymers to certain facets. In the case of obtaining optical metamaterials, the nanoparticles are of complex morphologies such as split rings and tuning forks, and have physical dimensions ranging from 50 - 100 nm.

Thus, future experiments will be conducted to verify the application of theoretical models such as OPM and OTM to larger and anisotropic particles such as nanoprisms. These experiments will guide the fabrication of assemblies of functional units such as metallic split-rings.

7.2.1.2 Self-assembly of binary nanoparticle superlattices via interpolymer complexation

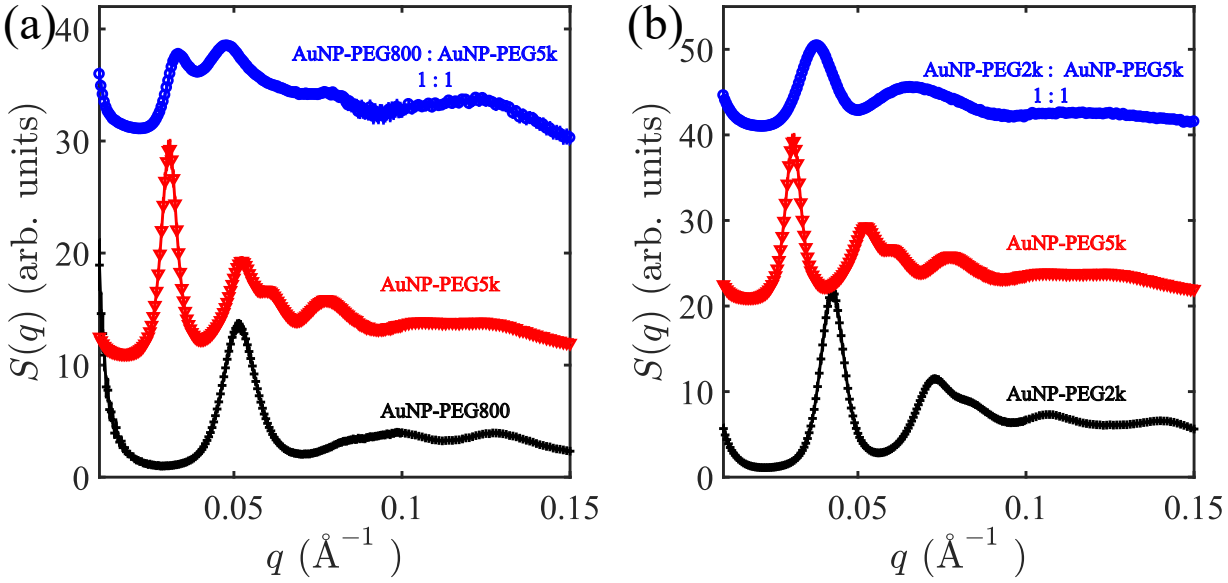

Figure 7.1. (a) Structure factor curves for assemblies obtained with 1 mM of PAA2kDa, 1 mM of HCl, and AuNP10-PEG800 (black), AuNP10-PEG5k (red), and an equimolar mixture of AuNP10-PEG800 and AuNP10-PEG5k (blue). The structure factor for the mixture appears to be a sum of structure factors obtained for pure nanoparticles, indicating the presence of two phases. (b) Structure factor curves for assemblies obtained with 1 mM of PAA2kDa, 1 mM of HCl, and AuNP10-PEG2k (black), AuNP10-PEG5k (red), and an equimolar mixture of AuNP10-PEG2k and AuNP10-PEG5k (blue). The structure factor for the mixture has a peak in between the peaks obtained for pure nanoparticles.

Crystal symmetries in nanoparticle superlattices have been controlled by co-assembling a binary mixture of nanoparticles having two different functionalizations (polymers or ligands) and/or two different core morphologies. Such superlattices are called binary nanoparticle superlattices (BNSL). Further, one of the nanoparticle cores can be a "dummy", i.e., it plays only a structural role and not a functional role. Using inter-polymer complexation as a strategy, similar BNSL can be assembled as those shown with evaporation mediated assembly, given the dominance of vdW forces in both. We have some preliminary results regarding this where gold nanoparticles functionalized with PEG chains of different lengths were mixed and allowed to assemble

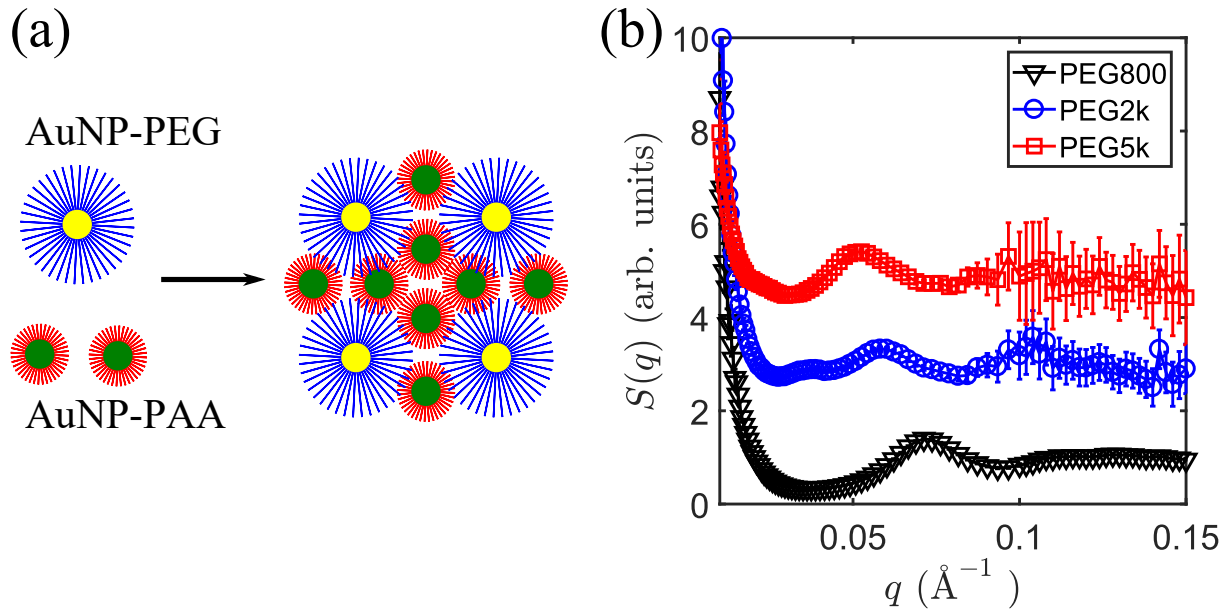

Figure 7.2. (a) Schematic showing the strategy for obtaining BNSL with PEG and PAA functionalized nanoparticles via interpolymer complexation. (b) Structure factor obtained for assemblies obtained with AuNP10-PEG with different PEG lengths and AuNP10-PAA3000 at 10 mM of HCl.

via IPCs. Structure factor obtained from SAXS for assemblies formed with an equimolar mixture of AuNP10-PEG800 and AuNP10-PEG5k, with 1 mM of PAA2k and 10 mM of HCl, are shown in Figure 7.1(a) as a blue curve. In this figure red and black curves correspond to assemblies formed separately with AuNP10-PEG800 and AuNP10-PEG5k respectively, with 1 mM of PAA2k and 10 mM of HCl. There are two prominent peaks in the blue curve which correspond well with the primary peaks observed for AuNP10-PEG800 and AuNP10-PEG5k assemblies respectively. This indicates that the sample has a mixture of two separate crystalline structures. With a mixture of AuNP10-PEG2k and AuNP10-PEG5k (Fig. 7.1(b)) however, there is a broad peak positioned in between the peaks corresponding to pure nanoparticle assemblies. While it is hard to conclude the structure of these assemblies due to lack of resolution, these results are promising towards the fabrication of BNSLs. Further tuning of the parameters to overcome possible kinetic barriers preventing the formation of large binary superlattices is needed.

Another potential route to obtain BNSL is by the co-assembly of nanoparticles functionalized with polymers that can form IPCs. For example, nanoparticles functionalized with PEG and PAA

can be assembled into different structures depending on the respective chain lengths, as shown schematically in Figure 7.2(a). Structure factor for assemblies obtained by this approach showed a single peak that shifts to lower values for longer PEG chains, indicating larger inter-particle distances (Fig. 7.2(b)). We hypothesize that the low crystallinity of the assemblies is due to the low grafting density of PAA on gold nanoparticles. Thus, by optimizing the grafting density and the molecular weight of the polymers, this approach can also lead to the formation of BNSL.

7.2.1.3 Self-assembly of nanoparticles functionalized with stimuli-responsive polymers

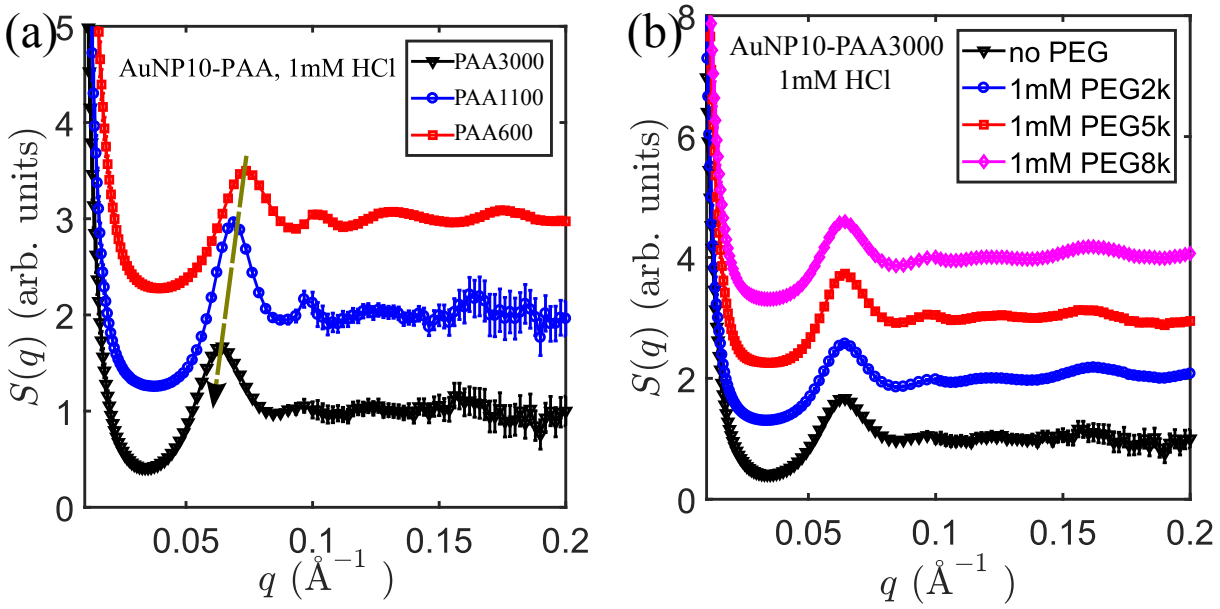

Figure 7.3. Structure factors for assemblies of AuNP10-PAA with varying PAA lengths, in the presence of 1 mM of HCl, without PEG (a), and with PEG (b).

Nanoparticle assemblies that can be reversibly assembled and disassembled using external triggers such as pH, salt and temperature. Different polymers such as PDEAEM, PNIPAM and Pluronics show phase changes in the room temperature range and they can be harnessed to obtain stimuli responsive nanoparticle assemblies. Polyacids such as poly(acrylic acid) show pH dependent conformation changes. At low pH, PAA is almost completely protonated and hence can form intra- and inter-chain hydrogen bonds, leading to nanoparticle assembly. Using atom transfer radical polymerization (ATRP) techniques, we have synthesized thiol-terminated poly(acrylic

acid) of varying molecular weights and functionalized gold nanoparticles with these polymers, following similar procedure as explained in our earlier work.[5] Figure 7.3(a) shows the structure factor of assemblies of PAA functionalized gold nanoparticles at low pH of ~ 3. Increasing molecular weight of PAA leads to increasing inter-particle distance in the assemblies. However there is only short ranged order, possibly due to the low grafting density of PAA. Adding PEG to these assemblies, so as to form IPCs, did not effect the structure factor (Fig. 7.3(b)).

Poly(N-isoprylacrylamide) (PNIPAM) is a well studied temperature responsive polymer that has a LCST at $\sim 32.4^{o}$C in aqueous solutions and shows a coil to globule transition as the temperature is raised beyond its LCST.[6,7] However, nanoparticles that are functionalized with PNIPAM do not show any significant phase change when the solution temperature is varied across the LCST.[8,9] In the presence of salts in the suspension, increasing the temperature induces aggregation of nanoparticles where the critical temperature depends on the salt concentration.[8,10] We investigated the salt dependent temperature responsive behavior of PNIPAM functionalized gold nanoparticles using SAXS and the results are shown in Figure 7.4(a). At room temperature, the assemblies formed with 0.5M NaCl show a FCC-like structure whereas at 80^{o}C, the second peak is taller than the first. Origins of this anomaly are not clear and further exploration of the effect of temperature on these assemblies is needed.

Similar to PEG, PNIPAM can also form IPCs with PAA. We obtained assemblies of PNIPAM functionalized gold nanoparticles with PAA. Strucutre factors obtained from SAXS of these assemblies are shown in Figure 7.4(b). Interestingly, assemblies are formed even in the absence of HCl and lowering the pH did not affect the structure factor significantly. This is likely due to the higher hydrophobicity of PNIPAM and the electrolytic properties of PAA. Increasing the temperature leads to sharpening of the peaks indicating improving crystallinity in the assemblies.

7.2.1.4 Self-assembly of nanoparticles onto patterned substrates via interpolymer complexation

The phenomenon of interpolymer complexation can be leveraged to obtain nanoparticle assemblies on solid substrates as shown in Figure 7.5(a). We functionalized template-stripped gold

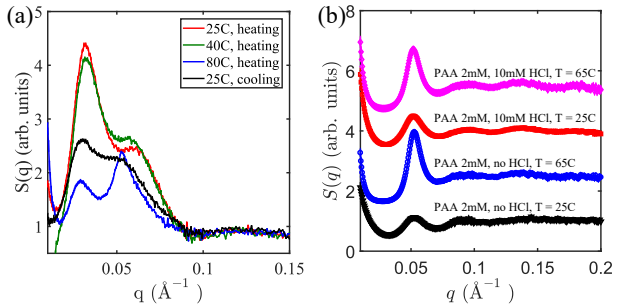

Figure 7.4. Structure factors for assemblies of AuNP10-PNIPAM with 2mM of PAA2k and HCl, at 25^{o}C and 65^{o}C.

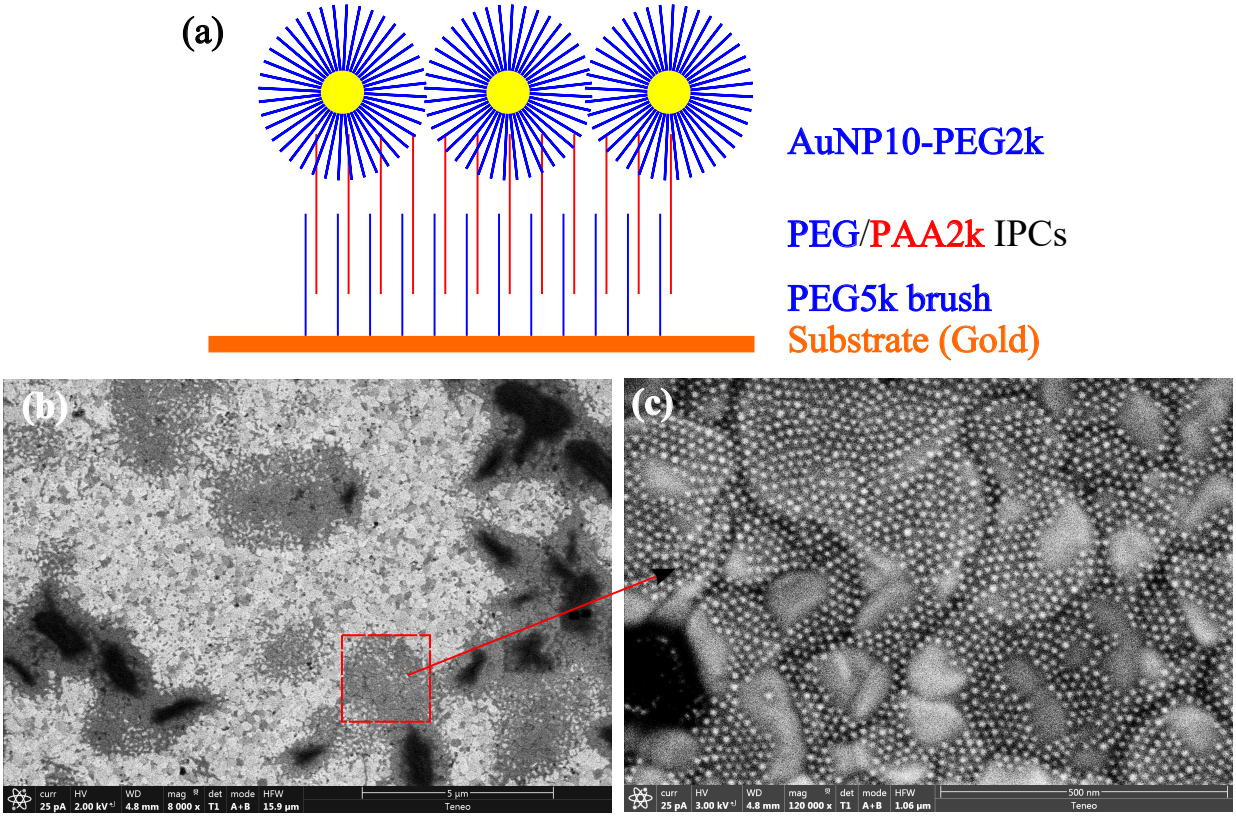

Figure 7.5. (a) Schematic of the procedure to obtain assemblies of nanoparticles on solid substrates using inter-polymer complexation. (b) and (c) SEM images of gold nanoparticle assemblies on template-stripped gold surfaces fabricated via inter-polymer complexation. The gold nanoparticles are functionalized with PEG2k while the gold substrate is functionalized with PEG5k. These results show that the assemblies are not formed uniformly over the surface, forming islands of monolayers and multilayers.

substrates with thiolated PEG2k and then treated the surface with 1mM of PAA2k, 1 mM of HCl and gold nanoparticles functionalized with thiolated PEG5k. The nanoparticles were let to assemble on the surface for 1 day after which the surface was rinsed with DI water and dried with nitro-

gen. Scanning electron microscopy (SEM) images of these surfaces showed that the nanoparticles had assembled into monolayers and multilayers with close-packing features in the monolayers (Fig. 7.5(b)). Tuning the parameters such as PEG brush lengths, PAA and HCl concentration, can lead to uniform monolayers on the surface. Further, patterns of PEG can be printed on the substrate by soft lithographic techniques to obtain large scale, patterned assemblies of nanoparticles.

7.2.1.5 Salt induced assembly of PVP functionalized nanoparticles

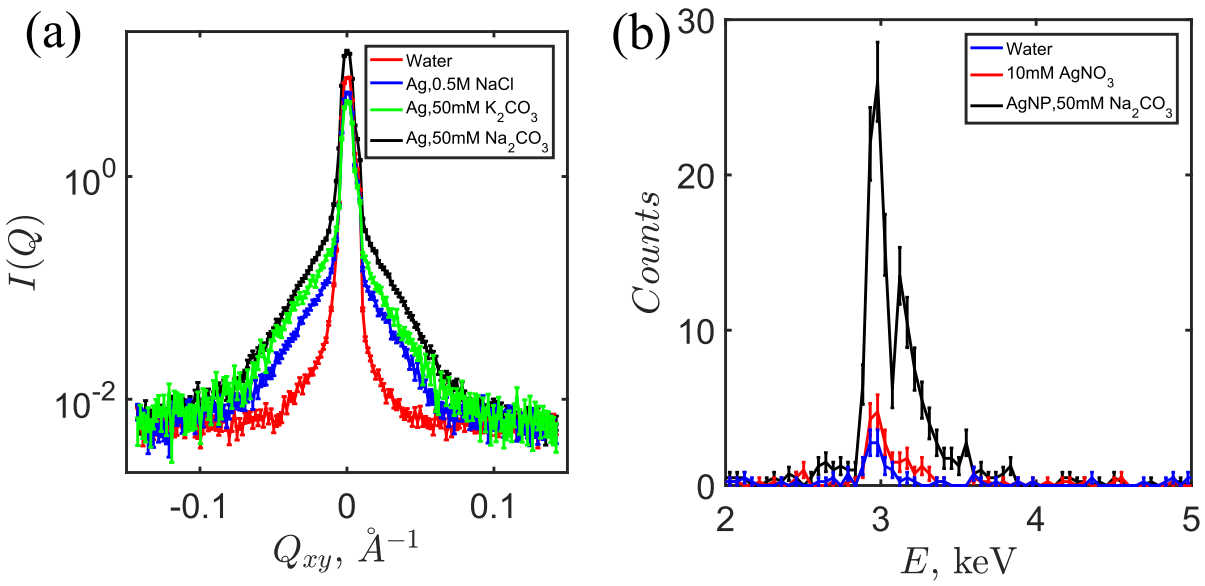

Figure 7.6. (a) GI-SAXS, and (b) GI-XRF results of liquid-vapor interface over the AgNP10-PVP solution with different salts.

Poly(vinyl pyrolidone) (PVP) is frequently used as a stabilizer in the synthesis of various metallic nanoparticles, especially silver nanoparticles. Given the unique plasmonic properties of silver nanoparticles, it is desirable to control self-assembly of these nanoparticles. Further, it is known that ligand exchange procedures with thiolated polymers lead to etching of silver NPs. One way to address this is use the properties of PVP coating on the synthesized NPs for self-assembly. Our preliminary experiments show that PVP-coated AgNP are salt responsive and populate the air-water interface when a salt is added to the suspension. Figure 7.6(a) shows GI-SAXS results obtained with 10 nm AgNP coated with 40kDa PVP, in the presence of various salts. The enhanced

intensity signal at low Q is consistent with the form factor of the nanoparticles, indicating the migration of nanoparticles to the air-water interface upon addition of salt. Absence of peaks indicates that the NPs are not correlated. Figure 7.6(b) shows the enhancement in fluorescence signals from Ag Lα and Lβ lines, corroborating the salt responsive interfacial assembly of PVP coated AgNPs. Based on these results, future experiments on the salt induced 2D and 3D assembly of PVP coated nanoparticles will be conducted.

7.2.2 Self-assembly of polymer functionalized nanoparticles with complexing block copolymers

Amphiphilic block copolymers such as Pluronic can show a range of microphases in their aqueous solutions depending on the chemical and physical conditions. Their ability to template the formation of various mesoporous oxides,[11] to stabilize metal nanoparticles[12] and their thermoresponsive behavior makes them an attractive candidate for the formation of assemblies of metallic nanostructures. Although Pluronic block copolymers mostly show face centered cubic or body centered cubic lattice structures, simulations predict that with suitable end modifications, they can co-assemble with nanoparticles to form lamellar and gyroid structures.[13] Depending on the relative affinity between the ends of the Pluronic chains and the nanoparticles, various morphologies in the nanocomposites have been predicted with increasing polymer and nanoparticle concentration in the gel.[13] Such effect of nanoparticles on the assembly of block copolymers has been reported in literature.[14–20] Utilizing these concepts, the following work is proposed.

7.2.2.1 Synthesis and characterization of gold nanoparticle – polymer nanocomposites with functionalized polymers and gold nanoparticles

Interactions between the nanoparticles and the polymer blocks are crucial in determining the phase behavior of the nanocomposites. As mentioned in the previous paragraph, by suitable end modifications of amphiphilic triblock copolymers like Pluronic, where the ends have high affinity to the nanoparticles, a variety of nanocomposite morphologies are predicted.[21,22] We have studied the assembly of PEG functionalized gold nanoparticles in Pluronic gels using SAXS. Pluronic F127

gels (30 wt%) show a FCC structure, and with the addition of AuNP5-PEG5k to the gels, the intensity is a sum of the gel's structure and the form-factor of the nanoparticles (Fig. 7.7). Thus the nanoparticles are stable and uniformly distributed in the gel, without affecting the gel's structure. Drying these gels leads to a lamellar structure, both with and without the gold nanoparticles.

Electrostatic forces between the nanoparticle and the polymers can also be used to assemble nanoparticles. We have synthesized pentablock copolymers of Pluronic with end blocks containing pendant tertiary amines that have pKa above 7. Gold nanoparticles stabilized by citrate, poly(acrylic acid) (PAA) and DNA have negative charges on the surface. It is expected that the negatively charged gold nanoparticles will have strong affinity to the positively charged ends on the pentablock copolymer. Further, formation of bicontinuous block copolymer morphologies (which are particularly attractive in obtaining chiral optical media) with electrostatic co-assembly of block copolymers and nanoparticles has been reported by several groups.[2,14,15] Thus future experiments on the mesoscale assembly of functionalized nanoparticles with block copolymers is proposed.

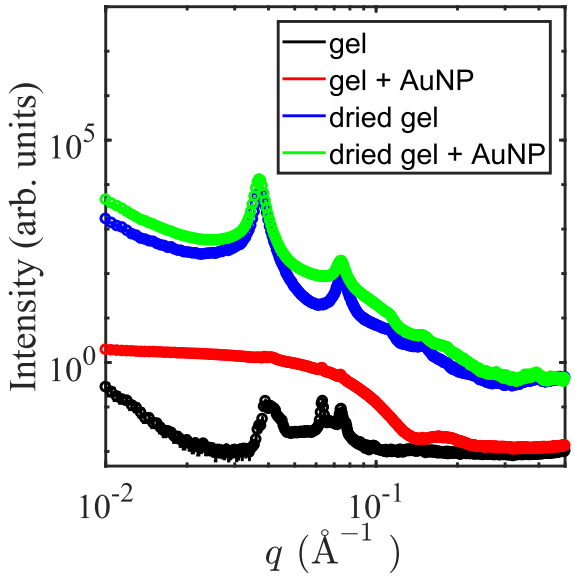

Figure 7.7. SAXS data for Pluronic gels mixed with PEG functionalized gold nanoparticles contained in capillaries as gels, and dried on kapton tape.

7.2.2.2 Electroless deposition of noble metals in gold nanoparticle – polymer nanocomposites

Continuous metallic films with structured voids between them have potential applications as metamaterials and photonic materials depending on their chirality, homogeneity and physical dimensions. Electroless deposition (ELD) in polymeric matrices produces networks of metals such as nickel and copper,[23,24] and is an established technology in depositing gold and silver on various substrates.[25,26] ELD requires a metal precursor, a reducing agent and a nucleating seed. The gold nanoparticles assembled in the previous step can be used as ordered array of seeds for ELD thereby retaining the periodic nature of the assembly in some dimensions. In fact, Pluronic itself acts as a reducing agent for Ag^+ and $AuCl_4^-$, especially at basic conditions.? We have found that uniform sized nanoparticles are formed by the reduction of $HAuCl_4$ in Pluronic gels under basic conditions, even in the absence of any seed particles. Figure 7.8(a) shows the SAXS data for dried gels synthesized by drying 27.3wt% Pluronic gels in 54 mM NaOH treated with different concentrations of $HAuCl_4$. The lamellar structure of the gels is not affected by the in-situ formation of gold nanoparticles in the gels. TEM images of the gold nanoparticles extracted from the gels show that they are fairly uniform in size and are spherical (Fig. 7.8(b)). Increasing the concentration of $HAuCl_4$ however was found to cause loss of gelation in the gels, and the formation of large irregular shaped gold crystals. Exploring the process parameters such as, block copolymer architecture, metal precursor, and reducing agents, for the formation of gyroid and lamellar phases with structural stability at high metallic loading is required to create these polymer-nanocomposites with unique optical properties.

In summary, we have developed novel synthesis and assembly procedures to obtain ordered structures of nanoparticles using self-assembling macromolecules. Challenges in the controlled assembly of nanoparticles into desired structures have been identified in this chapter, and a few proposals based on the results presented in this work have been put forth. In combination, these results pave the way for large scale fabrication of functional hybrid materials synthesized by bottom-up approaches, and have many potential applications in material science and engineering.

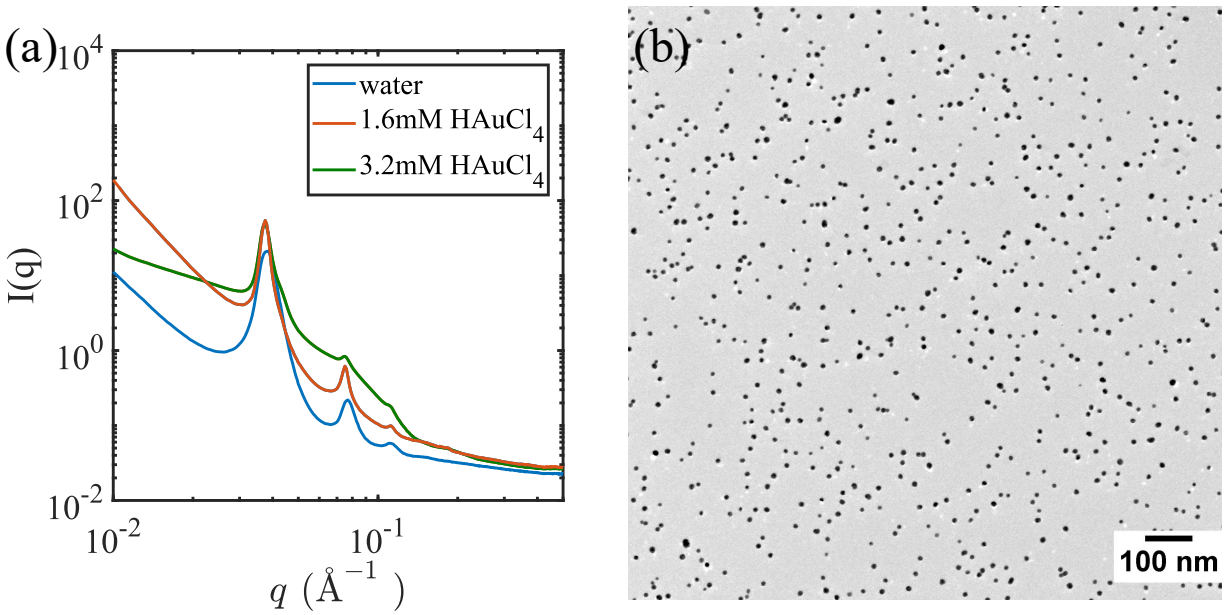

Figure 7.8. (a) SAXS data for dried Pluronic F127 gels in 54mM NaOH with varying amounts of $HAuCl_4$ showing the lamellar structure. (b) TEM of the gold nanoparticles extracted from the gels.

References

[1] Liu, X., Zhang, H., Nayak, S., Parada, G., Anderegg, J., Feng, S., Nilsen-Hamilton, M., Akinc, M., and Mallapragada, S. K. *Industrial & Engineering Chemistry Research* **54**(42), 10284–10292 (2015).

[2] Zhang, H., Wang, W., Mallapragada, S., Travesset, A., and Vaknin, D. *Nanoscale* **9**(1), 164–171 (2016).

[3] Park, S. Y., Lytton-Jean, A. K. R., Lee, B., Weigand, S., Schatz, G. C., and Mirkin, C. A. *Nature* **451**, 553 (2008).

[4] Nykypanchuk, D., Maye, M. M., van der Lelie, D., and Gang, O. *Nature* **451**(7178), 549–552 (2008).

[5] Zhang, H., Nayak, S., Wang, W., Mallapragada, S., and Vaknin, D. *Langmuir* (2017).

[6] Wu, C. and Wang, X. H. *Physical Review Letters* **80**(18), 4092–4094 (1998).

[7] Du, H., Wickramasinghe, R., and Qian, X. *The journal of physical chemistry. B* **114**(49), 16594 (2010).

[8] Yusa, S. I., Fukuda, K., Yamamoto, T., Iwasaki, Y., Watanabe, A., Akiyoshi, K., and Morishima, Y. *Langmuir* **23**(26), 12842–12848 (2007).

[9] Jones, S. T., Walsh-Korb, Z., Barrow, S. J., Henderson, S. L., del Barrio, J., and Scherman, O. A. *ACS Nano* **10**(3), 3158–3165 (2016).

[10] Maji, S., Cesur, B., Zhang, Z., De Geest, B. G., and Hoogenboom, R. *Polym. Chem.* **7**(9), 1705–1710 (2016).

[11] Yang, P., Zhao, D., Margolese, D., Chmelka, B., and Stucky, G. *Nature* **396**(6707), 152–155 (1998).

[12] Sakai, T. and Alexandridis, P. *Langmuir* **20**(20), 8426–8430 (2004).

[13] Sknepnek, R., Anderson, J. A., Lamm, M. H., Schmalian, J., and Travesset, A. *Acs Nano* **2**(6), 1259–1265 (2008).

[14] Jang, S. G., Kim, B. J., Hawker, C. J., and Kramer, E. J. *Macromolecules* **44**(23), 9366–9373 (2011).

[15] Kim, B. J., Fredrickson, G. H., Hawker, C. J., and Kramer, E. J. *Langmuir* **23**(14), 7804–7809 (2007).

[16] Kim, S., Yoo, M., Kang, N., Moon, B., Kim, B. J., Choi, S.-H., Kim, J. U., and Bang, J. *ACS Applied Materials & Interfaces* **5**(12), 5659–5666 (2013).

[17] Yoo, M., Kim, S., Jang, S. G., Choi, S.-H., Yang, H., Kramer, E. J., Lee, W. B., Kim, B. J., and Bang, J. *Macromolecules* **44**(23), 9356–9365 (2011).

[18] Villaluenga, I., Chen, X. C., Devaux, D., Hallinan, D. T., and Balsara, N. P. *Macromolecules* **48**(2), 358–364 (2015).

[19] Nam, T. W., Jeong, J. W., Choi, M.-J., Baek, K. M., Kim, J. M., Hur, Y. H., Kim, Y., and Jung, Y. S. *Macromolecules* **48**(21), 7938–7944 (2015).

[20] Ku, K. H., Shin, J. M., Klinger, D., Jang, S. G., Hayward, R. C., Hawker, C. J., and Kim, B. J. *ACS Nano* **10**(5), 5243–5251 (2016).

[21] Knorowski, C. D., Anderson, J. A., and Travesset, A. *Journal of Chemical Physics* **128**(16) (2008).

[22] Anderson, J. A., Sknepnek, R., and Travesset, A. *Physical Review E* **82**(2) (2010).

[23] Hsueh, H. Y., Huang, Y. C., Ho, R. M., Lai, C. H., Makida, T., and Hasegawa, H. *Advanced Materials* **23**(27), 3041–+ (2011).

[24] Cowman, C. D., Padgett, E., Tan, K. W., Hovden, R., Gu, Y., Andrejevic, N., Muller, D., Coates, G. W., and Wiesner, U. *Journal of the American Chemical Society* **137**(18), 6026–6033 (2015).

[25] Park, S. H., Prior, M. W., LaBean, T. H., and Finkelstein, G. *Applied Physics Letters* **89**(3) (2006).

[26] Yan, H., Park, S. H., Finkelstein, G., Reif, J. H., and LaBean, T. H. *Science* **301**(5641), 1882–1884 (2003).